Design of a Fast Antenna Characterization Method Exploiting Echoes

Mouad Djedidi

NNT: 2016SACLS348

Thèse de Doctorat

de

l'Université PARIS-SACLAY

préparée à

CentraleSupélec

ÉCOLE DOCTORALE N° : 575
Physique et Ingénierie : Électrons, Photons, Sciences du vivant (EOBE)

Spécialité de doctorat : Génie Électrique

Par

Mouad DJEDIDI

Design of a Fast Antenna Characterization Method Exploiting Echoes

Thèse présentée et soutenue à Gif-sur-Yvette, le 17/10/2016

Composition du Jury :

M. Jean-Yves DAUVIGNAC	Directeur de Recherche, LEAT	President du jury
M. Ala SHARAIHA	Professeur, Université de Rennes 1	Rapporteur
Mme. Susana LOREDO	Professeur, Université d'Oviedo	Rapporteur
M. Lars FOGED	Directeur Scientifique, SATIMO	Examinateur
M. Andrea COZZA	Professeur, CentraleSupélec	Directeur de thèse
M. Florian MONSEF	Maître de Conférences, Université Paris Sud	Encadrant et Invité

To my mother and father...
I hope you are always proud.

Acknowledgements

The works of this thesis have been carried out at the Laboratory of the Group of electrical engineering, Paris (GeePs), Pole of Electromagnetism (PIEM). I had the privilege of being surrounded by outstanding people, who had faith in me, and supported me throughout this journey, and to whom I 'll be forever indebted for helping me come to this achievement.

First, I would like to express my deep gratitude for my thesis director, Prof. Andrea Cozza, who I would not be able to thank enough for all what he did during my thesis. Thank you for believing in me, even when I did not. Thank you for your faith, help, understanding, and devotion. Thank you for your precious advises as well. I really consider myself lucky having you as a thesis director.

I would also like to thank my supervisor Dr. Florian Monsef. What an exceptionally nice person to work with. Thank you for your endless patience, support and guidance. I learned a lot working by your side both at professional and personal level.

I would like to thank Prof. Susana Loredo from University of Oviedo and Prof. Ala Sharaiha from Université de Rennes for accepting to review and evaluate my work. Many thanks to Prof. Jean Yves Dauvignac from Université de Nice Sophia-Antipolis and to Mr. Lars Foged, scientific director at MVG for accepting our invitation to take part of the defense committee.

I wish to address special thanks to all the GeePs and L2S laboratories staffs who crossed my path during this thesis. Many thanks to directors Prof. Claude Marchand and Prof. Silviu Niculescu who provided all necessary conditions for the success of this work, and to Prof. Lionel Pichon, director of PIEM, who was very supportive and always available to help us.

The list of amazing people who crossed my path is fortunately long. It was a joy sharing my office with Henri Vallon, Philippe Meton, and Guillaume Defrance. Thank you for your help, and for the memories. Special thanks to Mohamed Farouq, Moussa Kafal, Mohammed Serhir, Abdulrahman Yusuf, Mohammad-Waseem Arab, Mohammad Ibrahim, Djawad, Sofiane, Seif, Fethi, Abdelkerim and all who I did not mention but took any part of this amazing journey.

Words cannot express how deep I am grateful to be the son of Abdelkamel and Ouafa. Making you forever happy and proud is my ultimate dream.

I am grateful to my wife Saida, and to my little angle Khadija, simply for taking part in my life, giving me reasons to smile, and to move on everyday.

I thank God for his endless Mercy and blessings, among which the fulfillment of this work.

Summary

Current antenna radiation pattern measurement techniques share a common paradigm which states that useful information is exclusively carried by the generated test signal. This implies an excessive, time consuming, mechanical effort by rotating the antenna under test or displacing the probe system in order to cover different measurement angles until a complete scan is performed; a limitation that is typically overcome using costly multi-probe systems. Moreover, any reflection from the measurement site and test equipment is considered spurious as it perturbs the test signal and thus is minimized.

In this thesis, an antenna radiation pattern measurement concept challenging this common paradigm is introduced as a mean of accelerating the characterization process using cost-efficient systems. The proposed paradigm consists in the generation of a set of controlled echoes, using set-ups involving highly-reflective plates, which would directly contribute to the measurement alongside the line-of-sight signal by covering different measurement angles, and retrieving the ARP information carried by the set of all generated signals concurrently. Frequency diversity is used in order to generate a balanced system of equations where the unknown ARP vector is retrieved by inverting a matrix problem. Consequently, a considerable attention is paid into the conditioning of the mathematical model in order to ensure the system stability and accuracy.

Three configurations of different complexity levels in terms of controlled echoes are studied, with focus on the simplest configuration involving a single controlled echo. Models have been developed with design guidelines for the proposed configurations in terms of set-up dimensions and operating frequency bandwidth highlighting the mathematical viability of the concept. Practical issues were also assessed by studying the tolerance of developed models to systematic practical errors, as well as to the impact of an applied set of simplifying assumptions. The feasibility of the concept as well as its usefulness in accelerating the measurement process with respect to classical techniques were highlighted via numerical simulations. This thesis opens the door for exploiting echoes, generally regarded as a nuisance, in an antenna measurements context.

Contents

List of Figures

List of Tables

General Introduction

The work of this dissertation relates to the field of Antenna Measurement, more precisely Antenna Radiation Pattern (ARP) Measurement. ARP measurement aims at determining the antenna radiation pattern, which describes the angular distribution of the radiated energy by the antenna. This key characteristic is very relevant for applications involving antennas of all types, and is used in order to retrieve other important properties such as directivity and gain.

The fast development and growth of the telecommunication industry, especially over the last decade, and its generalization to everyday life have extended the role of antennas from classical fields, such as radio broadcasting and defense, to a larger scale of applications. The development and commercialization of modern intelligent systems, and the rise of connectivity concepts such as the Internet of Things (IoT), helped antennas conquering modern electronic devices and equipment. For instance, modern cars can have up to 24 different antennas installed up and on the vehicle [1]. A number that is expected to further rise in the upcoming years. Accordingly, a reliable knowledge of the radiation characteristics of deployed antennas is crucial for the proper functioning of the integral system. These characteristics, which include the ARP, the radiation efficiency, the operating bandwidth, etc., are generally retrieved and tested via measurement. This explains the relevance of the antenna measurement field in radio engineering from both industrial and academic point of views.

Several ARP measurement schemes and procedures have been developed and enhanced during the last century [2]. They are generally classified in terms of measurement conditions implied -in part- by the distance at which the measurement is performed into two categories: *Far-Field* (FF) techniques [3], and *Near-Field* (NF) techniques [4]. Although these techniques are exposed to different sets of non-idealities, they share the same type of *anechoic* measurement environment in which only the generated test signal is considered, whereas specular reflections from the measurement site and test equipment are minimized and discarded during the characterization process [5]. This follows from the common measurement paradigm forming the basis of classical measurements, which consists in acquiring the information carried by the generated test signal in order to retrieve the Antenna-under-Test (AUT) radiation characteristics in the corresponding measurement direction. Accordingly, any sort of reflection from the measurement site and test equipment is considered spurious as it perturbs the test signal value. In view of this, two main limitations of classical ARP measurement techniques may be outlined. The first limitation consists in the mechanical displacement effort needed to perform a complete

measurement. Commonly, either the AUT is rotated or the probe system is moved in order to acquire ARP information corresponding to different directions until a complete scan is achieved. This would result in an excessive measurement time which may be too expensive from an industrial point of view. Several techniques have been developed in order to overcome this limitation, most commonly multi-probe systems [6], which however come with higher cost with respect to traditional systems. The second limitation is related to the cancellation of echoes and specular reflections from the measurement site. Typically, ARP measurements take place indoor in *Fully Anechoic Chambers* (FAC) whose walls, floor and ceiling are covered with microwave absorbing material which in addition to its high cost, its maintenance should be taken into account.

Very recently, efforts have been made in order to characterize antennas in diffusive environments, i.e., in Reverberation Chambers (RC) [7][8][9][10][11]. The main advantage of RCs with respect to FACs is their relatively low installation and maintenance cost. However, counter-intuitive as it may seem, the developed techniques are performed in diffusive environments essentially to emulate free-space measurement conditions; as the targeted information is exclusively carried by the Line-of-Sight (LOS) signal between the source and the AUT, and hence contributions of various reflections resulting in the measurement site are discarded. Accordingly, these techniques share the same limitations in terms of mechanical displacement and measurement time as classical techniques.

The main thrust of this thesis is the growing need for faster ARP measurement capabilities. A novel rapid ARP measurement concept based on a principle of a spatial diversity that allows the acquisition of several ARP values corresponding to different measurement angles in each mechanical displacement is developed. The proposed concept provides a substantial novel contribution in the sense that the highlighted spatial diversity allowing to accelerate the measurement process is generated by exploiting echoes. Although echoes are exploited in other fields, such as in telecommunication with the notion of multi-path propagation [12] [13], to our knowledge the present work is the first contribution to exploit echoes in an antenna measurement context in order to accelerate the characterization process. The particularity of the proposed concept with respect to techniques performed in RCs is that echoes are generated in a controlled fashion. Hence, a deterministic approach is used in order to retrieve their characteristics rather than the statistical approach applied in reverberating environments. The concept have been numerically validated with promising results. A patent application on the concept has been published by the French *Institut National de la Propriété Industrielle* under the number WO2016055739 (A3).

The manuscript is organized as follows. The first chapter introduces basics of ARP measurement theory and necessary tools in order to develop the proposed concept. Then, classical measurement techniques as well as recently developed concepts are briefly presented with a discussion of common limitations. A global insight into the proposed concept is then provided with an outline of the thesis objectives.

The remaining chapters may be split into two parts. Chapters 2, 3 and 4 handle in detail the simplest form of the proposed concept in terms of controlled echoes, the single-plate configuration. In this case, a single controlled echo is generated and its contribution into the ARP measurement along with the LOS signal is assessed. Chapter 2 presents a detailed study of the model viability from a pure mathematical point of view. The problem being in matrix form, a conditioning study of the system matrix is conducted to verify the possibility of achieving well-conditioned systems using affordable measurement parameters in terms of set-up dimensions and operating bandwidth. A study of the configuration usefulness in reducing the mechanical displacement effort and thus accelerating the measurement process is also presented, with AUT rotation algorithms allowing to achieve maximum efficiency with respect to classical measurement, thus by cutting the measurement time by a factor of 2. Once the mathematical viability is assessed, a study of the model practical limitations is conducted in Chapter 3 in order to verify its physical viability. The tolerance of the developed model to practical systematic errors, and the impact of physical phenomena that are not taken into account in the mathematical formulation are assessed. After that, Chapter 4 presents numerical results highlighting the soundness of the concept and the effectiveness of the adopted model.

The second part, Chapter 5, explores the possibility of extending the proposed concept to more complex configurations involving more than a single controlled echo. After a brief discussion about possible methods of generating multiple controlled echoes, two configurations are studied based on results obtained with the single-plate configuration. The first configuration, the right dihedral configuration, allows the generation of three controlled reflections, while the second, the parallel plates configuration, allows the generation of an infinite set of controlled echoes. The soundness of developed models as wells as their theoretical efficiency in accelerating the measurement process are highlighted via numerical results.

Finally, a general conclusion regrouping the achievements of this thesis, as well as perspectives for future work are provided.

Chapter 1

Antenna Radiation Pattern Measurements - Context and Objectives

Contents

This chapter introduces the thesis research topic, *Antenna Radiation Pattern Measurement*. A theoretical background is first provided with definitions of key terms and basics of ARP measurement theory. Then, classical ARP measurement techniques and facilities are briefly presented, with focus on common limitations due to the underlying concepts. The objectives of the thesis are then detailed with a global insight into the proposed concept.

1.1 Introduction

The main objective of this thesis work is the development of a rapid ARP measurement concept challenging the common measurement paradigm forming the basis of state-of-the-art techniques which states that useful information is exclusively carried by the generated test signal. In this chapter, a brief introduction into ARP measurement theory is provided with definition of key terms and necessary tools to develop the proposed concept. An insight into common ARP measurement techniques is also provided in order to highlight their limitations in terms of mechanical effort and measurement time, which can be overcome using solutions involving expensive systems. It should be pointed out that antenna measurements bibliography is very wide and keeps expanding systematically with novel works aiming to improve the performance of classical techniques. However, the measurement paradigm being essentially the same as in classical techniques, the focus of this chapter is on classical techniques. Recent efforts aiming at performing ARP measurements in reverberating environments are briefly outlined in order to shed light on a possible misleading similarity with the proposed concept.

1.2 Theoretical Background

An antenna may be defined as any device capable of radiating or receiving electromagnetic waves [14]. Radiation characteristics of an antenna are defined by several figures, among which the ARP which describes the angular distribution of the radiated energy. Common types of ARPs are the field pattern which describes the angular distribution of the electric field intensity, and power pattern which is the radiated power per unit solid angle. In the present manuscript, ARP refers to the field pattern.

Other figures of merit characterizing antennas include the directivity D which compares the antenna radiated power in the direction of maximum emission to the power radiated by a lossless isotropic antenna. An isotropic antenna is a hypothetical antenna that radiates power uniformly in all directions. The radiation efficiency ϵ_R measures how much power is actually radiated by an antenna given an injected power by a transmitter. Multiplying the directivity by the radiation efficiency yields the antenna Gain G_a, which is more commonly quoted in antenna data-sheets as it regroups the two parameters. The operating bandwidth is the frequency range $[f_{min}, f_{max}]$ over which the antenna can operate properly; it is generally defined by an accepted return loss level, most commonly $S_{11} < -3$dB. The operating bandwidth is commonly specified by the *Fractional Bandwidth* (FBW), which is defined with respect to the central working frequency f_0 [15],

$$FBW = \frac{f_{max} - f_{min}}{f_0}. \tag{1.1}$$

Among the antenna characteristics affected by frequency is the ARP, whose sensitivity to the working frequency changes as function of the antenna type.

The ARP is a far-field concept; it describes the distribution of the radiated field at large distances from the antenna, commonly referred to as the far-field region. This region is characterized by a number of properties outlined hereafter,

- The absence of the radiated field radial component. The ARP, often expressed in spherical coordinates, is only function of the transverse components $\vec{F} = [F_\theta, F_\phi]$.
- The ARP is assumed unchanged with distance. Hence, each of the ARP transverse components only depends on the angular parameters θ and ϕ: $F_{\theta,\phi}(\theta, \phi)$.
- The electric field is dominated by the radiating component which represents the transmitted energy and whose amplitude dies off as the inverse of the radial distance r^{-1}. Reactive fields which represent the stored energy die off more rapidly as r^{-2} and r^{-3}, and hence are neglected in the far-field region.
- Assuming the AUT to be at the origin of the spherical coordinates system, the radiated electric field $\vec{E}(\vec{r})$ at some position in space $\vec{r}$ and the ARP value at the corresponding direction of generation are related by the far-field equation [1],

$$\vec{E}(\vec{r}) = G(r, f)\vec{F}(\theta, \phi), \tag{1.2}$$

  where $G(r, f)$ is the free-space Green's function which, in addition to the radial distance r, is function of the operating frequency,

$$G(r, f) = \frac{\mathrm{e}^{-\mathrm{j}kr}}{r}, \tag{1.3}$$

  where k is the wavenumber,

$$k = \frac{2\pi}{\lambda} = \frac{2\pi c}{f}, \tag{1.4}$$

  λ being the wavelength and c the speed of light. The free-space Green's function expresses the inverse distance dependence as well as the field phase. Note that the ARP vector is a complex quantity. However, most applications are concerned with the amplitude ARP rather than the complex representation.
- The radiated wave is locally plane and may be approximated B a plane wave. The electric and magnetic fields are perpendicular to each other and to the direction of propagation. The figure traced by the electric-field vector, while propagating, defines

[1] Notation: Arrow notation ($\vec{A}$) stands for geometrical vectors, bold notation (**A**) stands for matrix quantities, including one dimensional matrices (row and column vectors), whereas automatic font (A) describes scalar quantities.

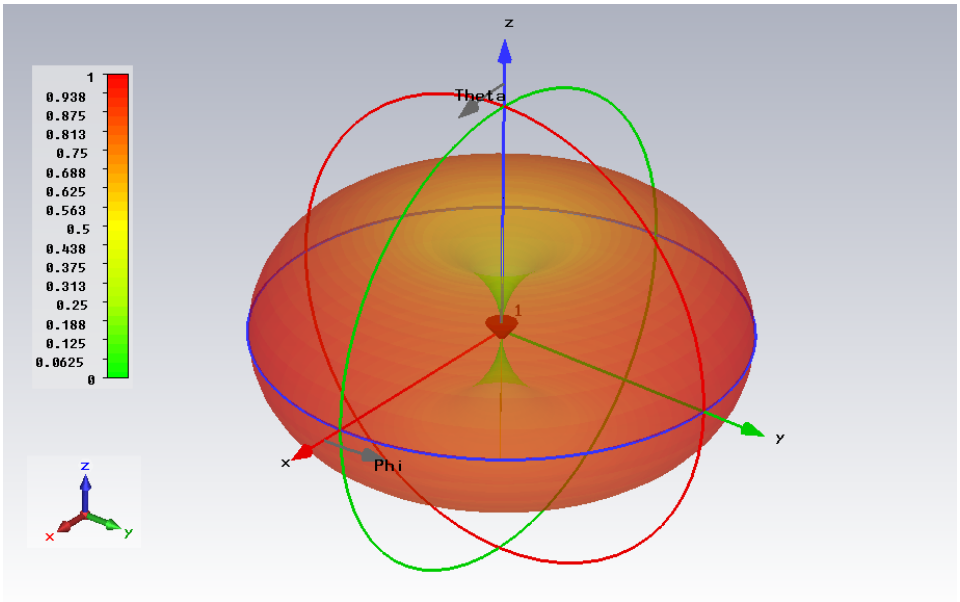

Figure 1.1 3D representation of a normalized ARP of a half-wave dipole operating at 1GHz retrieved via numerical simulation.

another fundamental antenna parameter, the *polarization*, which can either be linear, circular or elliptical.

A complete radiation pattern is three dimensional, and is obtained by scanning azimuthal angles between 0° and 360° and polar angles between 0° and 180°. An example of a 3D pattern is shown Fig. 1.1, which plots the ARP of a Half-Wave Dipole (HWD) operating at 1GHz. In practice, it is more convenient, and often sufficient, to measure a couple of 2D cuts over orthogonal planes. Common planar cuts are the E-plane which contains the electric field and the direction of maximum radiation, and the H-plane which contains the magnetic field and the direction of maximum radiation.

To conclude, the antenna radiation characteristics may be retrieved in transmit or receive modes. This follows from the principle of reciprocity, which is applicable to most antenna types, and which states that the antenna characteristics are the same in both modes. If the antenna is used in receive mode, the measurement requires the AUT to be illuminated by a uniform plane wave. The measurement direction (θ, ϕ) is estimated with respect to the antenna *phase center*, which is considered as the apparent radiation point [16].

1.3 Classical ARP Measurement Techniques

Several ARP measurement techniques have been developed -or are in the process of development- in order to retrieve ARPs. Depending the measurement conditions, implied in part by the distance at which the measurement is performed, theses techniques may be classified into two main

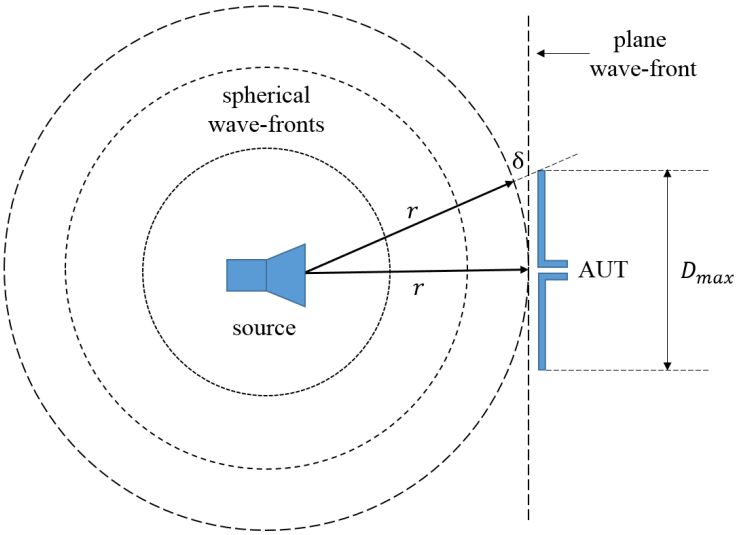

Figure 1.2 Estimating the the far-field distance as function of the AUT dimensions and the maximum tolerated phase tapper $k\delta$.

categories: far-field techniques and near-field techniques. In this section we are going to focus on classical measurement ranges, i.e., ranges that have been commonly used in order to perform ARP measurements.

1.3.1 Far-Field Range

Far-field techniques were naturally the first type of measurement techniques to be developed and used in order to perform ARP measurements. In the far-field range, the measurement distance is chosen such that far-field conditions are met. Although the actual far-field distance varies as function of the antenna type, a common criterion to estimate the far-field distance is given by the Fraunhofer distance,

$$d_{FF} = \frac{2D_{max}^2}{\lambda}, \tag{1.5}$$

where D_{max} is the maximum linear dimension of the radiating antenna. Although this criterion works well for a large scale of applications, it is an approximation that is based on a rather coarse assumption which is a maximum phase tapper of 22.5° over the tested aperture [17]. In order to understand this, refer to Fig. 1.2 which shows a measurement scenario where the AUT is in receive mode. The radii of spherical wavefronts radiated by the source augment as they propagate towards the AUT. Ideally, the AUT-source separation r would be infinite such that the incident wavefront on the AUT is planar. This not being the case, the incident wavefront on the AUT aperture is characterized by some curvature δ such that, [18],

$$(r+\delta)^2 = r^2 + \frac{D_{max}^2}{2}.$$

$$\delta = r\left(\sqrt{1+\left(\frac{D_{max}}{2r}\right)^2} - 1\right) \tag{1.6}$$

Assuming the AUT-source separation much larger than the AUT dimensions, Eq. 1.6 reduces to,

$$\delta = r\left(1+\frac{1}{2}\left(\frac{D_{max}}{2r}\right)^2 - 1\right) = \frac{D_{max}^2}{8r} \tag{1.7}$$

Setting the maximum tolerated phase tapper to 22.5°,

$$k\delta \leq \frac{\pi}{8}, \tag{1.8}$$

and using Eq. 1.7 to update the expression of δ yields the Fraunhofer distance (Eq. 1.5). This criterion is intended to reduce the far-field distance required to perform far-field measurements which, despite the applied approximation, may be very large for low frequency applications, or when the AUT size is large.

As function of the measured antenna and the working frequency, the far-field range may be installed outdoor or indoor. If installed outdoor, the AUT, generally in receive mode, is mounted over an elevated structure, such as a tower, real estate, or a mountain in order to protect it from environmental error sources mainly the specular reflections from objects surrounding the test zone. Guidelines on the measurement parameters, such as the range distance, heights of the AUT and the source above the ground, the type of the source antenna, etc., are detailed in [3].

An *elevated* range is characterized by the source antenna being also mounted over a high structure. A graphical representation of an elevated range is depicted in Fig. 1.3a [19]. The source antenna is chosen such that the corresponding field amplitude tapper over the AUT is less than 0.25dB, with its null being oriented towards the test tower base in order to minimize ground reflections. The height of the test tower is typically greater than $4D_{max}$. An alternative configuration requiring less real estate is the *slant* range, in which the source antenna is located close to the ground while pointing towards the AUT. Both configuration are generally referred to as free-space ranges as only the LOS signal is considered during the measurement whereas reflections from the ground and objects in the surrounding environment are minimized.

Another type of outdoor far-field ranges is the *ground reflection* range, in which the specular reflection from the ground is considered, as shown in Fig. 1.3b [20] [21, p. 1003]. This type of range is suitable in order to test antennas with large main lobes which would be very sensitive to ground reflections in free-space ranges. Hence, the range distance and the two antennas heights are adjusted such that the LOS signal and the specular reflection from the ground interfere constructively in the AUT region. This would yield wavefronts of uniform amplitude and phase

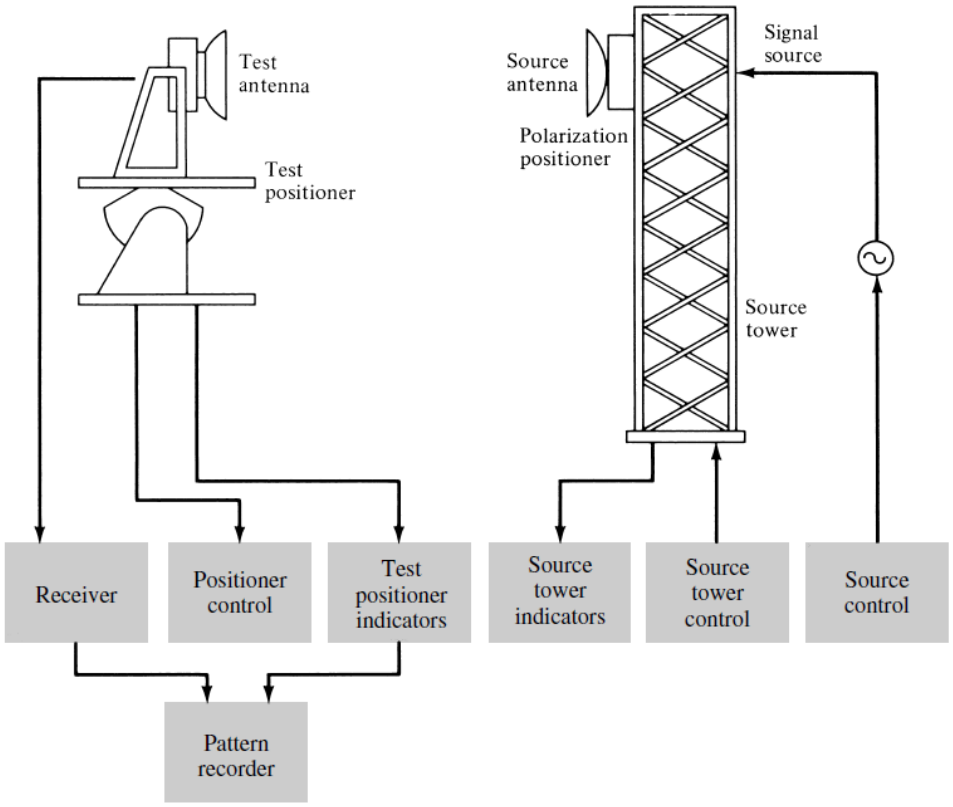

(a)

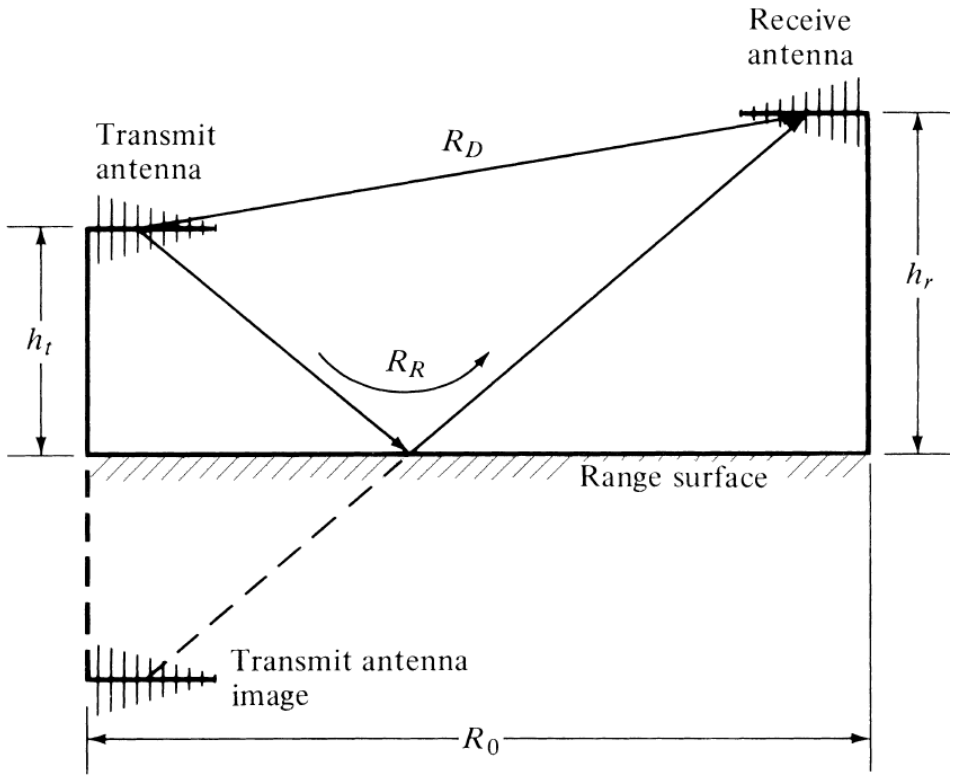

(b)

Figure 1.3 Typical outdoor far-field ranges allowing to preform direct ARP measurement (Images retrieved from [21]): (a) elevated range (b) ground reflection range.

distributions creating a *quiet* zone around the AUT. It is important to keep in mind that during the post-processing step only the LOS contribution is exploited in the characterization process. The ground reflection range requires the range surface to be smooth, along with reliable estimation of the ground reflection coefficient. In Fig. 1.3b, image theory [22, pp. 103-106] is used in order to model the specular reflection from the ground as if it were generated by a virtual source antenna, commonly referred to as the antenna *image*.

Generally, the measurement procedure in the presented ranges consists in fixing the source antenna orientation towards the center of the AUT, while rotating the AUT around the θ and ϕ rotational axes in order to retrieve the ARP sample corresponding to each targeted direction (θ, ϕ). Clearly, this procedure requires excessive mechanical rotation effort in order to perform a conventional measurement which results in a long measurement time.

Other limitations of traditional outdoor far-field ranges include,

- The range is exposed to several error sources, mainly the various reflections from the ground and objects in the surrounding environment, and parasitic electromagnetic radiations coming from other applications, making it difficult to keep the overall measurement error below an accepted level.
- The measurement is limited by climatic conditions.
- The range distance may be too large for measurements involving large AUTs or low operating frequencies.

Performing ARP measurements indoor, typically in fully anechoic chambers (FAC), provides the advantage of a more protected environment against spurious reflections, parasitic electromagnetic radiation, and climatic conditions. Far-field distances may be adapted to typical FAC dimensions for applications involving AUTs of small dimensions.

1.3.2 Compact Range

Compact Antenna Test Ranges (CATR) were developed in the sixties in order to allow performing direct far-field measurements in indoor facilities [21, pp. 1006-1014]. The CATR concept consists in creating far-field measurement conditions at distances considerably smaller than conventional far-field distances. This is accomplished by using a parabolic reflector which transforms the spherical wave generated by the source antenna into a plane wave propagating as a collimated beam towards the AUT, as shown in Fig. 1.4a. The AUT is positioned within a quiet zone whose dimensions are dictated by the size of the reflector (typically $50\% - 60\%$ of the reflector size), and over which the waves' amplitude and phase tappers depend on the reflector surface quality [23]. The CATR requires meeting free-space conditions for a reliable measurement, which is implied by the paradigm stating that useful information is exclusively carried by the test signal; the collimated signal from the parabolic reflector in this case. Accordingly, the LOS signal

between the source and the AUT, reflected signals from the test equipment and chamber walls, floor, and ceiling, as well as the diffracted fields by the reflector edges are all minimized. CATRs are generally installed in anechoic chambers [24] whose interior is fully covered by microwave absorbers in order to meet free-space requirements. The edge diffraction problem is minimized by using reflectors of special shapes intended to direct diffracted fields away from the quiet portion of the test zone. Figs. 1.4b-1.4c show respectively two of the most commonly used reflector types: the serrated-edge reflector which offers a good performance at medium and high frequencies for a relatively low price, and the rolled-edge reflector which offers a considerably better performance but for a higher price [25].

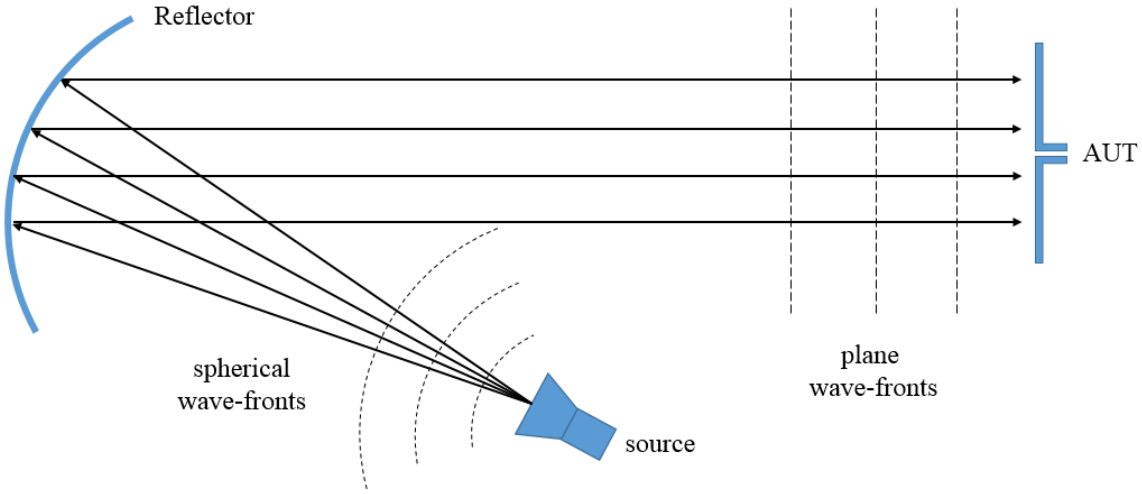

(a)

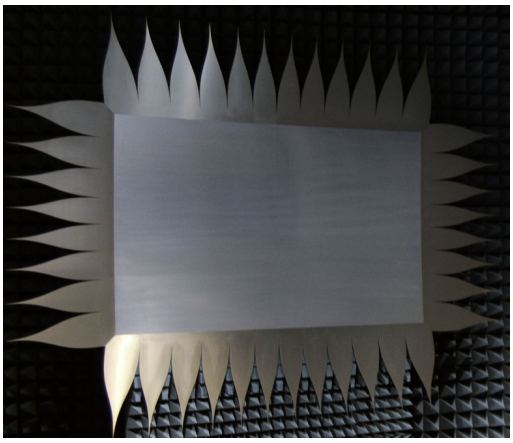

(b)

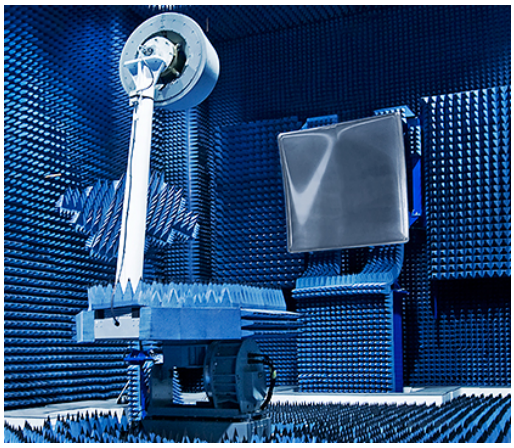

(c)

Figure 1.4 CATR allowing to perform direct far-field ARP measurement indoor: (a) graphical representation of the measurement scheme (b) serrated edge reflector (c) rolled edge reflector[2].

[2]Commercial reflectors designed by MVG, http://www.orbitfr.com/

As for traditional free-space far-field ranges, the CATRs are limited in terms of mechanical rotation and measurement time. This follows from the highlighted fact that only the collimated test signal is considered useful for the measurement whereas all other signals likely to interfere with the test signal are treated as spurious and are minimized. This implies one measured ARP sample per mechanical rotation. Another limitation of CATRs is generally its low performance at low frequencies (less than 1GHz). The lower frequency of operation of a CATR is determined by the size of the reflector to be typically about $25\lambda_1 - 30\lambda_1$, λ_1 being the largest operating wavelength. Apart from the fact that this would dictate larger reflector size, the amplitude ripple is generally higher at low frequencies. Moreover, as we are going to show in Chapter 3, the edge diffraction problem is amplified at low frequencies, which reduces the accuracy of the measurement.

Recent research works investigated the synthesis of plane waves for CATRs using other means mainly an array of source antennas [26] [27] and feed scanning [28]. In the first technique the phases of the fields generated by the different source antennas are adjusted such that they interfere constructively creating a quiet zone in the AUT region. This method requires sophisticated electronics for the feed system and shares the same limitations in terms of mechanical displacement and measurement time as the traditional CATR. In the second technique, a single source antenna is moved to different positions and the corresponding measurements are weighted in order to retrieve the ARP value corresponding to a single direction, which obviously requires more mechanical displacement effort and results in an even longer measurement time with respect to classical techniques.

1.3.3 Near-Field Range

The near-field range allows performing ARP measurements at very short distances from the AUT without fulfilling far-field conditions [4]. The ARP is retrieved by performing analytical NF-FF transforms. Based on Huygens principle [29], the tangential components of the near field generated by the AUT, which is generally in transmit mode, form a set of sources which reproduce the AUT radiation characteristics. A probe is used to measure these fields over a preselected surface, which may be planar, cylindrical or spherical. The complexity of analytical transforms, the sophistication of the measurement software and equipment, and the range of applications of the NF model augment from the planar to the cylindrical, and from the cylindrical to the spherical models. Sampling formulas for the probe positions exist for each model. The modal expansion principle [30] is then used in order to predict the field distribution at any distance from the AUT, including infinity which corresponds to the far-field ARP.

Near-field techniques are very popular and has attracted the attention of both industry and academia due to the advantages they offer, mainly the measurement accuracy and the small range dimensions, which resulted in a systematic improvement of the developed models. Nevertheless, one main limitation of NF techniques is the necessary mechanical displacement

effort to move the probe over the specified grid of positions which increases the measurement time. Multi-probe systems [6] have been developed in order to overcome this limitation. These systems, which involve complex microwave multiplexers are however considerably expensive. Alternative solutions to accelerate the measurement with less complex systems are the so called *indirect NF* methods, as opposed to the described classical approach which is referred to as the *direct NF* method [31]. Indirect measurements make use of the *Modulated Scatterer Technique* (MST) in which the field diffracted by a small probe is used in order to retrieve the AUT radiation characteristics [32]. Using an array of modulated probes requires a cost-effective low frequency modulator. However, such a technique have other limitations such as the mutual coupling between the different array elements.

1.4 Characterization Environments

1.4.1 Anechoic Environment

Except the ground reflection range, all of the presented ARP measurement techniques share a measurement environment free from echoes. Free-space outdoor ranges are typically installed in open, isolated regions, whereas typical indoor measurements take place in anechoic chambers. Any sort of reflection from the measurement range is regarded as spurious and is minimized.

1.4.2 Reverberating Environment

Recent efforts were made in order to perform ARP measurements in diffusive environments, which unlike free-space environments, are characterized by a very large number of specular reflections having uniform amplitude distribution and generated in random directions. Such techniques were tested in reverberation chambers whose main advantage with respect to anechoic chambers is their relatively low installation and maintenance cost.

One such a technique was proposed in [7], which consists in extracting the LOS information by performing the same measurement for different stirrer orientations such that the scattered field has zero mean distribution [33]. Another technique was proposed in [9], and consists in performing the measurement for different AUT positions lying in the LOS path linking it to a probe. The ARP sample corresponding to the tested direction is retrieved by averaging the performed measurements in order to extract the LOS information. The same author proposed an improved technique [10] intended to reduce the additional measurement time implied by the number of necessary measurements required to retrieve a single ARP sample. This technique consists in performing a single measurement while moving the AUT over the LOS path linking it to a source antenna. Based on the Doppler effect, signals received by the AUT undergo different frequency shifts depending on their angles of arrival (AoA) which takes its maximum at the LOS signal level. This allows to filter out contributions of the different reflections and

evaluate the AUT response to the LOS signal exclusively in order to retrieve the associated ARP sample. The last technique [11] uses the *Time Reversal Electromagnetic Chamber* (TREC) in order to coherently synchronize the generated echoes such that a deterministic plane wave with high angular resolution is created. The developed concept proposes an interesting method for accelerating ARP measurements. After a characterization step of the test zone in the presence of the AUT, it consists in using a set of test signals each generating a different field distribution inducing different incidence angles of the synthesized plane waves. The concept is intended to characterize Ultra-Wideband (UWB) antennas as the related application of time reversal requires large operating bandwidths.

From what preceded, one may notice that, counterintuitive as it may seem, ARP measurements are performed in reverberating environments essentially in order to emulate free-space conditions, as echoes do not directly contribute into the measurement and useful information is exclusively carried by the test signal (generally the LOS signal). Accordingly, we may conclude that, generally, recent ARP measurement techniques in reverberating environment share the same limitations in terms of mechanical displacement and measurement time as traditional measurement techniques. The last concept, in particular, proposes an improved method in order to accelerate the measurement process, which is however limited by the preliminary characterization step of the test zone, which requires un automated system.

1.4.3 Controlled-Echo Environment

The last measurement environment which, up to this work, only counted the ground reflection range, is the controlled-echoes environment. This environment is characterized by the generation of echoes that are involved in the measurement. However, unlike the reverberating environment, echoes in this case are controlled, i.e., their characteristics are known and predictable in a deterministic fashion. The ground reflection range counted a single controlled echo which, however, does not directly contribute into the measurement and is used to in order to create a quite zone around the AUT.

1.5 General ARP measurements Limitations

Each measurement technique has its own advantages and limitations. In this section, interest is on general limitations that are shared at least by most of state-of-the-art techniques.

1.5.1 Mechanical Displacement and Measurement Time

From what preceded, it is clear that the common measurement paradigm adopted by traditional concepts, stating that useful information is exclusivity carried by the generated test signal, generally the LOS signal, implies excessive mechanical displacement effort in order to retrieve ARP samples corresponding to different directions which results in a long measurement time.

The common adopted solution to overcome this limitation consists in introducing a spatial diversity allowing to measure several ARP samples in each mechanical displacement using multi-probe systems. Such systems require complex software and hardware implementation and usually come with high price.

1.5.2 Measurement Errors

All ARP measurements are subject to sets of systematic practical errors which depend on the adopted range, on the used equipment, and on the tested antenna. This makes it difficult to quantify the impacts of the different error sources in a general context. Moreover, quantifying error requires comparing the measurement to some reference that would be an ideal direct far-field measurement, which is clearly unfeasible. Nevertheless, adequate error analysis combining analytical and experimental approaches have been performed providing a general insight into contributions of different error sources [34] [35]. The cited efforts have been performed in indoor anechoic environments in a context of near-field measurements. Such environment provides the advantage of a more controlled measurement with respect to outdoor far-field ranges which are subject to a number of random environmental error sources.

Based on these analysis, and excluding errors specific to near-field measurements, we may classify general practical error sources that are common to all types of ranges into four main categories,

- Mechanical errors: This family regroups errors related to the positioning and orientation of the antennas involved in the measurement. It includes axes pointing and orthogonality, alignment between the AUT and the probe, and measurement distance errors.

- Electrical Errors: This family regroups error related to the radiated field, such as the amplitude and phase drift and noise, the non-uniformity of the measured field, leakage and crosstalk, etc.

- Probe-related errors: Practical radiation characteristics of the used probes may deviate from the assumed ones.

- Stray signals: This family mainly includes the set of echoes and specular reflections from the measurement site and test equipment.

Experiments have shown that, generally, the last family is the largest source of ARP measurement error [34]. This explains the considerable attention that echo identification and cancellation techniques were given with respect to other error sources [5].

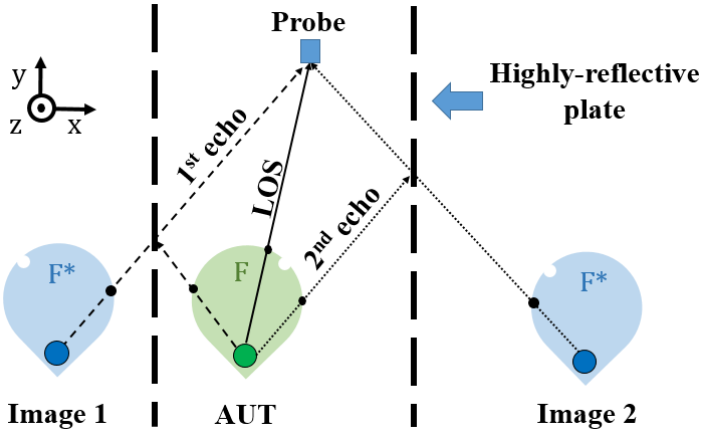

Figure 1.5 Configuration showing how controlled echoes bear useful information which is the ARP value at the corresponding angle of generation

1.6 Proposed Concept: Rapid ARP Measurement Exploiting Echoes

In the present thesis, an ARP measurement concept intended to accelerate the characterization process is proposed. The concept consists in the generation of a spatial diversity that allows retrieving several ARP samples for each mechanical displacement by exploiting *controlled* echoes. The measurement environment is then a controlled-echoes environment, but unlike the ground reflection range, echoes in this case directly contribute to the measurement. The key idea behind the concept is that echoes bear useful information: the ARP value at the corresponding direction of generation. The challenge is then how to retrieve this information.

A graphical representation of the proposed concept is depicted in Fig. 1.5. An AUT and a probe are placed within a set-up involving highly reflective plates. The AUT may be in transmit or receive modes. A transmit mode is considered throughout this work. By controlling the set-up dimensions, characteristics of generated echoes become predictable, including their number, angles of generation and paths traveled up to the probe. Using image theory, each echo may be modeled as a LOS signal generated by a corresponding image having the same radiation characteristics as the actual AUT. Hence, the configuration is equivalent to deploying several virtual sources which contribute into the measurement, as opposed to conventional multi-probe systems where the spatial diversity is created using real sources.

The field intercepted by the probe is the superposition of the fields generated by each source,

$$\vec{E} = \sum_{i}^{N_a} \vec{E}_i, \tag{1.9}$$

where each field is weighted by the ARP value of the corresponding direction of generation, N_a being the total number of sources, and thus the number of covered angles, which is equal to the number of generated echoes (images) N_i plus the LOS field,

$$N_a = N_i + 1. \tag{1.10}$$

Mathematically, the ability of retrieving the ARP samples corresponding to all considered signals requires generating a number of equations at least equal to the number of unknowns, i.e., N_a equations. One possible method to do so is to scale the set-up dimensions by moving the plates and the probe such that generated signals in the new configuration cover the same angles as the original configuration, and repeating the same process N_a times. This would, however, require an additional mechanical displacement effort with respect to traditional measurements which clearly contradicts the concept main objective, which is reducing the measurement time. The method proposed in this work to balance the mathematical model without introducing mechanical effort consists in scaling the set-up dimensions electrically by varying the operating frequency. Hence, the spatial diversity under-determining the mathematical model, is compensated by introducing frequency diversity. A closer insight into the proposed concept and to the related mathematical formulation is provided in the next chapter.

Chapter 2

Single plate Configuration: Theoretical Development

Contents

This chapter presents the proposed concept using the simplest configuration in terms of controlled echoes: the single-plate configuration. As a first step, the model is simplified in order to assess its viability from a pure mathematical point of view. The focus of this chapter is then the study of conditioning issues related to the mathematical model. Practical physical considerations are studied in the next chapter.

2.1 Model Presentation

The basic configuration in terms of controlled echoes generation is the single-plate configuration, which allows the generation of a single controlled echo, as shown in Fig. 2.1a. An AUT, in transmit mode, is positioned in the vicinity of a metallic plate, which is supposed lossless and sufficiently large to be considered as a perfect electric conducting (PEC) ground. If the AUT is assumed dimensionless, i.e., treated as a point source, then this configuration would result in the generation of two signals, the LOS signal which would directly impinge on the probe, and a reflected echo from the plate. If we assume a given radiation pattern F (see Fig. 2.1a), the wavefronts radiated by the AUT have amplitudes weighted by the ARP. As a consequence, the echo also bears a quite useful information: the value of the ARP at the corresponding angle of generation (black dots in Fig. 2.1a).

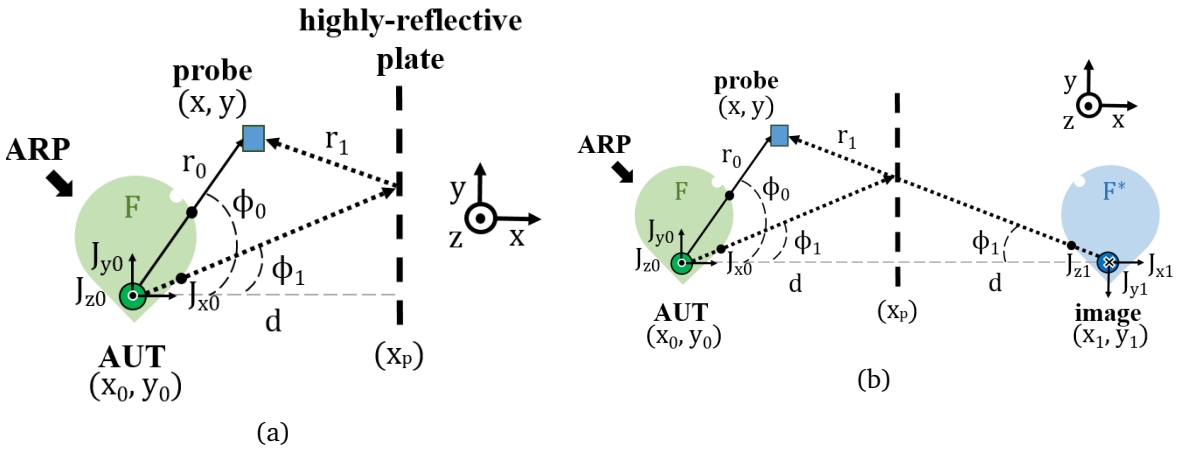

Figure 2.1 Configuration allowing the generation of a single controlled echo showing the related ARP information contained in it: (a) Physical representation (b) Equivalent representation using image theory.

With no loss of generality, the AUT and the probe are positioned in a common working 2D plane, namely the azimuthal *x*-*y* plane. The plate is parallel to the *y*-*z* plane at a distance *d* from the AUT. Controlling the set-up dimensions yields the ability of predicting the two signals path's characteristics. While predicting the LOS path is forward, the echo path is predicted by applying the law of reflection which implies that the echo angle of incidence on the plate is equal to the angle of reflection [36]. To simplify the procedure, it is convenient to model the configuration using image theory [22, pp. 103-106].

The equivalent image theory model of the configuration is shown in Fig. 2.1b. The effect of the PEC plate is modeled by an image of the AUT which is equidistant to the plate from

the shadow region. The set-up is then equivalent to handling two sources whose respective distances to the probe r_i and their angles of incidence ϕ_i can easily be expressed as follows,

$$r_i = \left[(x-x_i)^2 + (y-y_i)^2\right]^{1/2}, \quad i = 0,1, \tag{2.1}$$

$$\phi_i = \arctan\left(\frac{y-y_i}{x-x_i}\right), \quad i = 0,1, \tag{2.2}$$

the index 0 standing for the real source, whereas the index 1 stands for the virtual source. In this work the AUT will always be considered at the origin of the cartesian plane, hence $x_1 = 2d$, and $y_1 = y_0 = 0$. Placing both the AUT and the probe in the x-y plane with the plate being orthogonal to this plane implies that all the considered fields lie in this plane[1]. This particular configuration allows to perform measurement cuts over the azimuthal x-y plane.

Boundary conditions on the plate impose continuous transversal and null tangential fields. Consequently, the image excitation components J_{y1} and J_{z1} are reversed with respect to their AUT excitation counterparts, while the x component is unchanged. The plate has a mirror effect on the radiation pattern, i.e., the image ARP F^* is flipped left-to-right with respect to the AUT ARP. Analytically, this may be expressed as follows (refer to Fig. 2.1b),

$$F(\theta, \phi_1) = F^*(\theta, \pi - \phi_1). \tag{2.3}$$

Besides the ground reflection range, the configuration presented herein, i.e., a radiating element in front of a ground plane already exists in literature [37] [21, pp. 184–205] and have widely been used in practice, namely with grounded and ground plane antennas such as monopoles [38] which have several applications such as mobile antenna systems [39] and MAST radiators [40]. However, in these systems the ground is considered part of the antenna and is included in order to alter the radiating element free-space radiation characteristics to produce new characteristics. In this work, a different purpose is contemplated as the interest is about the radiating element free-space radiation pattern, and the plate is used in order to supply additional information about it rather than to produce a new radiation pattern. Another use of the proposed configuration was found in [41] where the author generated an intentional reflection using a rectangular metallic plate in a near-field anechoic measurement site in order to assess an echo suppression algorithm, and thus treating the reflection as a spurious noise. To our knowledge, generating an intentional echo in order to supply additional information about the radiating element free-space ARP, and thus treating it the same way as the LOS signal, is first being proposed in this work.

[1] Strictly speaking, the azimuthal angle ϕ is defined from 0 to 2π, whereas the range of the arctan function is $R_{\arctan} = [-\frac{\pi}{2}, \frac{\pi}{2}]$. As a matter of fact, non of the inverses of the three usual trigonometric functions span a 2π range. To overcome this, an adjustment angle is added as function of the probe position with respect to the AUT.

2.2 Mathematical Model

The proposed concept is applied to a far-field model. This means that the dimensions of the set-up, more precisely the distance between the AUT and the probe are such that far-field conditions are met. It should be pointed out, however, that the concept may as well be applied to a near field model. The work conducted here being essentially a feasibility study, the choice to adopt a far-field model was motivated by its simplicity compared to near field models.

2.2.1 Reference Coordinates System

The goal of the mathematical formulation of the proposed physical problem is to express the unknown spherical ARP vector $\vec{F} = [F_\theta, F_\phi]^T$ as function of the measurable cartesian field vector $\vec{E} = [E_x, E_y, E_z]^T$. Being in the far-field region, the formulation is based on the far-field equation (Eq. 1.2). The reference 3D coordinate system is shown in Fig. 2.2a [42]. The ARP vector is defined by its angular components. The azimuthal angle ϕ is defined between the x-axis and the projection of the radial vector $\vec{r}$ on the azimuthal x-y plane. The polar angle θ is defined between the z-axis and the radial vector.

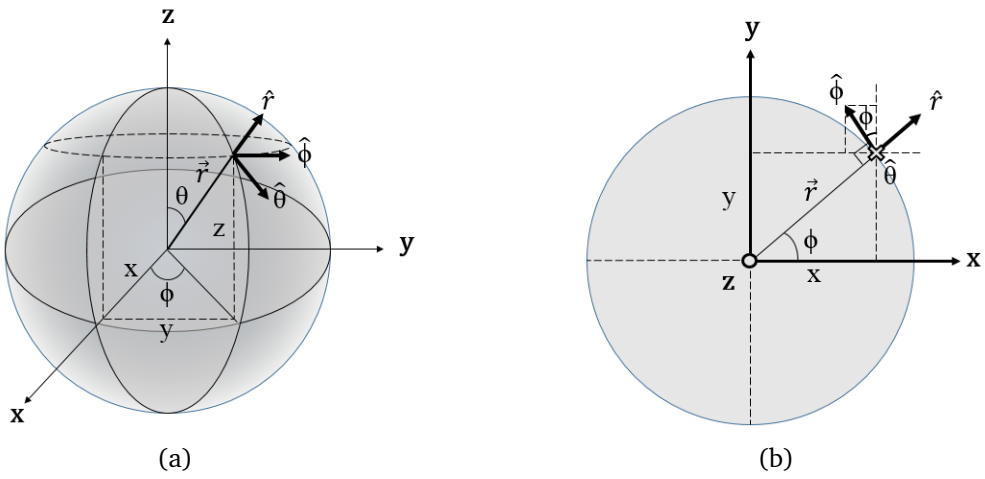

Figure 2.2 Spherical coordinates system (a) 3D representation (b) Azimuthal cut.

The general 3D problem is decomposed into transverse modes [43, pp. 362-366], i.e., Transverse Magnetic (TM) and Transverse Electric (TE) polarizations. The TM case is characterized by a single field component perpendicular to the incidence plane, and hence is a scalar case. Whereas the TE case is characterized by two field components parallel to the incidence plane and hence is a vectorial case. As we will show later, this approach is advantageous as it simplifies the mathematical study without any loss of generality. This approach is particularly advantageous as the AUT and the probe are both positioned in the azimuthal plane, i.e., $\theta = \frac{\pi}{2}$ whose corresponding coordinates system is shown in Fig. 2.2b. In this case, each ARP component is treated separately, with F_θ being exclusively dependent on E_z (TM), and F_ϕ on E_x and E_y (TE).

2.2.2 TM Case

According to Fig. 2.2b, $\hat{z} = -\hat{\theta}$. This is a forward consequence of working exclusively in the azimuthal plane, otherwise, a projection operator would be necessary to relate the two terms. As a consequence, in a free-space scenario F_θ would be directly related to E_z through the free-space Green's function,

$$E_z(r, f) = -E_\theta(\phi) = -G(r, f)F_\theta(\phi). \tag{2.4}$$

The polar angle parameter θ was omitted from the ARP term as it does not change over the azimuthal plane. Unless otherwise stated, this will be the case allover this text.

Taking into account both the AUT and the image contributions, modeled in Fig. 2.1b, the field intercepted by an ideal $\hat{z}$-polarized probe at a given working frequency f is the superposition of the individual fields radiated by each source:

$$\begin{aligned} E_z(f) &= -[G(r_0, f)F_\theta(\phi_0) - G(r_1, f)F_\theta^*(\pi - \phi_1)] \\ &= -\underbrace{G(r_0, f)F_\theta(\phi_0)}_{\substack{AUT \\ contribution}} \underbrace{+G(r_1, f)F_\theta(\phi_1)}_{\substack{image \\ contribution}}. \end{aligned} \tag{2.5}$$

The (-) sign inside the brackets stands for the reversed imageJ_{z1} excitation with respect to the AUT J_{z0} excitation. Notice that while the two ARP samples $F_\theta(\phi_0)$ and $F_\theta(\phi_1)$ are unknown, the two measurement angles ϕ_0 and ϕ_1 are known and totally predictable from the measurement set-up, as is the case for the two distances r_0 and r_1 defining the free-space Green's function (Eqs. 2.1 and 2.2).

Eq. 2.5 is composed of two unknowns. For the system to be well defined, at least an additional equation is needed. The method adopted herein is using frequency diversity by varying the working frequency such that at least two frequencies are used. Let us suppose for the moment that the ARP is frequency independent. Although this assumption may be valid for certain antenna types [44][45], the vast majority of antennas are frequency dependent, and as function of the working bandwidth, changing the operating frequency may dramatically alter the AUT radiation characteristics. As stated at the beginning of this chapter, at this stage we are mainly interested in the mathematical viability of the concept, which motivates the set of applied simplifying assumptions. One simple, but yet practical model is the model with two frequencies: the reference working frequency f_0 and an additional frequency f_1 which is used to balance the system,

$$\begin{bmatrix} E_z(f_0) \\ E_z(f_1) \end{bmatrix} = \begin{bmatrix} -G(r_0, f_0) & G(r_1, f_0) \\ -G(r_0, f_1) & G(r_1, f_1) \end{bmatrix} \begin{bmatrix} F_\theta(\phi_0) \\ F_\theta(\phi_1) \end{bmatrix}$$

$$\underbrace{\begin{bmatrix} E_z(f_0) \\ E_z(f_1) \end{bmatrix}}_{\mathbf{E}_z} = \underbrace{\begin{bmatrix} -\frac{e}{r_0}^{-j\frac{2\pi}{c}f_0 r_0} & \frac{e}{r_1}^{-j\frac{2\pi}{c}f_0 r_1} \\ -\frac{e}{r_0}^{-j\frac{2\pi}{c}f_1 r_0} & \frac{e}{r_1}^{-j\frac{2\pi}{c}f_1 r_1} \end{bmatrix}}_{\mathbf{G}_{TM}} \underbrace{\begin{bmatrix} F_\theta(\phi_0) \\ F_\theta(\phi_1) \end{bmatrix}}_{\mathbf{F}_\theta}, \tag{2.6}$$

where $\mathbf{F}_\theta$ is the unknown ARP vector made up by the two measured samples, $\mathbf{E}_z$ is the electric field vector measured at the two frequencies, and $\mathbf{G}_{TM}$ is the system matrix containing samples of the free-space Green's functions corresponding to each source at each frequency. According to Eq 2.6, the ARP at some given working frequency f_0 is retrieved thanks to information obtained at a different frequency, f_1. With no loss of generality, f_1 is assumed larger than f_0. The motivation behind this choice is provided in the next chapter. The working frequency band is defined by the frequency step $\Delta f = f_1 - f_0$. Normalizing this quantity with respect to f_0 yields the *upper* fractional bandwidth (UFBW):

$$\Delta f_u = \frac{\Delta f}{f_0} \tag{2.7}$$

Note that in this work, the UFBW is not fixed depending on the usual $S_{11} < -3$dB criterion, but is rather varied within the tolerated FBW range taking into account another important factor which is the mathematical system conditioning. Accordingly, the UFBW should be adapted to the AUT type. For instance wide-band antennas [46] offer a larger degree of freedom in terms of UFBWs than narrow-band antennas [47]. Conditioning issues are treated in the next section.

2.2.3 TE Case

The TE model in free space is by default overdetermined: each ARP component F_ϕ is related to two Cartesian field components E_x and E_y. This suggests that the corresponding model may be balanced without introducing frequency diversity.

Unlike the TM case, the spherical and Cartesian unit vectors are related by a base change operator $\mathbf{M}$ which, according to Fig 2.1b, is expressed as follows:

$$\begin{bmatrix} \hat{x} \\ \hat{y} \end{bmatrix} = \underbrace{\begin{bmatrix} M_{x\phi} \\ M_{y\phi} \end{bmatrix}}_{\mathbf{M}} \hat{\phi} = \begin{bmatrix} -\sin\phi \\ \cos\phi \end{bmatrix} \hat{\phi} \tag{2.8}$$

The free-space situation applies for the LOS field in the proposed model:

$$\underbrace{\begin{bmatrix} E_{x_0} \\ E_{y_0} \end{bmatrix}}_{\mathbf{E}_{car}} = \underbrace{\begin{bmatrix} M_{x_0\phi_0} \\ M_{y_0\phi_0} \end{bmatrix}}_{\mathbf{M_0}} E_\phi(\phi_0) = \underbrace{\begin{bmatrix} -\sin\phi_0 \\ \cos\phi_0 \end{bmatrix}}_{\mathbf{M_0}} E_\phi(\phi_0) \tag{2.9}$$

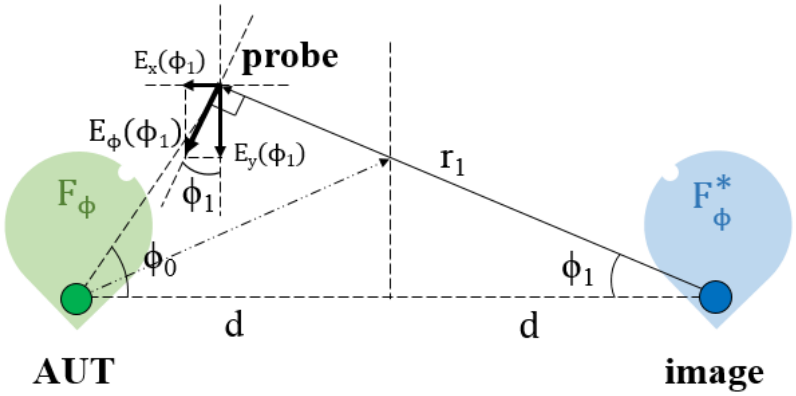

Figure 2.3 Spherical to cartesian base change of the TE field in the image case.

The image situation is slightly less forward as the corresponding base change operator has to obey boundary conditions implied by the plate. The geometry of the situation is shown in Fig. 2.3. The image field $E_\phi(\phi_1)$ is set such that it cancels out the LOS y-component along with ensuring the continuity of the x-component when their two corresponding angles are equal, i.e., for hypothetical positions over the plate. This leads to:

$$\begin{aligned}
&\begin{bmatrix} E_{x_1} \\ E_{y_1} \end{bmatrix} = \underbrace{\begin{bmatrix} M_{x_1\phi_1} \\ M_{y_1\phi_1} \end{bmatrix}}_{\mathbf{M_1}} E^*_\phi(\pi-\phi_1) = \underbrace{\begin{bmatrix} -\sin\phi_1 \\ -\cos\phi_1 \end{bmatrix}}_{\mathbf{M_1}} E^*_\phi(\pi-\phi_1), \\
&\underbrace{\begin{bmatrix} E_{x_1} \\ E_{y_1} \end{bmatrix}}_{\mathbf{E}_{car}} = \underbrace{\begin{bmatrix} -\sin\phi_1 \\ -\cos\phi_1 \end{bmatrix}}_{\mathbf{M_1}} E_\phi(\phi_1),
\end{aligned} \tag{2.10}$$

where the (-) sign in $\mathbf{M}_1(2)$ highlights the reversed image J_{y1} excitation with respect to the LOS J_{y0} excitation. Superposing the LOS and the image contributions yields the following system:

$$\begin{aligned}
&\begin{bmatrix} E_x \\ E_y \end{bmatrix} = \begin{bmatrix} M_{x_0\phi_0} & M_{x_1\phi_1} \\ M_{y_0\phi_0} & M_{y_1\phi_1} \end{bmatrix} \begin{bmatrix} E_\phi(\phi_0) \\ E_\phi(\phi_1) \end{bmatrix} \\
&\underbrace{\begin{bmatrix} E_x \\ E_y \end{bmatrix}}_{\mathbf{E}_{car}} = \underbrace{\begin{bmatrix} -\sin\phi_0 & -\sin\phi_1 \\ \cos\phi_0 & -\cos\phi_1 \end{bmatrix}}_{\mathbf{M}} \underbrace{\begin{bmatrix} E_\phi(\phi_0) \\ E_\phi(\phi_1) \end{bmatrix}}_{\mathbf{E}_\phi}
\end{aligned} \tag{2.11}$$

Each field component is related to the corresponding ARP value through the free-space Green's function:

$$\begin{bmatrix} E_x \\ E_y \end{bmatrix} = \begin{bmatrix} G_{f,r0}M_{x_0\phi_0} & G_{f,r1}M_{x_1\phi_1} \\ G_{f,r0}M_{y_0\phi_0} & G_{f,r1}M_{y_1\phi_1} \end{bmatrix} \begin{bmatrix} F_\phi(\phi_0) \\ F_\phi(\phi_1) \end{bmatrix}$$

$$\underbrace{\begin{bmatrix} E_x \\ E_y \end{bmatrix}}_{\mathbf{E}_{car}} = \underbrace{\begin{bmatrix} -\frac{\mathrm{e}^{-\mathrm{j}kr_0}}{r_0}\sin\phi_0 & -\frac{\mathrm{e}^{-\mathrm{j}kr_1}}{r_1}\sin\phi_1 \\ \frac{\mathrm{e}^{-\mathrm{j}kr_0}}{r_0}\cos\phi_0 & -\frac{\mathrm{e}^{-\mathrm{j}kr_1}}{r_1}\cos\phi_1 \end{bmatrix}}_{\mathbf{G}_{TE}} \underbrace{\begin{bmatrix} F_\phi(\phi_0) \\ F_\phi(\phi_1) \end{bmatrix}}_{\mathbf{F}_\phi} \tag{2.12}$$

Hence, the problem is balanced without introducing frequency diversity. Like in the TM case, Eq. 2.12 describes a well defined system, where the unknown ARP vector F_ϕ is related to the measurable cartesian field vector E_{car} through the system matrix $\mathbf{G}_{TE}$ which is totally predictable from the set-up parameters. The system matrix is formed by a applying a Hadamard product [48, p. 710] between the projection matrix $\mathbf{M}$ and a 2×2 matrix, $\mathbf{G}_0$, containing samples of the free-space Green's function corresponding to each source arranged by column:

$$\mathbf{G}_{TE} = \mathbf{G}_o \circ \mathbf{M} \tag{2.13}$$

with

$$\mathbf{G}_o = \begin{bmatrix} G_{f,r0} & G_{f,r1} \\ G_{f,r0} & G_{f,r1} \end{bmatrix} = \begin{bmatrix} \frac{\mathrm{e}^{-\mathrm{j}kr_0}}{r_0} & \frac{\mathrm{e}^{-\mathrm{j}kr_1}}{r_1} \\ \frac{\mathrm{e}^{-\mathrm{j}kr_0}}{r_0} & \frac{\mathrm{e}^{-\mathrm{j}kr_1}}{r_1} \end{bmatrix}.$$

2.2.4 General 3D Model

It is convenient to examine a general 3D model which would be valid for a random probe position in the Cartesian plane, and in which the four unknown ARP samples, i.e., the F_θ and F_ϕ components of both the LOS and image samples, are retrieved simultaneously. The procedure to develop such a model is quite similar to the developed transverse models; the goal is to find the unknown ARP vector in spherical form as function of the measurable field in Cartesian form. In free space, the spherical ARP vector is related to its Cartesian counterpart through a spherical-to-Cartesian base change operator,

$$\underbrace{\begin{bmatrix} F_x \\ F_y \\ F_z \end{bmatrix}}_{\mathbf{F}_{\text{car}}} = \mathbf{M} \underbrace{\begin{bmatrix} F_\theta(\theta,\phi) \\ F_\phi(\theta,\phi) \end{bmatrix}}_{\mathbf{F}_{\text{sph}}} \tag{2.14}$$

$$\text{with } \mathbf{M} = \begin{bmatrix} M_{x\theta} & M_{x\phi} \\ M_{y\theta} & M_{y\phi} \\ M_{z\theta} & M_{z\phi} \end{bmatrix} = \begin{bmatrix} \cos(\theta)\cos(\phi) & -\sin(\phi) \\ \cos(\theta)\sin(\phi) & \cos(\phi) \\ -\sin(\theta) & 0 \end{bmatrix} \tag{2.15}$$

The free space model applies to the LOS case. Taking into account the image contribution, and paying attention to the polarization of its related components due to boundary conditions

implied by the plate, the electric field intercepted by the probe is related to the ARP samples through the free-space Green's function,

$$\begin{bmatrix} E_x \\ E_y \\ E_z \end{bmatrix} = \left[\begin{array}{cc|cc} G(f_0,r_0)M_{x\theta_0} & G(f_0,r_0)M_{x\phi_0} & G(f_0,r_1)M_{x\theta_1} & G(f_0,r_1)M_{x\phi_1} \\ G(f_0,r_0)M_{y\theta_0} & G(f_0,r_0)M_{y\phi_0} & -G(f_0,r_1)M_{y\theta_1} & -G(f_0,r_1)M_{y\phi_1} \\ G(f_0,r_0)M_{z\theta_0} & G(f_0,r_0)M_{z\phi_0} & -G(f_0,r_1)M_{z\theta_1} & -G(f_0,r_1)M_{z\phi_1} \end{array}\right] \begin{bmatrix} F_\theta(\theta_0,\phi_0) \\ F_\phi(\theta_0,\phi_0) \\ F_\theta(\theta_1,\phi_1) \\ F_\phi(\theta_1,\phi_1) \end{bmatrix}. \tag{2.16}$$

Note that tangential components (y and z) corresponding to the image field are multiplied by a (-) sign in order to obey boundary conditions implied by the plate. The system described by Eq. 2.16 contains four unknowns versus three equations. An additional equation is required in order to balance the system, which is performed by applying Frequency diversity. Introducing an additional frequency results in an overdetermined systems of six equations for four unknowns,

$$\begin{bmatrix} E_x(f_0) \\ E_x(f_1) \\ --- \\ E_y(f_0) \\ E_y(f_1) \\ --- \\ E_z(f_0) \\ E_z(f_1) \end{bmatrix}_{\mathbf{E}} = \left[\begin{array}{cc|cc} G(f_0,r_0)M_{x\theta_0} & G(f_0,r_0)M_{x\phi_0} & G(f_0,r_1)M_{x\theta_1} & G(f_0,r_1)M_{x\phi_1} \\ G(f_1,r_0)M_{x\theta_0} & G(f_1,r_0)M_{x\phi_0} & G(f_1,r_1)M_{x\theta_1} & G(f_1,r_1)M_{x\phi_1} \\ ------ & ------ & ------ & ------ \\ G(f_0,r_0)M_{y\theta_0} & G(f_0,r_0)M_{y\phi_0} & -G(f_0,r_1)M_{y\theta_1} & -G(f_0,r_1)M_{y\phi_1} \\ G(f_1,r_0)M_{y\theta_0} & G(f_1,r_0)M_{y\phi_0} & -G(f_1,r_1)M_{y\theta_1} & -G(f_1,r_1)M_{y\phi_1} \\ ------ & ------ & ------ & ------ \\ G(f_0,r_0)M_{z\theta_0} & G(f_0,r_0)M_{z\phi_0} & -G(f_0,r_1)M_{z\theta_1} & -G(f_0,r_1)M_{z\phi_1} \\ G(f_1,r_0)M_{z\theta_0} & G(f_1,r_0)M_{z\phi_0} & -G(f_1,r_1)M_{z\theta_1} & -G(f_1,r_1)M_{z\phi_1} \end{array}\right]_{\mathbf{G}} \begin{bmatrix} F_\theta(\theta_0,\phi_0) \\ F_\phi(\theta_0,\phi_0) \\ F_\theta(\theta_1,\phi_1) \\ F_\phi(\theta_1,\phi_1) \end{bmatrix}_{\mathbf{F}},$$

$$\begin{bmatrix} E_x(f_0) \\ E_x(f_1) \\ --- \\ E_y(f_0) \\ E_y(f_1) \\ --- \\ E_z(f_0) \\ E_z(f_1) \end{bmatrix}_{\mathbf{E}} = \left[\begin{array}{cc|cc} \frac{e^{-jk_0r_0}}{r_0}\cos(\theta_0)\cos(\phi_0) & -\frac{e^{-jk_0r_0}}{r_0}\sin(\phi_0) & \frac{e^{-jk_0r_1}}{r_1}\cos(\theta_1)\cos(\phi_1) & -\frac{e^{-jk_0r_1}}{r_1}\sin(\phi_1) \\ \frac{e^{-jk_1r_0}}{r_0}\cos(\theta_0)\cos(\phi_0) & -\frac{e^{-jk_1r_0}}{r_0}\sin(\phi_0) & \frac{e^{-jk_1r_1}}{r_1}\cos(\theta_1)\cos(\phi_1) & -\frac{e^{-jk_1r_1}}{r_1}\sin(\phi_1) \\ ------ & ------ & ------ & ------ \\ \frac{e^{-jk_0r_0}}{r_0}\cos(\theta_0)\sin(\phi_0) & \frac{e^{-jk_0r_0}}{r_0}\cos(\phi_0) & -\frac{e^{-jk_0r_1}}{r_1}\cos(\theta_1)\sin(\phi_1) & -\frac{e^{-jk_0r_1}}{r_1}\cos(\phi_1) \\ \frac{e^{-jk_1r_0}}{r_0}\cos(\theta_0)\sin(\phi_0) & \frac{e^{-jk_1r_0}}{r_0}\cos(\phi_0) & -\frac{e^{-jk_1r_1}}{r_1}\cos(\theta_1)\sin(\phi_1) & -\frac{e^{-jk_1r_1}}{r_1}\cos(\phi_1) \\ ------ & ------ & ------ & ------ \\ -\frac{e^{-jk_0r_0}}{r_0}\sin(\theta_0) & 0 & \frac{e^{-jk_0r_1}}{r_1}\sin(\theta_1) & 0 \\ -\frac{e^{-jk_1r_0}}{r_0}\sin(\theta_0) & 0 & \frac{e^{-jk_1r_1}}{r_1}\sin(\theta_1) & 0 \end{array}\right]_{\mathbf{G}} \begin{bmatrix} F_\theta(\theta_0,\phi_0) \\ F_\phi(\theta_0,\phi_0) \\ F_\theta(\theta_1,\phi_1) \\ F_\phi(\theta_1,\phi_1) \end{bmatrix}_{\mathbf{F}}. \tag{2.17}$$

Eq. 2.17 describes a well defined system where the four unknown ARP samples are retrieved thanks to a measurable field vector and a totally predictable system matrix. However, as we are going to show in the next section, the accuracy of the calculated ARP results depends on a very important factor: the conditioning of the system matrix which is function of the configuration parameters. Studying conditioning based on Eq. 2.17 would be very tedious due to both the

matrix dimensions and complexity. The problem is simplified by exclusively working in the azimuthal plane ($\theta_0 = \theta_1 = \frac{\pi}{2}$). In this case, the system reduces to,

$$\begin{bmatrix} E_x(f_0) \\ E_x(f_1) \\ --- \\ E_y(f_0) \\ E_y(f_1) \\ --- \\ E_z(f_0) \\ E_z(f_1) \end{bmatrix}_{\mathbf{E}} = \left[\begin{array}{cc|cc} 0 & -\frac{e^{-jk_0r_0}}{r_0}\sin(\phi_0) & 0 & -\frac{e^{-jk_0r_1}}{r_1}\sin(\phi_1) \\ 0 & -\frac{e^{-jk_1r_0}}{r_0}\sin(\phi_0) & 0 & -\frac{e^{-jk_1r_1}}{r_1}\sin(\phi_1) \\ ------ & ------ & ------ & ------ \\ 0 & \frac{e^{-jk_0r_0}}{r_0}\cos(\phi_0) & 0 & -\frac{e^{-jk_0r_1}}{r_1}\cos(\phi_1) \\ 0 & \frac{e^{-jk_1r_0}}{r_0}\cos(\phi_0) & 0 & -\frac{e^{-jk_1r_1}}{r_1}\cos(\phi_1) \\ ------ & ------ & ------ & ------ \\ -\frac{e^{-jk_0r_0}}{r_0} & 0 & \frac{e^{-jk_0r_1}}{r_1} & 0 \\ -\frac{e^{-jk_1r_0}}{r_0} & 0 & \frac{e^{-jk_1r_1}}{r_1} & 0 \end{array}\right]_{\mathbf{G}} \begin{bmatrix} F_\theta(\frac{\pi}{2},\phi_0) \\ F_\phi(\frac{\pi}{2},\phi_0) \\ F_\theta(\frac{\pi}{2},\phi_1) \\ F_\phi(\frac{\pi}{2},\phi_1) \end{bmatrix}_{\mathbf{F}}, \tag{2.18}$$

which offers the possibility of decomposing the problem into the developed transverse models (Eqs. 2.6 and 2.12) without loss of generality, as retrieving ARP samples corresponding to different elevation levels may be performed by rotating the AUT rather than moving the probe. The adopted transverse decomposition provides the advantage of a much simpler conditioning study due to the reduced dimensions of the system matrices. Conditioning issues are treated in the next section.

2.3 Conditioning Issues

Retrieving the ARP samples corresponding to both the TM and TE cases consists in inverting the corresponding matrices equations (Eqs. 2.6 and 2.12):

$$\mathbf{F} = \mathbf{G}^{-1}\mathbf{E}. \tag{2.19}$$

However, as discussed in Sec. 1.5.2, and by recalling that any measurement is subject to a set of systematic errors, attention must be given to the robustness of the system and to its stability against errors [49, p. 36-38] in order to avoid their amplification while proceeding with the inversion.

2.3.1 Mathematical Stability: The Condition Number

The robustness of a matrix equation $\mathbf{A}x = b$ against input errors is indicated by the condition number of the system matrix $\kappa(\mathbf{A})$. The condition number measures how sensitive the solution x would be to error in the observation b or to error in the system matrix $\mathbf{A}$ itself [50, p. 345-347]. A well-conditioned system is described by a low condition number, and corresponds to a system where the input error is little -or not- amplified. Ideally $\kappa(\mathbf{A})$ would be equal to unity, and this corresponds to a matrix whose rows (and columns) form an orthogonal set. An ill-conditioned

system, in the contrary, is described by a high condition number and is characterized by a large input error amplification. As the condition number rises, the system matrix tends towards singularity, the limiting case, when $\kappa(\mathbf{A}) = \infty$, is characteristic of a singular matrix where no -unique- solution exists. Hence, a necessary -but not sufficient- condition for a matrix to be well-conditioned is that the matrix is non-singular, i.e., of full rank. Analytically, the condition number relates the norm of the relative input error, to the norm of the relative solution error [51, p. 475-478]. In the context of the proposed model, it may be expressed as follows,

$$\begin{aligned} \text{Error in observation, } \mathbf{E}: \ & \frac{\|\Delta\mathbf{F}\|}{\|\mathbf{F}\|} \leq \kappa(\mathbf{G}) \frac{\|\Delta\mathbf{E}\|}{\|\mathbf{E}\|} \\ \text{Error in Matrix, } \mathbf{G}: \ & \frac{\|\Delta\mathbf{F}\|}{\|\mathbf{F}+\Delta\mathbf{F}\|} \leq \kappa(\mathbf{G}) \frac{\|\Delta\mathbf{G}\|}{\|\mathbf{G}\|}. \end{aligned} \tag{2.20}$$

It is important to keep in mind that the norm of the relative input error multiplied by the condition number provides un upper bound of the solution error. The observation error $\Delta\mathbf{E}$ corresponds to the set of measurement errors which perturb the *correct* field value, and which combine with computer roundoff error. On the other hand, error in the system matrix $\Delta\mathbf{G}$ comes from the model limitations in describing the actual physical behavior of the radiated fields, and which also combines with roundoff error that emerges during the elimination steps processed by the solving algorithm [52]. Consequently, studying the model conditioning is central to assess its viability as the amplification of those errors could make the ARP error unacceptable.

The condition number $\kappa(\mathbf{G})$ is a property of the $\mathbf{G}$ matrix, and thus is impacted by the set-up dimensions and frequency parameters defining the matrix. The exact definition of the condition number is given as the ratio of the matrix norm with respect to the norm of its inverse, which is equal to the ratio of the largest to smallest matrix singular values [51],

$$\kappa(\mathbf{G}) = \frac{\|\mathbf{G}\|}{\left\|\mathbf{G}^{-1}\right\|} = \frac{\sigma_{max}}{\sigma_{min}}, \tag{2.21}$$

where σ_{max} and σ_{min} are respectively the matrix maximum and minimum singular values. Studying the condition number based on this formula is complicated as expressing the singular values analytically is tedious. An alternative approach adopted herein to bypass this difficulty is by studying of the degree of orthogonality of the matrix rows and columns by assessing the corresponding projection factors. A well-conditioned matrix corresponds to a small projection factor, and vice versa. The goal is then to minimize the projection factor in order to ensure the system stability. This is presented in the next two sections for each transverse case separately, the objective being to be able in each case to predict, as function of the system parameters, the optimal probe position in terms of conditioning, and to verify the possibility of generating well-conditioned positions using practical set-up dimensions and adaptable UFBWs to the various antenna types.

2.3.2 TM model

2.3.2.1 Projection Study and Optimal positions

The TM system matrix is exclusively made up by the free-space Green's samples defined by the LOS and image distances and the two working frequencies,

$$\mathbf{G}_{TM} = \begin{bmatrix} -\frac{e}{r_0}^{-j\frac{2\pi}{c}f_0 r_0} & \frac{e}{r_1}^{-j\frac{2\pi}{c}f_0 r_1} \\ -\frac{e}{r_0}^{-j\frac{2\pi}{c}f_1 r_0} & \frac{e}{r_1}^{-j\frac{2\pi}{c}f_1 r_1} \end{bmatrix} \tag{2.22}$$

The projection factor ρ is calculated by performing a dot product between the two normalized rows, such that its amplitude is up-bounded by unity,

$$\rho = \left[\frac{1}{r_0^{-2}+r_1^{-2}}\right]\left[\frac{e^{-j\frac{2\pi}{c}\Delta f r_0}}{r_0^2}+\frac{e^{-j\frac{2\pi}{c}\Delta f r_1}}{r_1^2}\right] \tag{2.23}$$

By factorizing the first term inside the second set of brackets, and rearranging the equation, we get,

$$\rho = e^{-j\frac{2\pi}{c}\Delta f r_0}\left[\frac{1+\left(\frac{r_0}{r_1}\right)^2 e^{-j\frac{2\pi}{c}\Delta f \Delta r}}{1+\left(\frac{r_0}{r_1}\right)^2}\right], \tag{2.24}$$

with $\Delta r = r_1 - r_0$. Conditioning is related to the magnitude of the projection factor[2]. Consequently the exponential term outside the brackets does not have an impact and the equation is simplified as follows,

$$\begin{aligned} \rho &= \left|\frac{1+\gamma^2 e^{-j\beta}}{1+\gamma^2}\right|, \\ \text{with } \gamma &= \frac{r_0}{r_1}, \\ \beta &= 2\pi\Delta f_u \Delta r. \end{aligned} \tag{2.25}$$

The distances ratio γ is by definition less than unity as the image distance is always greater than the LOS distance. In the phase term β, distances are normalized with respect to the central working wavenumber λ_0 and the frequency step is normalized with respect to the reference working frequency f_0.

The value of ρ is minimized by minimizing the numerator, which is the sum of two complex numbers as shown in Fig. 2.4. The expression of the numerator suggests two extreme condition-

[2]The term ρ will refer to the amplitude of the projection factor.

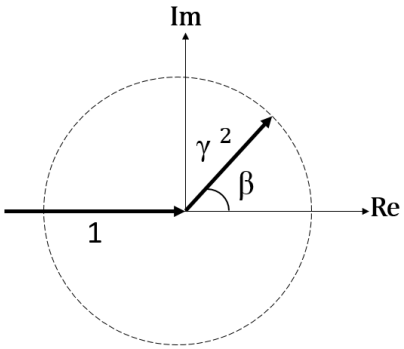

$$\text{Optimal case: } \beta = (2n+1)\pi \;\rightarrow\; \Delta r = \frac{2n+1}{2\Delta f}$$
$$\text{Worst case: } \beta = 2n\pi \;\rightarrow\; \Delta r = \frac{n}{\Delta f},\; n \in \mathbb{N} \tag{2.26}$$

Figure 2.4 Representation of the numerator of ρ as the sum of two complex numbers and the corresponding expressions of extreme conditioning cases.

ing cases. An optimal case when the complex term becomes real negative, i.e., when its phase is equal to an integer multiple of π. In this case the numerator, and thus ρ take its minimum value. In the contrary, if the complex term becomes real positive, i.e., when its phase is equal to an integer multiple of 2π, this results in a worst case as ρ takes a maximum value. These two cases correspond to optimal and worst positions respectively, and are both defined by the related Δr term expressed in Eq. 2.26. The locus of points defined by a constant difference of distances from two fixed points, referred to as the *foci* and which, in our case, are the AUT and the image positions, is either a straight line or a hyperbola.

The straight line case, which is a particular case, corresponds to $\Delta r = 0$, and according to Eq. 2.26 is a worst case (n=0). This is the locus of points equidistant from the foci and is defined by the perpendicular bisector of the line segment defined by the foci, which in our model corresponds to hypothetical positions over the plate. Although this case is physically unrealizable, it helps us understand the condition number behavior. Over the plate, the two distances r_0 and r_1 are equal, which results in the two columns of $\mathbf{G}_{TM}$ being identical and thus breaking their linear independence. Accordingly, $\mathbf{G}_{TM}$ becomes singular and the system is unsolvable. This suggests that positions near the plate are ill-conditioned as $\mathbf{G}_{TM}$ tends towards singularity in this region.

The general solution to Eq. 2.26 is a set of hyperbolas having positions of the AUT and the image as focal points and the plate as a conjugate axis. Equations of optimal and worst hyperbolas are then the following [53, pp. 101-104],

$$\frac{(x-d)^2}{a^2} - \frac{y^2}{b^2} = 1$$
$$a_n = \frac{\Delta r}{2} = \begin{cases} \frac{2n+1}{4\Delta f_u},\; n \in \mathbb{N} & \text{optimal hyperbolas} \\ \frac{n}{2\Delta f_u},\; n \in \mathbb{N}^* & \text{worst hyperbolas} \end{cases}$$
$$b_n = \sqrt{d^2 - a_n^2},\, b_n > 0. \tag{2.27}$$

The term a_n, referred to as the *real semiaxis*, is the determining factor of the hyperbola class. Eq. 2.27 suggests the existence of two classes of positions of particular interest, and which both follow hyperbolic spatial distributions. One class is the set of worst hyperbolas of positions over which the system can only be ill-conditioned, and thus are positions to avoid. The second class of hyperbolas in the other hand define optimal positions where conditioning is *locally* optimal. The level of conditioning over optimal hyperbolas is determined by the magnitude of the complex term of Eq. 2.25, γ^2 (refer to Fig. 2.4). This is highlighted by expressing ρ corresponding to optimal hyperbolas,

$$\rho = \frac{1-\gamma^2}{1+\gamma^2}. \tag{2.28}$$

Eq. 2.28 suggests an inverse proportionality between the distances ratio γ and the condition number: when γ approaches unity conditioning improves as this decreases ρ and vice versa. Expressing γ as function of ρ yields,

$$\gamma = \sqrt{\frac{1-\rho}{1+\rho}}. \tag{2.29}$$

In other words, Eq. 2.29 states that the system stability defines the ratio of distances separating the AUT and the image from the probe. The locus of points defined by a constant ratio of distances from two fixed points (foci) is either a straight line or a circle [54]. The straight line case is defined by $\gamma = 1$ and, as discussed earlier, corresponds to the set of equidistant positions that falls on the plate. This case is both physically unrealizable and by definition ill-conditioned as the set of corresponding points cannot counside with any optimal hyperbola which have the plate as their common conjugate axis. The solution is then a circle, which is commonly known as the circle of *Apollonius* [55] and which, in this text, will be referred to as the conditioning circle as its parameters depends on the chosen stability factor and define the level of conditioning over optimal hyperbolas. The conditioning circle parameters are listed below,

$$\begin{aligned} \text{center} &= \frac{-\gamma^2}{1-\gamma^2} 2d, \\ \text{radius} &= \frac{\gamma}{1-\gamma^2} 2d. \end{aligned} \tag{2.30}$$

To summarize, for a given set-up, mainly characterized by the AUT-plate separation d, the working UFBW defines a set of hyperbolas of positions where conditioning is locally optimal. The level of conditioning over optimal hyperbolas is governed by the chosen stability factor which defines a circle of positions. The optimal position is then the intersection between the optimal hyperbola and the conditioning circle. An example of optimal positions is shown in Fig. 2.5 which highlights the relationship between the projection factor (Fig. 2.5a) and the

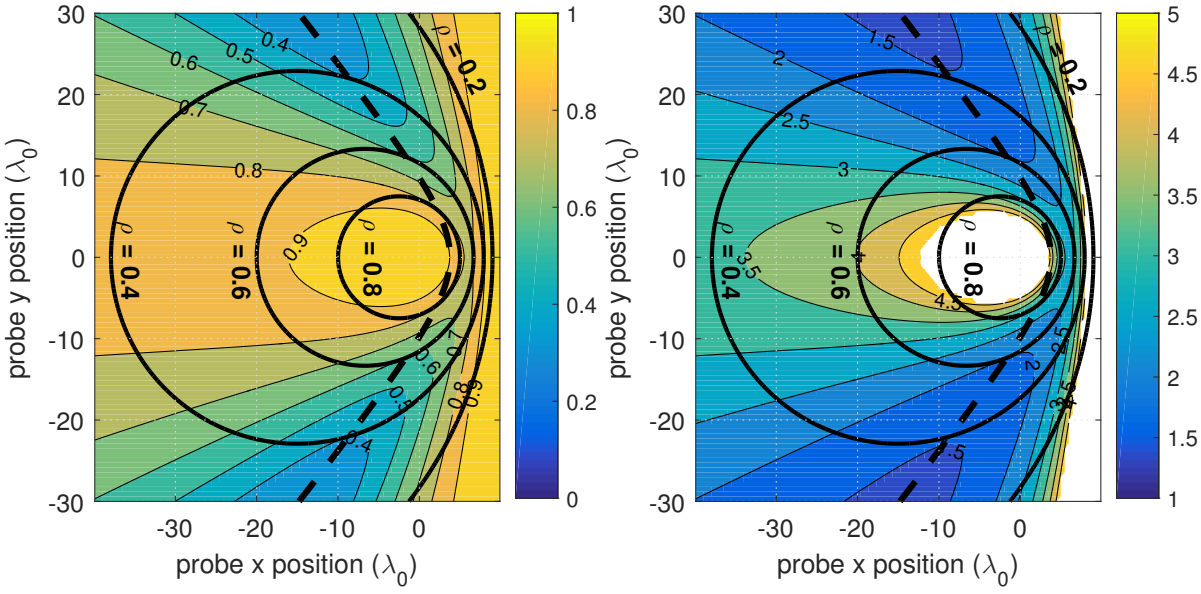

Figure 2.5 Relationship between the projection factor ρ and the condition number $\kappa(\mathbf{G}_{TM})$ and example of different optimal positions showing the impact of optimal hyperbolas (dashed) and conditioning circles (solid). Plate at $x_p = 10\lambda_0$, UFBW = 4%: (a) ρ (b) $\kappa(\mathbf{G}_{TM})$.

condition number (Fig. 2.5b). Note that the condition number is truncated at $\kappa(\mathbf{G}_{TM})_{\max} = 5$ for a proper plot. In this example the configuration parameters, i.e., $d = 10\lambda_0$ and UFBW=4% allowed the generation of a single optimal hyperbola (dashed). As we are going to show later, the number of optimal hyperbolas depends on the configuration parameters. Four conditioning circles corresponding to $\rho = [0.2, 0.4, 0.6, 0.8]$ are also plotted in the figures. Optimal positions related to each projection factor is the point of intersection of the corresponding conditioning circle with the optimal hyperbola. Properties of optimal hyperbolas and conditioning circles are discussed in detail hereafter.

2.3.2.2 Properties of Optimal Hyperbolas

Optimal hyperbolas are defined to the phase of the complex term of Eq. 2.25, which is the difference of the phases of the original $\mathbf{G}_{TM}$ entries. Consequently optimal hyperbolas depend on two parameters defining the configuration: frequency parameters, which are encompassed in the UFBW, and distances distribution which is controlled by the AUT-plate separation d. The expression of b_n, referred to as the imaginary semiaxis, in Eq.2.27 imposes a mutual condition

on the minimum distance d separating the plate from the AUT, and for the minimum operating UFBW in order to ensure the existence of at least a single optimal hyperbola,

$$b_n > 0 \longrightarrow d\Delta f_u > \frac{1}{4} \tag{2.31}$$

The AUT-plate separation is limited by the measurement site, while the applied UFBW depends on the AUT type. Hence, a trade-off has to be achieved between the two parameters in order to ensure the existence of optimal positions. A general relationship to indicate the number of generated optimal hyperbolas is expressed by the hyperbola eccentricity which, by definition, is greater than unity,

$$e_n = \frac{d}{a_n} = \frac{4d\Delta f_u}{2n+1} > 1. \tag{2.32}$$

If the condition for e_0 is not fulfilled, no optimal hyperbola exists. Beyond that, the number of existing optimal hyperbolas depend on the fulfillment of the condition corresponding to each hyperbola *order*. Raising the number of optimal hyperbolas is achieved by augmenting either the AUT-plate separation or the UFBW. However, it is important to note that rising the number of optimal hyperbolas rises the number of forbidden hyperbolas as well, as the latter follow a similar existence condition,

$$e_n^* = \frac{2d\Delta f_u}{n} > 1. \tag{2.33}$$

The $d.\Delta f_u$ product also determines the hyperbolas positions and shapes.

The hyperbola position is indicated by the position of the vertex which is located at a distance a_n away from the hyperbola center, i.e., the plate position. According to the expression of a_n in Eq. 2.27, the distance between the vertex and the plate is inversely proportional to the UFBW. The same can be seen in Fig. 2.6a where the first order optimal hyperbola is plotted for different UFBWs while the AUT-plate separation is fixed ($d = 10\lambda_0$). On the other hand, the AUT-plate separation impacts the distance between the vertex and the AUT,

$$d_n^{AUT-vertex} = d - a_n, \tag{2.34}$$

a_n being independent from d, Eq. 2.34 suggests direct proportionality between the AUT-plate and AUT-vertex separations. In other words, rising the AUT-plate separation pushes optimal hyperbolas away from the AUT and closer to the plate. This is shown in Fig. 2.6b where the first order optimal hyperbola is plotted for different AUT-plate separations while fixing the UFBW ($\Delta f_u = 4\%$). These remarks are also useful for determining positions of optimal hyperbolas as function of their order. Eq. 2.27 states that a_n is directly proportional to n, the hyperbola order. This means that as the order augments, the corresponding hyperbola moves further from the

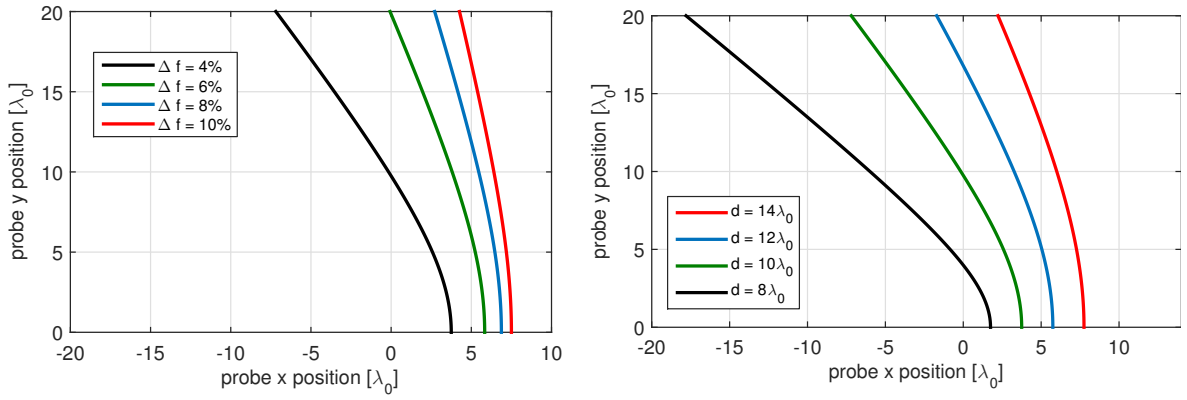

(a) (b)

Figure 2.6 Position and slope of the optimal hyperbola as functions of the configuration parameters: (a) as function of the UFBW, $d = 10\lambda_0$ (b) as function of the AUT-plate separation, $\Delta f_u = 4\%$.

plate towards the AUT. The same can be seen in Fig. 2.7 where the configuration parameters, $d = 10\lambda_0$ and $\Delta f_u = 20\%$, allowed the generation of four optimal hyperbolas.

The shape of the hyperbola is indicated by the slope of its asymptote, which is defined as the ratio of the imaginary semi-axis to the real semi-axis, and may be expressed in terms of the hyperbola eccentricity. The expression of the asymptote slope m_n of the n^{th} order optimal hyperbola is the following,

$$m_n = \frac{b_n}{a_n} = \sqrt{\left(\frac{d}{a_n}\right)^2 - 1} = \sqrt{e_n^2 - 1}. \tag{2.35}$$

The eccentricity being proportional to the $d.\Delta f_u$ product, this yields the following relationships regarding optimal positions with respect to the plate,

$$d.\Delta f_u \to \frac{2n+1}{4} : m_n \to 0 \Rightarrow \text{positions far from the plate,}$$
$$d.\Delta f_u \nearrow : m_n \to \infty \Rightarrow \text{positions near the plate.}$$

Fig. 2.6 highlights these relationships as augmenting either the AUT-plate separation or the UFBW augments the hyperbola asymptote slope making optimal positions move closer to the plate, whereas reducing either of the two parameters pushes optimal positions towards the x-axis. The rate of change of the hyperbola slope with respect to Δf_u and d is assessed by studying its derivative with respect to e,

$$\frac{dm}{de} = \frac{d\sqrt{e^2-1}}{de} = \frac{e}{\sqrt{e^-1}} \tag{2.36}$$

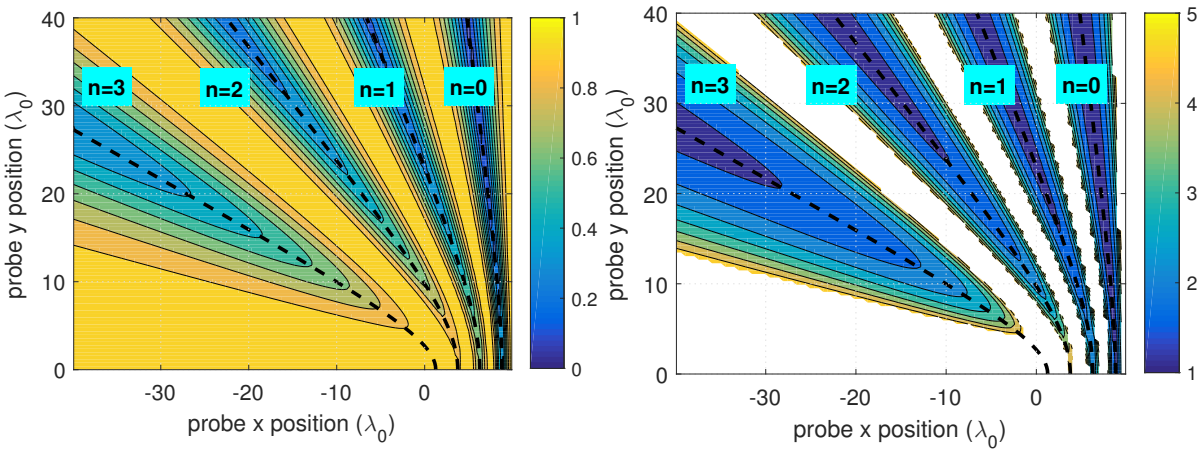

(a) (b)

Figure 2.7 Assessment of optimal hyperbola orders and zones of good conditioning as function of the hyperbola position, $d = 10\lambda_0$, $\Delta f_b = 20\%$, (a) ρ, (b) $\kappa(\mathbf{G}_T M)$.

According to this formula, we can distinguish two main cases,

$$e \to 1 \ (d \approx a,\ m \to 0 : \text{ positions far from the plate}) : \frac{\mathrm{d}m}{de} \to \infty$$

$$e >> 1 \ (d \nearrow,\ m \to \infty : \text{ positions near the plate}) : \frac{\mathrm{d}m}{de} \to 1$$

This highlights the fact that the slope of the hyperbola asymptote changes very rapidly for positions far from the plate (near the *x-axis*) and gets slower as the hyperbola approaches the plate. We may conclude by deduction that zones of good conditioning are larger for positions far from the plate, and get tighter as optimal positions approach the plate. The level of conditioning, however, depends on the conditioning circle intersecting the hyperbola on the position in question. Theses remarks are highlighted in Fig. 2.7 where zones of good conditioning related to higher order hyperbolas are larger than those related to lower order hyperbolas, the latter being closer to the plate. However, lower order hyperbolas show better conditioning levels as they are more likely to intersect conditioning circles corresponding to lower projection factors in regions closer to the plate. Properties of conditioning circles are discussed in the next section.

2.3.2.3 Properties of Conditioning Circles

Conditioning circles are related to the magnitude of the complex term of Eq. 2.25 which takes into account the distances distribution defining the magnitudes of the $\mathbf{G}_{TM}$ entries. Consequently, conditioning circles exclusively depend on the set-up parameters, mainly defined by the AUT-plate separation as well as the probe position which sets the distances distribution expressed by the ratio term γ as revealed by Eq. 2.30. The LOS distance being smaller than the image distance, this leads to the AUT being inside the conditioning circle as shown in Fig. 2.8.

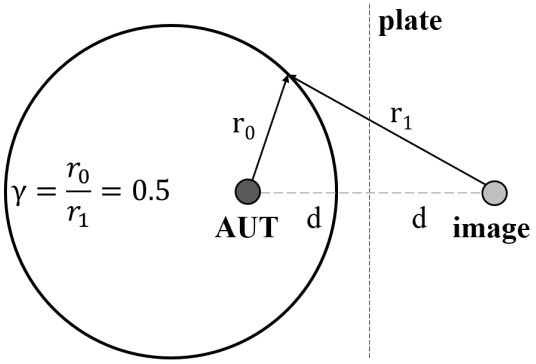

Figure 2.8 Example of a conditioning circle corresponding to a distances ratio $\gamma = \frac{1}{2}$ showing the AUT positioned inside the circle.

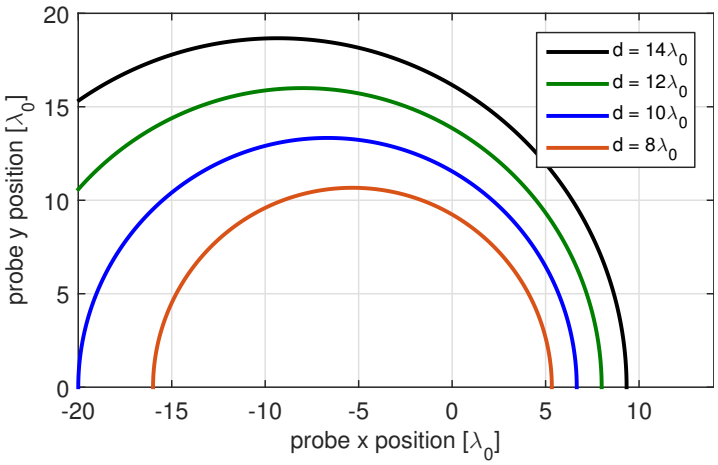

Figure 2.9 Radius of the optimal circle as functions of the AUT-plate separation.

Ideally, the set-up dimensions would be adjusted in order to achieve good conditioning circles of smaller radii in order to achieve good conditioned positions using realistic set-up dimensions.

Eq. 2.30 suggests direct proportionality between the circle's radius and the AUT-plate separation. This is shown in Fig. 2.9, where a $\rho = 0.6$ conditioning circle is plotted for different AUT-plate separations. This property is clearly advantageous as reducing the AUT-plate separation pushes optimal positions towards the AUT. In this example optimal positions corresponding to $\rho = 0.6$ are achieved at distances lower than $15\lambda_0$ for an AUT-plate separation $d = 8\lambda_0$.

Eq. 2.30 also suggests direct proportionality between the conditioning circle radius and the distances ratio γ, the latter being inversely proportional to the projection factor ρ. This means that achieving a better stability requires larger AUT-probe separations as the conditioning circle radius augments when reducing the projection factor. The same is depicted in Fig. 2.5. As ρ approaches zero, γ approaches unity (Eq. 2.29) making the circle radius tends toward infinity

(a straight line). In this case, it is still possible to use the circle segment near the plate which is always at a distance less than d from the AUT. However, as discussed in the previous section, this requires pushing the optimal hyperbola towards the plate by rising the working UFBW which, depending on the AUT type and the targeted stability, may not be feasible in practice. The limiting conditioning case ($\rho = 0$), discussed in Sec. 2.3.2.1, is a straight line coinciding with the plate. Hypothetical positions on the plate are however by default ill-conditioned as they cannot coincide with optimal hyperbolas. These remarks are summarized below:

$$\rho \to 0 \ \left(d \ \nearrow\right) : \text{positions far from the AUT}$$
$$\rho \to 1 \ \left(d \to \frac{1}{4\Delta f}\right) : \text{positions near the AUT}$$

To summarize, achieving an ideal position is impossible as is the case for the singular case; the former corresponding to either a position infinitely far from the AUT or to an infinite working UFBW, whereas the latter corresponds to a position over the plate. Otherwise, conditioning is inversely proportional to the distances spread: it declines when the image distance is relatively larger than the LOS distance, which is the case near the AUT. On the other hand, conditioning improves when the two distances get closer to each other, which is the case near the plate and far away from the AUT. The former requires larger working bandwidths, while the later requires larger set-up dimensions. Hence, in order to ensure that a relatively good conditioning circle intersects an optimal hyperbola at a *realistic* distance, a compromise between the set-up dimensions, frequency parameters and the choice of the projection factor has to be made.

2.3.3 TE Model

2.3.3.1 Basic Model

Unlike the TM case, the conditioning study of the TE model is less forward and rather qualitative due to the complexity of the system matrix:

$$\mathbf{G}_{TE} = \begin{bmatrix} -\frac{\mathrm{e}^{-\mathrm{j}kr_0}}{r_0}\sin\phi_0 & -\frac{\mathrm{e}^{-\mathrm{j}kr_1}}{r_1}\sin\phi_1 \\ \frac{\mathrm{e}^{-\mathrm{j}kr_0}}{r_0}\cos\phi_0 & -\frac{\mathrm{e}^{-\mathrm{j}kr_1}}{r_1}\cos\phi_1 \end{bmatrix} \tag{2.37}$$

As suggested by Eq. 2.37, $\mathbf{G}_{TE}$ is only affected by the set-up dimensions which impact the distances and angles distributions. Ideally, we would proceed like in the TM case by applying a dot product between the two rows and minimizing the corresponding projection factor in order to find the optimal position. This approach is however tedious as it requires eliminating the angles terms and replacing them with distances terms using the usual triangular identities, which complicates the procedure. An alternative approach to simplify the procedure is adopted

by recalling, as discussed in Sec. 2.2.3, that $\mathbf{G}_{TE}$ is formed by applying a Hadamard product between the projection matrix $\mathbf{M}$ which takes into account the angles distribution, and Green's matrix $\mathbf{G}_o$ which takes into account the distances distribution. The contribution of each matrix into conditioning is assessed separately, and optimal positions are retrieved by combining the impact of both matrices.

The impact of the projection matrix is highlighted by studying the projection factor corresponding to $\mathbf{G}_{TE}$ columns,

$$\rho_{\mathbf{M}} = \frac{\mathrm{e}^{-\mathrm{j}k\Delta r}}{r_0 r_1} \frac{\sin\phi_0 \sin\phi_1 - \cos\phi_0 \cos\phi_1}{\sqrt{(\frac{\sin^2\phi_0}{r_0^2} + \frac{\cos^2\phi_0}{r_0^2})(\frac{sin^2\phi_1}{r_1^2} + \frac{cos^2\phi_1}{r_1^2})}}. \tag{2.38}$$

Factorizing the distances terms outside the square root, and recalling that, for having a magnitude of unity, the exponential term does not contribute into conditioning, the projection factor simplifies to,

$$\rho_{\mathbf{M}} = \frac{\sin\phi_0 \sin\phi_1 - \cos\phi_0 \cos\phi_1}{\sqrt{(\sin^2\phi_0 + \cos^2\phi_0)(sin^2\phi_1 + cos^2\phi_1)}}. \tag{2.39}$$

As we can see, the projection factor ignores the impact of the distances separating the AUT and the image from the probe, and only takes into account the angles distribution. The projection factor is then minimized by minimizing the numerator,

$$\sin\phi_0 \sin\phi_1 - \cos\phi_0 \cos\phi_1 = 0 \tag{2.40}$$

The left-hand term corresponds to a a common trigonometric identity which simplifies Eq. 2.40 to,

$$\cos(\phi_0 + \phi_1) = 0 \tag{2.41}$$

The solution to this equation is the set of angles whose sum is equal to an integer multiple of $\frac{\pi}{2}$:

$$\phi_0 + \phi_1 = n\pi - \frac{\pi}{2}, \quad n \in \mathbb{Z}. \tag{2.42}$$

The locus of points satisfying this equation are positions which form a right triangle with the AUT and image positions. This corresponds to a circle of radius d that passes through the AUT and image positions, as shown in Fig. 2.10a. By analogy to the TM case, this circle will be refereed to as the *optimal* circle, as the projection factor takes minimum values over this circle, as shown in Fig. 2.10b. This translates the fact that the projection matrix is best conditioned when the two field vectors $E_\phi(\phi_0)$ and $E_\phi(\phi_1)$ are orthogonal to each other (Fig. 2.10a). The

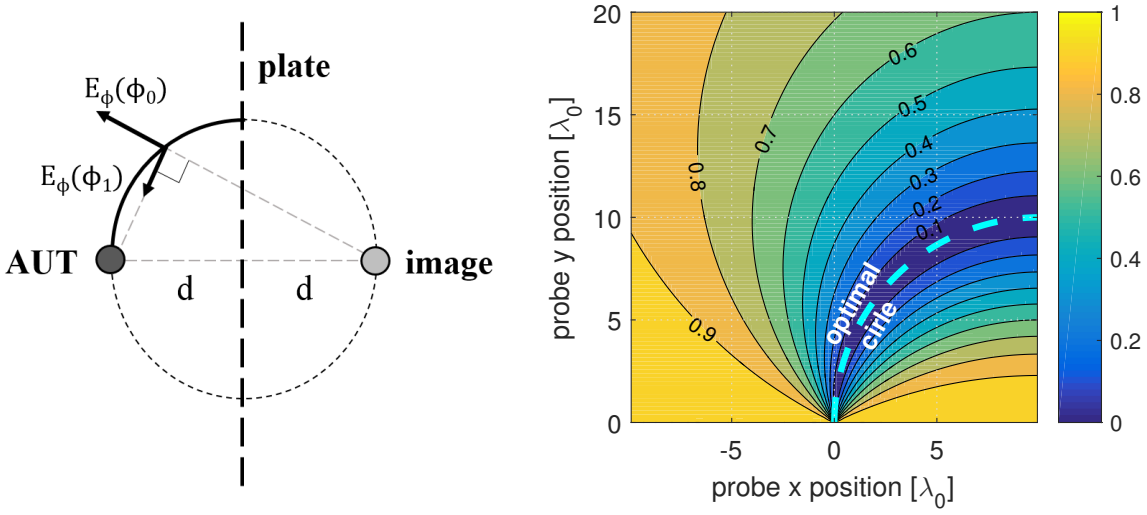

(a) (b)

Figure 2.10 Optimal positions introduced by the projection matrix: (a) sketch showing the optimal circle as the locus of points forming a right triangle with the AUT and image positions (b) ρ, plate at $x_p = 10\lambda$.

overall conditioning is *locally* optimal over the optimal circle; its level depending, like in the TM case, on the distances spread.

The distances distribution highlights the impact of Green's matrix, and affects conditioning the same way as in the TM case, via conditioning circles. Properties of conditioning circles where detailed in Sec. 2.3.2.3; to summarize: conditioning is inversely proportional to the distances spread, which in its turn is inversely proportional to the conditioning circle radius. Privileged conditioning circles have larger radii and are closer to the plate. The shape of the projection factor is then biased by the distances spread shown in Fig. 2.11a. Consequently, the overall conditioning combines both effects, and optimal positions are the intersection between the optimal circle and conditioning circles, as shown in Fig. 2.11b. This figure suggests that privileged positions are those closer to the plate around a distance$d$ from the horizontal axis.

To conclude, optimal positions in the basic TE case are exclusively governed by the AUT-plate separation and fall in the vicinity of the plate around a distance d from the horizontal axis. Otherwise, the condition number rises gradually as the radial distance from the optimal region augments. This provides the advantage of being able to achieve excellent condition numbers using typical set-up dimensions. However, the inability of moving optimal positions away from the plate might be disadvantageous in some cases, for instance, in a complete measurement scenario as positions near the plate are generally ill-conditioned in the TM model and require large UFBWs or AUT-plate separations in order to improve conditioning, or when using multiple probe positions. To overcome this issue, frequency diversity may be introduced in order to improve the overall conditioning pattern.

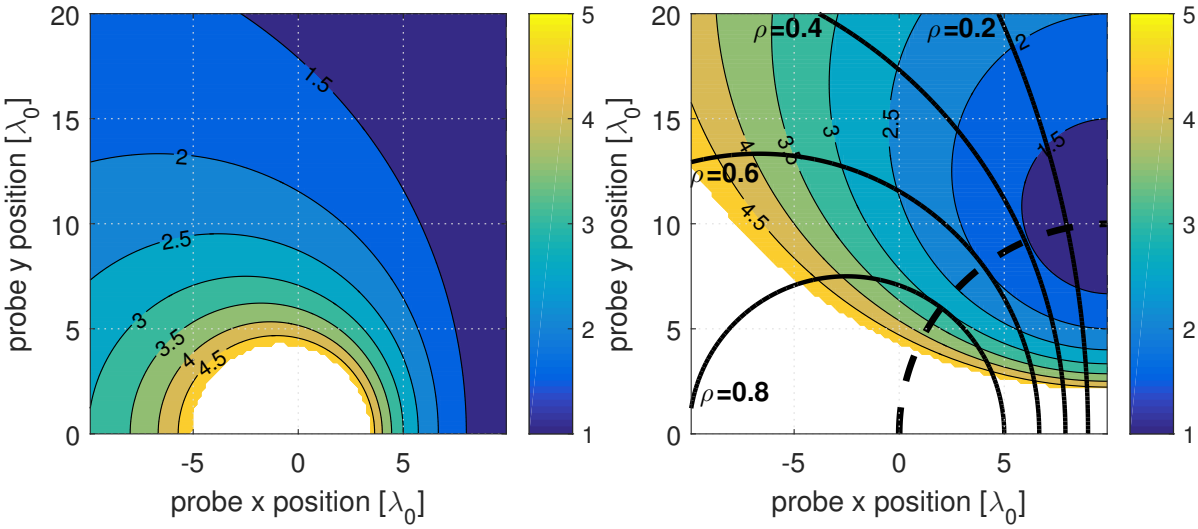

(a) (b)

Figure 2.11 Impact of the distances spread on the overall condition number $x_p = 10\lambda$: (a) γ^{-1} (b) $\kappa(\mathbf{G}_{TE})$, optimal circle (dashed), and conditioning circles (solid).

2.3.3.2 Applying frequency Diversity

It is possible to introduce frequency diversity in order to supply additional information about the system. Although this is not necessary in order to balance the mathematical model, it is advantageous in terms of conditioning as supplying additional information can only improve conditioning. For instance, using two frequencies like in the TM model, yields the following system,

$$\begin{bmatrix} E_x(f_0) \\ E_x(f_1) \\ --- \\ E_y(f_0) \\ E_y(f_1) \end{bmatrix} = \begin{bmatrix} G_{f_0,r0}M_{x\phi} & G_{f_0,r1}M_{x\phi} \\ G_{f_1,r0}M_{x\phi} & G_{f_1,r1}M_{x\phi} \\ ----- & ----- \\ G_{f_0,r0}M_{y\phi} & -G_{f_0,r1}M_{y\phi} \\ G_{f_1,r0}M_{y\phi} & -G_{f_1,r1}M_{y\phi} \end{bmatrix} \begin{bmatrix} F_\phi(\phi_0) \\ F_\phi(\phi_1) \end{bmatrix}$$

$$\underbrace{\begin{bmatrix} E_x(f_0) \\ E_x(f_1) \\ --- \\ E_y(f_0) \\ E_y(f_1) \end{bmatrix}}_{\mathbf{E}_{car}} = \underbrace{\begin{bmatrix} -\frac{e}{r_0}^{-jk_0r_0}sin\phi_0 & -\frac{e}{r_1}^{-jk_0r_1}sin\phi_1 \\ -\frac{e}{r_0}^{-jk_1r_0}sin\phi_0 & -\frac{e}{r_1}^{-jk_1r_1}sin\phi_1 \\ ----- & ----- \\ \frac{e}{r_0}^{-jk_0r_0}cos\phi_0 & -\frac{e}{r_1}^{-jk_0r_1}cos\phi_1 \\ \frac{e}{r_0}^{-jk_1r_0}cos\phi_0 & -\frac{e}{r_1}^{-jk_1r_1}cos\phi_1 \end{bmatrix}}_{\mathbf{G}_{TE}} \underbrace{\begin{bmatrix} F_\phi(\phi_0) \\ F_\phi(\phi_1) \end{bmatrix}}_{\mathbf{F}_\phi}. \tag{2.43}$$

The new system matrix is a 4×2 matrix highlighting the over-determination of the problem with four equations against two unknowns. Breaking down the system matrix, we have the new projection matrix:

$$\mathbf{M} = \begin{bmatrix} -\sin\phi_0 & -\sin\phi_1 \\ -sin\phi_0 & -\sin\phi_1 \\ ----- & ----- \\ \cos\phi_0 & -\cos\phi_1 \\ \cos\phi_0 & -\cos\phi_1 \end{bmatrix}. \tag{2.44}$$

Switching the 2nd and 3rd rows we can see that the new projection matrix is a double concatenation of the basic projection matrix. Consequently, it has the same behavior in terms of conditioning, i.e., the corresponding projection factor is minimized over the optimal circle. This can be understood by recalling that the projection matrix only depends on the set-up dimensions, hence, it is not affected by frequency parameters. This is not the case, however, for the Green's matrix, as varying the frequency induces a phase variation between its complex entries:

$$\mathbf{G}_o = \begin{bmatrix} \frac{e^{-jk_0r_0}}{r_0} & \frac{e^{-jk_0r_1}}{r_1} \\ \frac{e^{-jk_1r_0}}{r_0} & \frac{e^{-jk_1r_1}}{r_1} \\ ----- & ----- \\ \frac{e^{-jk_0r_0}}{r_0} & \frac{e^{-jk_0r_1}}{r_1} \\ \frac{e^{-jk_1r_0}}{r_0} & \frac{e^{-jk_1r_1}}{r_1} \end{bmatrix}. \tag{2.45}$$

The new Green's matrix is a double concatenation of a similar matrix to the TM case, the difference lying in the absence of the polarization (-) sign in the first column. However, this does not affect conditioning as the (-) sign is canceled once carrying out the calculations for the projection factor. This suggests that frequency diversity contributes with a new set of optimal positions in addition to the optimal circle: a set of optimal hyperbolas with exactly the same properties as in the TM case. To highlight this, the projection factor corresponding to $\mathbf{G}_{TE}$ columns is plotted in Fig. 2.12a, where a UFBW $= 4\%$ is used with the plate being at a distance $d = 10\lambda_0$ from the AUT. The resulting set of optimal positions is a superposition of the optimal circle and the optimal hyperbola. The projection factor ignores the impact of the distances distribution that defines conditioning circles. The pattern of the overall condition number, which takes into account all conditioning parameters, is plotted in Fig. 2.12b, showing a better spatial distribution than the basic model due to the contribution of the optimal hyperbola. Introducing frequency diversity in the TE case allows achieving optimal positions with satisfying conditioning levels at regions other than the default optimal circle. This is particularly advantageous in a complete measurement scenario as using the same frequency parameters for both the TM and

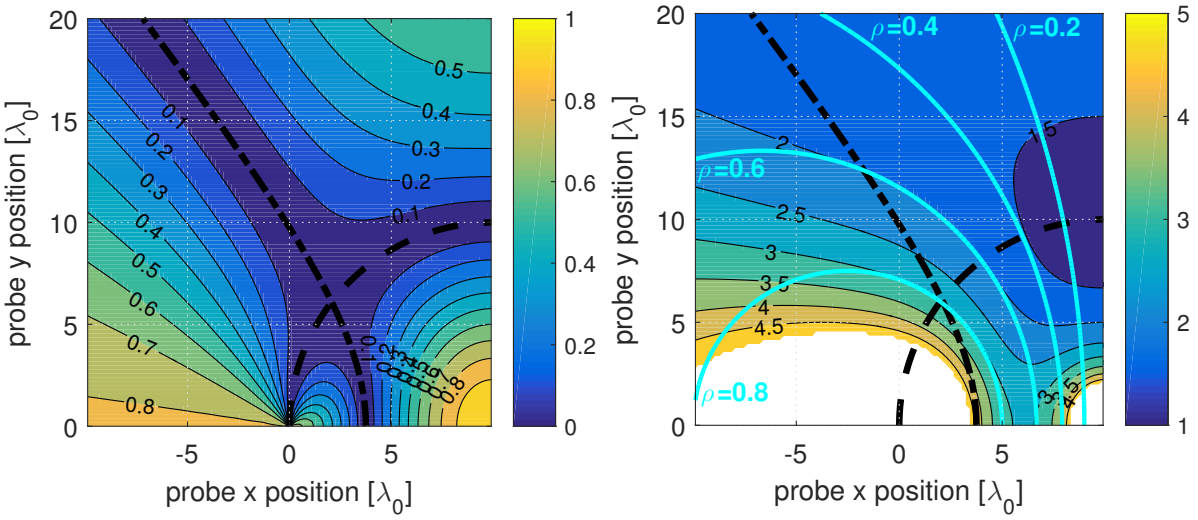

(a) (b)

Figure 2.12 Introducing frequency diversity to the TE model and the contribution of the optimal hyperbola (dot-sashed) to conditioning in addition to the optimal circle (dashed), $x_p = 10\lambda$, UFBW= 4%: (a) ρ_M, (b) $\kappa(\mathbf{G}_{TE})$.

TE modes allows generating sets of common optimal positions. If this is not case, a mechanical displacement effort would be necessary in order to move the probe to different optimal positions corresponding to each transverse model.

Retrieving the ARP vector in the overdetermined TE model consists in solving the corresponding pseudo-inverse problem. The Least-Squares (LS) solution is an optimal solution for such a problem,

$$\hat{\mathbf{F}} = \underset{\mathbf{F}}{\text{Arg min}} \, \|\mathbf{GF} - \mathbf{E}\|^2, \tag{2.46}$$

where the double vertical line symbol stands for the L2 norm.

2.3.4 Relationship Between the Projection Factor and the Condition Number

The conditioning study was carried based on the projection factor ρ. However, recalling that the precise indicator of the system stability being the condition number, it is convenient to study the relationship between the projection factor and the condition number in order to judiciously decide on the configuration parameters.

An approximative relationship between κ and ρ is achieved by exploring the following matrix identity [56, pp. 475-478]:

$$\Lambda_{\mathbf{A}^H\mathbf{A}} = \sigma^2_{\mathbf{A}}, \tag{2.47}$$

with **A** being an m-by-n matrix. Eq. 2.47 states that the eigenvalues Λ of the product of the hermitian transpose of some matrix with itself are the squares of the singular values σ of the matrix **A**. Suppose **A** is a 2-by-2 matrix whose product with its hermitian transpose gives,

$$A^H A = \begin{bmatrix} a_{11} & a_{12} \\ a_{21} & a_{22} \end{bmatrix}, \tag{2.48}$$

a_{11} and a_{22} being by definition real positive. The eigenvalues of $\mathbf{A}^H\mathbf{A}$ are found by solving $det(\mathbf{A}^H\mathbf{A} - \Lambda_{\mathbf{A}^H\mathbf{A}} I) = 0$, I being the identity matrix, which yields,

$$\Lambda_{\mathbf{A}^H\mathbf{A}_{1,2}} = \frac{a_{11} + a_{22} \pm \sqrt{(a_{11} - a_{22})^2 + 4|a_{12}|^2}}{2} \tag{2.49}$$

Assuming $a_{11} \approx a_{22}$, which means that the norms of the two rows of **A** are approximately equal, and which can be translated in the $\mathbf{G}_{TM}$ and $\mathbf{G}_{TE}$ cases as having the two distances separating the AUT and image from the probe being approximately equal. This assumption is of interest in our case as it as it characterizes optimal positions which have a low distances spread. Consequently, we have $4|a_{12}|^2 >> (a_{11} - a_{22})^2$ and Eq. 2.49 simplifies to,

$$\Lambda_{\mathbf{A}^H\mathbf{A}_{1,2}} = \frac{2a_{11} \pm \sqrt{4|a_{12}|^2}}{2} = a_{11} \pm 2|a_{12}|. \tag{2.50}$$

One can easily verify the following expression relating the projection factor of **A** to the entries of $\mathbf{A}^H\mathbf{A}$:

$$\rho_{\mathbf{A}} = \frac{|a_{12}|}{a_{11}}. \tag{2.51}$$

$|a_{12}|$ is simply the projection between the two rows of the original matrix **A**, and a_{11} is the square of the norm of the first row, which is assumed to be approximately equal to the norm of the second row. Hence a_{11} can stand for the product of the norms of the two rows. Accordingly, this further simplifies Eq. 2.50 to:

$$\Lambda_{\mathbf{A}^H\mathbf{A}_{1,2}} = a_{11}(1 \pm \rho_{\mathbf{A}}). \tag{2.52}$$

Applying the identity of Eq. 2.47, the singular values of **A** are the square roots of the eigenvalues of $\mathbf{A}^H\mathbf{A}$:

$$\sigma_{\mathbf{A}_{1,2}} = \sqrt{a_{11}(1 \pm \rho_{\mathbf{A}})}. \tag{2.53}$$

Finally, the mathematical expression of Eq. 2.21 defining the condition number as the ratio of the largest to the smallest matrix singular values is used to express $\kappa(\mathbf{A})$ as function of $\rho_{\mathbf{A}}$:

$$\kappa(\mathrm{A}) = \sqrt{\frac{1 + \rho_{\mathbf{A}}}{1 - \rho_{\mathbf{A}}}}. \tag{2.54}$$

This expression suggests, as shown in Fig. 2.13, that up to $\rho = 0.6$ the condition number is

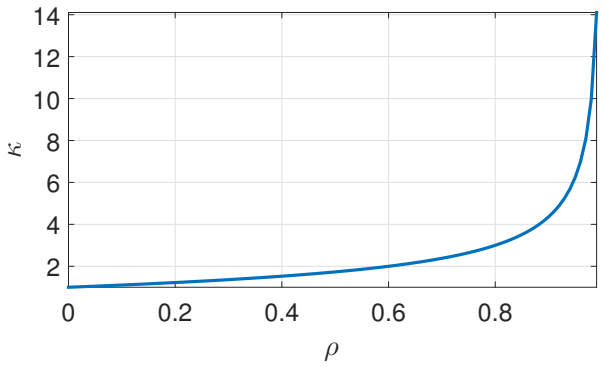

Figure 2.13 Approximative relationship between ρ and κ for a 2×2 square matrix assuming equality between diagonal elements.

fairly low (<2) and augments slowly with ρ. Between $\rho = 0.6$ and $\rho = 0.8$, the condition number is averagely low (<3) and keeps augmenting slowly with ρ. Beyond $\rho = 0.8$, the condition number undergoes dramatic amplification and the matrix tends towards singularity. These observations may be verified using the results carried in the conditioning study. In the TM case, Eq. 2.54 is exact over the optimal hyperbola (refer to Eq. 2.28) and the condition number is exactly equal to the distances spread,

$$\kappa(\mathrm{G}_{TM})_{opt} = \sqrt{\frac{1+\rho_{\mathbf{G}_{TM}}}{1-\rho_{\mathbf{G}_{TM}}}} = \frac{1}{\gamma} = \frac{r_1}{r_0}. \tag{2.55}$$

This is verified in Fig. 2.5 which plots the projection factor and the associated condition number in exact agreement with Eq. 2.54 over the optimal hyperbola. In the basic TE case (no frequency diversity), the agreement is quite good over the optimal circle as shown in Fig. 2.11b, where $\kappa(\mathbf{G}_{TE}) \approx 1.5$ for $\rho = 0.6$, and $\kappa(\mathbf{G}_{TE}) \approx 2.2$ for $\rho = 0.8$.

As a rule of thumb, optimal positions with projection factors up to 0.6 are considered well conditioned. Over $\rho = 0.6$ conditioning is tolerated up to 0.8 which is considered the limit of accepted optimal positions. The TM optimal position corresponding to $\rho = 0.6$ in Fig. 2.5b was achieved at a distance $12\lambda_0$ from the AUT with $d = 10\lambda_0$, and a UFBW= 4% which may be applied even to narrowband antennas. The conditioning study carried over this section proved the mathematical viability of the proposed concept and showed that it is possible to achieve good stability using typical measurement set-up dimensions and quite narrow FBWs.

2.4 Concept Objective: Reducing Mechanical Effort

The presented concept aims at accelerating the measurement process by introducing a spacial diversity that allows measuring several ARP samples in each acquisition. In the single-plate case,

the ability of measuring two ARP samples simultaneously suggests the possibility of cutting the measurement time up to one half with respect to classical techniques.

A range of measurement angles is spanned by introducing a mechanical effort either by moving the probe or by rotating the AUT. In order to achieve maximum efficiency in terms of mechanical effort reduction, and thus in terms of measurement time, no interference between covered angles should occur. This requires controlling the two measurement angles corresponding to each scenario and adapting them to the measurement sampling angle ϕ_s which is supposed to be constant over the measured range.

2.4.1 Positions-Angles Mapping

The relationship between the two measurement angles as function of the probe position is determined using the sine law [57, pp. 101-104]. This law relates the lengths of the sides of a triangle to the sines of its angles. Applying the sine law to the triangle whose vertices are the AUT, image, and probe positions, as shown in Fig. 2.14, yields:

$$\frac{\sin\phi_0}{\sin\phi_1} = \frac{r_1}{r_0} \tag{2.56}$$

Accordingly, the ratio of the sines of the measured angles is equal to the inverse of the ratio of the distances separating corresponding sources to the probe. Near the plate, the distances spread is reduced and hence the two angles become approximately equal. This situation would be of interest in the TE case where conditioning improves near the plate. Otherwise, it is easier to handle Eq. 2.56 if the two angles have an integer ratio, say m_a:

$$\phi_0 = m_a\phi_1, \quad m_a \in \mathbb{N} - \{0,1\}. \tag{2.57}$$

As we are going to show next, an integer ratio of the measurement angles is also advantageous for the measurement procedure. Accordingly, Eq. 2.56 becomes,

$$\frac{\sin m_a\phi_1}{\sin\phi_1} = \frac{r_1}{r_0}, \tag{2.58}$$

This equation, although looking simple, is quite complicated to solve when replacing the angles and distances terms by the cartesian variables x and y in order to find the corresponding probe position. One situation that allowed us achieve a canonical form is when the LOS angle is a double of the image angle, i.e., $m_a = 2$. In this case, Eq. 2.58 reduces to,

$$\cos\phi_1 = \frac{r_1}{2r_0}. \tag{2.59}$$

Developing Eq. 2.59 yields,

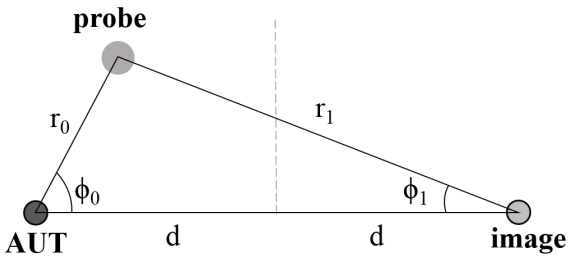

Figure 2.14 The relationship between the two measured angles as function of the probe position is obtained using the sine law.

$$\begin{aligned} \frac{2d}{\sqrt{(2d-x)^2+y^2}} &= \frac{\sqrt{(2d-x)^2+y^2}}{2\sqrt{x^2+y^2}} \\ \Rightarrow (2d-x)^2+y^2 &= 4d\sqrt{x^2+y^2} \\ \Rightarrow \left[(2d-x)^2+y^2\right]^2 &= 16d^2\left(x^2+y^2\right). \end{aligned} \tag{2.60}$$

Eq. 2.60 is a quartic equation that has four possible solutions. However, only one solution respects the initial constraint $\phi_0 = 2\phi_1$; the remaining solutions appear due to the applied trigonometric identities to develop the problem, and which are valid for other angles pairs than the suitable one. The accepted solution is a hyperbola with the following parameters:

$$\begin{aligned} &\frac{(x-\Delta x)^2}{a^2} + \frac{y^2}{b^2} = 1, \\ &\text{with:} \quad \Delta x = \frac{4d}{3} \\ &\qquad\quad a^2 = \frac{4d^2}{9} \\ &\qquad\quad b^2 = \frac{4d^2}{3}. \end{aligned} \tag{2.61}$$

Higher integral ratios of the two angles have hyperbola similar shapes, as shown in Fig. 2.15. However, they are difficult to express in canonical form. The choice of $m_a = 2$ offers the advantage of being able to analytically predict the corresponding positions as function of the AUT-plate separation. Positions yielding angles corresponding to higher integral ratios are however easily retrieved by numerically spanning the test zone. Once an angles ratio is chosen, the configuration parameters may be adjusted such that the optimal hyperbola is pushed closer to targeted positions in order to improve their conditioning level. An example is shown in Fig. 2.15 where the configuration parameters, $d = 10\lambda_0$ and $\Delta f_u = 6\%$, made the targeted positions corresponding to $m_a = 2$ fall in the vicinity of the first order optimal hyperbola.

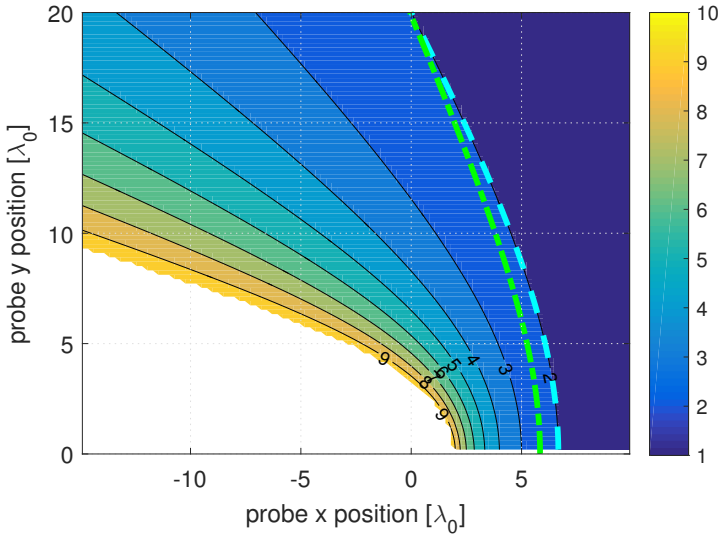

Figure 2.15 Ratios of measured angles $\frac{\phi_0}{\phi_1}$ as function of the probe position for an AUT-plate separation $d = 10\lambda_0$, and verification of the developed formula for $m_a = 2$ (dashed) with example showing the possibility of adjusting the configuration parameters ($\Delta f_u = 6\%$) such that the optimal hyperbola (dot-dashed) is very close to targeted positions.

2.4.2 Algorithms for Maximum Efficiency

Maximum mechanical effort reduction is attained by cutting the overall mechanical displacement effort to a half of that of a classical measurement. This requires no interference between targeted angles and already covered angles, which is achievable by controlling the relationship between the two measurement angles and the sampling angle ϕ_s for each displacement. Accordingly, the choice of rotating the AUT is privileged rather than moving the probe as it keeps the two measurement angles constant with respect to the reference coordinates system.

A forward rotation algorithm is characterized by a sampling angle equal to the difference between the two measurement angles, $\phi_s = \phi_0 - \phi_1$, and a rotation angle to $\phi_r = 2\phi_s$. Such an algorithm would be adequate for positions near the plate which yields close measurement angles and hence a reasonably small sampling angles. An example of the distribution of the difference of measurement angles is plotted in Fig. 2.16a for a set-up characterized by an AUT-plate separation $d = 10\lambda_0$. The figure shows that generally a horizontal probe-plate separation less than $2\lambda_0$ is required in order to generate sampling angles smaller than 10°. Otherwise, the vertical AUT-probe separation has to be kept relatively small compared to the horizontal AUT-probe separation (Eq. 2.2). Ideally the targeted range would be an integer multiple of the sampling angle, otherwise a minimum additional effort would be required in order to cover the remaining angles. For instance, achieving maximum efficiency in terms of mechanical rotation in a measurement spanning the azimuthal plane would require that the sampling angle is an integer ratio of 360°. An example of the application of the algorithm is depicted in Figs. 2.16b

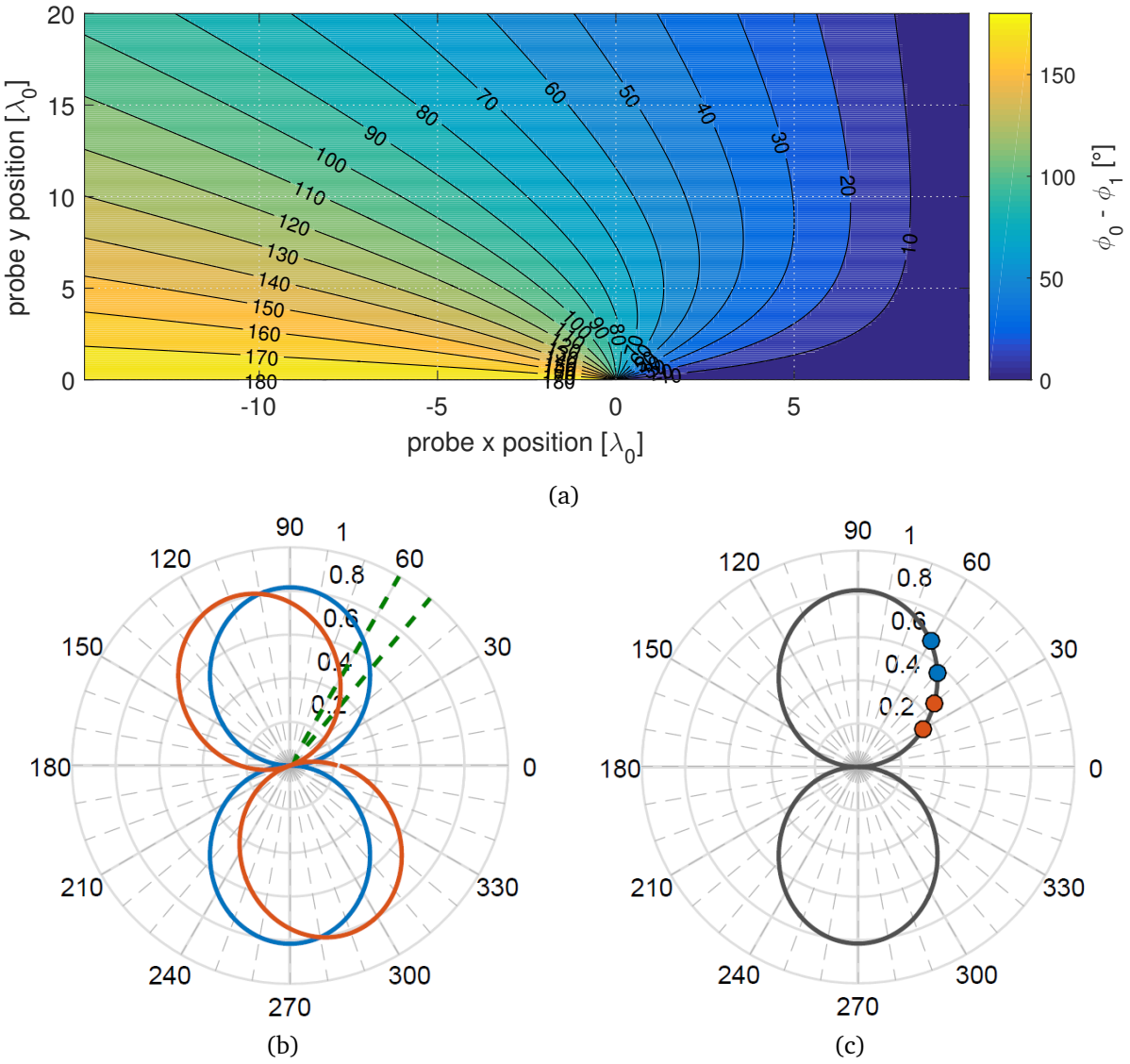

Figure 2.16 Example of the application of the forward rotation algorithm in order to avoid interference between targeted angles and already covered angles while rotating an AUT with directive ARP. $\phi_s = \phi_0 - \phi_1 = 10°$ (dashed), $\phi_0 = 60°$, $\phi_1 = 50°$: (a) $\phi_0 - \phi_1$, $d = 10\lambda_0$ (b) Two sets of consecutive orientations separated by a rotation angle $\phi_r = 2\phi_s$ (d) Covered angles corresponding to both sets of orientations.

and 2.16c for a sampling angle $\phi_s = 10°$. A rotation angle $\phi_r = 2\phi_s = 20°$ is systematically introduced in order to avoid interference between already covered angles and angles yet to cover. Accordingly, two linearly spaced, different angles are covered in each rotation, allowing to cut down the overall mechanical rotation effort to a half with respect to classical techniques. This algorithm is more adapted to the TE case where optimal positions are by default near the plate. The TM case requires the application of relatively large UFBWs in order to push the first order optimal hyperbola towards the plate. For instance, by comparing Figs 2.16a and 2.6a, one may notice that an UFBW> 10% is required in order to locate the first order optimal hyperbola inside the region characterized by $\phi_s < 10°$. Alternately, it is possible to use the lower portion of the optimal conditioned region when applying a narrow UFBW. For instance, by applying an UFBW= 4% (with $d = 10\lambda_0$), positions with small vertical separations with respect to the AUT in the region $x \in [4\lambda_0, 7\lambda_0]$ show conditioning levels below 3.

A more general algorithm for achieving maximum efficiency is possible by choosing an integer ratio between the LOS and image angles, m_a, along with setting an integer ratio between the image and sampling angles, say $m_b = \frac{\phi_1}{\phi_s}$. The developed algorithm is shown in Fig.2.17. The AUT is rotated by $\phi_r = \phi_s$ a number of times before applying a jump in order to avoid interference between already covered angles and angles yet to cover. The algorithm predicts as function of the chosen parameters (ϕ_0, ϕ_1, and ϕ_s) rotations where new targeted angles interfere with already covered angles and perform an adapted jump to avoid this interference. For a complete azimuthal span, this algorithm is only valid when the number of sampling angles n_s is an integer multiple of $m_b(m_a - 1)$:

$$n_s = n[m_b(m_a - 1)], \quad n \in \mathbb{N}^*. \tag{2.62}$$

If this condition is not satisfied, a minimum additional effort would be required to measure the remaining angles. An example of the application of the rotation algorithm is shown in Fig. 2.18, where $\phi_s = 15°$, $\phi_1 = 45°$, and $\phi_0 = 90°$. These parameters imply performing sets of three rotations ($m_b = 3$) before introducing a jump of 60° ($\phi_s[m_s(m_a - 1) + 1]$). For each rotation, two samples are measured, and are shown with the same color in Figs. 2.18b and 2.18d. In this scenario, 12 samples spanning 180° are covered by performing 6 rotations, highlighting the efficiency of the proposed concept.

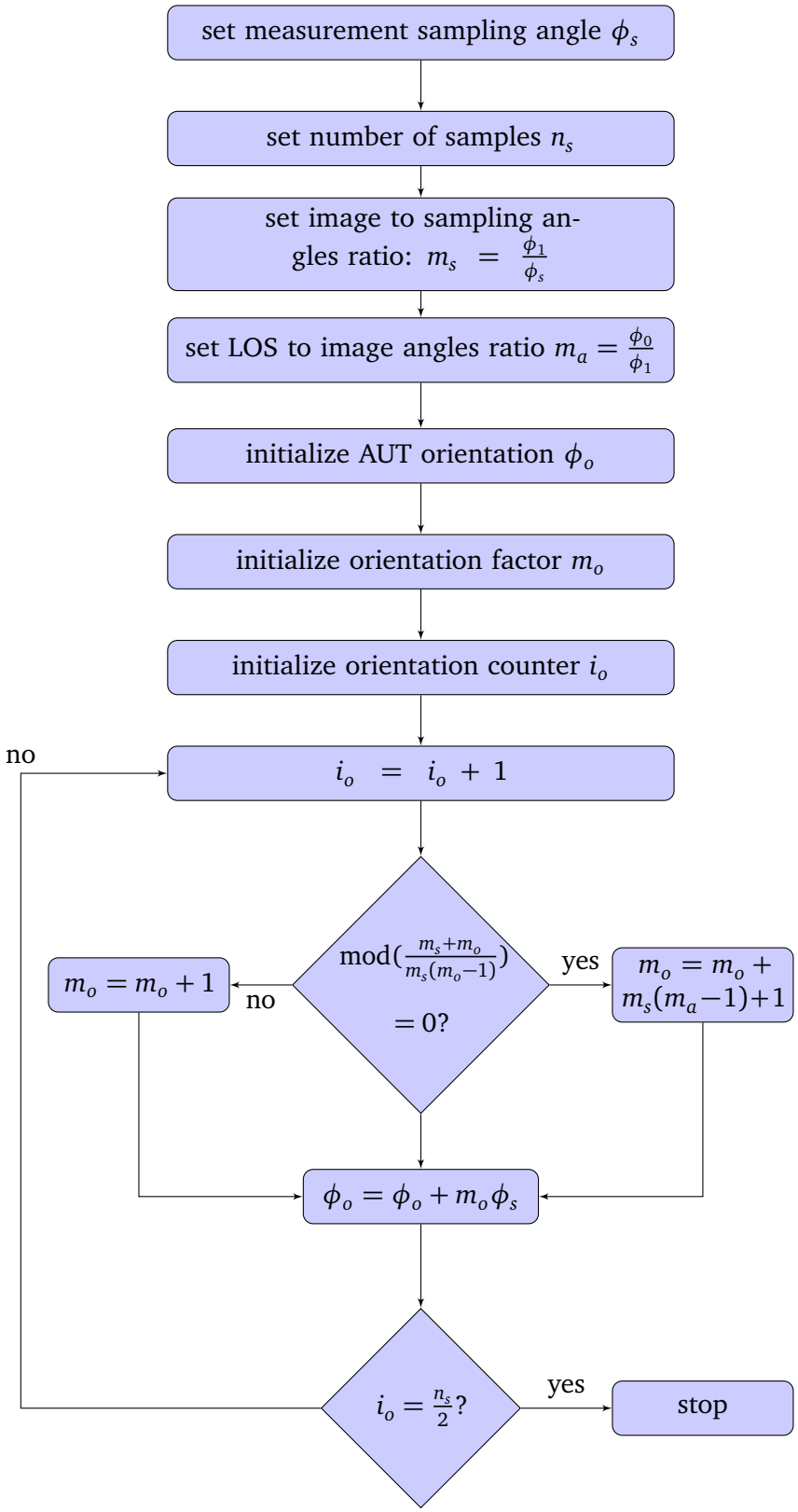

Figure 2.17 Algorithm for achieving maximum rotation efficiency based on integer ratios between the measurement angles

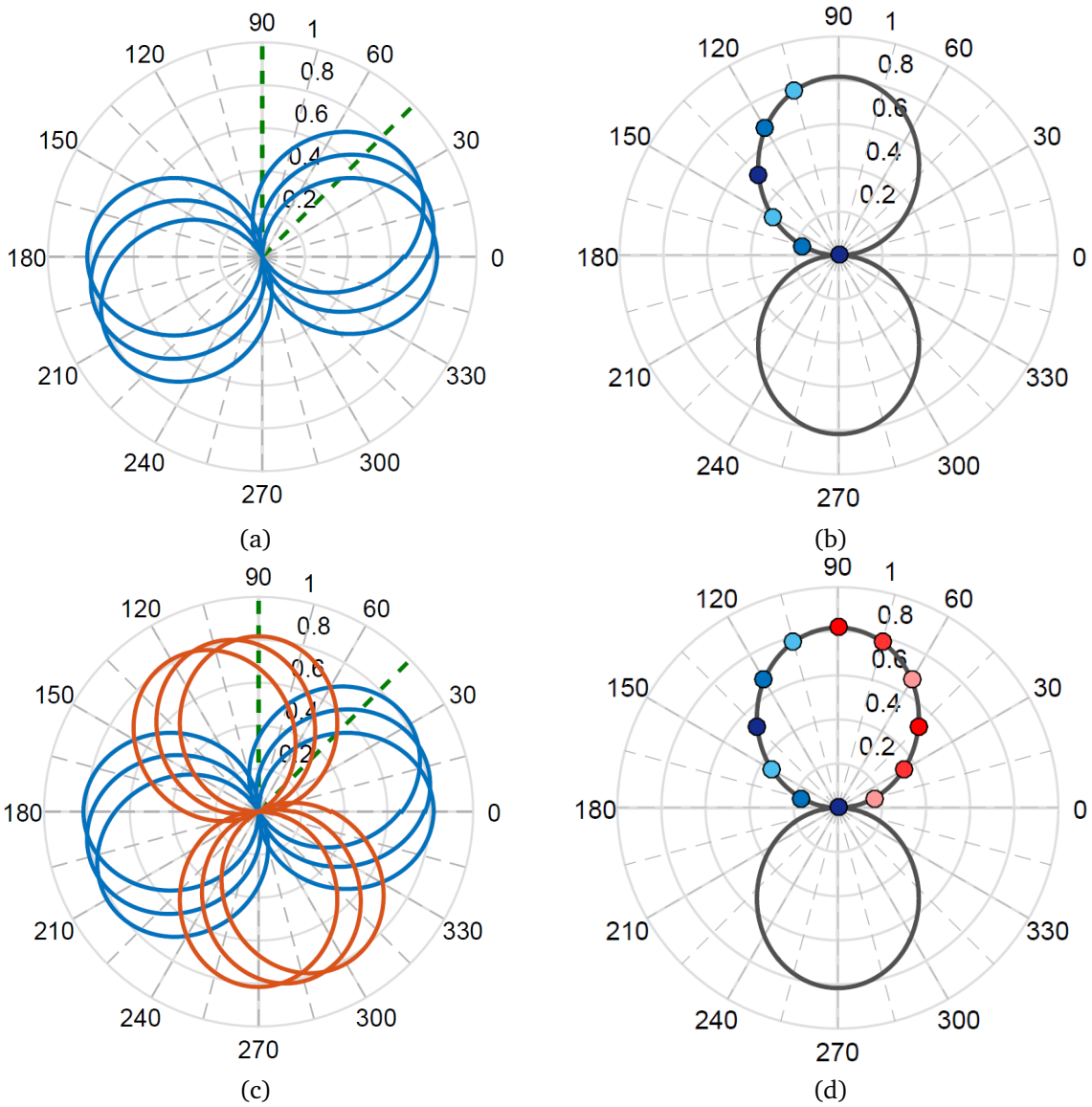

Figure 2.18 Example of the application of the general rotation algorithm in order to avoid interference between targeted angles and already covered angels while rotating an AUT with a directive ARP. $\phi_s = 15°$ (dashed), $\phi_1 = 3\phi_s = 45°$, $\phi_0 = 2\phi_1 = 90°$: (a) First set of rotations (b) Covered angles corresponding to the first set of rotations (c) Second set of rotations applied after an adapted jump (d) Covered angles corresponding to the both set of rotations.

Conclusion

This chapter presented the proposed concept using the simplest configuration in terms of controlled echoes: the single-plate configuration which allows the generation of a single controlled echo. The model was simplified in order to assess its viability from a mathematical point of view. The conditioning study highlighted the possibility of achieving mathematically stable systems using typical configuration parameters. General guidelines regarding optimal and worst positions in terms of conditioning are summarized in Table 2.1.

		Optimal Regions	**Worst Regions**
TM Model		Conditioning locally optimal over a set of optimal hyperbolas which are defined by the AUT-plate separation and the working UFBW. Conditioning level indicated by conditioning circles: it improves for larger AUT-probe separations.	_ Set of worst hyperbolas which are defined by the AUT-plate separation and the working UFBW. _ Immediate vicinity of the AUT. _ Near the plate (region width inversely proportional to the AUT-plate separation and to the working UFBW).
TE Model	**Basic Model**	Conditioning locally optimal over an optimal circle which is exclusively defined by the AUT-plate separation. Conditioning level indicated by conditioning circles: it improves near the plate at a vertical distance equal to the AUT-plate separation.	_ Immediate vicinity of the AUT. _ Far from the AUT (vertical distances much larger than the AUT-plate separation). _ Far from the plate.
	Introducing Frequency Diversity	Frequency diversity introduces sets of optimal hyperbolas in the same fashion as in the TM case.	Set of worst hyperbolas which are defined by the AUT-plate separation and the working UFBW.

Table 2.1 General guidelines regarding optimal and worst positions in terms of conditioning.

The theoretical efficiency of the proposed concept in accelerating the measurement process was also discussed and algorithms for achieving maximum efficiency were presented. The next chapter highlights practical limitations of the developed models.

Chapter 3

Single plate Configuration: Practical Considerations

Contents

Chapter 2 presented a simplified model of the proposed concept in order to assess its viability from a mathematical point of view. In this chapter, a study of the model practical limitations is conducted in order to verify its *physical* viability. Practical error sources are classified into two categories: general error sources which are in common with classical measurement techniques, and model-related errors which are the focus of this chapter. Model-related errors are quantified and limited either by reducing their impact or by updating the simplified model in order to take them into account.

3.1 Introduction

From a practical point of view, the proposed concept, like any measurement technique, is subject to a set of inevitable errors sources due to uncertainties related to the measurement system and practical limitations of used equipment. The tolerance of the proposed method to this type of error is assessed with emphasis on error factors with higher impacts, highlighting the importance of conditioning models developed in Chapter 2. The error spread between the ARP LOS and image samples is assessed as well, and an analytical formula is retrieved assuming an error factor with a Gaussian distribution which may conveniently model a general term combining the set of practical systematic errors [34]. Moreover, the models developed in Chapter 2 were based on a set of approximations and simplifying assumptions which may be summarized in: the coherence of the far-field model, the generation of only the LOS and image fields corresponding to the AUT free-space ARP, the infinite conductivity of the reflecting plate, and the ARP frequency independence. This approach was advantageous in simplifying the mathematical conditioning study yielding analytical formulas for optimal positions in terms of conditioning. Although these assumptions may hold under certain conditions, they cannot be systematically maintained as they ignore the effect of several physical phenomena that characterize the concept. Model limitations are studied and related error sources are quantified as function of the measurement parameters. Finally, linear regression is introduced in order to enhance the proposed method by reducing the ARP error resulting from phenomena that are not taken into account in the model, and by optimizing the model as well through the estimation of the frequency impact on the free-space ARP. Synthetic results to highlight these aspects are presented using a half-wave dipole (HWD).

3.1.1 Tested Antenna

The main AUT used in order to synthetically test the model is a half-wave dipole whose ARP is shown in Fig. 3.1. The dipole may exclusively be used in each transverse mode as function of its orientation with respect to the working azimuthal plane. TM operation is ensured when the dipole is parallel the z-axis. In this case the ARP over the azimuthal plane is isotropic, i.e., a circle. TE operation on the other hand is ensured when the dipole is parallel to the azimuthal plane. In this case the ARP is directive, with a directivity $D_r = 1.64$ (2.15 dBi). Assuming independence between the different error factors, the impact of frequency diversity on the free-space ARP is neglected when studying remaining error sources.

3.1.2 Test Zone

The basic tested configuration is characterized by an AUT-plate separation $d = 10\lambda_0$ and a $20\lambda_0 \times 20\lambda_0$ test zone bounded from the bottom by the AUT position, the origin, and from the right by the plate. A synthetic reference field is generated based on the far-field model using the

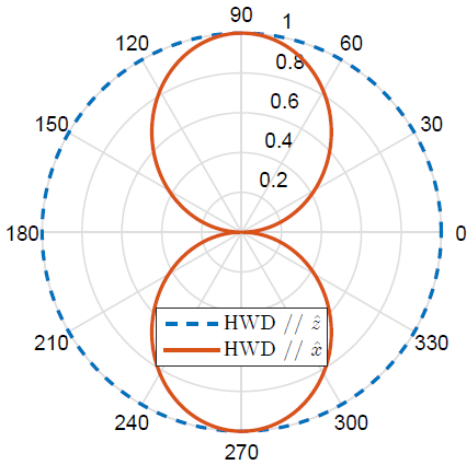

Figure 3.1 Normalized ARP azimuthal cuts of a HWD oriented parallel to the z-axis (dashed) and to the x-axis (solid), corresponding to TM and TE modes respectively.

reference ARP shown in Fig. 3.1. Then it is modified as function of tested parameters before proceeding with the inversion in order to retrieve the calculated ARP samples based on the proposed concept. The ARP error is then estimated by comparing the calculated ARP to the reference ARP. Unless otherwise stated, the local relative ARP amplitude error is considered throughout this chapter,

$$\epsilon_F = \frac{\left| \left\| \mathbf{F}_{\text{model}} \right\| - \left\| \mathbf{F}_{\text{ref}} \right\| \right|}{\left\| \mathbf{F}_{\text{ref}} \right\|}. \tag{3.1}$$

where $\mathbf{F}_{\text{model}}$ is the ARP vector calculated using the proposed concept, and $\mathbf{F}_{\text{ref}}$ is the reference ARP vector.

3.2 Model Tolerance to General Practical Errors

Common practical limitations of classical ARP measurements were presented in Sec. 1.5.2. These limitations are essentially related to the measurement system and vary as function of the adopted range. The concept being limited in this work to a far-field model, only related error sources are of concern. These may be summarized in probe parameters errors, impedance mismatch errors, receiver errors, alignment errors, unintentional reflections, and position errors. The first three error sources impact the concept pretty much like any other measurement technique. An alignment error, characterized by an elevation rotation error between the probe and the AUT coordinates systems would perturb the transverse models decomposition making longitudinal components contribute in the TM mode and the transversal component contributes in the TE mode. In the case of unintentional reflections, which are generally considered as

the most important error source, the concept may be considered advantageous as the plate is supposed to generate only controlled echoes, and thus it reduces the overall unintentional echoes budget. On the other hand, position errors may impact all the proposed set-up elements which result in perturbing the distances separating the AUT and the image from the probe. The field phase being sensitive to distance change, this would result in an error between predicted and measured fields when superposing the LOS and image contributions, which might induce a large ARP error. A synthetic evaluation of the mentioned error sources may be performed by combining their impacts using a Gaussian model [34]. This method is adopted herein and synthetic results are presented in Sec. 3.2.2. Position errors, in particular, are separately studied in Sec. 3.2.1 due to their suspected serious impact.

3.2.1 Impact of Position Uncertainty

Position errors induce an error on distances separating the AUT and the image from the probe:

$$r_i' = r_i + \delta r_i, \tag{3.2}$$

where δr_i is the distance error term corresponding to each source. This would impact the LOS and image fields magnitudes which are inversely proportional to the corresponding distances, but most importantly their corresponding phases which are more sensitive to distance errors:

$$\delta\beta_i = k\delta r_i = \frac{2\pi}{c} f\, \delta r_i. \tag{3.3}$$

The distance error term is amplified by the working frequency which would induce a large phase error if one of the two terms is high. In a classical measurement context, this would not be a serious matter as the focus is generally on the field magnitude. However, this is not the case in the present concept as the reference field is the vector sum of the two useful fields ($\vec{E} = \vec{E}_{\text{LOS}} + \vec{E}_{\text{image}}$). Consequently, an error on the fields phases perturb their summation adding another error term to the direct magnitude error.

Position uncertainty impacts all the set-up elements, but mainly the AUT as the physical position uncertainty is coupled with uncertainty over the AUT phase center position. The latter being considered as the apparent radiation point, it is function of the measurement direction and the working frequency [58]. It is then important to study the tolerance of the proposed model to position errors. To do so, a position uncertainty factor is used to alter original positions using a Gaussian model and the corresponding ARP error is recorded. The outcome is averaged over 1000 trials. Results are shown in Fig. 3.2 where a position uncertainty factor $\sigma_{pos} = 3$mm is used to perturb the AUT, plate and probe positions assuming a TM model. Figs 3.2a and 3.2b show the ARP error for an operating frequency $f_0 = 1$GHz, for which the position uncertainty factor is equal to $\sigma_{pos} = 10^{-2}\lambda_0$. The impact is very weak in the optimal conditioning region introducing an error below -50dB. As suggested by Eq. 3.3, the position error impact is proportional to the

working frequency. The same can be seen in Figs. 3.2c and 3.2d where an operating frequency $f_0 = 10$GHz is used and for which the position uncertainty factor is equal to $\sigma_{pos} = 10^{-1}\lambda_0$. Error in this case is considerably high exceeding, for the image case, -35dB in the optimal conditioning region and -20dB near regions of ill-conditioning.

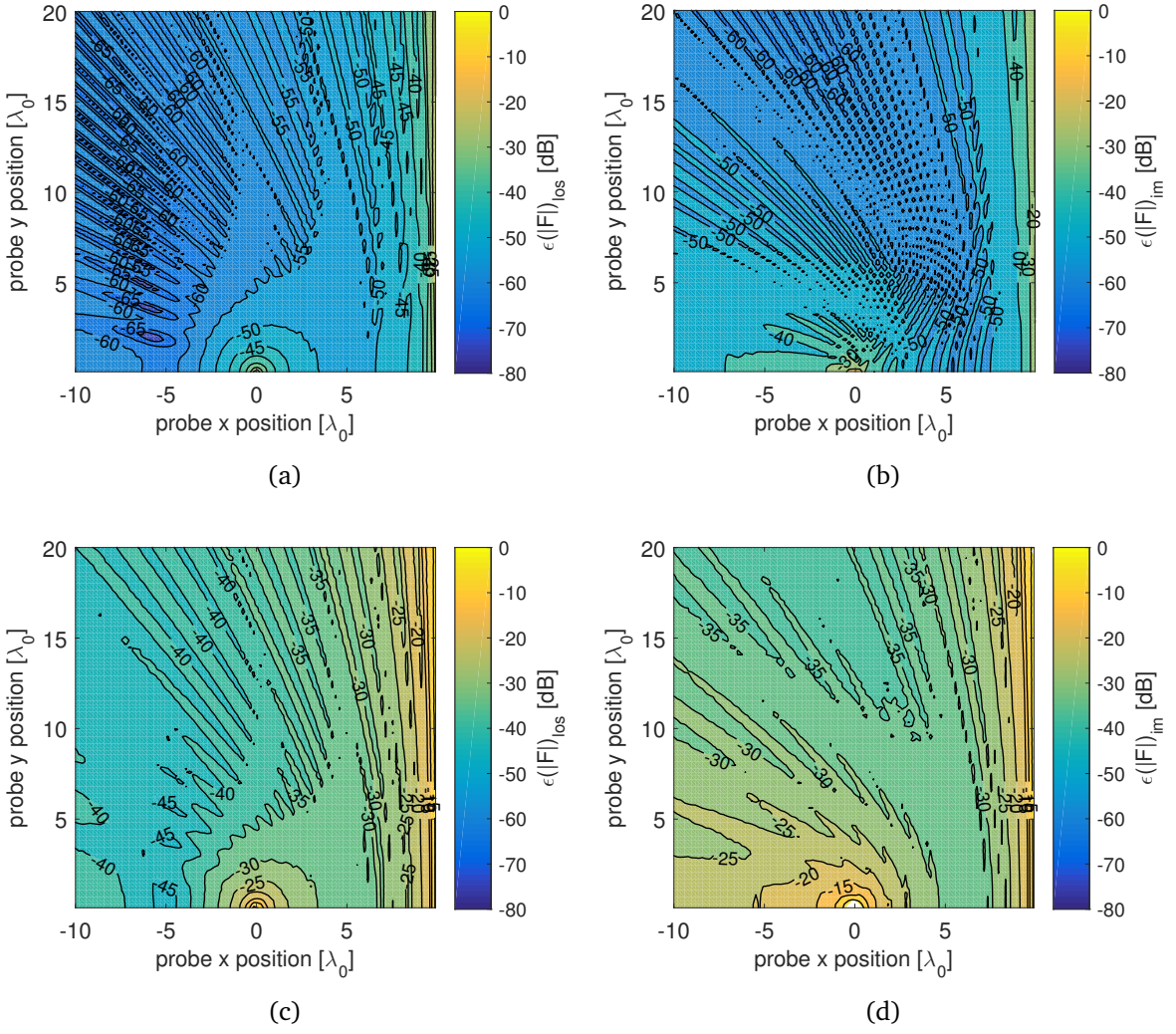

Figure 3.2 ARP error as function of position uncertainty. TM case, $SNR = \infty$, $\sigma_{pos} = 3mm$, $N_t = 1000$, $\Delta f_u = 4\%$, $d = 10\lambda_0$: (a) $\epsilon(\mathbf{F})_{los}$, $f_0 = 1$GHz (b) $\epsilon(\mathbf{F})_{im}$, $f_0 = 1$GHz (c) $\epsilon(\mathbf{F})_{los}$, $f_0 = 10$GHz (d) $\epsilon(\mathbf{F})_{im}$, $f_0 = 10$GHz.

These results highlight the important impact position errors could have if the position uncertainty factor is high with respect the working wavelength. One may notice that the image error is larger than the LOS error. This may be explained by noticing that the image position is determined as function of both the AUT and the plate positions. Consequently, their corresponding error factors are superposed at the image level amplifying as a result the image

position error. However, as we are going to show later, this is not the only explanation as the problem formulation defines the error spread between the LOS and image samples. These results also highlight the importance of conditioning models when error impacts the measurement. For instance, at 10GHz only positions around the optimal hyperbola show tolerable error levels (> -30dB) for both LOS and image sample.

3.2.2 Impact of Generalized noise

Assuming ideal conditions, i.e., that no noise impacts the measurement (SNR $= \infty$), the ARP vector is error clear independently of conditioning, as shown in Fig. 3.3. Figs. 3.3a and 3.3b show the conditioning patterns corresponding respectively to a TM case with an UFBW $= 4\%$ and to the basic TE case (UFBW $= 0\%$).

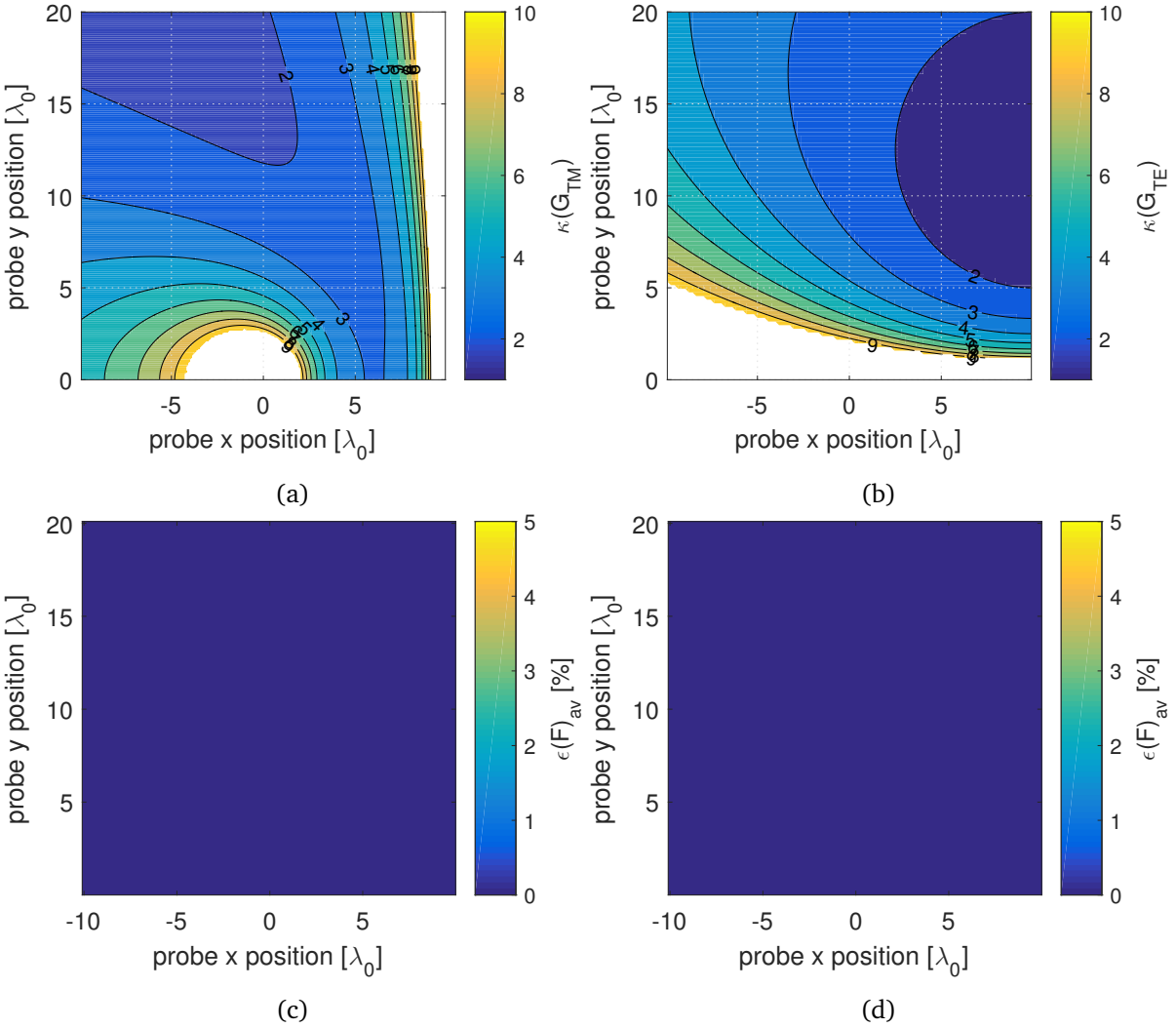

Figure 3.3 Performing the inversion assuming ideal conditions, $d = 10\lambda_0$: (a) $\kappa(G_{TM})$, UFBW $= 4\%$ (b) $\kappa(G_{TE})$ (c) average ARP error $\epsilon(\mathbf{F})_{av}$, TM (d) average ARP error $\epsilon(\mathbf{F})_{av}$, TE.

In the TM case, the system is well conditioned over the optimal hyperbola and improves as the AUT-probe separation grows attaining optimal values ($\kappa(\mathbf{G}_{TM}) < 2$) near the upper left corner. In the TE case, optimal values are achieved near the plate at a vertical distance $y \approx d$ ($\kappa(\mathbf{G}_{TE}) < 1.5$), otherwise the condition number rises gradually as the probe is radially moved outward the optimal region. Notice that condition numbers are up-bounded by 10 for proper plot. Figs. 3.3c and 3.3d show the corresponding relative ARP error levels as function of the probe position, averaged in both cases between the LOS and image samples errors,

$$\epsilon(\mathbf{F})_{av} = \frac{\epsilon(\mathbf{F})_{\text{LOS}} + \epsilon(\mathbf{F})_{\text{im}}}{2}. \tag{3.4}$$

The practically null error levels reveal that computer roundoff error may be neglected even if the system is ill-conditioned.

Practical conditions are described by a certain noise level due to measurement systematic errors which are modeled by introducing a constant additive white Gaussian noise (AWGN). The noise level is adjusted by setting a Signal-to-Noise ratio (SNR) with respect to the reference field. The outcome is averaged over $N_t = 1000$ trials. Fig. 3.4 shows the impact of noise on ARP results as function of the probe position in the TM case (U<ZSFBW = 4%), for three SNR values: 60dB, 40dB, and 30dB. The corresponding conditioning pattern is shown in Fig 3.3a. One may immediately notice the impact of conditioning on ARP results: error patterns are identical in the three cases and follow the conditioning pattern, with their levels being consistent with corresponding noise levels. The LOS samples show quite stable error levels compatible with the inserted noise levels except in the singular region near the plate where it undergoes rapid amplification. The impact is however more important over image samples where error is amplified almost all-over positions outside the optimal conditioning region. The image error is particularly high in the vicinity of the AUT which is not the case over LOS samples. These results highlight the importance of the conditioning models in ensuring the viability of the calculated ARP results in the presence of the inevitable measurement noise. It is rather hard to give values for typical SNRs characterizing classical measurements as they depend on each measurement site and on the set of used equipment. However, 40dB seems a quite realistic choice in regrouping all the set of systematic errors encountered in practice. Accordingly, the proposed model is viable using optimal positions where the calculated ARP maintains the same error level over both LOS and image samples.

One may notice from Fig. 3.4 that the image error is generally higher than the LOS error for the same perturbation factor. At this stage, it is convenient to analytically study the error spread between the LOS and image ARP samples.

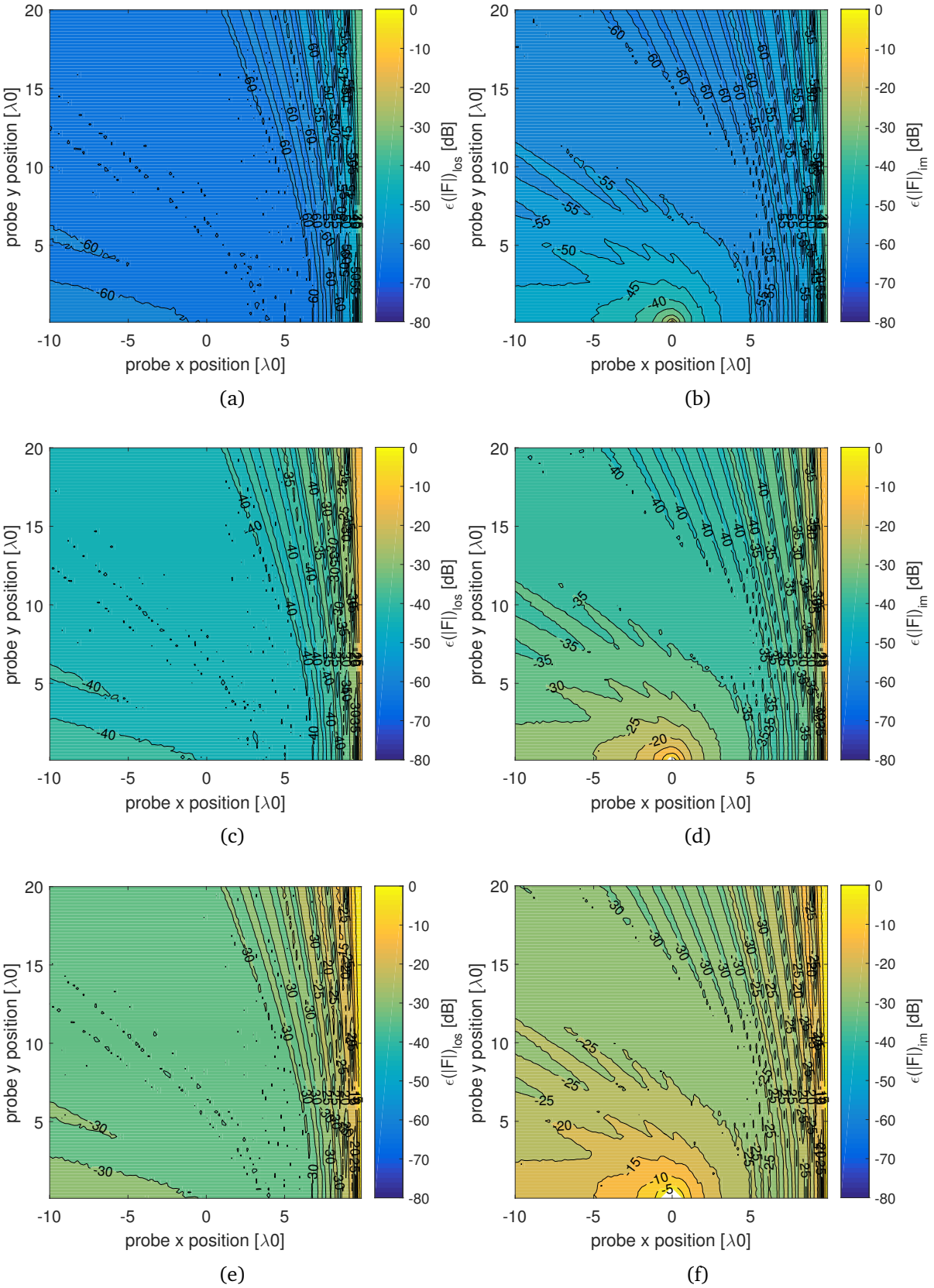

Figure 3.4 Impact of practical systematic errors on the calculated ARP as function of the probe position, TM case. $N_t = 1000$, $\Delta f_u = 4\%$, $d = 10\lambda_0$: (a) $\epsilon(\mathbf{F})_{los}$, $SNR = 60dB$ (b) $\epsilon(\mathbf{F})_{im}$, $SNR = 60dB$ (c) $\epsilon(\mathbf{F})_{los}$, $SNR = 40dB$ (d) $\epsilon(\mathbf{F})_{im}$, $SNR = 40dB$ (e) $\epsilon(\mathbf{F})_{los}$, $SNR = 30dB$ (f) $\epsilon(\mathbf{F})_{im}$, $SNR = 30dB$.

3.2.3 Error Distribution

The formulation of the mathematical model allows to analytically express the relationship between the ARP LOS and image errors. Suppose that the reference field is subject to some noise,

$$\mathbf{E} = \mathbf{E}_s + \mathbf{n}, \tag{3.5}$$

where $\mathbf{E}_s$ is the reference field which is the sum of the LOS and image fields, and $\mathbf{n}$ is a random noise vector. It follows that the calculated ARP vector $\hat{\mathbf{F}}$ is the sum of the *correct* ARP vector $\mathbf{F}_s$ and an ARP error vector δF:

$$\begin{aligned} \hat{\mathbf{F}} &= \mathbf{G}^{-1}\mathbf{E} \\ \hat{\mathbf{F}} &= \underbrace{\mathbf{G}^{-1}\mathbf{E}_s}_{\mathbf{F}_s} + \underbrace{\mathbf{G}^{-1}\mathbf{n}}_{\delta\mathbf{F}}, \end{aligned} \tag{3.6}$$

where $\mathbf{G}$ is the system matrix. Each component of the ARP error vector, i.e., the LOS and image errors, is related to the noise vector through a row of the inverse of the system matrix $\mathbf{G}^{-1}$:

$$\delta\mathbf{F}_i = \left[G^{-1}\right]_i \mathbf{n}, \tag{3.7}$$

By recalling that the error term regrouping practical systematic errors may be modeled using a Gaussian distribution, let us assume for simplicity that the noise vector follows a standard normal distribution $\mathbf{n} \sim \mathcal{N}(0,1)$. By definition if $\mathbf{X} = \sigma\mathbf{n} + \mu$, then $\mathbf{X} \sim \mathcal{N}(\mu, \sigma^2)$. It follows from Eq.3.7:

$$\delta\mathbf{F}_i \sim \mathcal{N}(0, \sum_j |\left[G^{-1}\right]_{ij}|^2), \tag{3.8}$$

Eq. 3.8 states that the LOS and image ARP errors follow a Gaussian distribution with a variance equal in each case to the sum of the square of the entries of each row of the inverse of the system matrix. A useful figure of merit is $N = \frac{\sigma_1^2}{\sigma_0^2}$ describing the ratio of the perturbation observed at the ARP sample corresponding to the image to that corresponding to the LOS. The simplicity of the problem allows to analytically express N as expressing the inverse of the system matrix is forward:

$$\mathbf{G}^{-1} = \frac{1}{|\mathbf{G}|}\begin{bmatrix} G_{22} & -G_{12} \\ -G_{21} & G_{11} \end{bmatrix}, \tag{3.9}$$

where $|\mathbf{G}|$ is the determinant of the matrix $\mathbf{G}$. It follows,

$$N = \frac{|G_{22}|^2 + |G_{12}|^2}{|G_{11}|^2 + |G_{21}|^2}. \tag{3.10}$$

It is easily verified that Eq. 3.10 gives the square of the ratio of distances separating the image and the AUT from the probe in both the TM and TE models:

$$N = \frac{r_1^2}{r_0^2} \tag{3.11}$$

The square root of the last term yields the ratio of the *Standard Deviations* (SD) at the image and LOS levels which is equal to the ARP error spread:

$$\sqrt{N} = \frac{r_1}{r_0} = \gamma^{-1}. \tag{3.12}$$

This states that an error following a Gaussian distribution affects more the image sample than the LOS sample, and that the ratio of the respective ARP errors is expressed by the ratio of distances separating the image and the AUT from the probe. This highlights the importance of the distances spread which also governs conditioning through conditioning circles. Consequently, the ARP error spread pattern in this case is a duplicate of conditioning circles. This is verified in Fig. 3.5 where the ARP error at the image level is compared to the ARP error at the LOS level after introducing an AWGN corresponding to an arbitrary SNR (60dB in this case) and averaging over 1000 trials. The agreement is excellent with conditioning circles.

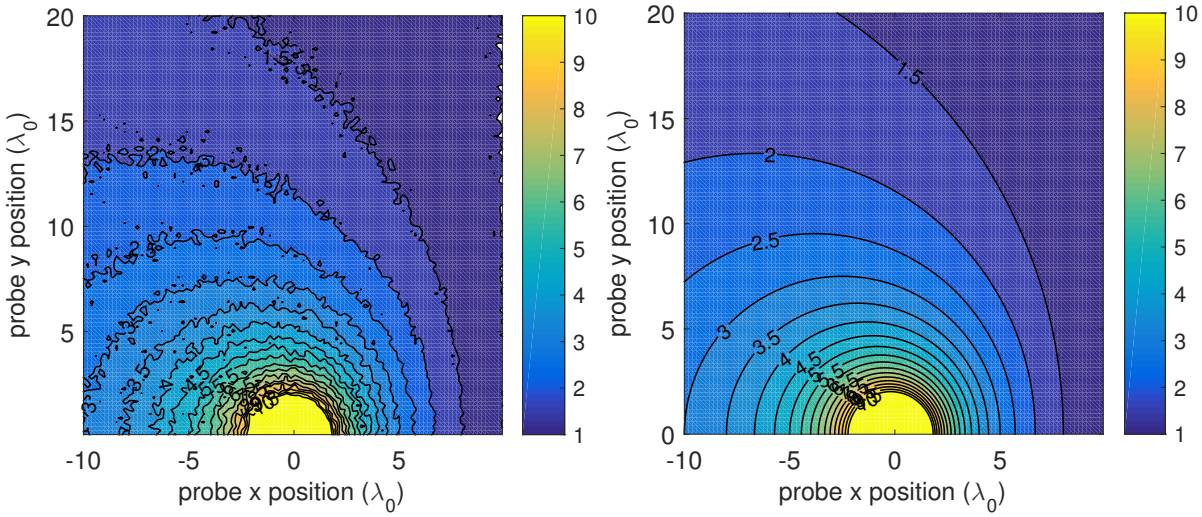

(a) (b)

Figure 3.5 Verification of the standard deviation formula expressing the ARP error spread between the image and LOS samples in terms of the distances spread. $d = 10\lambda_0$, $SNR = 60$dB, $N_t = 1000$ trials: (a) $\frac{\epsilon(\mathbf{F})_{im}}{\epsilon(\mathbf{F})_{los}}$ (b) $\frac{r_1}{r_0}$.

To conclude, optimal positions in terms of conditioning are characterized by a small ARP error spread between the LOS and image samples. As the condition number rises, image samples tend to become more vulnerable to error than LOS samples. As a general rule of thumb, images

samples are more vulnerable to noise than LOS samples. The ARP error spread is proportional to the distances spread.

3.3 Model Systematic Errors

Model related limitations are due to the set of assumptions applied to simplify the model. One forward limitation comes from the fact that the developed formalism is based on a far-field model. The far-field expression being itself an approximation, this assumes placing the probe at very large electric distances from the AUT. Otherwise, the far-field approximation does not precisely describe the field intercepted by the probe, and the assumption that the ARP does not change with distance may become too approximate. Moreover, in Chapter 2 the AUT was assumed dimensionless and the plate infinitely large, which is not the case in practice. Waves vertically impinging on the plate are reflected back towards the AUT. The latter having finite physical dimensions, this would stimulate two phenomena: an induced current by the reflected wave which would modify the AUT radiation resistance, and a field diffracted by the AUT aperture. On the other hand, the plate being of finite dimensions, it diffracts incident fields on its edges and corners. These considerations are depicted in Fig. 3.6.

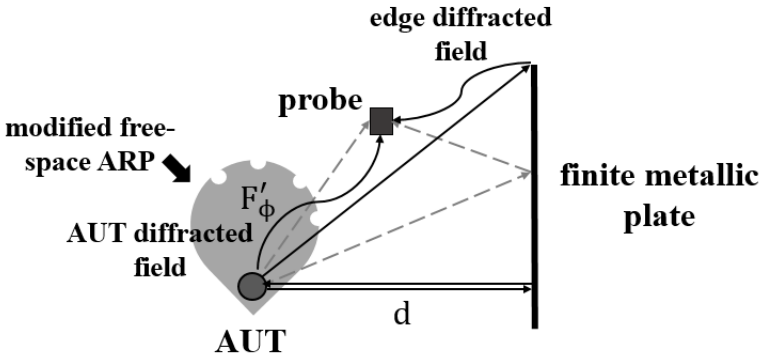

Figure 3.6 Practical considerations relative to the single-plate configuration: impact on the AUT free-space radiation characteristics and diffracted fields by the AUT aperture and plate edges and corners (solid) which interfere with the useful fields (dashed).

Changing the AUT radiation resistance means changing its free-space radiation characteristics inducing an error in the free-space ARP information acquired in the presence of the plate. On the other hand, the diffracted fields by the AUT aperture and the plate edges and corners interfere with the LOS and image fields. In the current formalism, the diffracted fields do not contribute into the measurement and thus are considered as *spurious* fields. Consequently, these fields are not taken into account in the mathematical model. Instead, their impact is quantified and minimized in order to produce the most accurate results.

The model is optimized by integrating losses due to the finite conductivity of the metallic plate. This is performed by inserting an adapted reflection coefficient in the image column of the systems matrices. It should be noted that for radio frequencies, metals with good conductivity introduce very small losses which may be neglected in the single-plate scenario. Studying aspects related to the plate losses becomes a priority when considering multiple reflections. Nevertheless, the impact of the plate infinitesimal losses on the ARP results is assessed in Sec. 3.3.5. The model is further optimized by integrating the frequency impact to account for changes in the field amplitude and phase as function of the working frequency. The method adopted herein to estimate this change is by applying linear regression. The same technique is used in order to enhance the proposed method by reducing the ARP error acquired by the direct inversion. The application of linear regression in order to both enhance the method and optimize the model is presented in Sec. 3.4.

3.3.1 Error due to the Far Field Model Assumption

The common criterion for the far-field distance is given by the Fraunhofer distance which is based on a maximum phase tapper $\Delta\beta_E = 22.5°$ over the tested aperture (see Sec. 1.3.1). Although this criterion works well for a large scale of applications, one may easily notice that it does not guarantee that far-field conditions are absolutely met. It should be noted that, apart of the AUT dimensions which set the Fraunhofer distance, the "actual" far-field distance over which error due to the far-field model assumption may be neglected changes as function of the tested antenna. In order to highlight the model limitation due to the far-field assumption, a Hertzian dipole is used. This elementary source, which has infinitesimal dimensions, has the corresponding free-space radiated field expressed as follows, when it is oriented parallel to the z-axis [59],

$$E_\theta = \frac{I\ell}{4\pi j\epsilon_0\omega}\left(\frac{1}{r^3}+\frac{jk}{r^2}-\frac{k^2}{r}\right)e^{-jkr}\sin(\theta), \tag{3.13}$$

$$E_r = \frac{I\ell}{2\pi \mathrm{j}\epsilon_0\omega}\left(\frac{1}{r^3}+\frac{jk}{r^2}\right)e^{-jkr}\cos(\theta), \tag{3.14}$$

$$E_\phi = 0, \tag{3.15}$$

where $I\ell$ is the dipole moment, ϵ_0 the free-space permittivity, ω the working angular frequency, and k the wavenumber. The radial component E_r is generally neglected when assuming far-field conditions as it decays more rapidly compared to transverse components. Considering the fields on the working azimuthal plane ($\theta = \pi/2$), which correspond to the TM case, the fields

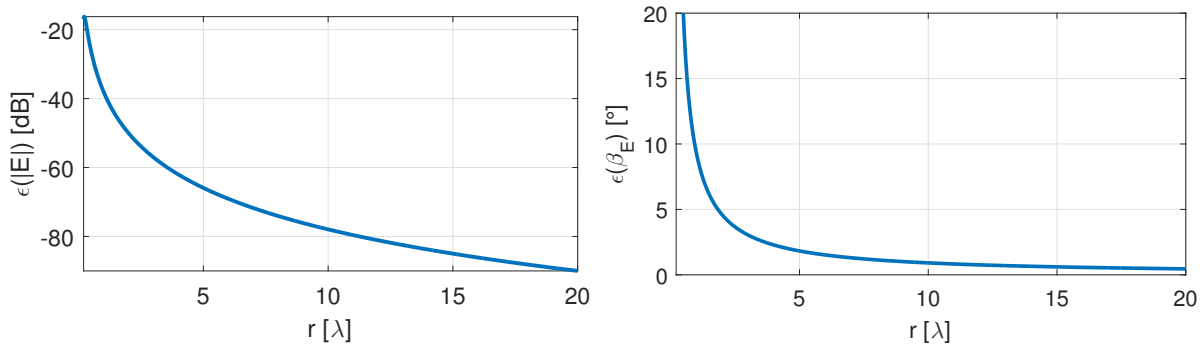

(a) (b)

Figure 3.7 Error due to the far-field assumption using a TM-operating Hertzian dipole as function of the measurement distance: (a) Magnitude error (b) Phase error.

expressions reduce to,

$$E_\theta = A\left(\frac{1}{r^3} + \frac{jk}{r^2} - \frac{k^2}{r}\right)e^{-jkr}, \tag{3.16}$$

$$\text{with } A = \frac{I\ell}{4\pi j\epsilon_0\omega},$$

$$E_r = E_\phi = 0. \tag{3.17}$$

As we would expect, only the polar component exist and the corresponding radiation pattern is isotropic. The far-field region is characterized by the absence of reactive fields; i.e., the field components which decay as function of r^{-2} and r^{-3}. Accordingly, the far-field model of the TM radiated field is expressed as follows,

$$E_\theta^{FF} = -\frac{e^{-jkr}}{r}Ak^2. \tag{3.18}$$

Error due to the far-field model assumption is then calculated by comparing the latter far-field expression with the more precise expression of Eq. 3.16. Results are shown in Fig. 3.7. The magnitude error is large in the vicinity of the antenna, attaining -26dB at $r = \lambda/2$ but converges rapidly towards very low levels as the distance grows attaining -50dB at $r = 2\lambda$. However, by recalling that the antenna has infinitesimal length, typically $\ell < \lambda/50$ [21, pp. 151–170], the Fraunhofer distance would correspond to the immediate vicinity of the antenna which shows a large magnitude error. The phase error is quite larger exceeding 5° at $r = 2\lambda$ and 1° up to around $r = 10\lambda$. These results highlight the possible error that could emerge when relying on the Fraunhofer distance in order to apply the far-field model.

The studied example shows that error due to the far-field model assumption is only function of the radial distance separating the measurement point from the antenna. This is not true if the

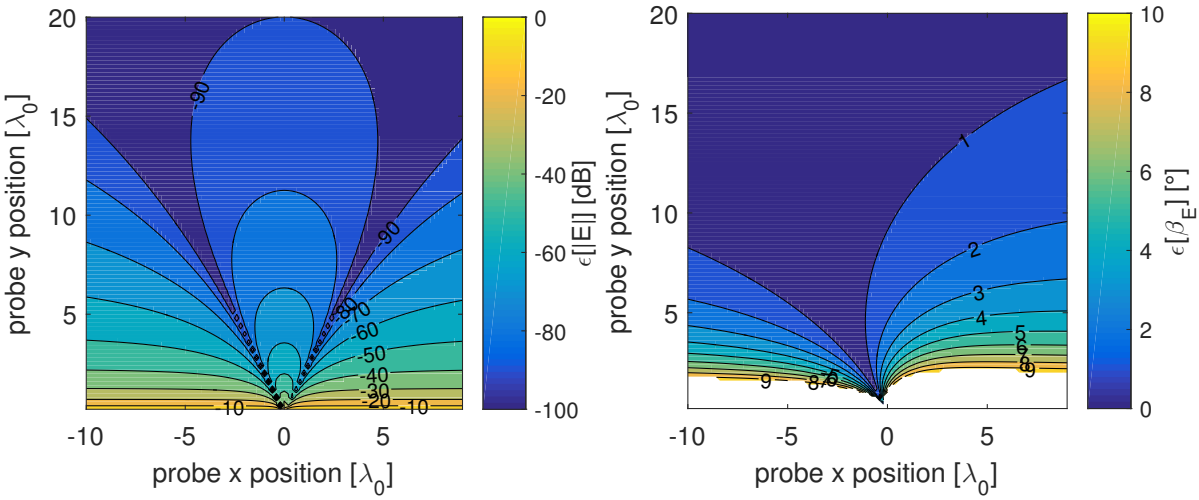

Figure 3.8 Error due to the far-field assumption using a TE-operating Hertzian dipole as function of the measurement point position: (a) Magnitude error (b) Phase error.

antenna is oriented otherwise, say when it is oriented parallel to the x-axis corresponding to a TE mode. In this case, the field components over the working azimuthal plane are expressed as follows,

$$E_\phi = A\left(\frac{1}{r^3} + \frac{jk}{r^2} - \frac{k^2}{r}\right)e^{-jkr}\sin(\phi), \tag{3.19}$$

$$E_r = 2A\left(\frac{1}{r^3} + \frac{jk}{r^2}\right)e^{-jkr}\cos(\phi), \tag{3.20}$$

$$E_\theta = 0. \tag{3.21}$$

Unlike the TM case, the TE case is characterized by the contribution of the radial component making the reference field the sum of Eqs. 3.19 and 3.20. Consequently, this would amplify error due to the far-field model assumption as it does not take into account the radial component contribution, whereas according to the far-field model, the TE radiated field is expressed as follows,

$$E_\phi^{FF} = -\frac{e^{-jkr}}{r}\left[Ak^2\sin\phi\right]. \tag{3.22}$$

According to Eq. 3.22, the ARP is sinusoidal with the nulls being directed towards the x-axis, which corresponds to the limits of the $\phi = [0°, 180°]$-range. Hence, error due to the far-field model assumption in this case is also function of the measurement angle which defines the intensities of the different field components. The same can be seen in Fig. 3.8 where error due

to the far-field model assumption is plotted as function of the measurement point position. The figure shows that both amplitude and phase errors are dramatically amplified over positions corresponding to weak power emission (directions near the nulls) even at distances as large as $10\lambda_0$. This may be explained by noting that the radial component takes its maximum value over these positions ($\cos(\phi)$), whereas the far-field model, neglecting the contribution of the radial component, predicts very weak transverse component levels ($\sin(\phi)$).

These results highlight a further limitation of the far-field model which does not take into account the impact of the radiation patterns corresponding to the different field components, including the radial component. Accordingly, care must be given to the probe position in the context of the proposed concept in terms of the radial distance and ARP nulls in order to limit errors due to the far-field model assumption. The study carried in this section is useful to understand the same issues when handling antennas with similar behaviors such as the HWD later in this document.

3.3.2 Interaction with the Plate: Impact on the Free Space Radiation Resistance

The current generated in the AUT in the proposed set-up is the superposition of two components, the amplitude of the first depends on the power supplied by the transmitter and the free-space radiation resistance, while the second depends on the amplitude of the normally reflected wave. The amplitude of the normally reflected wave depends on the AUT-plate separation d as well as on the ARP value in the direction towards the plate. Changing the total generated current in the AUT is equivalent to changing its free-space radiation resistance. Ideally, the amplitude of the normally reflected wave would be as small as possible to ensure a minimum variation of the AUT free-space radiation characteristics. This suggests augmenting the AUT-plate separation. However, the fact that the amplitude of the current component relative to the transmitter is by default greater than the amplitude of the current component due to the reflected wave suggests that minimizing the latter with respect to the former requires moderate AUT-plate separations. In [37] it is suggested that distances in the order of a half wavelength are sufficient to neglect the contribution of the normally reflected wave. To verify this, Friis transmission equation [60] is used in order to determine the ratio of the reflected power by the plate P_r to the free-space radiated power by the AUT P_t, which may be denoted as the AUT propagation return loss S_{11}^p:

$$S_{11}^p = \frac{P_r}{P_t} = \frac{G_a(0°).G_a(0°)}{[4\pi(2d)]^2} = \frac{G_a(0°)^2}{(8\pi d)^2}, \tag{3.23}$$

where $G_a(0°)$ stands for the gain of the AUT in the horizontal direction towards the plate ($\phi = 0°$), and d is normalized with respect to the working wavelength. If the AUT is lossless and omnidirectional ($G_a = 1$), Eq. 3.23 reduces to:

$$S_{11}^p = \frac{1}{(8\pi d)^2}. \tag{3.24}$$

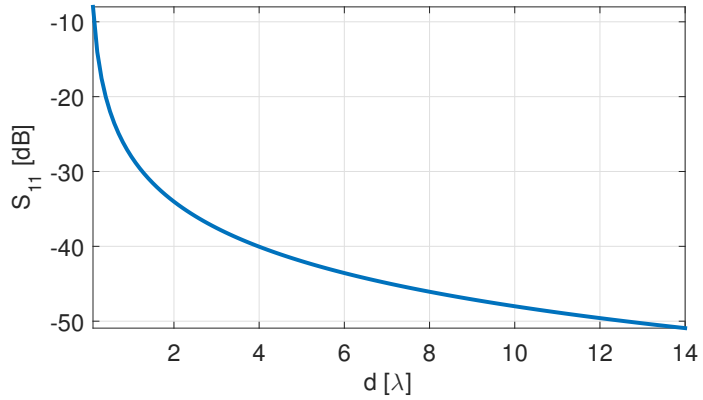

Figure 3.9 Intensity of the normally reflected wave with respect to the free-space generated wave as function of the AUT-plate separation accounting for the impact of the plate on the AUT free-space radiation resistance.

According to this expression, the propagation return loss is inversely proportional to the square of the AUT-plate separation. Fig.3.9 shows the evolution of the propagation return loss as function of the AUT-plate separation. It shows that as soon as d approaches 1λ the reflected power is considerably smaller than the free-space radiated power ($S_{11}^p = -30$dB). For AUT-plate separations larger than 4λ the impact of the reflected power becomes very weak ($S_{11}^p < -40$dB), highlighting the possibility of minimizing the plate impact on the AUT free-space radiation resistance using small AUT-plate separations.

3.3.3 Diffraction by the AUT Aperture

In addition to the circuit impact, which is modifying the AUT radiation resistance, the normally reflected wave has a propagation impact as it is diffracted by the AUT aperture, interfering as a result with the useful LOS and image fields. According to results carried over the previous section, the power density of the normally reflected wave at the AUT level, which depends on the AUT-plate separation and the AUT radiation pattern, is small compared to the power density of the free-space radiated wave for useful AUT-plate separations. For example, the power density of the normally reflected wave is -40dB below the power density of the free-space radiated power for an AUT-plate separation $d > 4\lambda_0$ (Fig. 3.9). However, the intensity of the AUT-diffracted wave is also function of the AUT Radar Cross Section (RCS) which may limit or amplify the diffraction impact. In order to verify the AUT diffraction impact, it is useful to express the ratio of the useful signals powers to the diffracted signal power, which may be denoted as the Signal-to-Noise Ratio (SNR) relative to the AUT diffraction. This is performed by expressing the field intensity of the AUT-diffracted wave at the probe level using the Radar

Range equation [21, pp 96-98],

$$P_d = \frac{P_t G_a(0°)}{4\pi(2d)^2} . \frac{A_r \sigma}{4\pi r_0^2}, \tag{3.25}$$

where P_d is the diffracted signal power measured by the probe, P_t the transmitted power to the AUT, A_r the effective aperture of the probe, and σ the AUT RCS. The first ratio term corresponds to the incident power density of the normally reflected wave on the AUT, say W_{inc}, such that,

$$\begin{aligned} P_d &= W_{inc} \frac{A_r \sigma}{4\pi r_0^2}, \\ \text{with } W_{inc} &= \frac{P_t G_a(0°)}{4\pi(2d)^2}. \end{aligned} \tag{3.26}$$

The incident power density on the AUT may alternatively be expressed as function of the incident field intensity E_{inc} and the free-space intrinsic impedance η_0,

$$W_{inc} = \frac{||E_{inc}||^2}{\eta_0} = \frac{||G(f, 2d)F(0°)||^2}{\eta_0}, \tag{3.27}$$

where $G(f, 2d)$ stands for the free-space Green's function corresponding to the path taken by the normally reflected wave before impinging on the AUT, and $F(0°)$ is the value of the ARP in the corresponding direction ($\phi = 0°$). The far-field expression is applied in Eq. 3.27 to describe the incident wave which is locally plane due to the reflection. Replacing W_{inc} in Eq. 3.26 by the expression of Eq. 3.27 yields,

$$P_d = \frac{||G(f, 2d)F(0°)||^2}{\eta_0} \frac{A_r \sigma}{4\pi r_0^2}. \tag{3.28}$$

The diffracted power measured by the probe may as well be expressed as function of the diffracted wave power density W_d,

$$\begin{aligned} P_d &= A_r W_d, \\ \text{with } W_d &= \frac{||E_d||^2}{\eta_0}, \end{aligned} \tag{3.29}$$

where E_d stands for the diffracted field by the AUT measured at the probe level. It follows that the amplitude of the diffracted field may be expressed as follow,

$$||E_d|| = \sqrt{\eta_0 W_d} = \sqrt{\frac{\eta_0 P_d}{A_r}}. \tag{3.30}$$

Finally, replacing the diffracted power in Eq. 3.30 by its expression in Eq. 3.28 yields,

$$\begin{aligned} ||E_d|| &= \left\|G(f,2d)F(0^\circ)\right\| \sqrt{\frac{\sigma}{4\pi r_0^2}} \\ &= \left\| \frac{\mathrm{e}^{-jk2d}}{4dr_0} F(0^\circ) \right\| \sqrt{\frac{\sigma}{\pi}}. \end{aligned} \tag{3.31}$$

According to this expression, the amplitude of the diffracted field is directly proportional to the square root of the AUT RCS and inversely proportional to approximately seven times the product of the AUT-probe and AUT-plate separations ($4\sqrt{\pi}dr_0$), suggesting a rapid attenuation of the diffracted field when augmenting the AUT-plate separation. It should be noted that this expression assumes uniform diffraction by the AUT aperture, which may be regarded as a worst case as practically the diffracted field pattern would be characterized by a certain directivity [61]. It should also be noted that Eq. 3.31 describes the diffracted field directly impinging on the probe, i.e., the LOS AUT diffraction. The presence of the plate implies the generation of a reflected signal relative to the AUT-diffracted field in the same fashion as for the useful LOS and image fields. Strictly speaking, the proposed configuration results in an infinite set of AUT-diffracted fields as each diffracted wave normally impinging on the plate is reflected back towards the AUT resulting in a new LOS and reflected AUT diffractions. However, the oscillating normally reflected wave being rapidly attenuated, only the first order diffracted LOS and reflected fields are taken into account. The amplitude of the sum of these two fields is then considered. This is done by taking into account the phase terms of the two fields, i.e., the complete free-space Green's function corresponding to each diffracted signal path, which yields,

$$\begin{aligned} ||E_d|| &= \left\| G(f,2d)F(0^\circ)\sqrt{\frac{\sigma}{4\pi r_0^2}}\mathrm{e}^{-jkr_0} - G(f,2d)F(0^\circ)\sqrt{\frac{\sigma}{4\pi r_1^2}}\mathrm{e}^{-jkr_1} \right\| \\ &= \left\| \frac{\mathrm{e}^{-jk2d}}{4d} F(0^\circ)\sqrt{\frac{\sigma}{\pi}} \left[\frac{\mathrm{e}^{-jkr_0}}{r_0} - \frac{\mathrm{e}^{-jkr_1}}{r_1} \right] \right\|. \end{aligned} \tag{3.32}$$

The (-) sign inside the brackets stands for the 180° phase shift of the reflected wave which is implied by boundary conditions on the plate. To account for the impact of the AUT diffraction, an SNR relative to the LOS and image cases is expressed as follows:

$$SNR_i = \left\| \frac{E_i}{E_d} \right\|^2 = \left\| \frac{\frac{\mathrm{e}^{-jkr_i}}{r_i} F(\phi_i)}{\frac{\mathrm{e}^{-jk2d}}{4d} F(0^\circ)\sqrt{\frac{\sigma}{\pi}} \left[\frac{\mathrm{e}^{-jkr_0}}{r_0} - \frac{\mathrm{e}^{-jkr_1}}{r_1} \right]} \right\|^2, \quad i = 0, 1. \tag{3.33}$$

The index 0 standing for the LOS case and the index 1 standing for the image case. Rearranging the right-hand term yields the SNR corresponding to each case:

$$\begin{aligned} SNR_0 &= \frac{16\pi d^2}{\sigma \xi_0^2 \left\| 1 - \gamma e^{-j2\pi\Delta r} \right\|^2}, \\ \text{with } \xi_0 &= \frac{F(0°)}{F(\phi_0)}. \end{aligned} \tag{3.34}$$

$$\begin{aligned} SNR_1 &= \frac{16\pi d^2}{\sigma \xi_1^2 \left\| 1 - \gamma^{-1} e^{j2\pi\Delta r} \right\|^2}, \\ \text{with } \xi_1 &= \frac{F(0°)}{F(\phi_1)}, \end{aligned} \tag{3.35}$$

γ being the distances ratio introduced in Chapter 2 and distances being normalized with respect to the working wavelength. Eq. 3.34 and Eq. 3.35 logically suggest that the SNRs are directly proportional to the AUT-plate separation and inversely proportional to the AUT RCS. They also propose sets of optimal and worst positions in term of the AUT diffraction in the same fashion as for conditioning in the TM case, i.e., in the form of hyperbolas. Maximizing the SNRs requires minimizing the corresponding denominators which is done by setting the phase of the complex term to an integer multiple of 2π. This corresponds to a situation where the two diffractions are out of phase so their contributions nearly cancel each other. Minimizing the SNRs on the other hand requires maximizing the corresponding denominators which is done by setting the phase of the complex term to an integer multiple of π, corresponding to a situation where the two diffractions are in phase such that their contributions add. These remarks correspond to the following situations,

$$\begin{aligned} &\text{Optimal case: } \Delta r = n \\ &\text{Worst case: } \Delta r = \frac{1}{2} + n,\ n \in \mathbb{N} \end{aligned} \tag{3.36}$$

Eq. 3.36 defines two sets of optimal and worst hyperbolas of positions in term of the AUT diffraction where SNRs are respectively locally highest and locally lowest. Equations of these hyperbolas and their parameters are expressed as follows,

$$\frac{(x-d)^2}{a_n^2} - \frac{y^2}{b_n^2} = 1$$

$$a_n = \frac{\Delta r}{2} = \begin{cases} \frac{n}{2}, & \text{optimal hyperbolas} \\ \frac{1+2n}{4}, & \text{worst hyperbolas} \end{cases}$$

$$b_n = \sqrt{d^2 - a_n^2}, b_n > 0. \quad n \in \mathbb{N}. \tag{3.37}$$

These hyperbolas have globally the same parameters as the TM case conditioning hyperbolas (refer to Sec. 2.3.2.2), which may be summarized as: the number of hyperbolas is directly proportional to d, with their slopes approaching infinity, i.e., becoming vertical, when they approach the plate. The level of SNR over optimal hyperbolas is defined by the amplitude of the complex term of Eqs. 3.34 and 3.35, which is the distances ratio. This corresponds to conditioning circles defined by γ for the LOS case and γ^{-1} for the image case. The SNR is optimized when both terms approach unity, i.e., when the two distances r_0 and r_1 are approximately equal. This corresponds to positions near the plate and far away from the AUT. In other words, optimal positions in terms of the AUT-diffraction coincide with optimal positions in terms of conditioning, as both are governed by the distances spread. Fig. 3.10 highlights the mentioned remarks over the $20\lambda \times 20\lambda$ test zone using a vertical HWD which implies an isotropic ARP, i.e., $\xi_i = 1$. Figs. 3.10a to 3.10d show the SNRs as function of the AUT-plate separation assuming a hypothetical isotropic RCS $\sigma = 1\lambda^2$. As one would expect, the LOS SNRs are generally higher than the image SNRs as the image fields are more attenuated due to the higher distances separating images from the probe. For an AUT-plate separation $d = 5\lambda$, the LOS SNR exceeds 40dB over optimal hyperbolas up to around 60dB near the plate at vertical distances around 20λ from the AUT. Otherwise, the SNR may go down to 26dB over worst hyperbolas. The image SNR is generally lower than the LOS SNR and gets extremely low in regions around the AUT (<10dB) but improves relatively as the AUT-probe separation grows reaching values near the LOS case over certain optimal positions. Rising the AUT-plate separation to $d = 10\lambda$ improves both the general SNR pattern and the corresponding levels for both the LOS and image cases. Figs. 3.10e and 3.10f show the SNRs for a smaller RCS $\sigma = 0.5\lambda^2$ with an AUT-plate separation $d = 10\lambda$. The LOS SNR is considerably high showing worst values around 40dB and attaining maximum values around 70dB at optimal positions near the plate. The image SNR is quite high for positions outside the region surrounding the AUT, showing values between 40dB and 60dB at optimal positions.

Results of the impact of the AUT-diffracted field on the calculated ARP samples, which are also impacted by conditioning, are shown in Fig. 3.11 for a TM model with an UFBW = 4% using the same configurations of Fig. 3.10 [1]. Figs. 3.11a and 3.11b show the ARP results for an isotropic RCS $\sigma = 1\lambda_0^2$ and an AUT-plate separation $d = 5\lambda_0$. The impact is generally important over the test zone. The optimal region with respect to the AUT diffraction, which is the vicinity of the plate, coincides with the worst region with respect to conditioning given the used parameters for the TM model, as pushing the first order optimal hyperbola towards the plate requires enlarging either the the UFBW or the AUT-plate separation. Consequently,

[1] Note that contour lines are deactivated in Fig. 3.11 for better plot; as will be the case whenever necessary throughout this text.

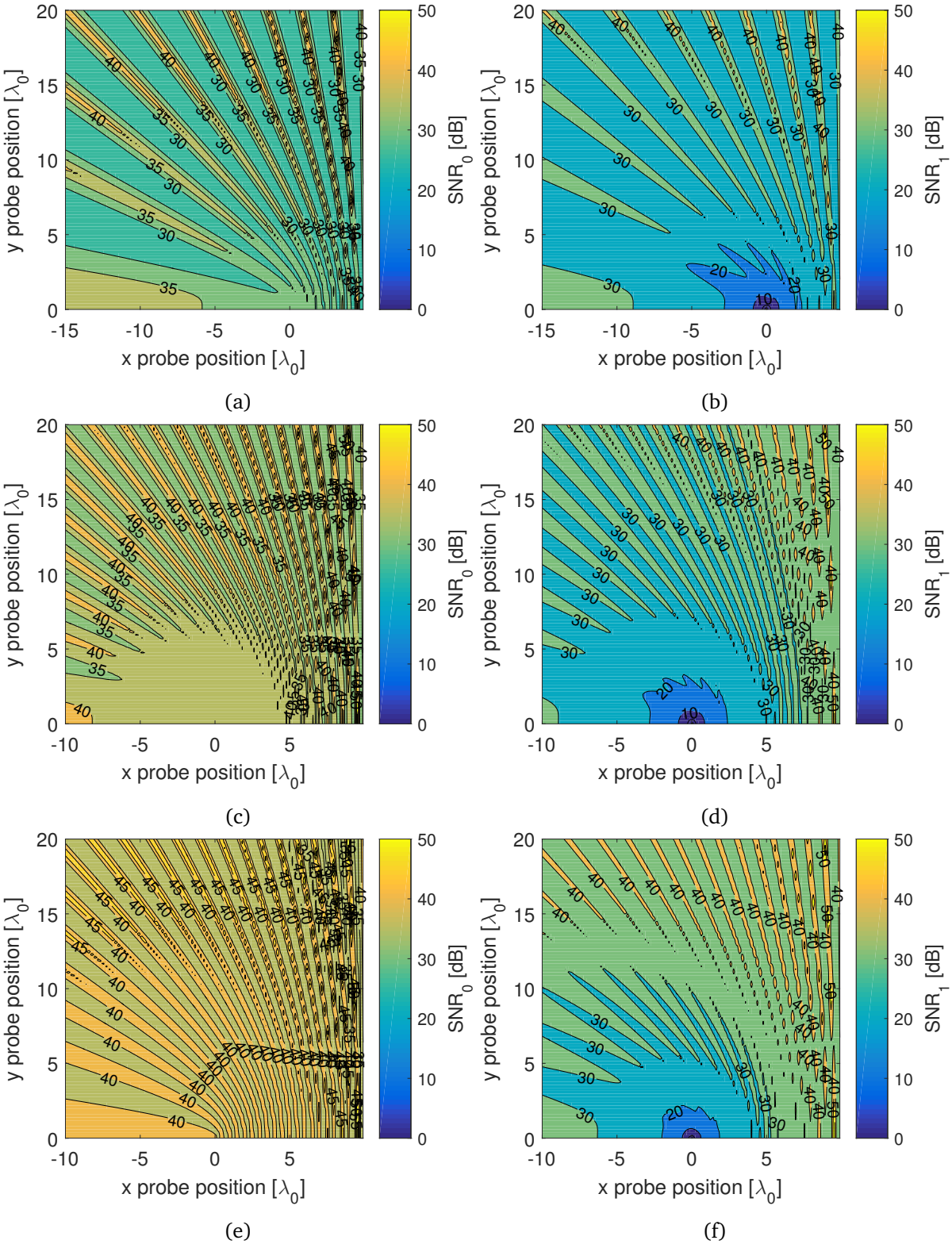

Figure 3.10 Power ratios of useful fields to the AUT-diffracted field as function of the probe position for different AUT-plate separations and AUT RCSs: (a) SNR_0, $d = 5\lambda$, $\sigma = 1\lambda^2$ (b) SNR_1, $d = 5\lambda$, $\sigma = 1\lambda^2$ (c) SNR_0, $d = 10\lambda$, $\sigma = 1\lambda^2$ (d) SNR_1, $d = 10\lambda$, $\sigma = 1\lambda^2$ (e) SNR_0, $d = 10\lambda$, $\sigma = 0.5\lambda^2$ (f) SNR_1, $d = 10\lambda$, $\sigma = 0.5\lambda^2$.

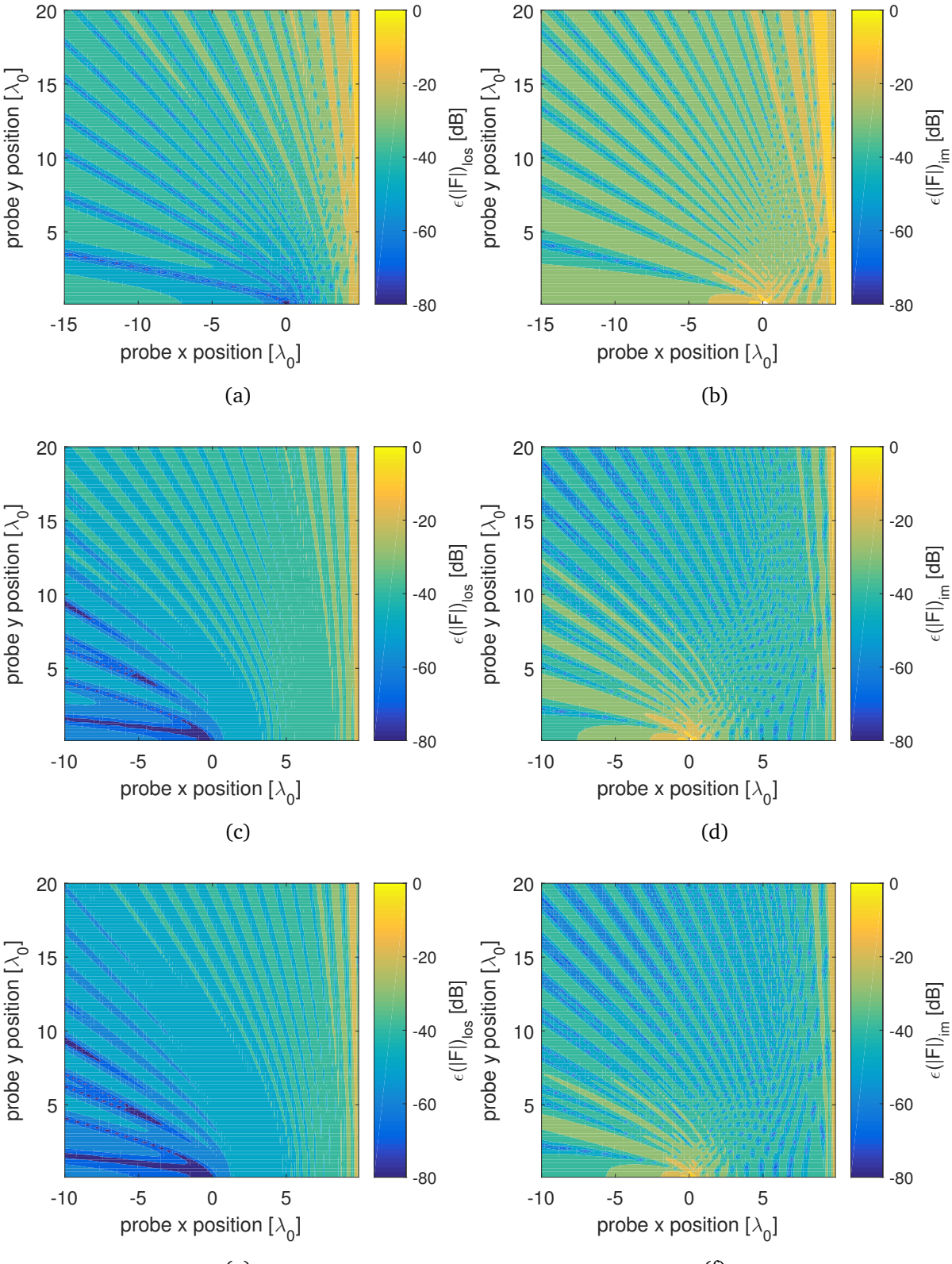

Figure 3.11 ARP error as function of the probe position for different AUT-plate separations and AUT RCSs, TM case, $\Delta f_u = 4\%$: (a) $\epsilon(\mathbf{F})_{los}$, $d = 5\lambda_0$, $\sigma = 1\lambda_0^2$ (b) $\epsilon(\mathbf{F})_{im}$, $d = 5\lambda_0$, $\sigma = 1\lambda_0^2$ (c) $\epsilon(\mathbf{F})_{los}$, $d = 10\lambda_0$, $\sigma = 1\lambda_0^2$ (d) $\epsilon(\mathbf{F})_{im}$, $d = 10\lambda_0$, $\sigma = 1\lambda_0^2$ (e) $\epsilon(\mathbf{F})_{los}$, $d = 10\lambda_0$, $\sigma = 0.5\lambda_0^2$ (f) $\epsilon(\mathbf{F})_{im}$, $d = 10\lambda_0$, $\sigma = 0.5\lambda_0^2$.

error is largely amplified over worst AUT-diffraction hyperbolas in this region, exceeding −5dB in the immediate vicinity of the plate in the image case. The remaining worst AUT-diffraction hyperbolas in the image case all exceed −25dB of error, which however is gradually attenuated as the probe is moved away from the plate. On the other hand, optimal AUT-diffraction hyperbolas present very low error levels in both the LOS and image cases, being below −40dB up to −60dB at certain probe positions. These results reveal the obligation to position the probe over optimal AUT-diffraction hyperbolas when the RCS is relatively high or when the AUT-plate separation is small. The error patterns generally improve when augmenting the AUT-plate separation. Figs. 3.11c and 3.11d show the results for $d = 10\lambda_0$ using the same RCS. Error at the optimal conditioning region is bounded at −35dB in the LOS case and at −32dB in the image case over worst AUT-diffraction hyperbolas. The same may be achieved for lower AUT RCS levels, as shown in Figs. 3.11e and 3.11f where an RCS $\sigma = 0.5\lambda_0^2$ is used with an AUT-plate separation $d = 10\lambda_0$. In this case, the image error is bounded at values around −36dB in the optimal conditioning region.

The AUT ARP and its orientation with respect to both the plate and the probe also plays an important role in determining the intensity of the AUT-diffracted field with respect to the useful fields, as stated by Eqs. 3.34 and Eq. 3.35. In order to verify this, the horizontal HWD (TE-directive case) is rotated and ARP errors are recorded for a fixed probe position. The optimal position with respect to conditioning is chosen by placing the probe in the vicinity of the plate at a vertical distance equal to the AUT-plate separation $d = 10\lambda$, hence $(x_{opt}, y_{opt}) = (9.5\lambda, 10\lambda)$ (refer to Table 2.1). Over this position, the system matrix has a very low condition number $\kappa(\mathbf{G}_{TE}) = 1.05$. Results are shown in Fig. 3.12a for the basic TE model (using a single frequency $n_f = 1$) where the ARP error levels are plotted against the AUT orientation ϕ_o. The reference AUT orientation with respect to the azimuthal plane is shown in Fig. 3.1, the main lob being oriented towards the y-axis and the nulls towards the x-axis. The LOS error is generally very small except in the region where $\phi_o = [45°, 50°]$ where it explodes. In this region the ARP null is oriented towards the measurement angles ($\phi_0 \approx \phi_1$), which implies that the useful fields are comparable or even weaker than the AUT diffraction. The ideal situation corresponds to the reference ARP orientation where the null is oriented towards the plate. In this case both the LOS and image errors may be neglected. The image error is generally important. It undergoes rapid amplification when the null is being directed towards ϕ_1, which corresponds to the region where $\phi_o = [0°, 40°]$. In this region the image error exceeds −25dB after a 30° rotation. On the other hand, when the lobe is being directed towards ϕ_1, or when the null is closer to the plate direction i.e., $\phi_o = [50°, 180°]$ the image error is reduced. However, the current parameters allow achieving image errors below −40dB only for 17% of possible AUT orientations. This would clearly be an important limitation once an azimuthal scan is performed, recalling that rotating the AUT is the privileged choice rather than moving the probe as it allows controlling the two measurement angles (see Sec. 2.4). It is however interesting to note the advantage carried by introducing frequency diversity in minimizing the ARP error. This is shown in Fig.

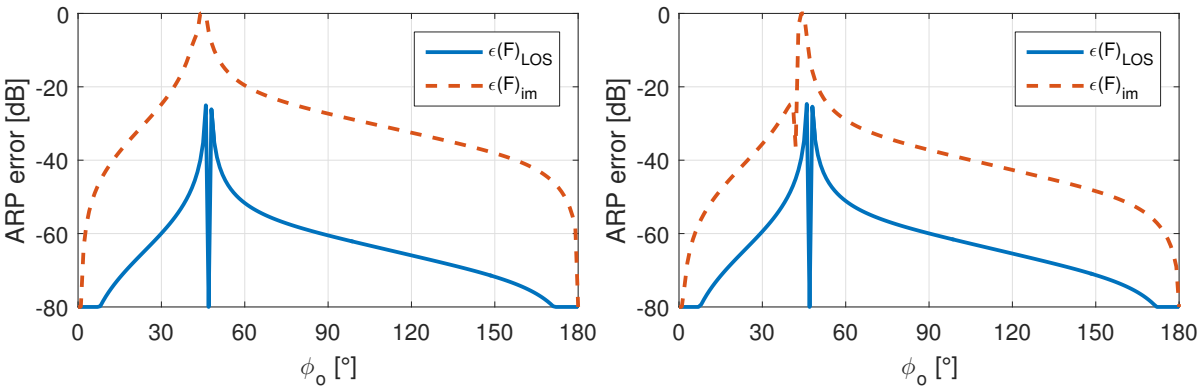

Figure 3.12 ARP error as function of the AUT orientation for a fixed optimal probe position $(x_{opt}, y_{opt}) = (9.5\lambda, 10\lambda)$ and impact of the AUT-diffracted field. TE case, $d = 10\lambda$, $\kappa(\mathbf{G}_{TE}) = 1.05$, $\sigma = 1\lambda^2$ (a) basic TE model, $n_f = 1$ (b) introducing frequency diversity, $n_f = 2$, UFBW=4%

3.12b, where two frequencies are used with an UFBW = 4%, allowing to achieve image errors below −40dB for 60% of possible AUT orientations. We shall point out that in this study the ARP was assumed unchanged as function of frequency, which is not true in the dipole case. The interest being here to highlight the advantage carried by frequency diversity in improving the ARP results, its impact on the free-space ARP is neglected for the moment and will be studied in a later section. Frequency diversity was initially introduced to the TE model in order to improve the general conditioning pattern by over-determining the system. From a conditioning point of view, this is not necessary in this scenario as the probe is already positioned on the optimal conditioning position. Consequently, the condition number is barely affected. However, the over-determination of the problem allows improving ARP results as the pseudo-inverse algorithm applies some sort of error averaging in order to solve the system. This approach is referred to as *regression* and will be presented later as it is used in order to enhance the robustnesses and the accuracy of the proposed method.

These results highlight the important impact the AUT diffraction could have if the tested antenna has larger RCS than $1\lambda^2$. In this case larger AUT-plate or AUT-probe separations are required in order to reduce the AUT diffraction impact. If this approach is unfeasible due to measurement site limitations, an alternative possible approach could be using microwave absorbers, such as absorbing foams, at the point of the normal reflection over the plate in order to reduce the intensity of the normally reflected wave. These types of absorbers have optimal performance at normal incidence. Another possible solution could be truncating the plate at a certain distance above the AUT vertical level such that the horizontal ray is not reflected back towards the AUT. However, in this case care must be given to fields diffracted by the plate discontinuity. This topic is treated in the next section.

3.3.4 Diffraction by the Plate Edges and Corners

The metallic plate introduced in the proposed set-up is assumed very large compared to the AUT-probe separation in order to approach an ideal image model. In practice, this may require unpractical physical dimensions. In this case, the geometrical and electrical discontinuities resulting from truncating the plate introduce diffracted fields that interfere with the useful fields, perturbing as a result the measurement. The intensity of the diffracted fields mainly depends on positions of the AUT and the probe with respect to the plate discontinuities. Assuming that the plate has a rectangular shape, diffracted fields are caused by the plate four edges and corners. Several techniques to model diffracted fields have been developed, giving different degrees of accuracy in terms of measurement regions [62]. A brief theoretical background is presented in order to account for the main high-frequency techniques that aim to describe the propagation of electromagnetic waves in the presence of discontinuities. Then, a general insight into the impact of diffracted fields in the context of the proposed concept is provided.

3.3.4.1 Theoretical background

The main high-frequency methods to describe the propagation of electromagnetic waves in the presence of geometrical and electrical discontinuities are listed below:

- **Geometrical Theory of Diffraction (GTD)**: Developed by J. B. Keller in the 1950s, the GTD is an asymptotic high-frequency method considered as an extension to Geometrical Optics (GO) [63]. GO is based on Fermat's principle which states that light traveling between two points takes the path that requires the least time, i.e., the shortest path [64]. If the medium is homogeneous then the path is a straight line, which brings the definition of *rays*. According to GO, electromagnetic radiation incident on some medium with different electric properties may either be reflected or refracted. If the medium is PEC, incident rays on the medium undergo total internal reflection. Accordingly, GO predicts no electromagnetic radiation in the shadow region and fails to describe diffracted fields if the medium contains any sort of discontinuities. The GTD introduces diffracted ray fields in addition to the usual GO ray fields whenever an electromagnetic wave hits an edge, corner, vertex or any discontinuity. The diffracted fields propagate in all directions, including the shadow region, and depend on diffraction coefficients in the same fashion as for GO ray fields which depend on reflection and refraction coefficients. However, in its original development, the GTD was valid only at regions far from ray-shadow and reflection boundaries where it exhibited singular behavior predicting infinite diffracted fields [65].

- **Uniform Geometrical Theory of Diffraction (UTD)**: Soon after the development of GTD, R. G. Kouyoumjian and P. H. Pathak worked on improving its performance and extended the solution to all regions in space [66]. They introduced transition functions in order to

keep the diffraction coefficients bounded and continuous across shadow boundaries. The UTD was then systematically updated to handle, in addition to edge diffraction, a wider class of problems such as the scattering by smooth convex surfaces, corner diffraction, and double diffractions [65].

Ray tracing techniques (GO, GTD and UTD) describe high frequency electromagnetic radiation without requiring surface current integrations over excited objects and have the advantage of providing an intuitive picture of the propagation mechanism of electromagnetic waves.

- **Physical Theory of Diffraction (PTD)** : This method was developed by P. Y. Ufimtsev who, unlike Keller, worked on extending the Physical Optics (PO) theory in order to include diffraction phenomenae [67]. The PO approximation uses ray optics in order to determine the illuminated and shadow regions of a PEC body of an arbitrary shape. The field equivalence theory is then used in order to estimate the surface currents which define the scattered field via surface current integration [22, pp. 125–128]. Accordingly, PO like GO predicts no electromagnetic radiation into the shadow region and thus it fails to describe diffracted fields. To overcome this, Ufimtsev introduced correction currents in order to approximate the actual scattering currents. PO is an intermediate method between GO which does not take into account the wave aspect of electromagnetic radiation, and full wave electromagnetism, considered as the precise theory. One commonly used full wave computational method is briefly presented hereafter.

- **Method of Moments (MoM)**: The MoM is a frequency domain method which provides a full wave solution to Maxwell's equations in integral form. Generally, the MoM is used to solve problems of the form [68],

$$\mathscr{L}(f) = g, \tag{3.38}$$

where g is a known excitation, f an unknown response, and $\mathscr{L}$ a linear operator relating the two quantities. R. F. Harrington introduced the MoM into electromagnetics in order to solve Maxwell's equations. He used it to solve for the source electric current in the electric field integral equation (EFIE). The EFIE expresses the electric field at some point of space as function of the electric current distribution over the radiating object, which may be a scattering element. Accordingly, the unknown source current is expressed as function of a known excitation field defining the boundary conditions of the problem. The source current $\mathbf{J}(\mathbf{r}')$ is expressed using a series of well-known basis functions f_n referred to as *expansion* functions,

$$\mathbf{J}(\vec{r}') = \sum_{n}^{N} \alpha_n f_n, \tag{3.39}$$

where α_n are constants to be determined. It follows that the surface of the radiating object is discretized into N pieces or $cells$. The accuracy of the method depends on the choice of the expansion function and the number of discretization cells, the latter being function of the excitation frequency. In numerical simulation this is referred to as $meshing$, which defines, in addition to the simulation precision, the required computational resources. *Weighting* functions are then introduced in order to balance the mathematical problem by generating a system of N equations resulting in a matrix equation where the unknown current is determined by inverting the problem. Once the current distribution is determined, the generated electric field at any point in space may be calculated using the EFIE. The system matrix, commonly referred to as the *impedance* matrix has to be well-conditioned in order to ensure reliable results. The MoM may be used in order to predict all the scattering properties of structures of arbitrary shapes including higher order terms such as edge and corner diffractions. However, it is more adapted to problems involving small radiating/scattering surfaces, otherwise large computational resources are required in order to obtain satisfying results.

3.3.4.2 Estimation of the Impact of the Plate Diffracted Fields Using GTD

A simple insight into the impact of higher order scattered fields by the plate is synthetically presented here. The impact of diffracted fields is mainly caused by the plate edges rather than corners whose contributions are very weak compared to the edges [25]. The impact of the (y+)-edge diffracted field is assessed using the GTD method due to the easiness of its implementation. This method allows us to estimate the level of the diffracted field as function of the probe position with respect to the edge.

According to the GTD, edge diffracted rays corresponding to the same incident ray form a cone known as *Keller's cone* [63]. The ray angle of incidence on the edge is equal to the diffraction angle of each ray defining the cone. If the incident ray is normal to the edge, all diffracted rays lie in the plane of incidence forming a cylindrical wave centered at the edge. By recalling that the plate in the proposed set-up is parallel to the *y-z* plane and orthogonal to the working azimuthal plane, these two cases correspond respectively to rays diffracted by edges parallel to the azimuthal plane (+z and -z edges), and rays diffracted by edges normal to the azimuthal plane (+y and -y edges). The two situations are depicted in Fig. 3.13. The diffracted fields are expressed as function of edge diffraction coefficients. In the normal incidence case, the diffracted cylindrical wave is expressed as follows,

$$\mathbf{E}_d = \mathbf{E}_{edge} \frac{\mathrm{e}^{-\mathrm{jkr_d}}}{\sqrt{r_d}} D \tag{3.40}$$

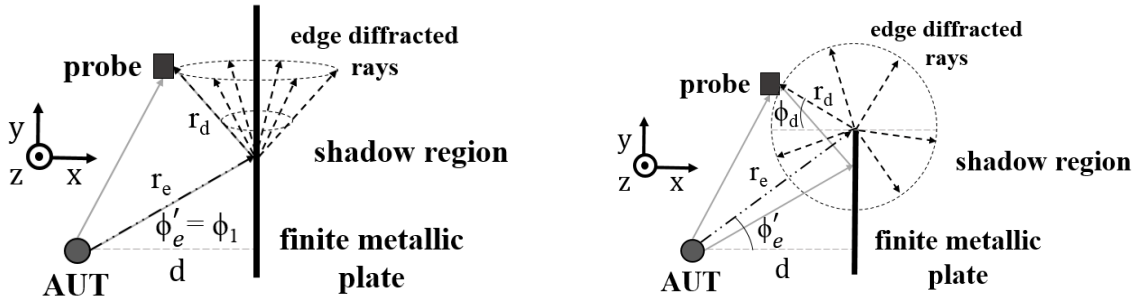

(a) (b)

Figure 3.13 Edge diffracted rays (dashed) assuming a rectangular plate: (a) Oblique incidence case: diffraction by edges parallel to the azimuthal plane (z+ and z-) (b) Normal incidence case: diffraction by the edges normal to the azimuthal plane (y+ and y-).

where $\mathbf{E}_{edge}$ is the field incident on the edge diffraction point, $\mathbf{r}_d$ the distance separating the measurement point from the edge diffraction point, and D is the diffraction coefficient. D depends on the edge incidence angle ϕ'_e, the diffraction angle ϕ_d (refer to Fig. 3.13b), and on the working frequency,

$$D = -\frac{e^{i\frac{\pi}{4}}}{2(2\pi k)^{\frac{1}{2}}}\left[\sec\frac{1}{2}(\phi_e - \phi_d) \pm \csc\frac{1}{2}(\phi_e + \phi_d)\right], \tag{3.41}$$

where $\phi_e = \phi'_e - \pi/2$. The upper sign holds for the TM polarization, commonly referred to as *soft* polarization, while the lower sign holds for the TE polarization, referred to as the *hard* polarization. Fig. 3.14 compares the (y+)-edge diffraction coefficient corresponding to each case as function of the diffraction angle ϕ_d. For a better visualization, the diffraction coefficients are up-bounded to unity in order to avoid their explosion in the singularity region where the GTD fails. The singularity region is the boundary between the region where no reflected rays exist (to the right of the singularity region) and the region where reflected rays exist (to the left of the singularity region) which is thus the region of interest with respect to the proposed concept. Consequently, the limitation of the GTD in the singularity region has no serious impact on the study carried herein as the probe is by definition moved away from the singularity region towards the reflection region in order to ensure the image contribution via the reflected ray. Fig. 3.14 highlights the impact rising frequency has on reducing the magnitude of the diffraction coefficient. Fig. 3.14 also highlights an interesting fact which is that optimal positions with respect to edge diffraction are positions near the plate ($\phi_d \to -90°$) which, as discussed in previous sections, is the region of existence of optimal positions with respect to conditioning (TE case) and AUT-diffraction. This is also true for the remaining three edges. The TM case (soft polarization) is less impacted by edge diffraction with respect to the TE case (hard polarization).

The impact of the y+ edge diffraction is assessed by expressing the ratio of the useful fields powers to the power of the diffracted field, i.e., the SNRs with respect to edge diffraction.

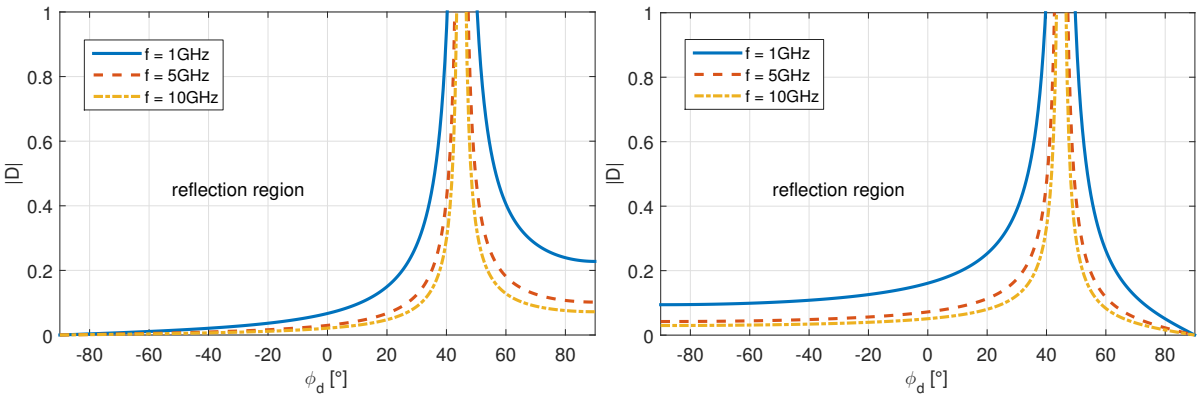

(a) (b)

Figure 3.14 Diffraction coefficients corresponding to the y+ edge. The plate being truncated at $h_{y+} = 10\lambda$, $d = 10\lambda$: (a) TM-soft polarization (b) TE-hard polarization.

Assuming that the AUT-edge separation is sufficiently large such that the field incident on the edge is expressed using the far-field model, Eq. 3.40 may be rewritten as follows,

$$\begin{aligned}\mathbf{E}_d &= \frac{\mathrm{e}^{-\mathrm{jk}\mathbf{r}_\mathrm{e}}}{\mathbf{r}_e}\mathbf{F}(\phi_e')\frac{\mathrm{e}^{-\mathrm{jk}\mathbf{r}_\mathrm{d}}}{\sqrt{\mathbf{r}_d}}D,\\ &= \frac{\mathrm{e}^{-\mathrm{jk}(\mathbf{r}_\mathrm{d}+\mathbf{r}_\mathrm{e})}}{\mathbf{r}_e\sqrt{\mathbf{r}_d}}\mathbf{F}(\phi_e')D,\end{aligned} \tag{3.42}$$

where $\mathbf{r}_e$ is the distances separating the edge diffraction point from the AUT. Accordingly, the SNRs corresponding to the LOS and image cases are expressed as follows,

$$\begin{aligned}SNR_i &= \left\|\frac{\mathbf{E}_i}{\mathbf{E}_d}\right\|^2 = \left\|\frac{\frac{\mathrm{e}^{-jkr_i}}{\mathbf{r}_i}\mathbf{F}(\phi_i)}{\frac{\mathrm{e}^{-\mathrm{jk}(\mathbf{r}_\mathrm{d}+\mathbf{r}_\mathrm{e})}}{\mathbf{r}_e\sqrt{\mathbf{r}_d}}\mathbf{F}(\phi_e')D}\right\|^2\\ SNR_i &= \left[\frac{\mathbf{r}_e\sqrt{\mathbf{r}_d}}{\mathbf{r}_i||\xi_i D||}\right]^2 \text{ with } \xi_i = \frac{\mathbf{F}(\phi_e')}{\mathbf{F}(\phi_i)},\quad i = 0,1.\end{aligned} \tag{3.43}$$

Eq. 3.43 suggests that image SNRs are lower than LOS SNRs; both being inversely proportional to distances separating the AUT and the image from the probe. Eq. 3.43 also suggests that the SNRs are improved for positions away from the diffraction point ($\mathbf{r}_d \nearrow$) but near the corresponding source ($\mathbf{r}_i \searrow$). Taking into account the diffraction coefficient impact, it follows that optimal positions with respect to the (y+)-edge diffraction are positions in the vicinity of the AUT in the LOS case, and positions in the vicinity of the plate in the image case. This is verified in Fig. 3.15 where the SNRs corresponding to different situations are plotted for an AUT-plate separation $d = 10\lambda$. Figs 3.15a to 3.15d show the SNRs using a HWD with an operating frequency $f_0 = 1$GHz in both TM and TE modes with the plate being truncated at

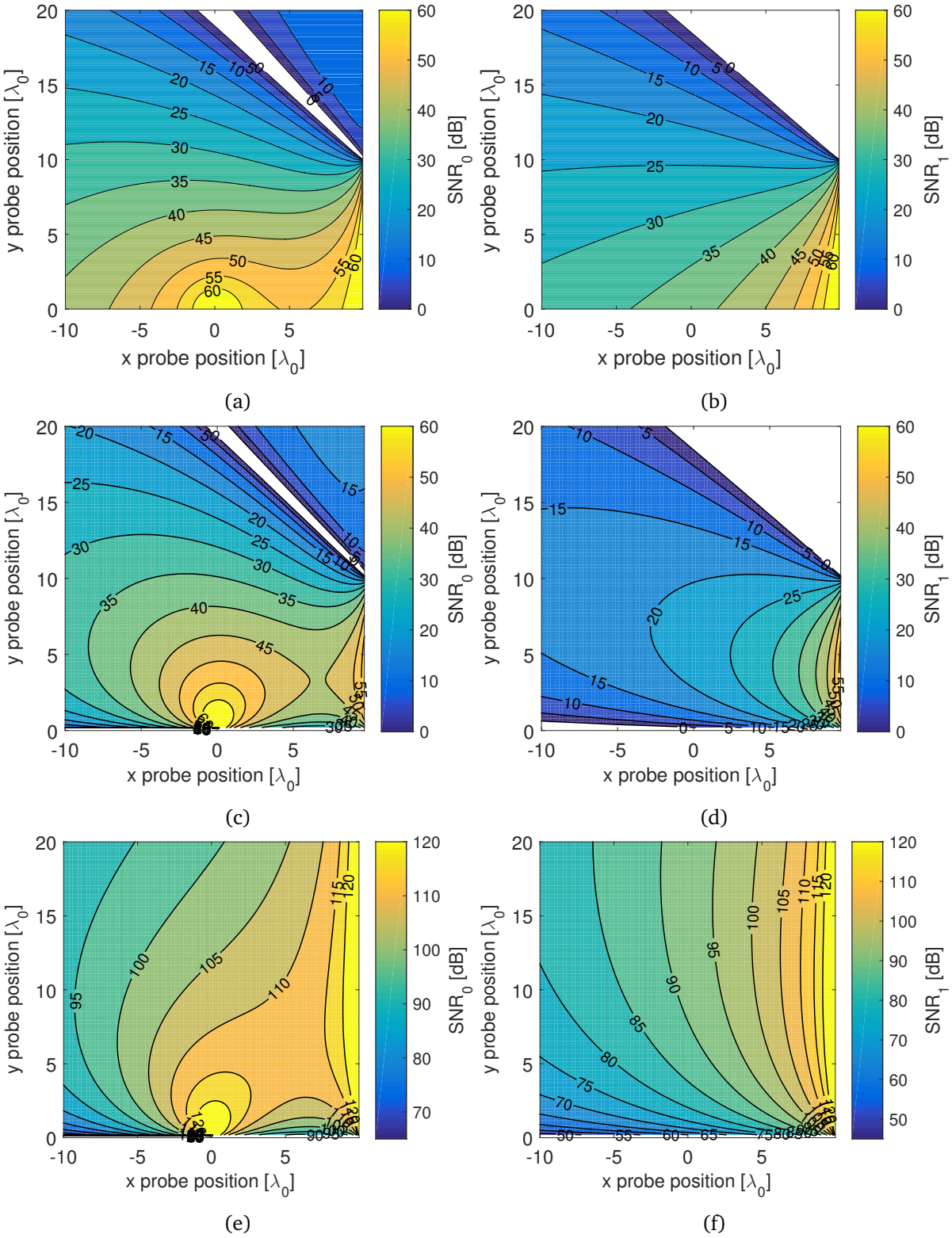

Figure 3.15 Power ratios of useful fields to the (y+)-edge diffracted field as function of the probe position for two operating frequencies, $f_1 = 1$GHz and $f_2 = 10$GHz. $d_i = 10\lambda_i$, $h = 10\lambda_1$: (a) SNR_0, TM case, $f_0 = 1$GHz (b) SNR_0, TE case, $f_0 = 1$GHz (c) SNR_1, TM case, $f_0 = 1$GHz (d) SNR_1, TE case, $f_0 = 1$GHz, (e) SNR_1, TE case, $f_0' = 10$GHz (f) SNR_1, TE case, $f_0' = 10$GHz.

$h_{y+} = 10\lambda_0$, which corresponds to a physical length of 3m. For the TM polarization, it is possible to achieve good SNR levels (>40dB) for both the LOS and and image cases only at positions between the AUT horizontal level and the plate, and vertically up to few wavelengths below the edge level. Recall that the TM case corresponds to an isotropic ARP, so the SNRs patterns are mainly dependent on the diffraction coefficient patterns. This is not in the TE-directive case where SNRs patterns are altered the ARP. The SNRs in this case are very low for valid positions, i.e., for positions sufficiently far from the AUT in order to respect the far-field model. The LOS SNR is merely high in the vicinity of the AUT in the main lob direction, and very low towards the nulls. The edge level being at a vertical distance equal to $h_{y+} = 10\lambda_1$, only positions below $y = 5\lambda_1$ show tolerable SNRs (>35dB). In the image case, the SNR is generally very low for the chosen parameters oscillating around 30dB at its best between the singularity region and regions pointed by the image ARP null. It follows that the y+ truncation should be pushed away to distances greater than $h_{y+} = 10\lambda$ in order to achieve satisfying SNR levels. Moreover, it is important to recall that the studied impact corresponds only to the y+ edge. By taking into account the impacts of the remaining edges and corners the SNRs are further reduced, which may, as function of the plate dimensions, make the impact of the plate diffracted fields intolerable. Notice that Figs. 3.15a and 3.15c depict the singularity region where the GTD fails, which show lower SNR levels than 0dB (white region).

The edge diffraction problem is reduced at higher frequencies. This is due in part to the impact of frequency on the diffraction coefficient, as shown in Fig. 3.14, but also due to the fact that the same plate physical dimensions correspond to larger electrical dimensions at higher frequencies. For instance, if the same plate is used at a frequency $f_0' = 10$GHz, this would imply that the edge is at a distance $h_{y+} = 100\lambda_0'$. Consequently, the optimal region with respect to edge diffraction is enlarged over the test zone, and the impact of the AUT directivity is minimized. This is shown in Figs. 3.15e and 3.15f for the TE case, the plate being at $d = 10\lambda_0'$. In this case the image SNR is no less than 70dB over the majority of the test zone. If enlarging the plate dimensions is not possible, alternative solutions to reduce the diffracted fields may be applied, such as curved edge or serrated edge reflectors. The later are widely used in CATRs (see Sec. 1.3.2). They are intended to direct diffracted signals away from the quite zone, where only the useful specular signal from the reflector should exist. This is somewhat quite similar to the requirements of the concept proposed herein as the goal is to create a test zone where only the useful LOS and image signals shall exist.

The impact of the (y+)-edge diffracted field at the ARP level using the same configurations is shown in Fig. 3.16. Figs 3.16a and 3.16b depict the ARP error in the TM case with a working frequency $f_0 = 1$GHz and an UFBW=4%, showing a very weak impact on LOS samples with error being below -40dB almost all-over positions in the reflection region. This is not the case for image samples, where positions with tolerated error are mainly below the edge level. The impact is more important in the TE case where even LOS samples are subject to error that may exceed -25dB outside the optimal conditioning region, whereas image samples show large

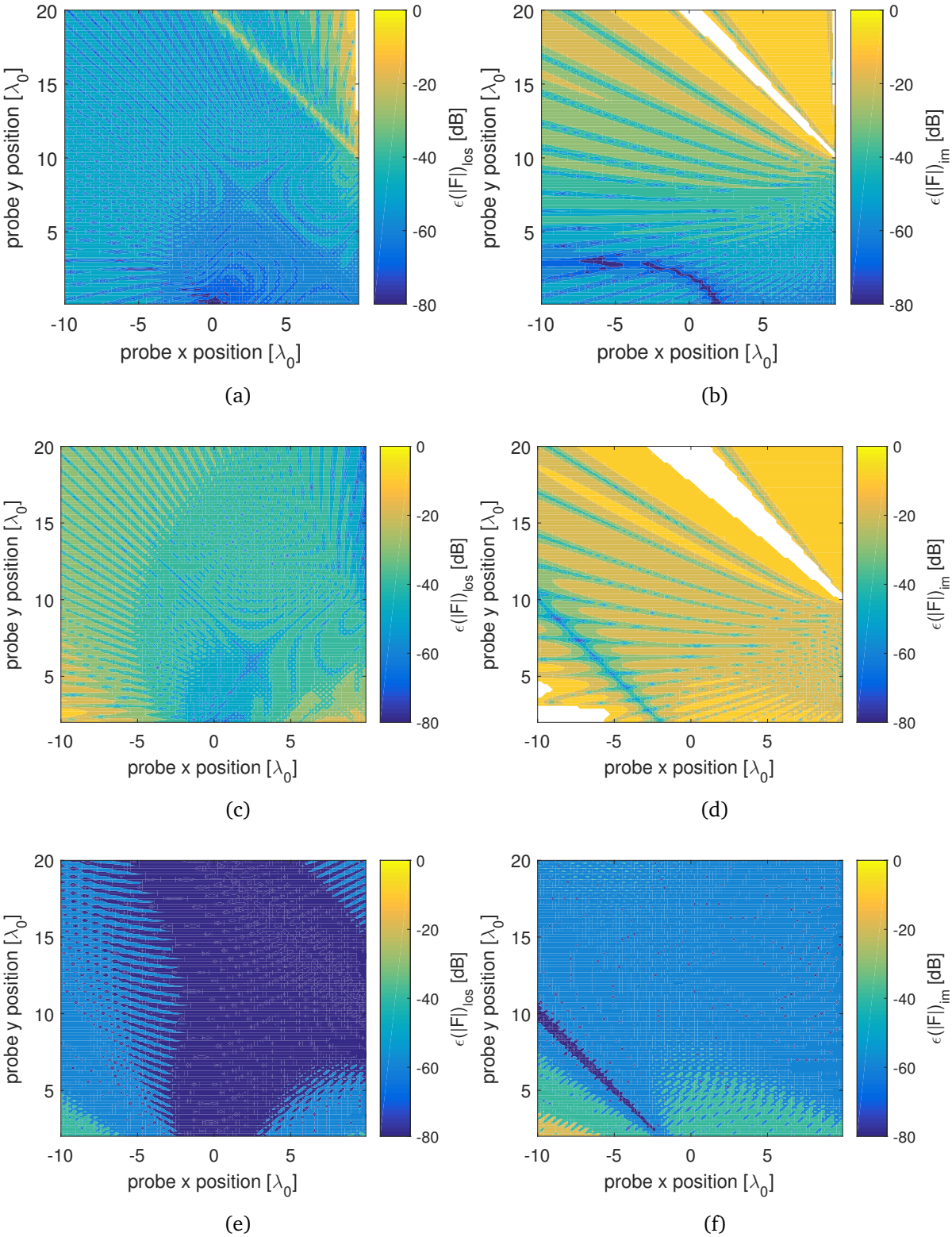

Figure 3.16 ARP error due the (y+)-edge diffracted field for two operating frequencies: $f_0 =$ 1GHz and $f_0' = 10$GHz. $d_i = 10\lambda$, $h = 10\lambda_0$: (a) $\epsilon(\mathbf{F})_{los}$, TM case, $f_0 = 1$GHz (b) $\epsilon(\mathbf{F})_{im}$, TM case, $f = 0$GHz, UFBW=4% (c) $\epsilon(\mathbf{F})_{los}$, basic TE case, $f_0 = 1$GHz, UFBW=4% (d) $\epsilon(\mathbf{F})_{im}$, basic TE case, $f_0 = 1$GHz, (e) $\epsilon(\mathbf{F})_{los}$, basic TE case, $f_0' = 10$GHz (f) $\epsilon(\mathbf{F})_{im}$, basic TE case, $f_0' = 10$GHz.

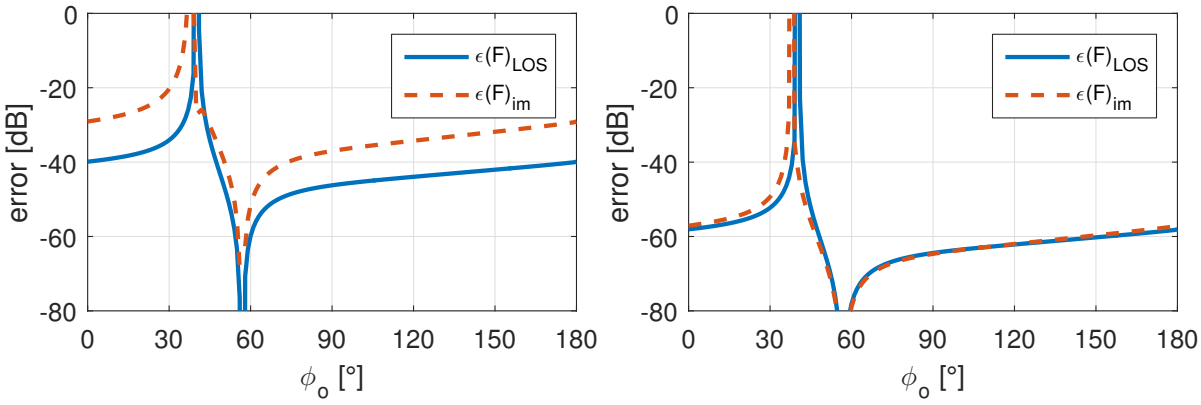

(a) (b)

Figure 3.17 ARP error as function of the AUT orientation for a fixed probe position $(x, y) = (8\lambda, 10\lambda)$ and impact of the (y+)-edge-diffracted field. TE case, $f_0 = 1$GHz, $d = 10\lambda_0$, $h_{y+} = 15\lambda_0$, $\kappa(\mathbf{G}_{TE}) = 1.4$: (a) Basic TE model, $N_f = 1$ (b) Introducing frequency diversity, $N_f = 2$, UFBW= 4%.

error levels exceeding −20dB almost all-over the test zone. It is important to recall that TE results are impacted by the directivity of the corresponding ARP, since all positions below the edge correspond to a weaker ARP level with respect to the edge ARP level given the default ARP orientation. The advantage of the TE case is that optimal regions with respect to both conditioning and plate diffraction are both near the plate. This however requires that the (y+)-edge be situated at a distance greater than d from the AUT horizontal level, otherwise it results in truncating the optimal conditioning region which limits positions with tolerated error, as is the case in this scenario ($h_{y+} = d$). Rising the working frequency while maintaining the plate physical dimensions largely improves the ARP results. Figs 3.16e and 3.16f show the TE results for a working frequency $f_0' = 10$GHz. In this case the edge diffraction problem is practically eliminated, with ARP error being generally below −60dB for both LOS and image cases. Nevertheless, it is worth mentioning that although at high frequencies the edge diffraction problem is minimized, in this case the plate surface quality becomes a concern as any non-ideality over the plate surface may produce spurious fields [69].

To conclude, the vulnerability of the TE case to the edge diffraction problem may be reduced by introducing frequency diversity which both improves conditioning and minimizes ARP error by over-determining the model. Fig. 3.17 compares the ARP error between the basic TE model and when introducing frequency diversity using a well-conditioned probe position $(x, y) = (8\lambda, 10\lambda)$ having $\kappa(\mathbf{G}_{TE}) = 1.4$ and a reference working frequency $f_0 = 1$GHz. The ARP error is recorded as function of the AUT orientation in order to highlight the impact of the directivity to the ARP results. The plate is truncated at $h_{y+} = 15\lambda_0$ and the probe is vertically shifted below the optimal position ($y_{\text{opt}} = d = 10\lambda_0$) in order to reduced the intensity of the edge diffracted field

with respect to the useful fields. The efficiency of frequency diversity in reducing the ARP error is very clear as the LOS error is reduced by a factor of about −20dB and the image error by a factor of −30dB compared to the basic model. The used parameters along with frequency diversity allowed achieving ARP error below −40dB over 96% of spanned angles, highlighting the utility of introducing frequency diversity to the TE model, as well as the manageability of the edge diffraction problem in a general context.

3.3.5 Impact of the plate losses

Up to this point, the plate was assumed PEC, allowing to model the proposed concept using image theory. Although metals with good conductivity may be approximated as perfect conductors, it is convenient to study the impact of infinitesimal losses due to the plate finite conductivity.

The reflected signal from the plate, $\mathbf{E}_r$, may be expressed in terms of a scalar reflection coefficient Γ which takes into account the magnitude reduction due losses resulting from the finite conductivity of the plate:

$$\mathbf{E}_r = \Gamma \mathbf{E}_i,\ \Gamma < 1, \tag{3.44}$$

where $\mathbf{E}_i$ is the incident field on the plate. Notice that this is not a reflection coefficient in the strict sense, as reflection coefficients depend on the angle of incidence, and take into account the polarization of the incident field [21, pp. 151–230]. Recall that the polarization of the reflected field is already taken into account in the system matrices assuming PEC conditions. The PEC approximation is maintained and the impact of small perturbations at the reflected field magnitude level is assessed. It is also worth mentioning that as function of the frequency of the incident field, the plate introduces losses due to the skin effect. These losses are however too small at microwave frequencies for good conductors. Accordingly, the image signal is weighted by a scalar reflection coefficient modeling the magnitude reduction due to the reflection. This is done by multiplying the image columns of the system matrices by the reflection coefficient,

$$\mathbf{G} = \begin{bmatrix} G_{11} & \Gamma G_{12} \\ G_{21} & \Gamma G_{22} \end{bmatrix}. \tag{3.45}$$

Let us now study the impact an error in estimating the real value of the reflection coefficient would have on ARP results. Assuming ideal conditions, the correct ARP vector would be expressed as follows,

$$\mathbf{F} = \mathbf{G}^{-1}\mathbf{E},$$

$$\text{where } \mathbf{G}^{-1} = \frac{1}{|\mathbf{G}|}\begin{bmatrix} \Gamma G_{22} & -\Gamma G_{12} \\ -G_{21} & G_{11} \end{bmatrix}, \tag{3.46}$$

$$\text{and } |\mathbf{G}| = \Gamma\left(G_{11}G_{22} - G_{12}G_{21}\right). \tag{3.47}$$

Suppose the ARP vector is calculated using a system matrix characterized by a different reflection coefficient Γ'. It follows,

$$\mathbf{F}' = \mathbf{G}'^{-1}\mathbf{E}$$
$$\text{where } \mathbf{G}'^{-1} = \frac{1}{|\mathbf{G}'|}\begin{bmatrix}\Gamma' G_{22} & -\Gamma' G_{12}\\ -G_{21} & G_{11}\end{bmatrix} \tag{3.48}$$
$$\text{and } |\mathbf{G}'| = \Gamma'\left(G_{11}G_{22} - G_{12}G_{21}\right). \tag{3.49}$$

The ARP error terms corresponding to the LOS and to the image may be found by comparing the calculated ARP components to the correct ARP components. In the LOS case this yields,

$$\frac{\mathbf{F}'(1)}{\mathbf{F}(1)} = \frac{|\mathbf{G}|}{|\mathbf{G}'|}\frac{\Gamma'\begin{bmatrix}G_{22} & G_{12}\end{bmatrix}\mathbf{E}}{\Gamma\begin{bmatrix}G_{22} & G_{12}\end{bmatrix}\mathbf{E}}$$
$$\frac{\mathbf{F}'(1)}{\mathbf{F}(1)} = \frac{\Gamma\left(G_{11}G_{22} - G_{12}G_{21}\right)}{\Gamma'\left(G_{11}G_{22} - G_{12}G_{21}\right)}\frac{\Gamma'}{\Gamma}$$
$$\frac{\mathbf{F}'(1)}{\mathbf{F}(1)} = 1 \Longrightarrow \epsilon(|\mathbf{F}|)_{\text{los}} = 0\%. \tag{3.50}$$

Accordingly, the LOS samples are not affected by reflection coefficient errors. The image error may be found in the same fashion,

$$\frac{\mathbf{F}'(2)}{\mathbf{F}(2)} = \frac{|\mathbf{G}|}{|\mathbf{G}'|}\frac{\begin{bmatrix}G_{21} & G_{11}\end{bmatrix}\mathbf{E}}{\begin{bmatrix}G_{21} & G_{11}\end{bmatrix}\mathbf{E}}$$
$$\frac{\mathbf{F}'(2)}{\mathbf{F}(2)} = \frac{\Gamma\left(G_{11}G_{22} - G_{12}G_{21}\right)}{\Gamma'\left(G_{11}G_{22} - G_{12}G_{21}\right)} = \frac{\Gamma}{\Gamma'}$$
$$\epsilon(|\mathbf{F}|)_{\text{im}} = 100\left|\frac{\Gamma}{\Gamma'} - 1\right| \ [\%]. \tag{3.51}$$

Eq. 3.51 states that an error in the estimation of the reflection coefficient is translated with the same amount to an error over image samples. These results are verified in Fig. 3.18, where a reflection coefficient error $\delta\Gamma = 1\%$ is inserted by performing the inversion with $\Gamma' = 1$ instead of $\Gamma = 0.99$ using a TM model with an UFBW= 4%. The LOS samples are not affected as they show a practically null error level. On the other hand, a constant 1% error independent of conditioning is noticed at the image samples level. These results are useful in highlighting the impact of the plate infinitesimal losses on the ARP results while assuming PEC conditions.

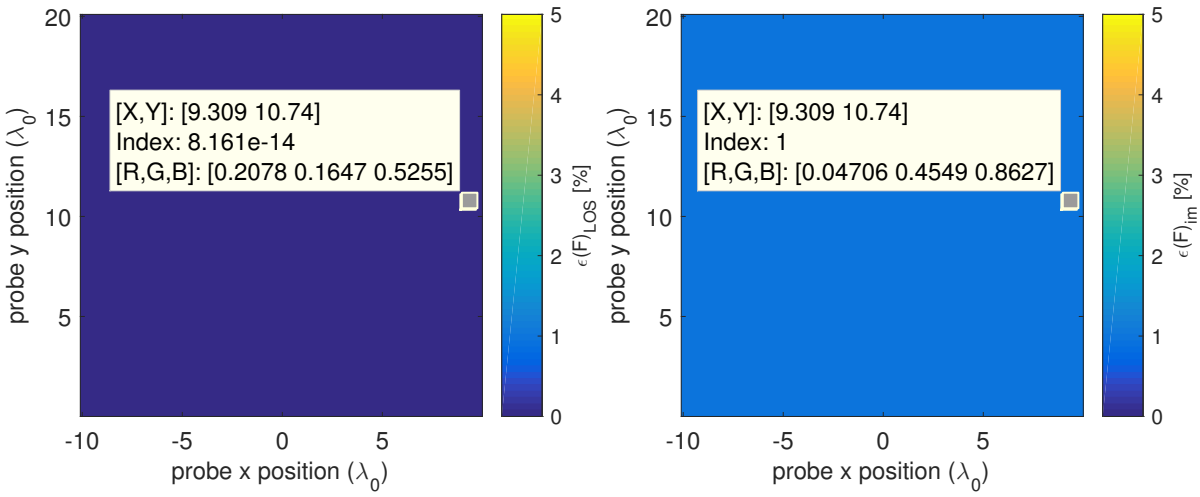

(a) (b)

Figure 3.18 ARP error as function of the probe position given an error in the estimation of the plate's reflection coefficient. TM case, UFBW=4%, $d = 10\lambda_0$, $\Gamma = 0.99$, $\Gamma' = 1$ (a) $\epsilon(|\mathbf{F}|)_{\text{los}}$, (b) $\epsilon(|\mathbf{F}|)_{\text{im}}$.

3.3.6 Combining Error Sources

At this stage, impacts of the main error sources were separately studied, the question of combining them arises naturally. It is worth emphasizing that the goal of such studies is to provide a general insight into the impact of error sources on the proposed model; the actual impact would be function of several parameters such as the quality of the measurement range and used equipment in addition to the operation frequency and the tested antenna. Let us take for instance a scenario where measurement conditions are characterized by an SNR=40dB with an AUT having a hypothetical isotropic RCS $\sigma = 0.5\lambda_0^2$ and the plate being truncated at $h_{h+} = 15\lambda_0$. Suppose also that the measurement is characterized by an error of 0.5% in the estimation of the reflection coefficient and a position uncertainty factor $\sigma_{pos} = 3$mm. Results are shown in Fig. 3.19 applying an operating frequency $f_0 = 1$GHz for both transverse models, the TE model being used in the updated form ($N_f = 2$). The LOS error is generally tolerable over the majority of the test zone, oscillating around -40dB on optimal conditioning regions for both the TM and TE cases. The importance of conditioning models is highlighted over image results, which show that only optimal regions with respect to conditioning show levels of tolerable error. This is especially true for the TE case where optimal regions with respect to conditioning, AUT diffraction, and edge diffraction all lie in the vicinity of the plate, showing error levels around -40dB in this region. The TM case offers a larger low-error zone, mainly due to the lower impact of edge diffraction, but error levels are generally unstable, oscillating between tolerable levels and high levels in this region. This is mainly due to the fact that the optimal conditioning region does not coincide with optimal regions with respect to AUT and edge diffractions.

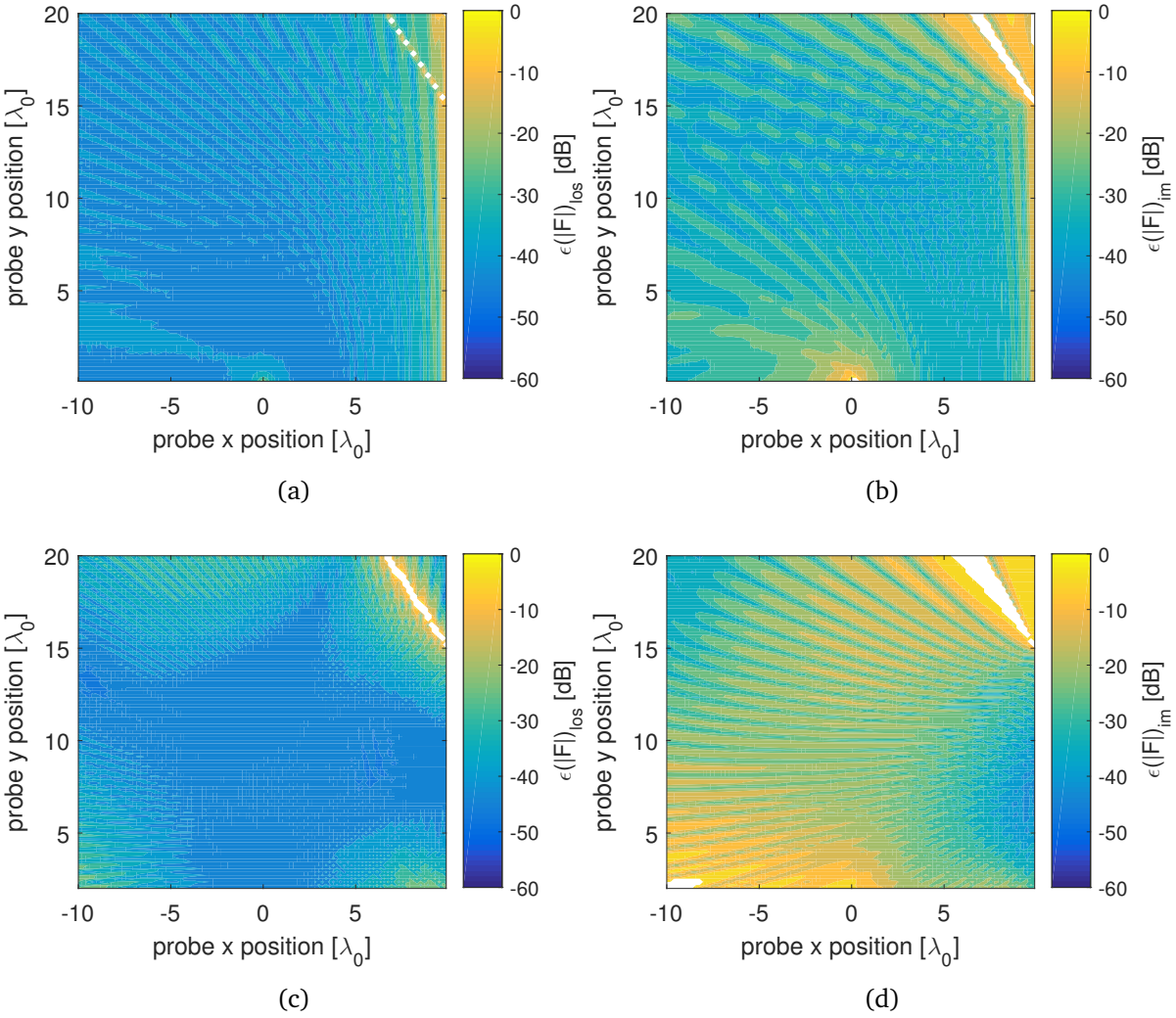

Figure 3.19 ARP error as function of the probe position combining the different error sources. $f_0 = 1$GHz, $d = 10\lambda_0$, $h = 15\lambda_0$, $\sigma = 0.5\lambda_0^2$, SNR $= 40$dB, $\sigma_{pos} = 3$mm: (a) $\epsilon(|\mathbf{F}|)_{\text{los}}$, TM case, UFBW$= 4\%$ (b) $\epsilon(|\mathbf{F}|)_{\text{im}}$, TM case, UFBW$= 4\%$ (c) $\epsilon(|\mathbf{F}|)_{\text{los}}$, TE case, $N_f = 2$, UFBW$= 4\%$ (d) $\epsilon(|\mathbf{F}|)_{\text{im}}$, TE case, $N_f = 2$, UFBW$= 4\%$.

Rising the working frequency is advantageous in terms of edge diffraction, but disadvantageous in terms of the plate surface quality and position uncertainty. For instance, a plate having $10\lambda_0 \times 10\lambda_0$ dimensions, which would correspond to 3m×3m for $f_0 = 1$GHz, may be considered infinite for a frequency equal to 10GHz. So we may conclude that in terms of measurement site requirements, the concept is more adapted to high frequencies, as physically small test zones guarantee the viability of the far-field model and small plate dimensions eliminate the edge diffraction problem. However, in this case attention should be payed to position errors as position uncertainty factors augment with respect to the working wavelength. This is highlighted in Fig. 3.20 where an operating frequency $f_0 = 10$GHz is used in a TM model maintaining essentially the same parameters used in the previous scenario expect for the plate truncation which is situated at a distance $h_{y+} = 30\lambda_0$ (90cm). Results are plotted for different position uncertainty factors. Figs. 3.20a and 3.20b show the ARP error for $\sigma_{pos} = 3\text{mm} = \lambda_0/10$ which is relatively high resulting in an averagely high error level on image samples, which oscillates around −30dB in the optimal conditioning region. A more realistic scenario is realized by a applying a different position uncertainty factor at the AUT level in order to model the uncertainty which would arise over the phase center. Suppose that the plate and the probe are positioned with an uncertainty $\sigma_{pos} = 3\text{mm} = \lambda_0/10$, but the uncertainty over the AUT phase center rises the AUT position uncertainty to $\sigma_{AUT} = 6mm = 1/5\lambda_0$. Results are plotted in Figs. 3.20c and 3.20d showing a slightly higher error than the previous case oscillating between −40dB and 35dB over LOS samples and between $30dB$ and −25dB over image samples in the optimal conditioning region, while exceeding −25dB outside this region for image samples. These results highlight the important impact position errors could have at high frequencies.

Globally, we may conclude that the different model limitations are manageable and several solutions to limit their impacts are possible. The importance of conditioning models are highlighted showing, as function of measurement conditions, cases where only optimal probe positions could be used. In the upcoming section, the robustness of the proposed method is enhanced by introducing linear regression which is used in order to reduce the ARP error. The same technique is applied in order to estimate the remaining outlined model limitation, the ARP dependence on the working frequency.

3.4 Enhancing the Method Robustness

As discussed in the previous sections, the impact of the different error sources may dramatically reduce the accuracy of the ARP results. This is especially true for probe positions corresponding to weak power emission which are vulnerable to all types of error sources and may be regarded as singular positions. Moreover, image samples are more vulnerable to error than LOS samples.

One method to reduce the ARP error is by introducing linear regression. Unlike the direct inversion method which is processed *locally*, i.e., in which ARP samples are retrieved via independent calculations relative to each measurement, i.e., relative to each probe position or

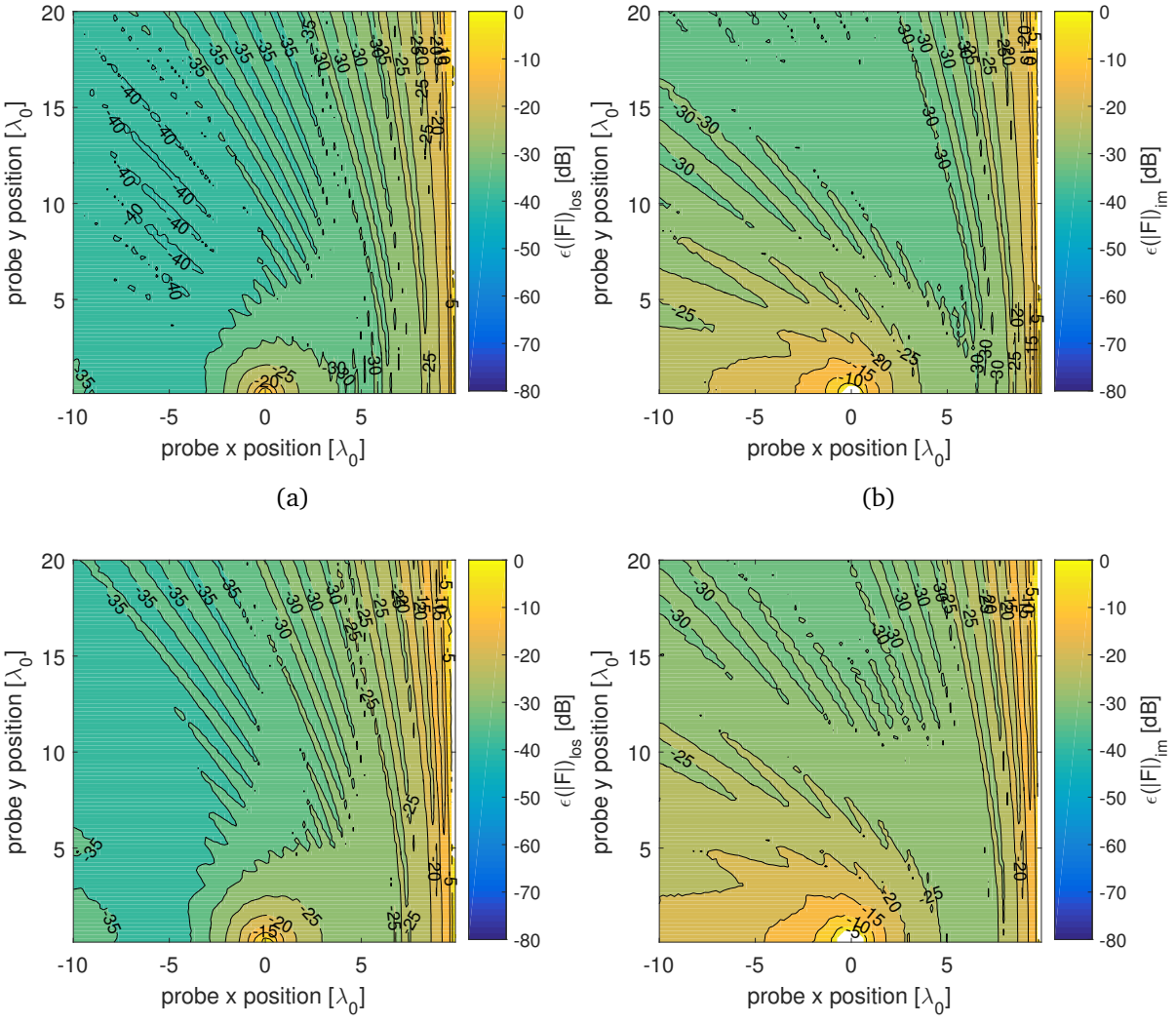

Figure 3.20 ARP error as function of the probe position combining the different error sources. TM case, $f_0 = 10$GHz, $d = 10\lambda_0$, $h = 30\lambda_0$, $\sigma = 0.5\lambda_0^2$, SNR $= 40$dB: (a) $\epsilon(|\mathbf{F}|)_{los}$, $\sigma_{pos} = 3$mm (b) $\epsilon(|\mathbf{F}|)_{im}$, $\sigma_{pos} = 3$mm (c) $\epsilon(|\mathbf{F}|)_{los}$, $\sigma_{pos} = 3$mm, $\sigma_{AUT} = 6$mm (d) $\epsilon(|\mathbf{F}|)_{im}$, $\sigma_{pos} = 3$mm, $\sigma_{AUT} = 6$mm.

AUT orientation, linear regression retrieves ARP samples by combining information acquired at a number of measurements by means of a set of basis functions referred to as *regression* functions, and hence the inversion is processed *globally*.

3.4.1 Introduction to Linear Regression

Linear regression is a modeling method generally used in order to fit a model to a set of observed data [70]. The most widely used regression technique is the linear Least-Squares (LS) regression [71]. This technique may be very efficient in reducing the ARP error provided that a sufficient number of ARP samples is acquired. In order to do so, the dependent variable, the field vector, corresponding to a set of N_m measurements is expressed in terms of a set of N_r well-known regression functions instead of the ARP vector (Eq. 2.19),

$$\mathbf{E} = \mathbf{GR}\boldsymbol{\beta}, \tag{3.52}$$

where $\mathbf{G}$ is an $N_f N_m \times N_a N_m$ block diagonal matrix formed by the system matrices corresponding to each measurement, $\mathbf{R}$ an $N_a N_m \times N_r$ regression matrix retrieved by interpolating the regression functions at the global set of measurement angles, and $\boldsymbol{\beta}$ is an unknown $N_r \times 1$ vector containing the regression coefficients which weights the independent input data ($\mathbf{GR}$) in order to produce the desired output ($\mathbf{E}$) [2]. For the regression to be efficient, the number of ARP samples $N_a N_m$ would be larger than the number of regression functions N_r, such that input data contains enough information to estimate the unknown regression coefficients that best fits the model into the set of observed data. This would yield an over-determined system where the fitted ARP samples are retrieved by solving for $\boldsymbol{\beta}$,

$$\hat{\boldsymbol{\beta}} = \text{Arg}\min \|\mathbf{GR}\boldsymbol{\beta} - \mathbf{E}\|^2. \tag{3.53}$$

Hence, the performance of the regression depends on the input data on the one hand, and on regression parameters on the other hand.

Input data may be modeled by ARP samples retrieved via direct inversion. For the regression to be efficient, calculated ARP samples should be *well* dispersed around the reference ARP, which is most likely to occur when the number of ARP samples is large. In the single-plate case, this requires performing several measurements, either by rotating the AUT or by moving the probe, the global number of ARP samples being the double of the number measurements.

Regression parameters may be summarized in the type and number of regression functions. These parameters define how regression functions are distributed over a given angular range. Two extreme cases may be distinguished. The first being the disjoint regression functions

[2] Note that the term β has previously been used in order to refer to phase quantities, as will be the case over the rest of the text. Exclusively in this section, the common notation of the weights vector $\boldsymbol{\beta}$ is maintained in order to refer to the regression coefficients.

case where each regression function covers a different angle and may be modeled by a set of Kronecker δ functions covering adjacent discrete angles [72, pp. 5–6],

$$R_i(\phi_j) = \delta_{ij}, \tag{3.54}$$

where,

$$\delta_{ij} = \begin{cases} 0 & \text{if } i \neq j, \\ 1 & \text{if } i = j. \end{cases} \tag{3.55}$$

This type of basis functions may be referred to as *local* functions as each function exists within a limited angular range, which in this case is defined by the corresponding pointed angle. Hence, ideally an infinite number of δ functions would be necessary to cover any continuous angular range. An approximative graphical representation of this case is depicted in Fig. 3.21a, showing each basis function pointing to a different measurement angle with no interference between adjacent basis functions. This extreme case models the direct inversion method, as each basis function contains information about a single data sample which would yield an inversion where ARP samples are retrieved via independent calculations. The second extreme case is the*global* regression functions case where all regression functions are dispersed over a 2π-range, and hence each basis function would cover the entire measurement angular range. An example of this type of basis functions are Fourier regression functions which are -by default- defined over a 2π-range,

$$R_n(\phi) = \mathrm{e}^{jn\phi}, \quad n \in [0, N_r - 1] \tag{3.56}$$

where n is the mode number defining the phase distribution of each function; the total number of modes being defined by the chosen number of regression functions N_r. An example of a set of Fourier regression functions is shown in Fig. 3.21b for$N_r = 5$. In this case, the performance of the regression may be limited as fitting the model to a set of observed data may become difficult with each basis function containing different information about the global data set. An adequate regression functions set would offer a compromise between the two extreme cases; it would be a set of local basis functions reasonably interfering with each other such that each subset would contain information about a different subset of data samples. One type of local regression functions that offer control over their patterns are Gaussian Radial Basis Functions (RBFs) [73],

$$R_n(\phi) = \mathrm{e}^{-\frac{(\phi-\phi_n)^2}{2s^2}}. \tag{3.57}$$

where ϕ_n is the central angle pointed by each basis function and s is the spread which defines the range of covered angles around ϕ_n. This type of regression functions may be confined in a limited angular range that would correspond to the exact range spanned by ARP samples (half the azimuthal plane for example), and offer the advantage of controlling their number and

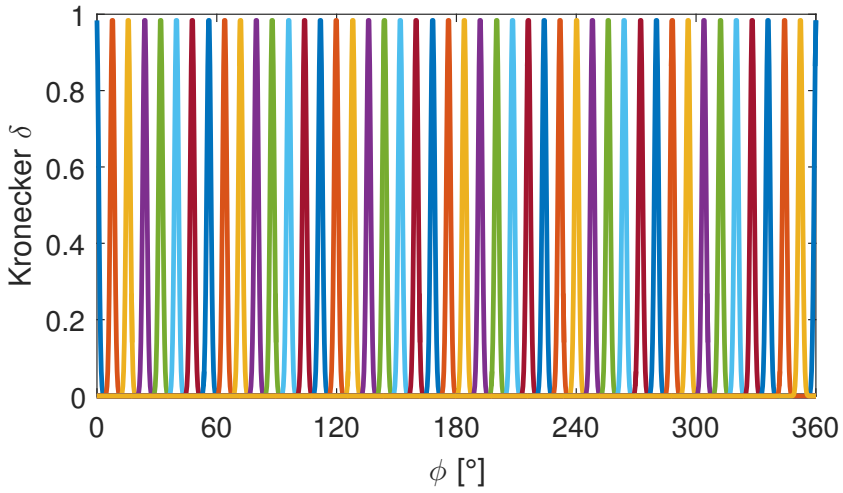

(a)

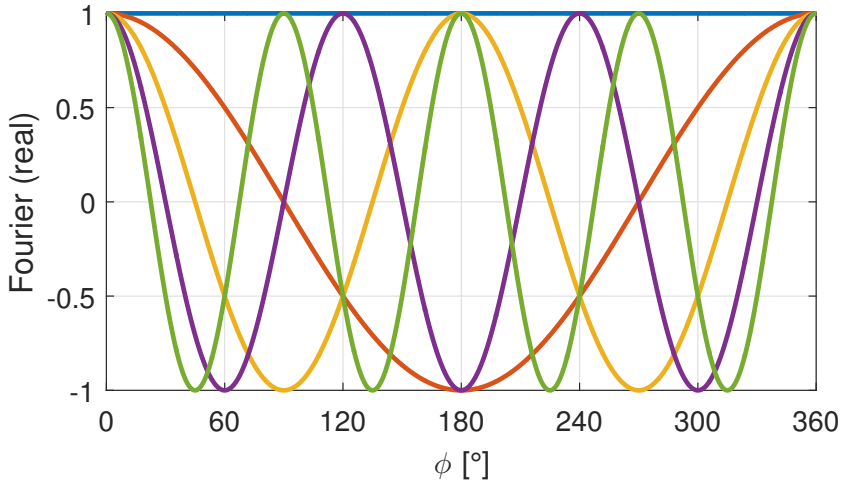

(b)

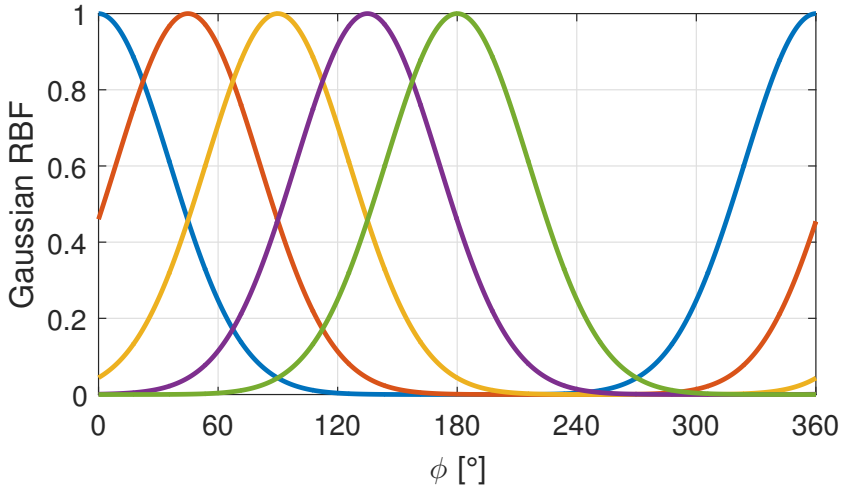

(c)

Figure 3.21 Example of regression functions (a) Approximation to Kronecker δ functions spanning 360°-range (b) Fourier, real part, $N_r = 5$ (c) Gaussian RBFs confined in a 180°-range, $N_r = 5$, $s = 36°$.

spread in order to best fit the model to the set of ARP samples. An example of five Gaussian RBFs with a spread $s = 36^\circ$ confined in half the azimuthal plane is shown in Fig. 3.21c.

3.4.2 Application to ARP Results

Examples highlighting the usefulness of linear regression in reducing the ARP error and related issues are presented in synthetic scenarios where the reference field is perturbed using an AWGN based on a low SNR=20dB calculated with respect to the maximum field power over a set of 10 probe positions linearly spaced between $x \in [-9\lambda_0, 9\lambda_0]$ at a constant vertical distance $y = 5\lambda_0$, the plate being at a distance $d = 10\lambda_0$ from the AUT. The perturbed field is averaged over $N_t = 1000$ trials.

Ideally, one of the regression functions would approximately match the reference ARP for a given regression coefficient in order to fit all ARP samples with high accuracy. This would be possible if some a priori information about the tested ARP is available. The same can be seen in Fig. 3.22a where a single Fourier basis function corresponding to the lower mode (a circle) is very efficient in reducing the ARP error corresponding to the HWD TM-isotropic case from ±5dB to less than ±0.1dB. Notice that image samples ($\phi < 30^\circ$) retrieved via direct inversion show larger error levels than LOS sample. The efficiency of Fourier regression in this case is however reduced if additional basis functions are included, highlighting the limitation of global regression functions pointed out in Sec 3.4. This is shown in Fig. 3.22b where three basis functions are used, reducing the ARP error to around ±1dB.

The TE-directive case with the HWD being oriented parallel to $\hat{x}$ is characterized by even larger absolute error levels over image samples retrieved via direct inversion ($|\epsilon(|\mathbf{F}|)_{im}| > 7$dB) as they correspond to directions of weak power emission (Figs. 3.22c-3.22f). Using Fourier regression with $N_r = 5$ reduces ARP error up to ±3dB, as shown in Fig. 3.22c. Gaussian RBF regression functions, being local, are more efficient in this case as sets of ARP samples corresponding weak and strong power emissions are pointed by different regression functions, such that the model is locally fitted to each section of the ARP. A reasonable interference between the basis functions is however required such that different sections are not fitted independently. The same can be seen in Fig. 3.22d where a set of five RBF basis functions with a spread $s = 36^\circ$ confined in half the azimuthal plane (Fig. 3.21c) reduce the absolute error up to around ±1dB. However, as discussed earlier, the basis functions parameter should be chosen with care in order for the regression to be efficient. For example, reducing the spread would limit the information acquired by each basis function as they would point to smaller sets of data samples. The opposite case, which is enlarging the spread, would approximate the global regression functions case as the different basis functions would strongly interfere with each other such that each basis function would contribute with different information about the global data set. The number of basis functions is also important given the chosen spread. A small number of weakly-interfering basis functions would make sections of data samples independent of each

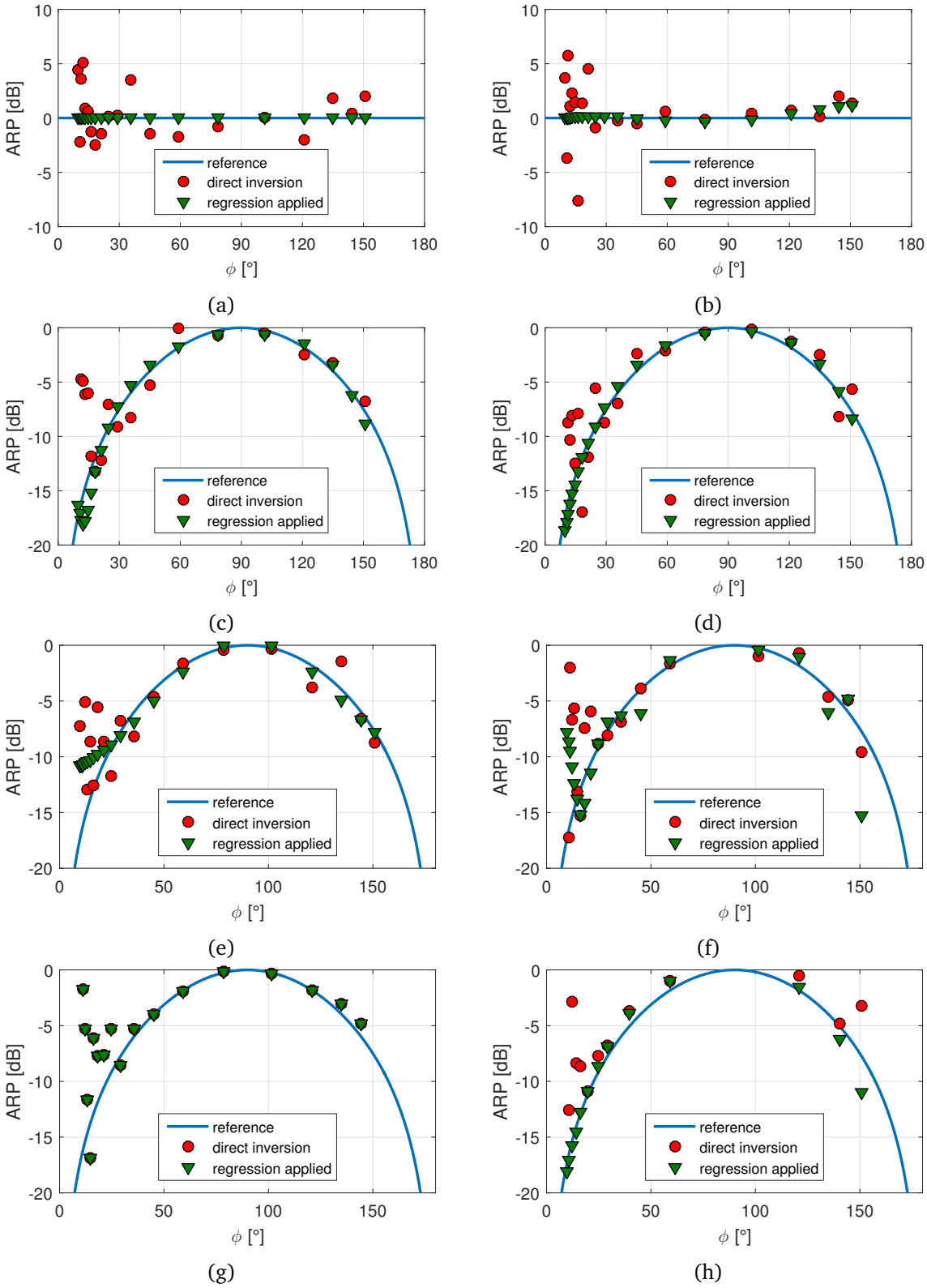

Figure 3.22 Introducing linear regression to the proposed model in a synthetic scenario using a HWD and 10 probe positions $(x, y) = (-9\lambda_0 : 2\lambda_0 : 9\lambda_0, 5\lambda_0)$, $d = 10\lambda_0$, SNR = 20dB. Isotropic-TM case, UFBW=4%: (a) Fourier regression, $N_r = 1$ (b) Fourier regression, $N_r = 3$. Directive-TE case, $N_f = 1$ (c) Fourier regression, $N_r = 5$ (d) RBF regression, $N_r = 5$ (e) RBF regression, $N_r = 3$ (e) RBF regression, $N_r = 90$, $s = 1°$ (e) RBF regression, $N_r = 10$ (f) RBF regression, $N_r = 5$, with 8 probe positions.

other and thus would fit the model locally in each section, as shown Fig. 3.22e, where $N_r = 3$. On the other hand, enlarging the number of basis functions would result in an*over-fitting* case where the different informations provided by different basis functions about the same data sets make the regression coefficients misleading, as shown in Fig. 3.22f where $N_r = 10$. The extreme case, as pointed earlier, when a large number of non-interfering basis functions is used, which implies a small spread, would make each basis function contain exclusive information about a single data sample, yielding independent calculations in order to retrieve the ARP samples in the same fashion as in the direct inversion method. The same can be seen in Fig. 3.22g, where a set of 90 basis functions with $s = 1^\circ$ yielded the same ARP samples retrieved via direct inversion. Finally, the number of measurements, and thus input data samples, also impacts the performance of the regression, as less data is equivalent to less information collected by basis functions. This is shown in Fig. 3.22h, where 8 probe positions are used with optimal regression parameters (those used in Fig. 3.22d), limiting the performance of the regression in the LOS region ($\phi > 30^\circ$) to ±5dB.

Globally, we may conclude that, in a noisy environment, if a sufficient number of measurements is performed, regression may be very efficient in reducing ARP error to levels below ±1dB provided that regression parameters are well chosen.

3.4.3 Estimating the ARP Frequency Dependence

An additional application of linear regression, other than reducing the ARP error, is the estimation of the frequency impact on the ARP. Up to this point, the ARP was assumed frequency-independent; an assumption that is not valid for most antenna types as generally the ARP is frequency-dependent. The simplified model described by Eq. 2.19 may be updated by introducing a new matrix $\boldsymbol{\alpha}$ that takes into account the frequency impact on the ARP,

$$\mathbf{E} = \boldsymbol{\alpha}\mathbf{G}\mathbf{F}, \tag{3.58}$$

$$\text{with } \boldsymbol{\alpha}_{TM} = \begin{bmatrix} 1 & 0 \\ 0 & \alpha \end{bmatrix}, \tag{3.59}$$

$$\text{and } \boldsymbol{\alpha}_{TE} = \left[\begin{array}{c|c} \boldsymbol{\alpha}_{TM} & 0 \\ \hline 0 & \boldsymbol{\alpha}_{TM} \end{array}\right], \tag{3.60}$$

where α is a complex term that models the amplitude and phase variations underwent by the ARP when operating the AUT at the second working frequency f_1. In order to highlight the importance of well estimating α to the accuracy of the proposed method, consider the examples

shown in Fig. 3.23, where a synthetic TM-field is generated using some α-term modifying exclusively its phase at the second operating frequency (UFBW=4%), while ARP samples are calculated assuming frequency independence ($d = 10\lambda_0$). Figs. 3.23a-3.23b show the ARP error for an estimation error of the phase variation of 1°. The LOS error is quite low, being below −40dB almost all-over the test zone. The image error, however, exceeds −40dB as soon as the probe is moved outside the optimal conditioned region. The ARP error is amplified for larger estimation errors of the frequency impact, as shown in Figs. 3.23c-3.23d where an estimation error of the phase variation of 3° amplified the LOS error to levels below −40dB and image error up to levels around −25dB in the optimal conditioned region. Taking into account contributions of the remaining error sources, a reliable estimation of the frequency impact is necessary in order to ensure a satisfying accuracy of the calculated ARP results.

Eq. 3.58 describes a non-linear system of equations in α containing two sets of unknowns, the ARP vector $\mathbf{F}$ and $\boldsymbol{\alpha}$. Regression is introduced in order to solve for the two quantities,

$$(\hat{\boldsymbol{\beta}}, \hat{\boldsymbol{\alpha}}) = \text{Arg min} \, \|\boldsymbol{\alpha}\mathbf{G}\mathbf{R}\boldsymbol{\beta} - \mathbf{E}\|^2. \tag{3.61}$$

Global optimization techniques may be used in order to solve Eq. 3.61 [74]; an issue that is not covered in this work and is left as a perspective. In this section a study of the convexity of the cost function is conducted in order to assess the possibility of existence of optimal solutions. The formal approach consists in studying Hessian matrix of the cost function which contains the corresponding second partial derivatives [75]. This approach, being cumbersome, is also left as a perspective due to time constrains. An alternative simpler approach is considered by numerically spanning the space of solutions by assessing different values of α (amplitude and phase) and looking for possible minima. This requires choosing an adequate set of probe positions and regression parameters in order for the regression to best fit the model for each tested α value. An example of a synthetic scenario where an $\alpha = 1.1e^{j10^\circ}$ is used in order to generate the field at the second working frequency is shown in Fig. 3.24 for various situations in a configuration characterized by an AUT-plate separation $d = 10\lambda_0$. Fig. 3.24a corresponds to a TM-isotropic case using a single probe position $(x, y) = (0\lambda_0, 20\lambda_0)$ with a single Fourier basis function corresponding to the lower mode. The cost function in this case is convex, with the minima corresponding exactly to the inserted α value. This is however a particular situation as the used basis function matches the tested ARP. A more general case would necessitate more probe positions in order to acquire sufficient information about the ARP, as is the case in the TE-directive mode. Using five Gaussian RBF basis functions with a spread $s = 36°$, neither one nor two probe positions were sufficient to generate a convex cost function, as shown in Figs. 3.24b-3.24c. Three probe positions, in the contrary, generated a convex cost function with the minimum corresponding to the correct α value, as shown in Fig. 3.24d. These results highlight the possibility of solving for the unknown α-term and the ARP vector by adequately applying linear regression provided that a sufficient number of measurements is performed.

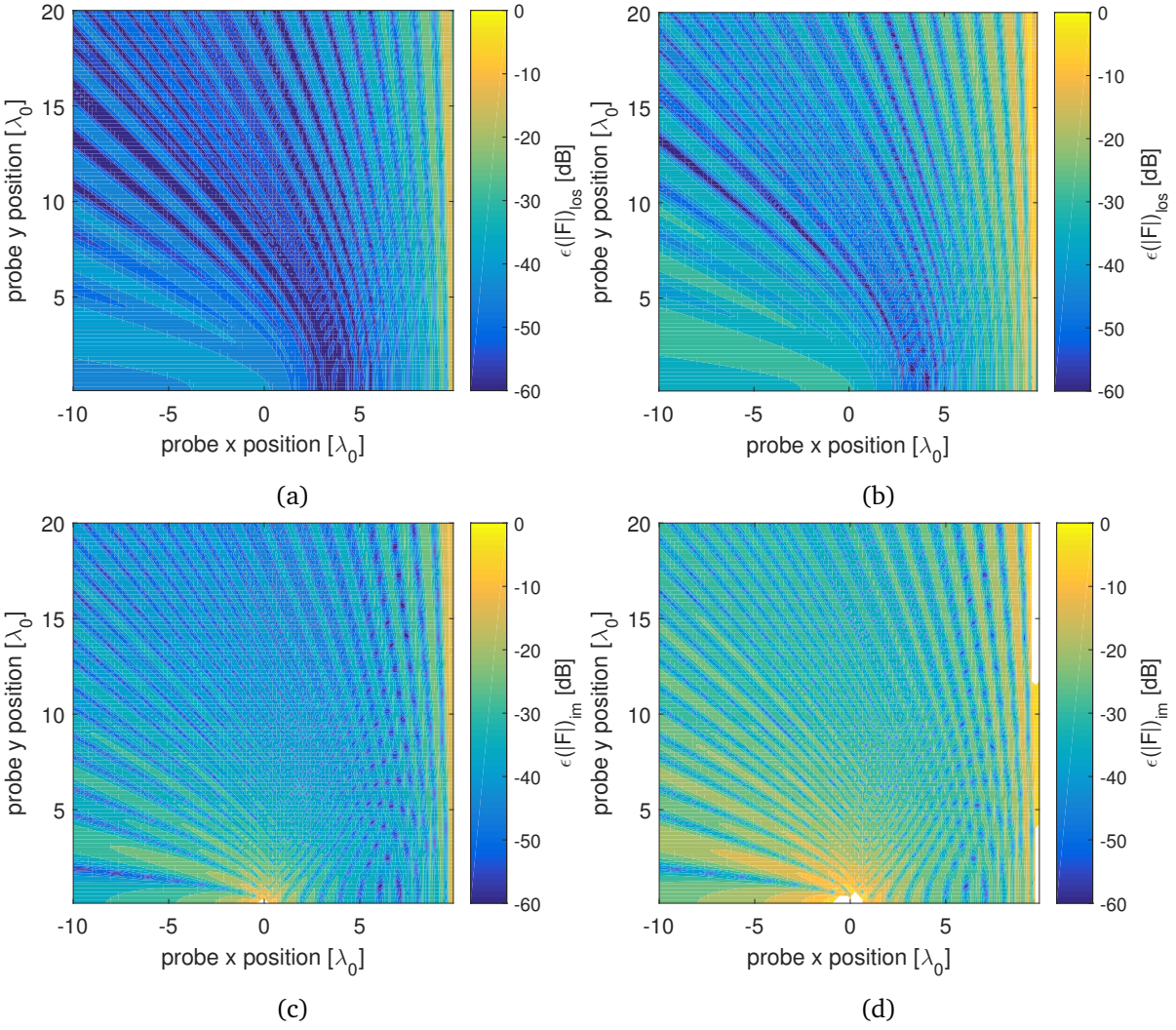

Figure 3.23 ARP error due to error in estimating α which models the ARP frequency dependence. Synthetic scenario, TM case, $d = 10\lambda_0$, UFBW=4% (a) $\epsilon(|\mathbf{F}|)_{\text{los}}$, 1° phase error (b) $\epsilon(|\mathbf{F}|)_{\text{im}}$, 1° phase error (c) $\epsilon(|\mathbf{F}|)_{\text{los}}$, 3° phase error (d) $\epsilon(|\mathbf{F}|)_{\text{im}}$, 3° phase error.

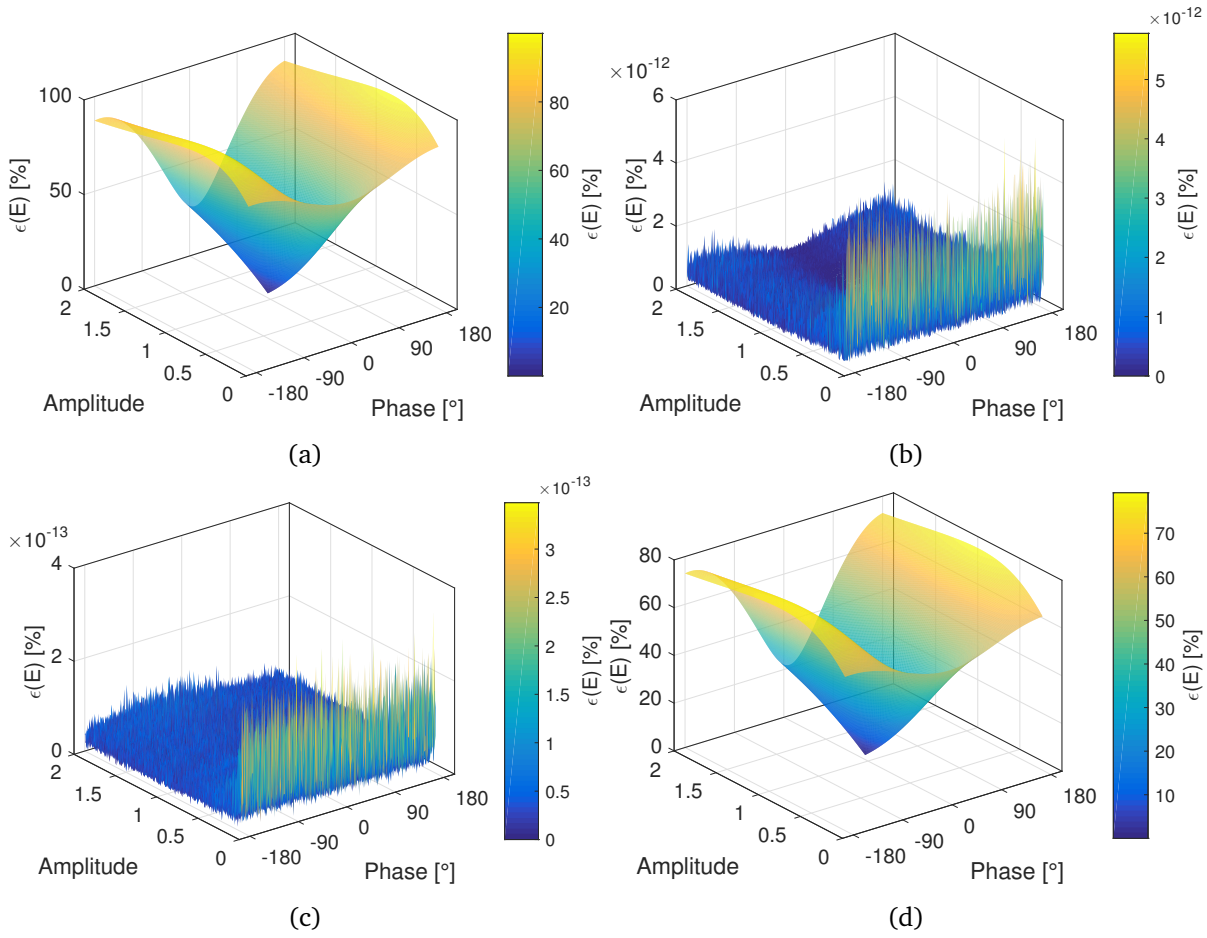

Figure 3.24 Assessment of the the convexity of the cost function of the proposed model taking into account the frequency impact in a synthetic scenario where the field at the second frequency is generated using $\alpha = 1.1e^{j10^{\circ}}$. $d = 10\lambda_0$ (a) TM-isotropic case, single probe position $(x, y) = (0\lambda_0, 20\lambda_0)$, Fourier regression, $N_r = 1$ (b) TE-directive case, single probe position $(x, y) = (0\lambda_0, 20\lambda_0)$, RBF regression, $N_r = 5$, $s = 36^{\circ}$ (c) TE-directive case, 2 probe positions $(x, y) = (-6\lambda_0 : 6\lambda_0 : 0\lambda_0, 20\lambda_0)$, RBF regression, $N_r = 5$, $s = 36^{\circ}$ (d) TE-directive case, 3 probe positions $(x, y) = (-6\lambda_0 : 3\lambda_0 : 0\lambda_0, 20\lambda_0)$, RBF regression, $N_r = 5$, $s = 36^{\circ}$

The presented scenario showed that the proposed approach allowed the estimation of the ARP frequency dependence with success using a minimum number of measurements and without a priori information about the ARP.

Conclusion

In this chapter the various practical limitations of the adopted model were theoretically studied in order to verify the physical viability of the proposed concept. A study of the impact of the set of approximations applied in order to simplify the mathematical formulations predicted the manageability of the different model related errors sources. General remarks regarding model-related errors are recapitulated in Table 3.1.

Model-Related Error Source	**General Remarks**
Far-field approximation	The Fraunhofer criterion should be applied with care especially if the ARP is directive as the contribution of the field radial component may become important in directions of weak power emission.
Impact of the plate on the AUT radiation resistance	Moderate AUT-plate separations (d>$2\lambda_0$) are sufficient to consider free space radiation characteristics.
Diffraction by the AUT aperture	The AUT diffracted field is dominated by the first order LOS diffraction and the corresponding reflection from the plate defining optimal and worst hyperbolas of positions with respect to the AUT diffraction. The optimal region is defined in the vicinity of the plate.
Diffraction by the plate edges and corners	Diffracted fields by the plate are dominated by the edge-diffractions. The edge diffraction coefficients dictate that optimal positions are near the plate. The TE (hard polarization) case, which is more affected by the edge diffraction than the TM case, is enhanced by introducing frequency diversity. Generally, the edge diffraction problem is reduced at high frequencies.
Impact of the plate losses	Infinitesimal losses introduced by the plate exclusively impact image samples with the same amount of error of the estimation of the plate's reflection coefficient

Table 3.1 General remarks regarding model-related error sources.

The tolerance of the developed models to the inevitable practical systematic errors was assessed as well, highlighting the importance of conditioning models developed in the previous chapter. Linear regression was then introduced in order to enhance the robustness of the proposed method by reducing the ARP error associated to the direct inversion. Regression was used in order to optimize the model as well by estimating the ARP frequency dependence. The adopted approach consisted in numerically spanning the space of solutions minimizing the corresponding cost function. Global optimization techniques may be used in order to solve the problem in a more *formal* fashion.

Chapter 4

Single plate Configuration: Numerical Validation

Contents

Chapter 3 presented a synthetic validation of the proposed concept based on the assumption of the coherence of the adopted model. In this chapter, the feasibility of the concept is numerically validated using an electromagnetic simulation software: *FEKO*. A brief presentation of the software and its features is first provided before presenting the set of tested antennas. Then, a set of simulations is performed prior to the application of the concept in order to measure the impact of systematic error sources. The far-field distance, the impact on the AUT radiation resistance, and the AUT diffraction are assessed in terms of tested antennas. After that, the proposed method is validated by performing the inversion using an infinite PEC ground with an estimation of the frequency impact whenever needed. Finally, more realistic configurations involving finite metallic plates are considered to highlight the feasibility of the concept.

4.1 Software Presentation: FEKO

4.1.1 Introduction

The various simulations to numerically validate the concept and assess related issues are mainly performed using FEKO. The name FEKO stands for the abbreviation of the German translation of *Field computations involving bodies of arbitrary shape* [76]. As suggested by the name, FEKO is a comprehensive electromagnetic simulation software intended for applications involving electromagnetic field analysis of structures of arbitrary shapes. It integrates a set of multiple numerical methods to solve Maxwell's equations which makes it suited for a wide range
Bio-Electromagnetics and Biomedical Applications.

The core of the FEKO solver is the Method of Moments, which was presented in Sec. 3.3.4.1. However, FEKO allows to hybridize it with other techniques or even replace it as function of the simulated model. In the context of the proposed concept, one main criterion in choosing the numerical simulation method is the size of the plate which may potentially impact computational resources, i.e., memory, CPU and time resources, required to perform the simulation. Techniques used to handle the plate in configurations simulated in the present chapter are described hereafter. Further references may be found in Sec. 3.3.4.1.

4.1.2 Metallic Structures Handling in FEKO

FEKO provides several options to handle metallic structures that are present in the calculation domain. These options allow to deal with reflected and diffracted fields depending on the problem in question, as is the case with the plate considered in our model, and whose dimensions imply that one option may be more suitable than the other.

- MoM: This is the full wave option. In this case the plate is considered as a radiating structure and is discretized to calculate the current distribution over its surface. Although this may be the most accurate option, as discontinuities characterizing the plate are taken into account independently of their shape, it is disadvantageous in terms of memory requirements and processing time. If the plate dimensions are large with respect to the wavelength, which is basically the case in the proposed concept, the number of cells necessary to mesh the plate augment as well, implying the allocation of a large memory space and performing a large number of calculations which result in a long simulation time. Moreover, some FEKO licenses are memory restricted, which means that if the number of configuration cells exceeds some level, the configuration may not be simulated.

  The MoM is best suited for free-space simulations. This is due to the fact that it is a *source method*, which means that only the radiating structure -the AUT in this case- is meshed. This is in contrast with field methods which require meshing the propagation domain

even if it is free space. Accordingly, the MoM is used in order to retrieve AUTs free-space characteristics and to assess the far-field distances and the image models as well.

- Multilevel Fast Multipol Method (MLFMM) [77]: This technique is an alternative formulation of the MoM to make it applicable to larger structures with almost the same accuracy. The logic behind MLFMM is the iterative subdivision of the computational space, which is modeled by the impedance matrix, into smaller subspaces, i.e., smaller matrices. Then, only non-empty matrices are considered in the calculations which results in efficient computational resources reduction. MLFMM is best suited for electrically large structures having geometries with low complexities. If the complexity of the simulated geometry is high, the MoM is a better option. In this chapter, the MLFMM is used in order to simulate a curved edge plate intended to reduce the edge diffraction problem.

- UTD: FEKO allows the design of UTD polygonal plates which, unlike the default plates, are not discretized by the MoM. Instead, the solver only takes into account reflection points from the plate surface and diffraction points from the edges and corners. This technique is well suited for electrically large structures, and has the advantage of considerably reducing computational resources independently of the size of the simulated structure. However, the current formalization of this option doest not take into account edges of complex shapes as only flat edges are supported [76]. This makes the UTD option the most suited for simulations involving rectangular finite plates.

- Infinite ground plane: FEKO proposes several types of infinite ground planes, including a PEC ground plane. This option is very effective in terms of computational resources as no discretization is performed over the ground surface. Instead, the free-space Green's function corresponding to the model is used to calculate the radiated field. This option is very useful as it removes the edge diffraction problem, allowing to effectively assess other issues, such as the impact of the plate on the AUT free-space radiation resistance, and the AUT diffraction.

4.2 Tested Antennas

Two antennas are used in order to numerically validate the concept: a HWD which was already introduced in Chapter 3 for the synthetic validation, and a biconical antenna which may be considered as a wideband version of the dipole. The choice of adopting these two antennas was motivated by a number of reasons outlined hereafter:

- Both antennas are very simple to design as implementing wires (HWD) and conic sections (bicone) is forward under FEKO. The two antennas are shown in Fig. 4.1a. Both AUTs are designed to operate over a working frequency $f_0 = 1$GHz, the bicone having larger dimensions in order to highlight aspects related to the far-field distance approximation.

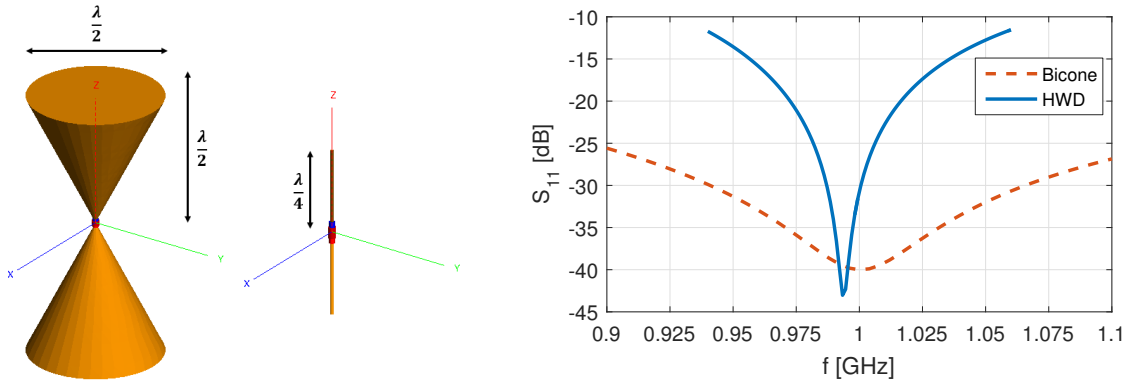

(a) (b)

Figure 4.1 Antennas used for the numerical validation of the proposed concept: (a) AUTs dimensions (b) Corresponding reflections coefficients and operating bandwidths.

- As already mentioned, the HWD is a narrow-band antenna, while the bicone is wideband. Reflection coefficients of the two designed AUTs as function of frequency are shown in Fig. 4.1b. It shows that the bicone is very well adapted over the conventional 20% FBW fixed to characterize wideband antennas [78], whereas the S_{11} corresponding to the HWD is below -15dB over a narrow FBW$=$ 8% and below -10dB over a FBW$=$ 12%. These properties allow to highlight the frequency impact on the free-space radiation pattern as function of the AUT type, and to asses the adopted approach to solve this issue.
- The two antennas have similar omnidirectional radiation patterns which, as function of the AUT orientation, allow verifying aspects related the ARP directivity. Figs. 4.2a and 4.2b show the azimuthal ARP cuts when both AUTs are parallel to the z and x axes respectively, for a voltage excitation of a magnitude equal to 1V.
- Both antennas may exclusively be operated under TM or TE polarization as function of their orientation. As presented in Sec. 3.1.1 for the HWD, TM operation is ensured when the AUT is parallel to $\hat{z}$, and corresponds to an isotropic ARP, while TE operation is ensured when the AUT is parallel to the azimuthal plane, and corresponds to a directive ARP. This allows to study each proposed transverse model separately, without loss of generality.
- Finally, the phase centers of both AUTs are easily located and correspond to the excitation point at the center of each AUT axis. Controlling the phase center position allows to numerically eliminate position errors in order to focus the feasibility study on model related issues.

These advantages allows to highlight various aspects related to the developed models. The basic $20\lambda_0 \times 20\lambda_0$ test zone used in the previous chapter is maintained, with the plate being generally at a distance $d = 10\lambda_0$ from the AUT.

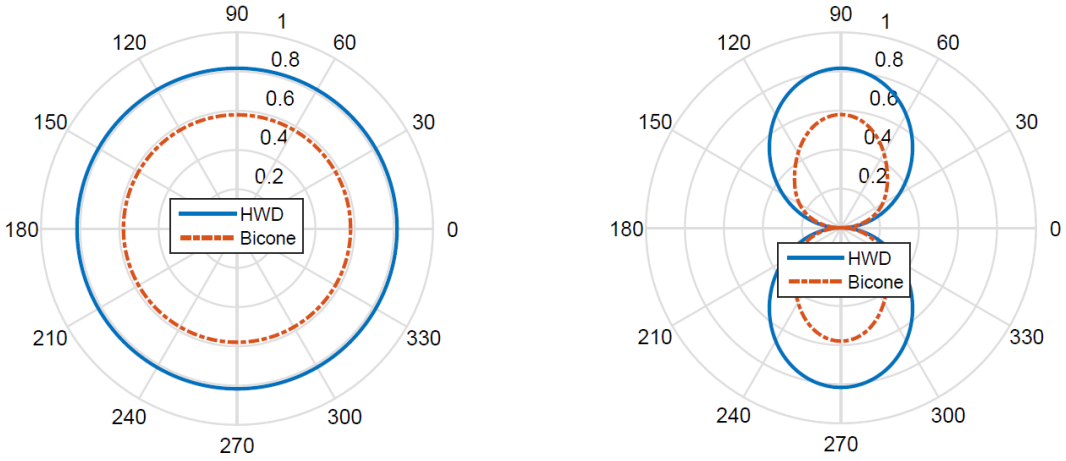

(a) (b)

Figure 4.2 ARP cuts [V] of tested antennas as function of their orientation (a) Isotropic ARP cut, AUT parallel to $\hat{z}$ (b) Directive RP cut, AUT parallel to $\hat{y}$

4.3 Simulation Error Budget

The objective of this section is to assess the different error factors that could affect the simulations and to measure their corresponding impacts. The studied error sources are essentially related to model limitations, namely the far-field model assumption, the impact of the plate on the AUT free-space radiation characteristics, and the AUT diffracted field. This allows, as a first step, to have an estimate of the possible error that could emerge when testing the proposed method using a rather theoretical configuration characterized by an infinite plate. More realistic configurations are then simulated in order to assess the impact of truncating the plate.

4.3.1 Far-Field Distance Assessment

A set of free-space simulations are performed in order to quantify error due to the far-field model assumption as function of the probe position. This allows to locate valid positions with respect to the adopted far-field model before processing the measurement simulation. The viability of the theoretical criterion given by the Fraunhofer distance is also assessed in terms of tested antennas. The Fraunhofer distances corresponding to tested antennas are easily calculated by applying Eq. 1.5, given their dimensions shown in Fig. 4.1a,

$$\begin{aligned} d_{\mathrm{FF}}^{\mathrm{HWD}} &= \frac{\lambda_0}{2}, \\ d_{\mathrm{FF}}^{\mathrm{Bicone}} &= 2\lambda_0. \end{aligned} \tag{4.1}$$

The largest linear dimension of the bicone being the double of that of the dipole, its related Fraunhofer distance is consequently four times larger. Theoretically, based on distances predicted

by Fraunhofer's criterion, the adopted test zone dimensions shall allow the fulfillment of far-field conditions. Error related to the far-field model assumption is quantified by comparing the simulated free-space electric field at each probe position to a field calculated using the far-field expression based on the simulated AUT free-space radiation pattern,

$$\epsilon_{FF} = \frac{\left\| \mathbf{E}_{\text{sim}} - \mathbf{GF}_{\text{sim}} \right\|}{\left\| \mathbf{GF}_{\text{sim}} \right\|}. \tag{4.2}$$

The study is carried for the TM-isotropic and TE-directive cases separately.

4.3.1.1 TM-Isotropic Case

Results for the isotropic case are shown in Fig. 4.3. Error patterns are homogeneous and decay as function of the radial distance from the AUT. This suggests that error due to the far-field model assumption in the considered TM-isotropic scenarios is only function of the AUT-probe separation. Error levels corresponding to the same physical dimensions are higher in the biconical case due to its larger dimensions, which is in a general accordance with the Fraunhofer criterion. However, the exact Fraunhofer distances corresponding to both antennas show large error levels, namely -10dB in the dipole case and -17dB in the bicone case. This highlights the facts that the "actual" far-field distance is function of the operating antenna, and that the Fraunhofer distance may be too approximative for several antenna types. One may notice that error levels are relatively high even at several multiples of the Fraunhofer distance. For instance, the error at $r = 3d_{\text{FF}}$ is around -18dB in the dipole case and -25dB in the bicone case. This is mainly due to the phase error which is considerably high in the vicinity of the AUT.

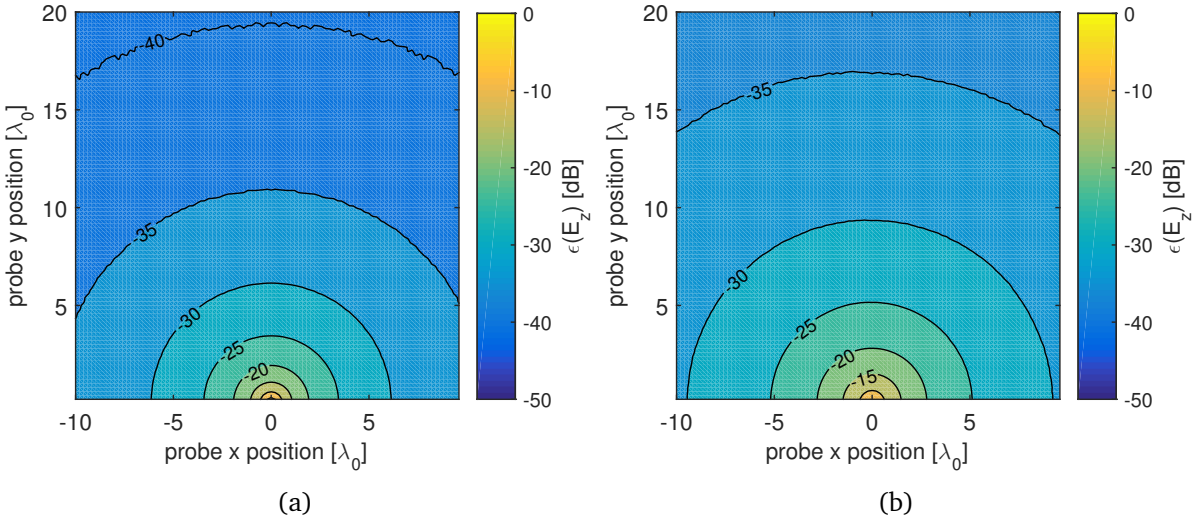

Figure 4.3 Free-space field error [dB] due to the far-field model assumption, TM-isotropic case: (a) $\epsilon(E_z)_{\text{HWD}}$ (b) $\epsilon(E_z)_{\text{bicone}}$

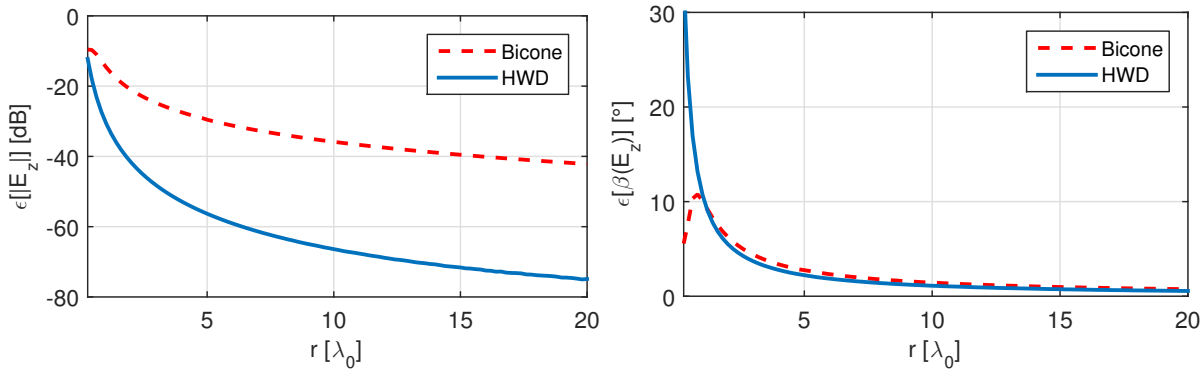

(a) (b)

Figure 4.4 A more detailed figure of the free-space field error due to the far-field model assumption, TM-isotropic case: (a) Relative amplitude error (b) Absolute phase error

A more detailed error figure is shown in Fig. 4.4 where the relative amplitude and absolute phase errors are plotted separately. Fig. 4.4a shows very low amplitude errors especially in the dipole case where it is around -40dB at distances as small as $2\lambda_0$ and around -60dB at $5\lambda_0$. The global error is amplified by the phase error, shown in Fig. 4.4b, which is very high at small distances exceeding 10° at $r = 1\lambda_0$ in the dipole case, and 5° at $r = 2\lambda_0$ in the bicone case. In Chapter 3, it was stated that the proposed method is very sensitive to phase errors which perturb the fields vector sums. The phase error impact was highlighted when studying position errors which modify the phases of both useful fields but mainly the image field. However, this is not the case with error due to the far-field model assumption which is reduced at the image field given the fact that images are by definitions situated at larger distances from measurement points compared to the AUT. Consequently, positions with tolerable LOS phase error would result with a moderate global amplitude error. By recalling that most applications are concerned with the antenna amplitude radiation pattern, the resulting global phase error would not be a serious issue. Taking these considerations into account, we may consider the distance$r = 4d_{\mathrm{FF}}$ as a reliable far-field distance for both tested antennas in the TM mode.

4.3.1.2 TE-Directive case

Before assessing error at the measurable cartesian E_x and E_y field components, it is convenient to have knowledge about their corresponding cartesian radiation patterns. The latter are easily retrieved from the TE azimuthal ARP component F_ϕ through the base change operator presented in Sec 2.2.3. Fig. 4.5 show the cartesian ARP components corresponding to the reference TE orientation (AUT axis parallel to $\hat{x}$). Both patterns are directive with F_x containing a single lob in each half-plane with nulls pointing towards $\phi = 0^\circ$ and $\phi = 180^\circ$, whereas F_y contains two

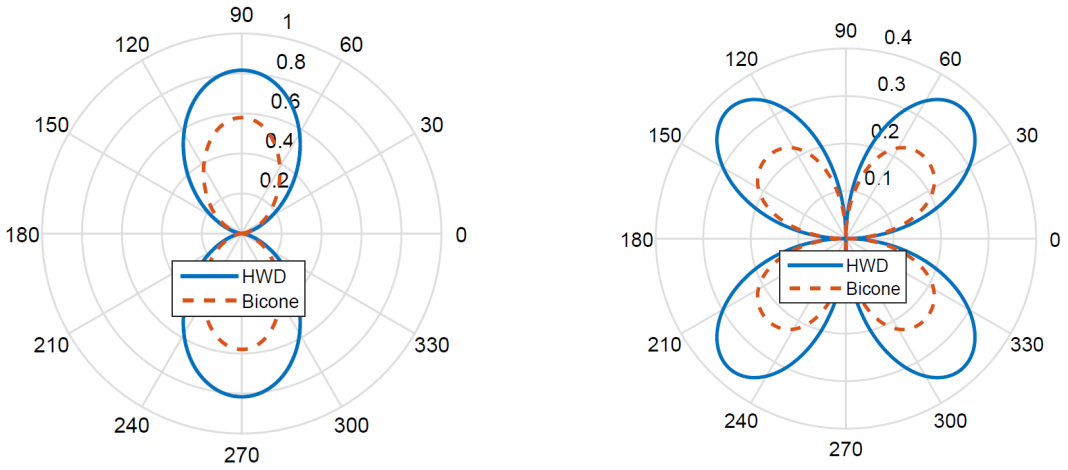

(a) (b)

Figure 4.5 Free space Cartesian ARPs of TE operated AUTs [V]: (a) F_x (b) F_y

lobes in each half-plane and two additional nulls pointing towards $\phi = 90°$ and $\phi = 270°$. E_x is the dominant component for both AUTs.

Corresponding error patterns are plotted in Fig. 4.6. As one would expect, error generally decays as function of the radial AUT-probe separation, and is more important in the bicone case due to its larger dimensions. However, unlike the TM-isotropic case, error dramatically grows in directions of weak power emission and totally explodes towards the nulls. This is in agreement with observations carried in Sec. 3.3.1 when studying the model limitation due to the far-field model assumption using a Hertzian dipole. Considering the similar radiation characteristics of the tested antennas which may be modeled as a superposition of a large number of Hertzian dipoles, error amplification in directions of weak emission is logically explained by the contribution of the field radial component which is ignored in the far-field model. Consequently, even larger distances would be required in order to reduce error due to the far-field model assumption in these directions, which may be unpractical. Furthermore, recalling the studies conducted in the previous chapter in order to assess the different error sources, and which predicted a common important impact in directions of weak power emission, we would expect that the global ARP error in these directions would be very large in the intended simulations. Otherwise, error levels seem tolerable at the chosen reliable far-field distance ($r = 4d_{\mathrm{FF}}$) attaining values below -30dB in the lobes' directions for both AUTs in the dominant E_x component. Directions of very weak power emission may be considered as singular directions and related ARP results may be improved using linear regression.

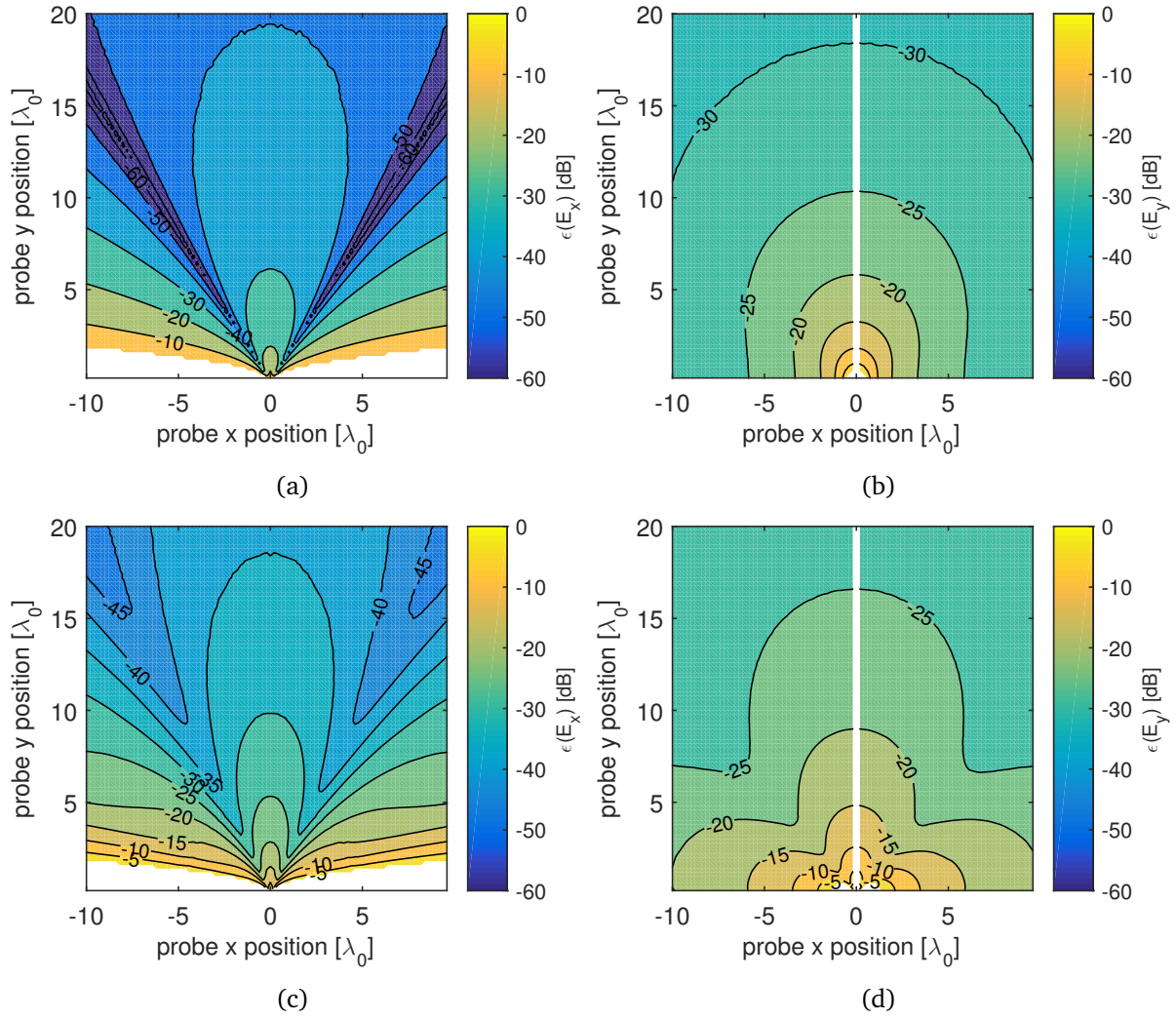

Figure 4.6 Free space field error [dB] due to the far-field model assumption, TE-directive case: (a) $\epsilon(E_x)_{\text{HWD}}$ (b) $\epsilon(E_y)_{\text{HWD}}$ (c) $\epsilon(E_x)_{\text{bicone}}$ (d) $\epsilon(E_y)_{\text{bicone}}$

4.3.2 Impact of the plate on the AUT Free Space Radiation Resistance

The impact of the plate on the AUT free-space radiation resistance is verified by comparing the return loss in the presence of an infinite PEC ground with the free-space return loss. Results are plotted in Fig. 4.7 for various AUT-plate separations. The impact is most notable for the smallest assessed distance $d = 2\lambda_0$, which, in the HWD case, moves the resonance frequency closer to 1GHz without really changing the return loss pattern. The impact on the return loss pattern is more important in the bicone case where the resonance around the reference frequency $f_0 = 1$GHz disappears. However, the AUT remains well adapted over the studied 20% FBW ($S_{11} < -20$dB). For AUT-plate separations greater than $d = 2\lambda_0$, the impact of

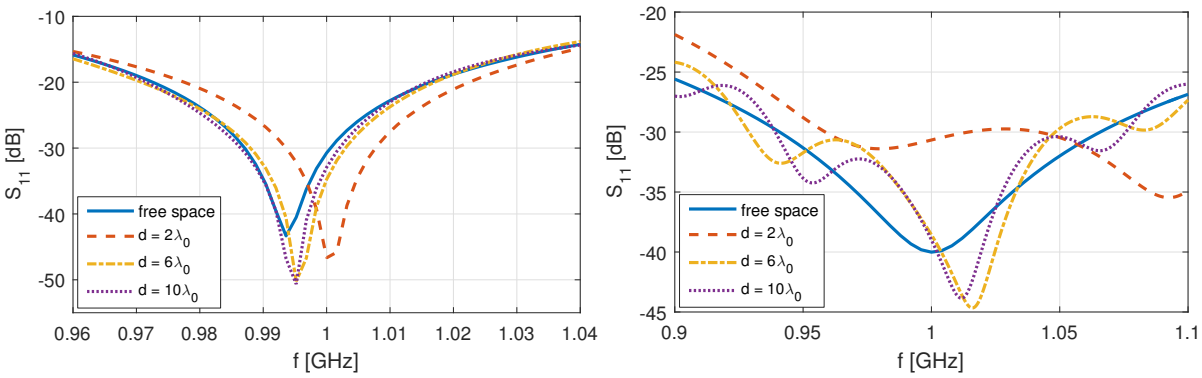

Figure 4.7 Impact of the AUT-plate separation on the AUT return loss: (a) HWD (b) Bicone.

the plate on both the return loss shape and levels becomes very weak. This is in accordance with the study conducted in Sec.3.3.2 where we derived a theoretical expression based on Friis formula suggesting a very weak impact of the plate on the AUT radiation resistance for AUT-plate separations greater than $d = 2\lambda_0$. This may further be verified by comparing the radiated power in the presence of the plate to the free-space radiated power. Assuming equal excitations in both cases, this is expressed as follows for the reference working frequency f_0:

$$\frac{P_r^{'}(f_0)}{P_r(f_0)} = \frac{1-|\Gamma'|^2}{1-|\Gamma|^2}, \tag{4.3}$$

where the prime stands for the case characterized by the presence of the plate. Fig. 4.8 shows the relative power error as function of the AUT-plate separation. Error being below 0.1% for AUT-plate separations equal or greater than $d = 2\lambda_0$, the impact of the plate on the AUT free-space radiation resistance in the simulated configurations may be neglected.

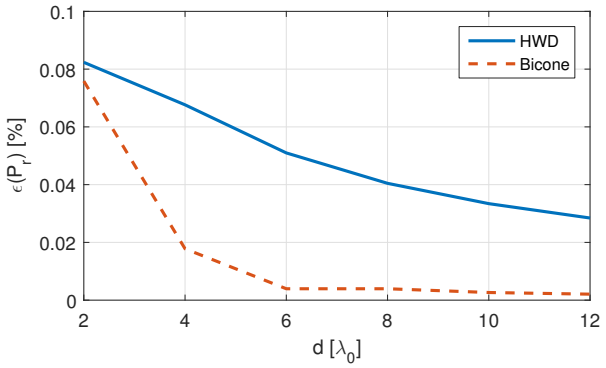

Figure 4.8 Relative power error with respect to the free-space radiated power as function of the AUT-plate separation.

4.3.3 Impact of the AUT-diffraction on the Image Model

Simulating the concept using an infinite plate allows to effectively verify the impact of the AUT diffraction on the image model. In this case, the AUT diffracted field is the only spurious field interfering with the useful LOS and image fields.

Before assessing the levels of the AUTs diffractions, it is convenient to have an idea about the RCS's of tested antennas. Fig. 4.9 plots azimuthal cuts of the simulated RCS's using a plane wave linearly polarized parallel to the AUTs axes, which may model both transverse modes. The figure shows relatively low RCS's levels, being below $0.4\lambda_0^2$ in the bicone case, and around $0.85\lambda_0^2$ in the dipole case whose RCS over the working azimuthal plane is isotropic, and which may be approximated as a Rayleigh diffraction as the cross section of the wire elements forming the dipole is very small with respect to the wavelength (radius= $\lambda_0/225$). Recalling the theoretical study conducted in Sec. 3.3.3 and the order of tested RCS' s, we would expect a low impact of the AUT diffraction for both AUTs.

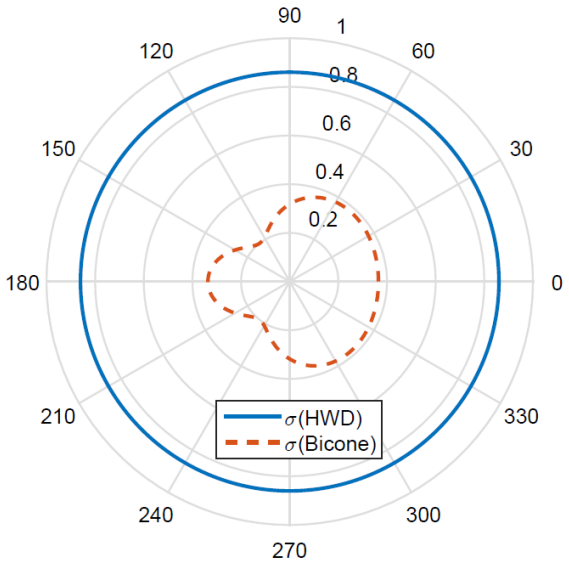

Figure 4.9 Azimuthal cuts of the simulated RCS's $[\lambda_0^2]$ of tested antennas using a plane wave linearly polarized parallel to the AUTs axes

The simulated AUT-diffracted field is retrieved by subtracting from the field in the presence of the infinite plate the sum of the simulated free-space fields of the AUT in its original position and the AUT at the image position,

$$\mathbf{E}_d^{AUT} = \left\| \mathbf{E}_{\text{sim}}^{h\infty} - \mathbf{E}_{\text{sim}}^{\text{LOS+im}} \right\|, \tag{4.4}$$
$$\text{with } \mathbf{E}_{\text{sim}}^{\text{LOS+im}} = \mathbf{E}_{\text{sim}}^{\text{LOS}} + \mathbf{E}_{\text{sim}}^{\text{im}}$$

where $\mathbf{E}_{sim}^{h\infty}$ is the simulated field in the presence of the infinite plate, and $\mathbf{E}_{sim}^{\text{LOS}}$ and $\mathbf{E}_{sim}^{\text{im}}$ are the simulated useful LOS and image fields retrieved via separate free-space simulations. The AUT feed orientation is reversed when the AUT is placed at the image position in the TM mode and when oriented parallel to $\hat{y}$ in the TE mode, and kept unchanged when using the reference TE mode orientation ($//\hat{x}$) in order to obey boundary conditions implied by the plate. The impact of the AUT diffracted field is then measured by comparing its intensity to the intensity of each simulated useful field,

$$\epsilon_i^d = \left\| \frac{\mathbf{E}_d^{AUT}}{\mathbf{E}_i} \right\|^2, \quad i = 0, 1, \tag{4.5}$$

the index 0 standing for the LOS case and the index 1 standing for the image case. Results are shown in Figs. 4.10 and 4.11 using the basic test zone characterized by an AUT-plate separation $d = 10\lambda_0$. Fig. 4.10 compares error levels of both AUTs operated in TM mode. One may notice an excellent agreement between the error patterns of Fig. 4.10 and SNR patterns generated in the theoretical study conducted in Sec. 3.3.3 where we assumed isotropic radiation and scattering characteristics of the tested antenna. This agreement is especially close in the dipole case which has both an isotropic ARP and an isotropic RCS over the working azimuthal plane. As predicted by the developed analytical formula, the diffracted field is essentially made up by the contribution of two components; the LOS diffraction and the reflected diffraction by the plate. These two components interfere constructively and destructively defining sets of locally optimal and worst positions in terms of the AUT diffraction in forms of hyperbolas, as shown in Fig. 4.10. Moreover, the level of error is defined by the same set of circles which define conditioning levels, resulting in optimal positions with respect to the AUT diffraction being pushed away from the AUT and closer to the plate. This may be clearly noticed in Fig. 4.10b which plots error with respect to the image field in the dipole case, and shows that the region in the vicinity of the plate is dominated by a low error level (< -40dB) unlike the remaining regions where error oscillates between low and relatively higher levels described by the mentioned hyperbolas. However, error is generally quite low given the testing parameters, which are characterized by a low RCS level, and a sufficiently large AUT-plate separation. This is true except for the region surrounding the AUT at the image field level where the AUT diffracted field becomes comparable to the image field. Consequently, we would expect image samples to undergo large error in this region. The impact of the AUT diffraction is about 5dB-10dB higher in the dipole case with respect to the bicone case due to its larger RCS.

The dipole is used in order quantify the impact of the AUT diffraction in the TE mode. Results are shown in Fig. 4.11 using two orientations. Figs 4.11a and 4.11b show error over the $\mathbf{E}_x$ component using the reference AUT orientation which is the optimal orientation in terms of the AUT diffraction as the null is directed towards the plate. The LOS error is extremely weak being below -70dB allover the test zone. The image error is generally very weak as well, except

in the immediate region surrounding the AUT where it exceeds −20dB. If the AUT is oriented otherwise, error levels generally increase over both the LOS and image fields. The same can be seen in Figs 4.11c-4.11f where error over both TE components is plotted with the AUT being oriented parallel to $\hat{y}$. Error is generally tolerable in directions of strong power emission (around −40dB), but dramatically grows in directions of weak power emission and totally explodes near the nulls. These results highlight again the vulnerability of positions corresponding to weak power emission to model systematic errors.

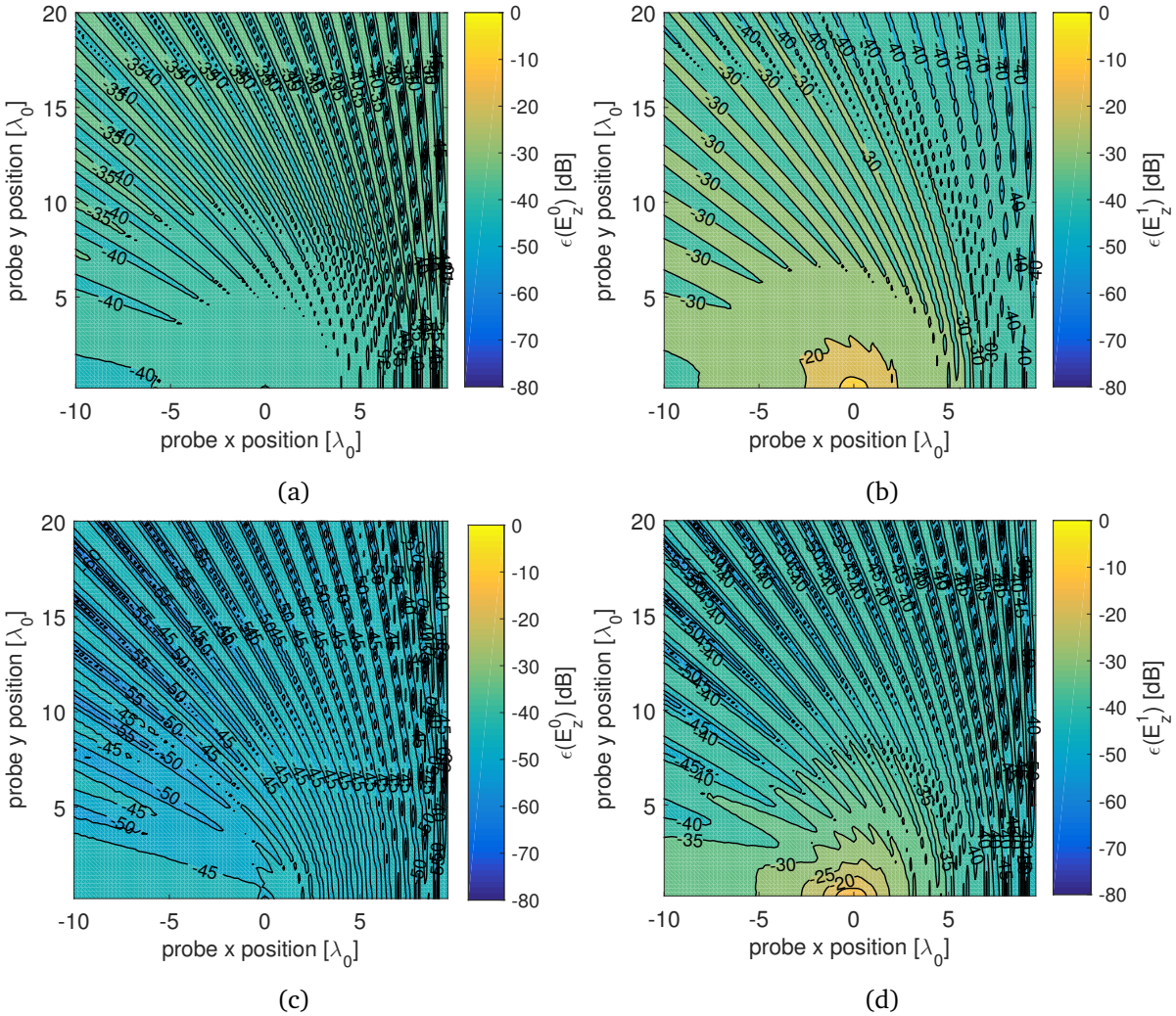

Figure 4.10 Field error as function of the probe position and impact of the AUT-diffracted field. TM mode, plate at $x_p = 10\lambda_0$: (a) Impact on the LOS field, HWD (b) Impact on the image field, HWD (c) Impact on the LOS field, bicone (d) Impact on the image field, bicone.

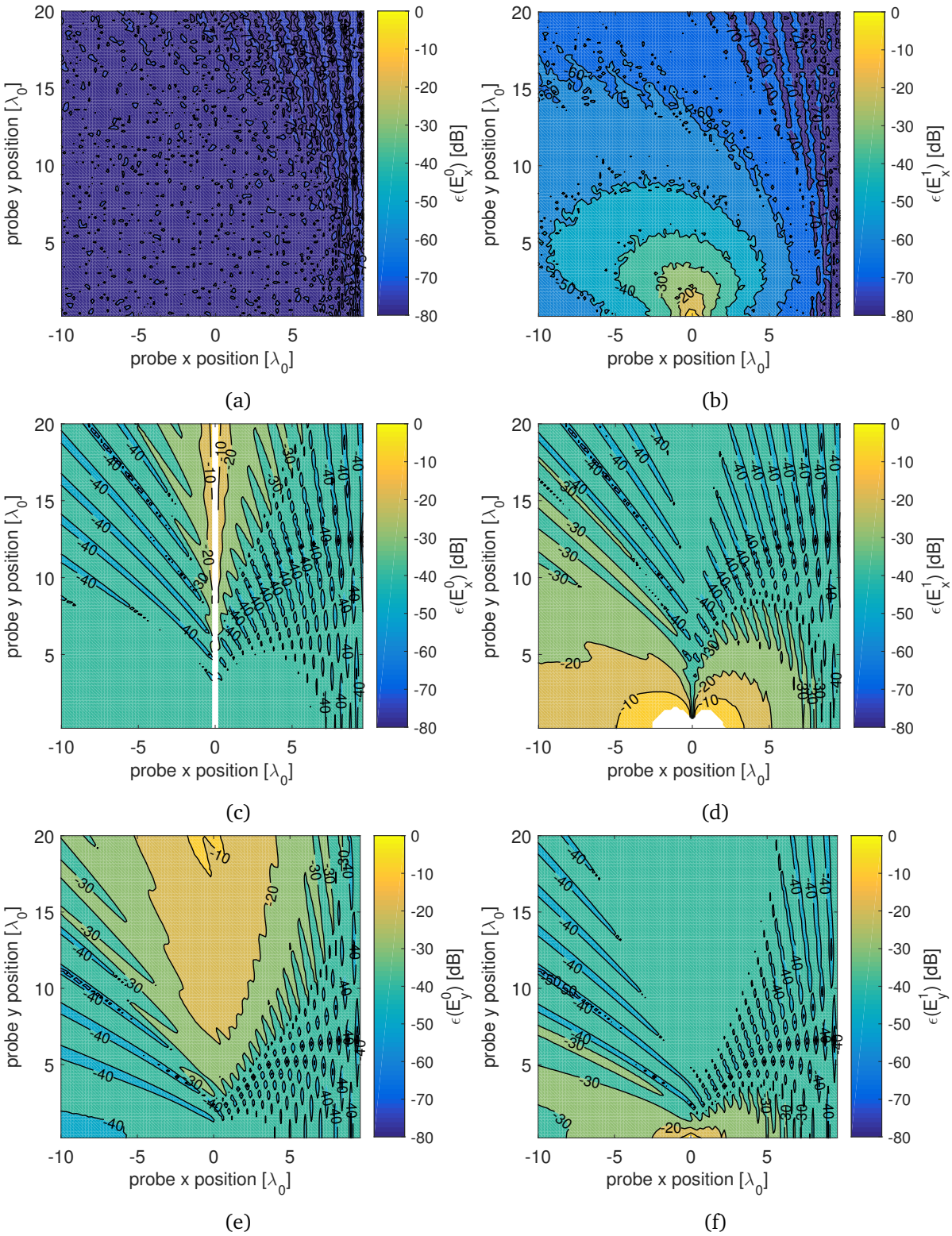

Figure 4.11 Field error as function of the probe position and impact of the AUT-diffracted field as function of the AUT orientation using a HWD in TE mode, plate at $x_p = 10\lambda_0$: (a) Impact on the LOS field, $\mathbf{E}_x$, HWD $//\hat{x}$ (b) Impact on the image field, $\mathbf{E}_x$, HWD $//\hat{x}$ (c) Impact on the LOS field, $\mathbf{E}_x$, HWD $//\hat{y}$ (d) Impact on the image field, $\mathbf{E}_x$, HWD $//\hat{y}$ (e) Impact on the LOS field, $\mathbf{E}_y$, HWD $//\hat{y}$ (f) Impact on the image field, $\mathbf{E}_y$, HWD $//\hat{y}$.

Generally, we may conclude that the impact the AUT diffracted field in terms of tested antennas is very low for positions relatively far from the AUT, except for positions corresponding to weak power emission.

4.3.4 Combining Error Impacts

Taking into account observations carried in what preceded, we may outline the following conclusions regarding the infinite plate scenario:

- The impact of the plate on the AUT free-space radiation characteristics may be neglected for both antennas given the adopted test zone dimensions.
- Positions in the vicinity of the AUT show large error levels over both the LOS and image fields. The LOS error is due to the non-validity of the far-field model assumption for distances in the order of the Fraunhofer distance corresponding to each AUT. Whereas the image error is due to the impact of the AUT-diffracted field whose level is comparable to the image field level near the AUT.
- As function of the AUT orientation, positions corresponding to low-power emission show very large error levels. This large error is due to the superposition of the contributions of reactive fields, the radial field component, and the AUT diffracted field which are not taken into account in the mathematical models and whose levels become even larger than the reference field level near the ARP nulls. The impact of this error is minimized at the calculated ARP level by introducing linear regression.

These remarks are highlighted by verifying the overall error impact of the infinite plate scenario, which is performed by comparing the simulated field in the presence of the infinite plate to the sum of the useful fields calculated using the proposed model. Results are plotted in Fig. 4.12 for the three Cartesian field components. Figs. 4.12a and 4.12b show relatively low error levels (around -30dB) in the TM-isotropic case for positions respecting the chosen reliable far-field distance ($r = 4d_{\mathrm{FF}}$). Error corresponding to the HWD is very low over the majority of the test zone, oscillating between -50dB and -60dB for AUT-probe separations larger than $10\lambda_0$. Figs. 4.12c-4.12d plot results corresponding to the reference TE orientation showing large error in directions of weak power emission. For instance, error over the dominant E_x component is very high (< 20dB) over a $25°$ range starting from each half x-axis. Otherwise, the accordance between the simulation and the model is is very good with error oscillating between -40dB and -50dB over the E_x component and around -30dB over the E_y component.

Accordingly, the proposed method shall perform well in positions respecting the chosen reliable far-field distance, with results corresponding to *singular* directions of low-power emission to be improved using linear regression. However, it is important to keep in mind that the final ARP error is also function of conditioning which, as function of the probe position, may further

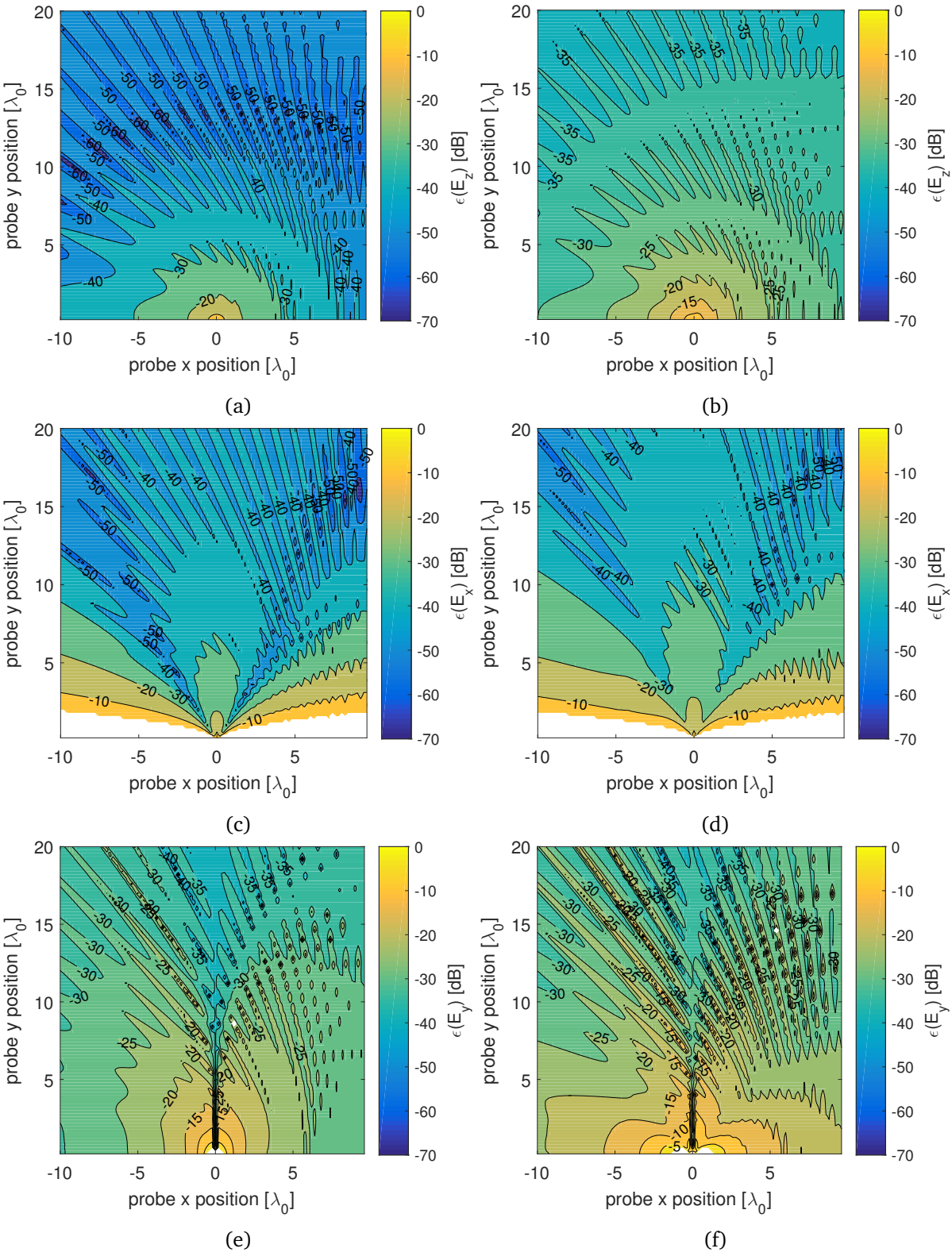

Figure 4.12 Estimation of the overall error perturbing the infinite plate scenario by comparing the simulated field in the presence of infinite plate to the field calculated using the proposed model, $x_p = 10\lambda_0$: (a) $\epsilon(E_z)_{HWD}\ [dB]$ (b) $\epsilon(E_z)_{bicone}\ [dB]$ (c) $\epsilon(E_x)_{HWD}\ [dB]$ (d) $\epsilon(E_x)_{bicone}\ [dB]$ (e) $\epsilon(E_y)_{HWD}\ [dB]$ (f) $\epsilon(E_y)_{bicone}\ [dB]$

amplify the highlighted error. Moreover, the validity of the results in the TM case depend on the accuracy of estimating the ARP frequency dependence.

4.4 Infinite Plate Scenario

The proposed method is tested in a hypothetical noise free environment using an infinite PEC ground. It should be noted that FEKO allows the generation of infinite PEC grounds only over the $z = 0$ plane. Consequently, proper frame transformation is applied in order to resolve fields characteristics in the working reference frame. The impact of frequency diversity, necessary for the application of the TM model, is first estimated before proceeding with the inversion.

4.4.1 α Estimation

The α-term corresponding to each working UFBW is estimated using the approach developed in Sec. 3.4.3. RBF regression with $N_b = 5$ and $s = 36°$ is applied to data collected from three measurements performed by moving the probe: $x = -9\lambda_0, -2\lambda_0, 5\lambda_0$; the vertical distance y being varied as well in order to assess the impact of error due to the far field model assumption on the estimation. Fig. 4.13 show examples of the minimization of the cost function by spanning the space of solutions in a TM-isotropic scenario for both tested AUTs (UFBW= 4%). It clearly shows that the HWD is more impacted by the frequency change compared to the bicone, whose corresponding α is closer to unity.

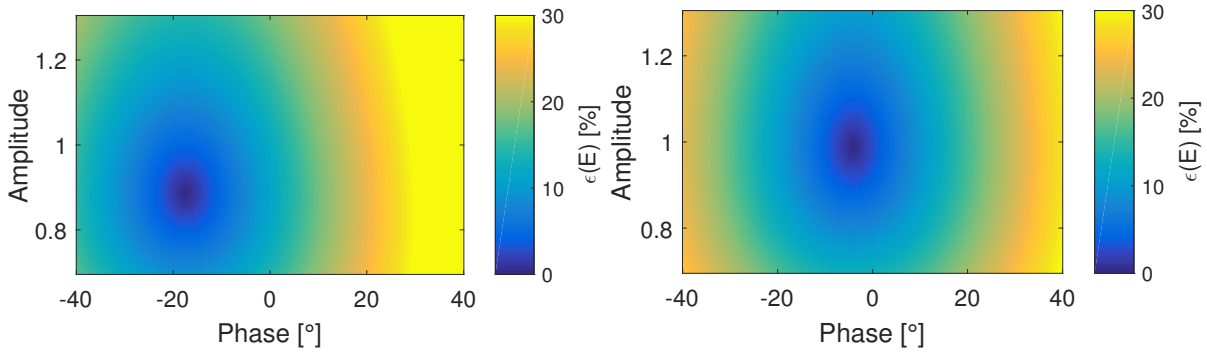

(a) (b)

Figure 4.13 Example of the estimation of α using RBF regression with $N_b = 5$ and $s = 36°$ over 3 probe positions, $(x, y) = (-9\lambda_0 : 7\lambda_0 : 5\lambda_0, 20\lambda_0)$. TM-isotropic case, UFBW= 4%: (a) HWD (b) Bicone.

Detailed results are shown in Table 4.1 highlighting the higher sensitivity of the HWD to frequency diversity compared to the bicone which is mainly affected over the field phase. Results are generally stable in terms of the AUT-probe separation except in the bicone case at larger UFBWs than 6%, where the closest set of probes to the AUT show a phase error of 0.5° compared

		y $[\lambda_0]$		
	UFBW	5	10	20
HWD	1%	$0.99e^{-j5.6^\circ}$	$0.99e^{-j5.5^\circ}$	$0.99e^{-j5.5^\circ}$
	2%	$0.95e^{-j10.7^\circ}$	$0.96e^{-j10.6^\circ}$	$0.96e^{-j10.6^\circ}$
	3%	$0.91e^{-j14.3^\circ}$	$0.92e^{-j14.3^\circ}$	$0.92e^{-j14.3^\circ}$
	4%	$0.89e^{-j17.1^\circ}$	$0.89e^{-j17.2^\circ}$	$0.89e^{-j17.1^\circ}$
	6%	$0.85e^{-j24.1^\circ}$	$0.84e^{-j24.1^\circ}$	$0.84e^{-j24.1^\circ}$
Bicone	1%	$1e^{-j0.8^\circ}$	$1e^{-j0.8^\circ}$	$1e^{-j0.7^\circ}$
	2%	$1e^{-j1.8^\circ}$	$1e^{-j1.8^\circ}$	$1.01e^{-j1.8^\circ}$
	4%	$0.99e^{-j3.7^\circ}$	$0.99e^{-j3.7^\circ}$	$0.99e^{-j3.8^\circ}$
	6%	$0.99e^{-j4.6^\circ}$	$0.98e^{-j4.9^\circ}$	$0.99e^{-j4.8^\circ}$
	8%	$0.98e^{-j6.7^\circ}$	$0.97e^{-j7.2^\circ}$	$0.98e^{-j7.0^\circ}$

Table 4.1 Estimating α corresponding to the simulated field as function of the operating UFBW and the AUT-probe vertical separation.

to the further sets, which is due to the fact that far-field conditions are not conveniently met at such distances from the AUT ($< 8\lambda_0$) in the bicone case. Results corresponding to the most distant set ($y = 20\lambda_0$) will be considered in the calculations.

4.4.2 Performing the Inversion

TM and TE models are tested separately. In both cases the reference radiation pattern is retrieved via free-space simulation. The calculated ARP samples are then locally compared to the reference ARP values in order to estimate the ARP error.

4.4.2.1 TM-Isotropic Case

Both AUTs are first tested using an UFBW= 4% with adapted α values shown in Table. 4.1. The corresponding condition number pattern over the basic test zone was already presented in Chapter 2 and 3 (Figs 2.5 and Fig. 3.3a), and is characterized by a good distribution of low values over the majority of the test zone except in the singular regions around the AUT and near the plate. ARP error patterns of the LOS and image samples as function of the probe position are shown in Fig. 4.14. In this figure both the amplitude and phase errors are taken into account,

$$\epsilon_F = \frac{\left\|\mathbf{F}_{\text{model}} - \mathbf{F}_{\text{ref}}\right\|}{\left\|\mathbf{F}_{\text{ref}}\right\|}. \tag{4.6}$$

Taking into account the conditioning impact, which is amplifying error near the AUT and the plate for both LOS and image samples, results are in accordance with observations carried in the previous section. As shown in the figure, the LOS error is directly related to the AUT

dimensions, being higher in the bicone case than in the dipole case. Levels below −40dB in the optimal conditioned region are achievable at distances higher than $7\lambda_0$ in the dipole case which is about 14 times the corresponding Fraunhofer distance, and at distances larger than $14\lambda_0$ in the bicone case which is about 7 times the corresponding Fraunhofer distance. The image error is higher than the LOS error in the dipole case due to the impact of the AUT diffraction, oscillating between −35dB and −40dB in the optimal conditioned region. This is not the case with the bicone whose corresponding AUT diffraction is very weak. Consequently, image error is lower than the LOS error given the fact that image samples are more protected against error due to the far-field model assumption than LOS samples.

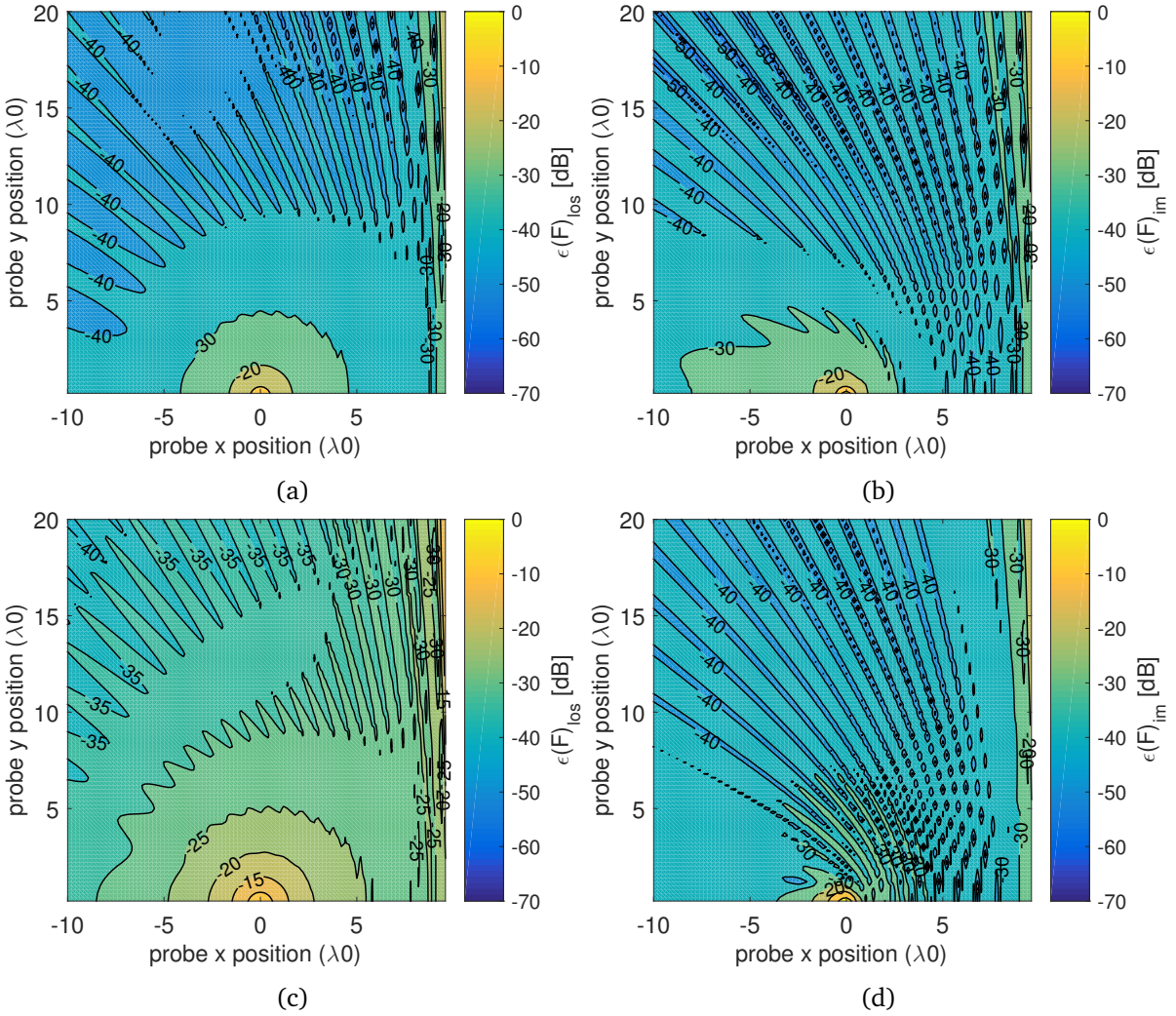

Figure 4.14 ARP error as function of the probe position in a hypothetical scenario characterized by an infinite PEC plate. TM case, $x_p = 10\lambda_0$, UFBW= 4%: (a) LOS error, HWD (b) Image error, HWD (c) LOS error, bicone (d) Image error, bicone.

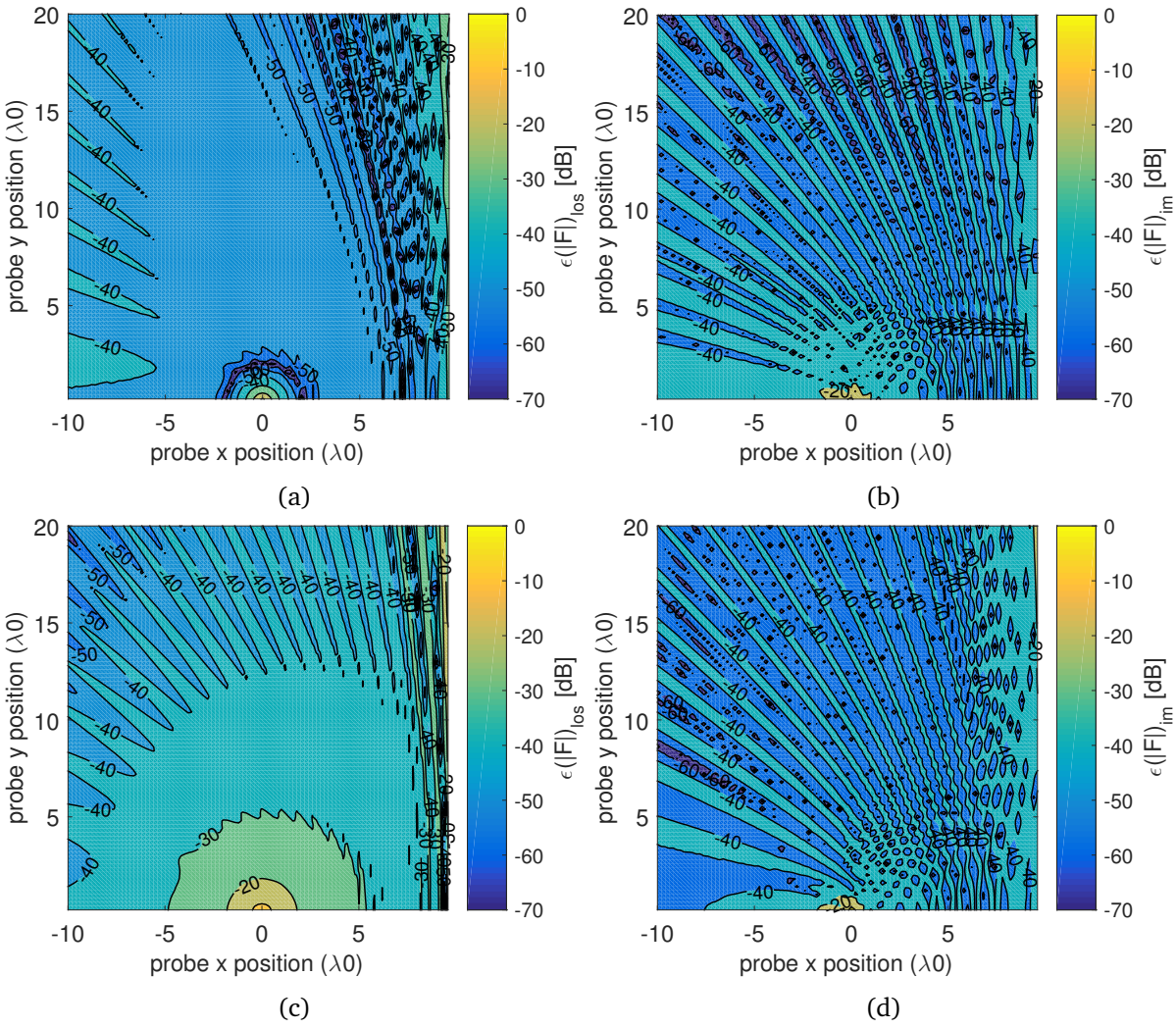

Figure 4.15 ARP amplitude error as function of the probe position in a hypothetical scenario (infinite PEC plate). TM case, $x_p = 10\lambda_0$, UFBW= 4%: (a) LOS error, HWD (b) Image error, HWD (c) LOS error, bicone (d) Image error, bicone.

Globally, we may conclude that the method performs well in optimal conditioned regions if the configuration parameters are carefully chosen in order to reduce the overall system error, as practical systematic errors combined with the edge diffraction may dramatically amplify the measurement error.

The considered results also highlight the ability of the proposed method to measure the ARP phase in addition to the amplitude. By considering exclusively amplitude radiation patterns, which are the most relevant for most applications, interest will be on the relative amplitude error calculated using Eq. 3.1. Results for the relative amplitude error for the same configurations are plotted in Fig. 4.15. Error is considerably reduced by omitting the phase error contribution, attaining levels below −40dB over the majority of the test zone in the dipole case, and enlarging

the useful LOS region up to half of the test zone in the bicone LOS case. These results further highlight the feasibility of the proposed method in retrieving ARP values with satisfying precision provided that the system parameters are well adapted to the measurement conditions. Let us for instance assess the impact of conditioning on the ARP results given the considered low-noise environment. In the previous example, the impact of conditioning was limited to narrow regions near the AUT and the plate because the chosen working bandwidth together with the AUT-plate separation were such that the optimal hyperbola crosses the test zone diagonally. Accordingly, the optimal conditioned region was well distributed over the test zone. This would not be the case if other d-UFBW pairs are used. For instance, if a narrower UFBW is used, as discussed in Sec. 2.3.2, this may prevent the existence of optimal hyperbolas, which would limit the region of tolerable condition numbers away from the plate, and thus would require larger set-up dimensions. In the contrary, if a wider UFBW is used, this would lead to the generation of worse conditioning hyperbolas, near which the condition number explode, and which are then positions to avoid. These considerations are shown in Fig. 4.16 where the relative amplitude error is plotted for a couple of UFBWs. In this figure, the amplitude error is averaged between the LOS and image samples in order to provide a general insight on the conditioning impact,

$$\epsilon_F = \frac{\epsilon_{F_{los}} + \epsilon_{F_{im}}}{2}. \tag{4.7}$$

Figs. 4.16a and 4.16b show results when applying a UFBW= 1%. In this case, the ill-conditioned region near the plate is enlarged up to almost half of the test zone with error levels being generally above −30dB. This would be disadvantageous in a complete measurement context by recalling that the region near the plate is by definition the optimal conditioned region for the basic TE model. Figs. 4.16c and 4.16d show results when applying an UFBW = 8%. In this case two optimal hyperbolas exist generating two optimal regions near and far from the plate where error is generally below −40dB, and between which a worst hyperbola yields an ill-conditioned region where error is amplified up to levels as high as −3dB. Augmenting the UFBW is advantageous in enlarging the optimal region near the plate, but may be disadvantageous if probe displacements are to be performed due to the existence of quite large ill-conditioned regions within the test zone. These results highlight the importance of well setting the measurement parameters in terms of set-up dimensions, the working UFBW, and probe positions as more realistic configurations are characterized by a larger error level which would be otherwise amplified to unaccepted levels.

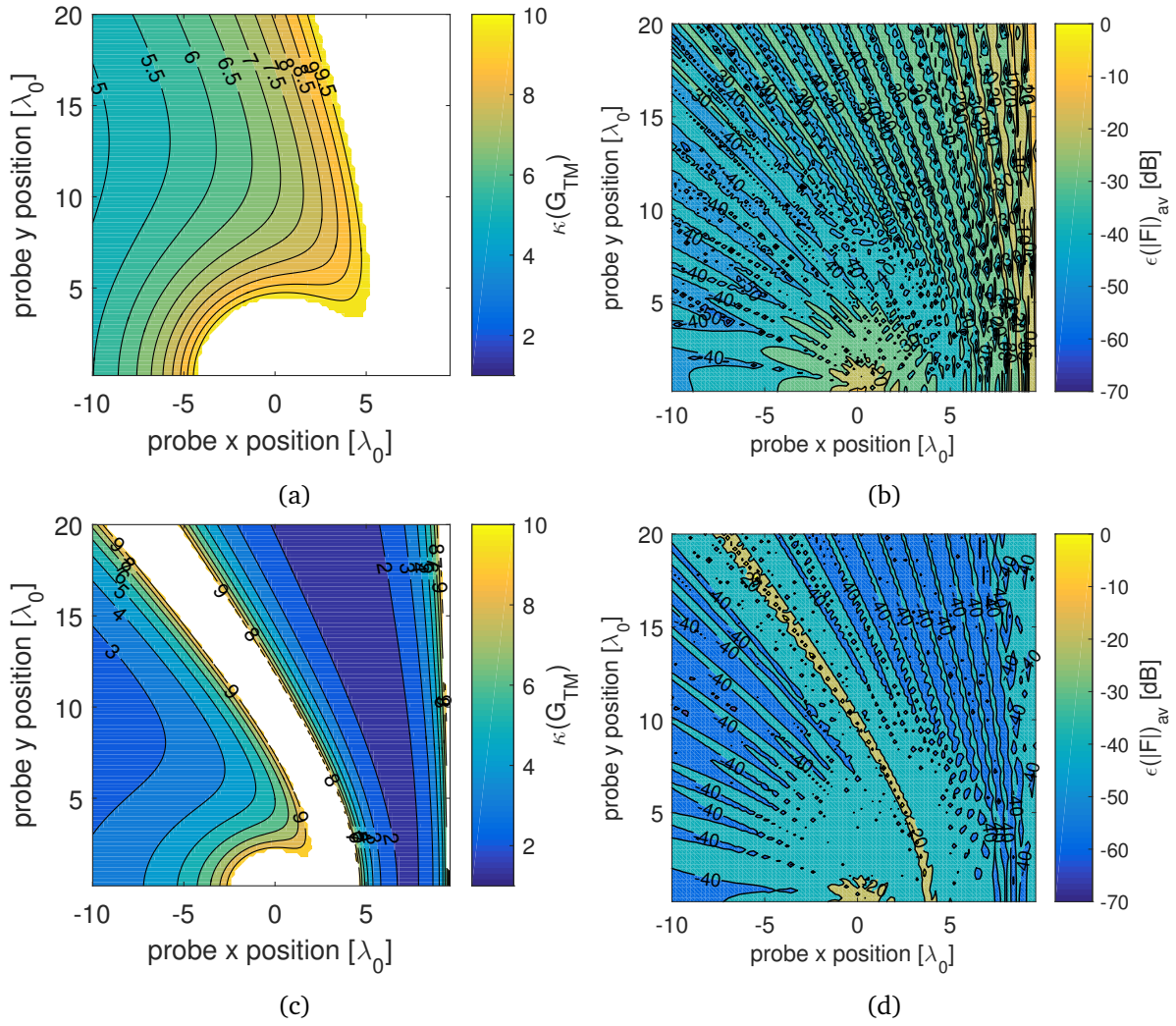

Figure 4.16 ARP amplitude error as function of the probe position for different UFBWs impacting the global conditioning pattern. Hypothetical scenario (infinite PEC plate), bicone, TM case, $x_p = 10\lambda_0$: (a) $\kappa(\mathbf{G}_{TM})$, UFBW= 1% (b) Average amplitude error, UFBW= 1% (c) $\kappa(\mathbf{G}_{TM})$, UFBW= 8% (d) Average amplitude error, UFBW= 8%.

4.4.2.2 TE-Directive case

The condition number pattern over the test zone for the basic TE case was already introduced in Chapters 2 and 3 (Figs. 2.11 and 3.3b), and is characterized by an optimal region situated near the upper right corner around the optimal position which is near the plate at a vertical distance $y_{opt} = d = 10\lambda_0$. Otherwise, the condition number augments far from the plate and explode at low vertical AUT-probe separations. The latter ill-conditioned region corresponds to the singular directions of low-power emission of the reference TE orientation. Accordingly, the highlighted large error in this region is further amplified by conditioning in this case. The same can be seen in Figs. 4.17a-4.17d where the LOS and image amplitude errors are plotted for

both tested antennas as function of the probe position. The impact of conditioning is clearer at the image level where error undergoes more amplification in the left half of the test zone. LOS samples away from the nulls are generally calculated with satisfying precision, < -40dB in the dipole case and < -30dB in the bicone case. Error is more important over image samples, being tolerated almost exclusively in sections of the optimal conditioned region pointed out by the lobe. This may be clearly seen in Figs 4.17e and 4.17f where the bicone is rotated with $\phi_o = -45°$ with respect to the reference orientation such that the ARP lobe is oriented towards the optimal region. In this case, error over both LOS and image samples in the optimal conditioned region is below -40dB, with directions corresponding to weak power emission being always characterized by large error levels (< -20dB). These results highlight two limitations of the direct inversion method. The first being exclusively related to the basic TE model, which is the fact that optimal conditioned positions are located in a limited region near the plate. Whereas the second is a general limitation of the proposed model which is the vulnerability of positions corresponding to weak power emission to different sorts of error sources.

The limitation of the basic TE model with respect to conditioning may be overcome by introducing frequency diversity which, as function of chosen parameters, allows the generation of optimal positions in different regions of the test zone. As discussed in Chapter 2, this would allow the generation of common optimal positions for both transverse models which would be advantageous in reducing mechanical displacement and thus the measurement time. Moreover, introducing frequency diversity has an additional advantage of improving the overall ARP results, which is a consequence of the over-determination of the problem which yields the application of an error averaging through regression by the LS solving algorithm. An example of the advantages carried by introducing frequency diversity to the TE model is shown in Fig. 4.18 where two frequencies are applied with a UFBW $= 3\%$ using the HWD in the reference TE orientation. Fig. 4.18a plots the corresponding condition number pattern which is characterized by a larger optimal region with respect to the basic TE model, which is induced by the generated optimal hyperbola. In this example, a relatively narrow UFBW is applied such that the generated optimal hyperbola is directed far from the plate in order to effectively extend the optimal region over the test zone. Consequently, ill-conditioned positions are limited over narrow regions around the AUT and near the bottom right corner. Corresponding error patterns are plotted in Figs. 4.18b and 4.18c showing generally very low error levels. The LOS error is below -40dB almost all-over the test zone except in the mentioned narrow ill-conditioned regions. One can see how frequency diversity effectively reduced the ARP error even in positions corresponding to singular directions of weak power emission. Image error is relatively higher but widely improved with respect to the basic TE model, oscillating between values below -30dB and -50dB outside the ill-conditioned regions. These results highlight the advantage carried by frequency diversity in overcoming the limitation of the basic TE conditioning model, and in improving results corresponding to weak power emission.

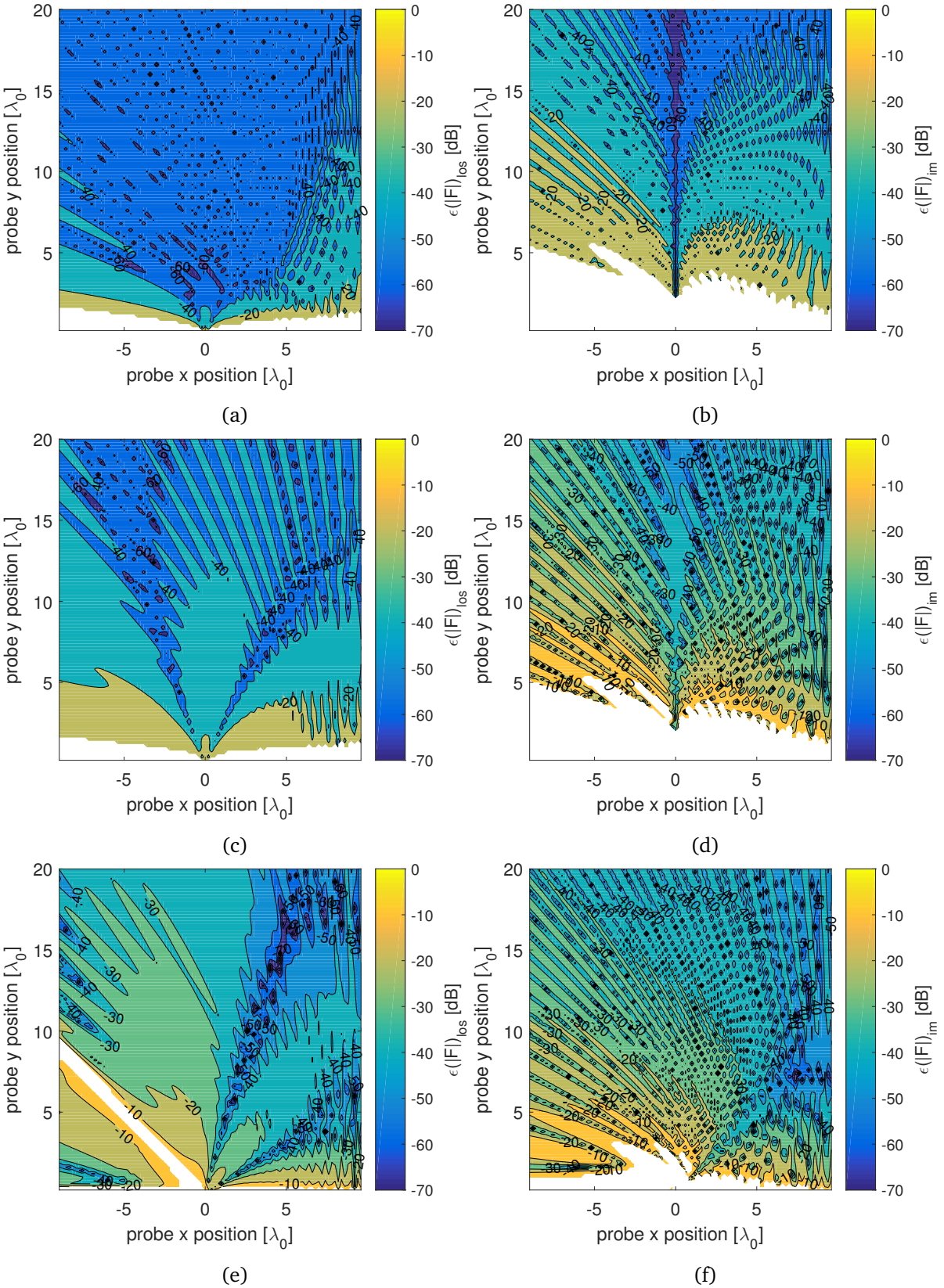

Figure 4.17 Performing the inversion with a hypothetical infinite PEC plate and related ARP amplitude error. Basic TE case, no frequency diversity, $x_p = 10\lambda_0$: (a) LOS error, HWD (b) Image error, HWD (c) LOS error, bicone (d) Image error, bicone (e) LOS error, bicone, $\phi_o = -45°$ (f) Image error, bicone, $\phi_o = -45°$.

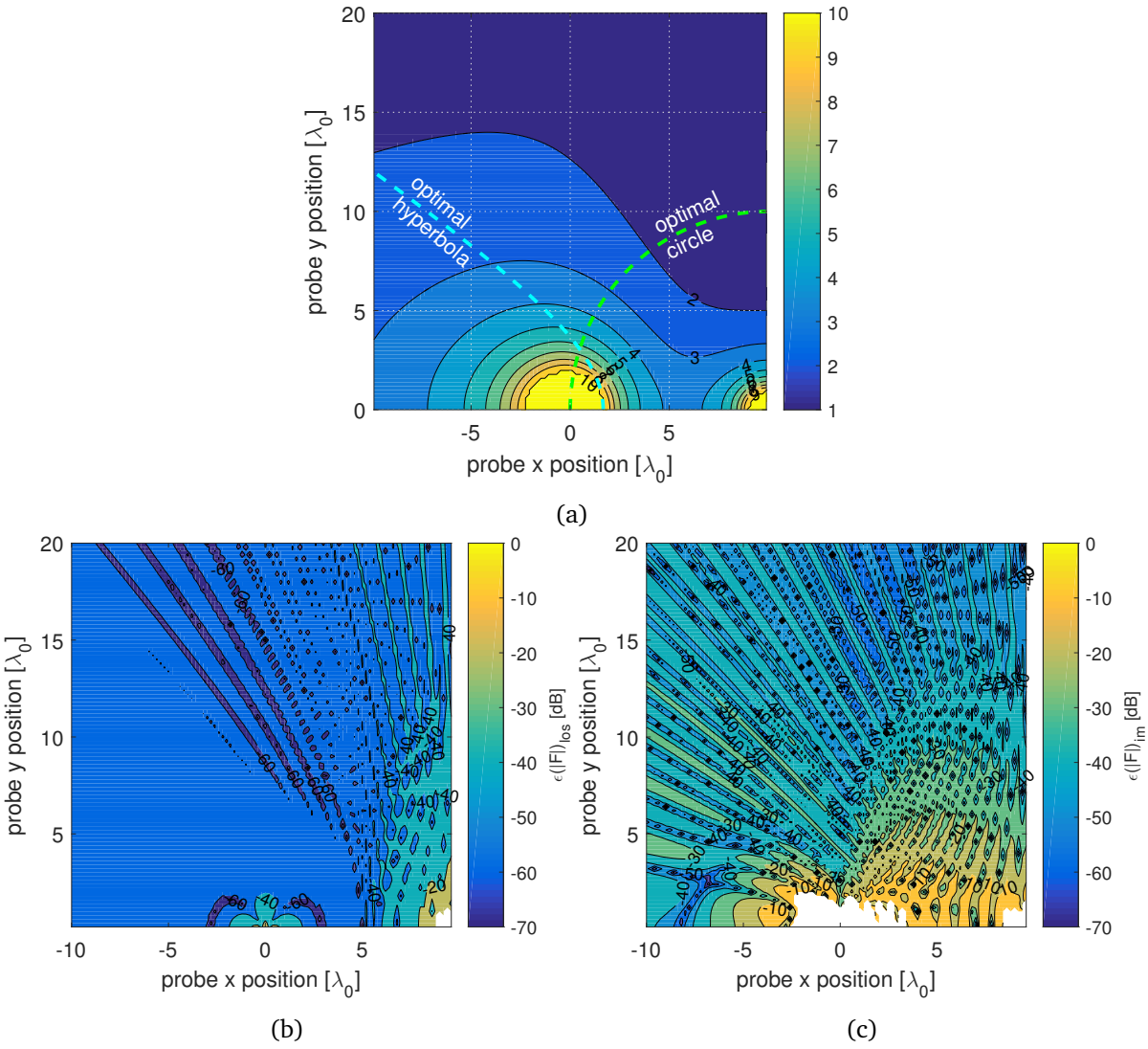

Figure 4.18 ARP error as function of the probe position in a hypothetical scenario characterized by an infinite PEC plate and impact of introducing frequency diversity to the basic TE model. HWD, $x_p = 10\lambda_0$, UFBW= 3%: (a) $\kappa(\mathbf{G}_{TE})$ (b) LOS amplitude error (c) Image amplitude error

The limitation of the direct inversion method in positions corresponding to weak power emission may further be overcome by applying linear regression. As discussed in Sec. 3.4, the performance of the regression technique depends on several factors related to the set of measured data, and to the regression parameters including the type and number of regression functions. An example highlighting the efficiency of regression is shown Fig. 4.19 for an infinite plate scenario using the HWD in the reference TE orientation. A horizontal cut of 10 equally spaced probe positions is used, with $y = 5\lambda_0$ and $x_i = -10\lambda_0 : 2\lambda_0 : 8\lambda_0$. Referring to Fig. 4.17, one can see that image samples, especially those corresponding to probes in the left half of the test zone, show very large error levels that exceed 0dB at certain positions. An RBF regression is used with 5 regression functions distributed over the upper half of the azimuthal plane with each basis function having a spread of 36°. Figs 4.19b and 4.19c show the calculated ARP samples and related error for the basic TE model. The impact of regression in improving results corresponding to image samples is very clear. Relative error is generally stabilized at −30dB preventing image samples from drifting away from the reference ARP. This example shows that even LOS samples, which show low error levels, are further improved by regression, which however may not be a general case. Figs 4.19d and 4.19e show results corresponding to the same configuration when applying frequency diversity with a UFBW= 3%. In this case the original error is relatively low which limits the regression performance, making it essentially vital exclusively at certain positions with relatively large error levels.

Globally, the regression is very efficient in reducing the ARP error. In this scenario, the *absolute* ARP error was reduced from ±15dB to ±0.5dB in the basic TE case, and from ±2dB to ±0.5dB when introducing frequency diversity. The studied example highlights the limitation of moving the probe in order to perform angular scans. In this scenario, image samples cover a narrow 20° range while LOS samples cover 120°. The efficiency of the proposed concept in reducing mechanical displacement is highlighted via a rotation scenario hereafter.

4.4.3 Rotation Scenario

In Sec. 2.4.2, two rotation algorithms were developed in order to achieve maximum efficiency in terms of mechanical rotation. Both algorithms are based on the idea of avoiding the redundancy of covering already-covered angles. In this section, the efficiency of the proposed concept in reducing mechanical displacement is highlighted by applying the general rotation algorithm based on integer ratios of measurement angles (refer to Sec. 2.4.2). In order to visualize the rotation steps, the HWD in TE mode is used due to its directivity. An angles ratio $m_a = \frac{\phi_0}{\phi_1} = 2$ is chosen by placing the probe at a distance equal to the double of the AUT plate separation at the same horizontal level as the AUT, i.e., $(x, y) = (0, 20\lambda_0)$, as shown in Fig. 4.20a. In this case, $\phi_0 = 90°$ and $\phi_1 = 45°$. Frequency diversity is introduced in order to improve the system conditioning by applying an UFBW = 4% such that the optimal hyperbola is closer to the probe position. Conditioning levels are plotted at the same figure showing the optimal conditioning

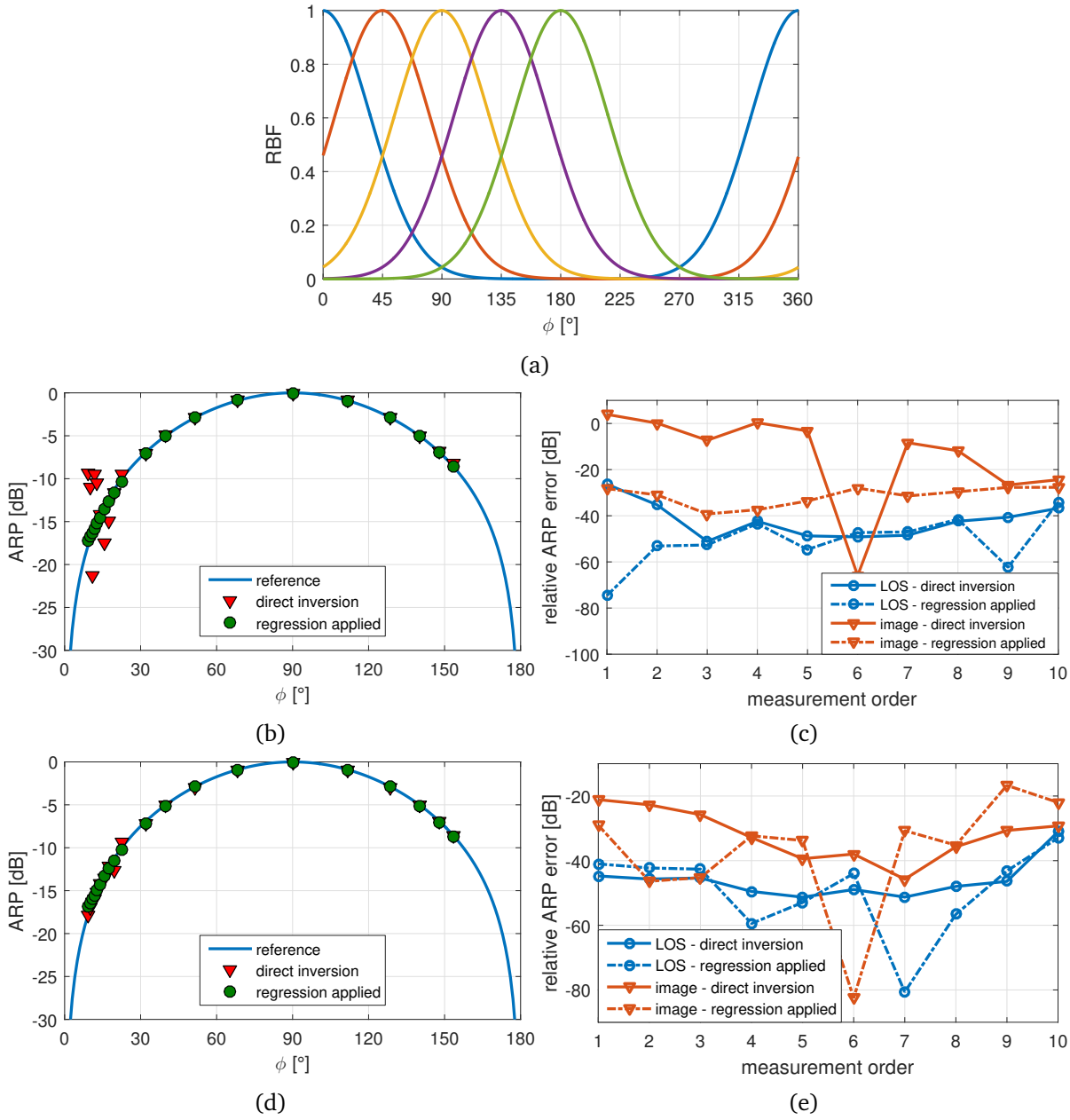

Figure 4.19 Applying linear regression to improve ARP results corresponding to directions of weak power emission using a HWD in the reference TE orientation with 10 probe positions $(x_i, y_i) = (-10\lambda_0 : 2\lambda_0 : 8\lambda_0, 5\lambda_0)$, $x_p = 10\lambda_0$: (a) Regression functions, RBF, $n_b = 5$, spread $= 36°$ (b) Calculated ARP samples, basic TE mode (c) Relative ARP error, basic TE mode (d) Calculated ARP samples, $n_f = 2$, UFBW=3% (e) Relative ARP error, $n_f = 2$, UFBW=3%.

region $\left(\kappa(\mathbf{G}_{TE}) < 2\right)$ extended over the chosen probe position. These parameters ensure the system stability during all the rotation steps.

The sampling angle is set equal to $\phi_s = 9°$, consequently the ratio between the image angle and the sampling angle is equal to $m_s = \frac{\phi_1}{\phi_s} = 5$. This implies the application of 5 rotations, equal to ϕ_s each, covering a range of 90° before introducing a jump equal to $6\phi_s = 54°$ in order to avoid interference between already covered angles and angles yet to be covered. Then, another set of of 5 rotations is performed in order to measure the next 45° range, covering an overall range of 180°. The algorithm may very well be applied to the whole azimuthal plane. In this scenario, it is restricted to half the plane due to the symmetry of the measured ARP. These considerations are shown in Fig. 4.20b where each rotations set is plotted using a different color.

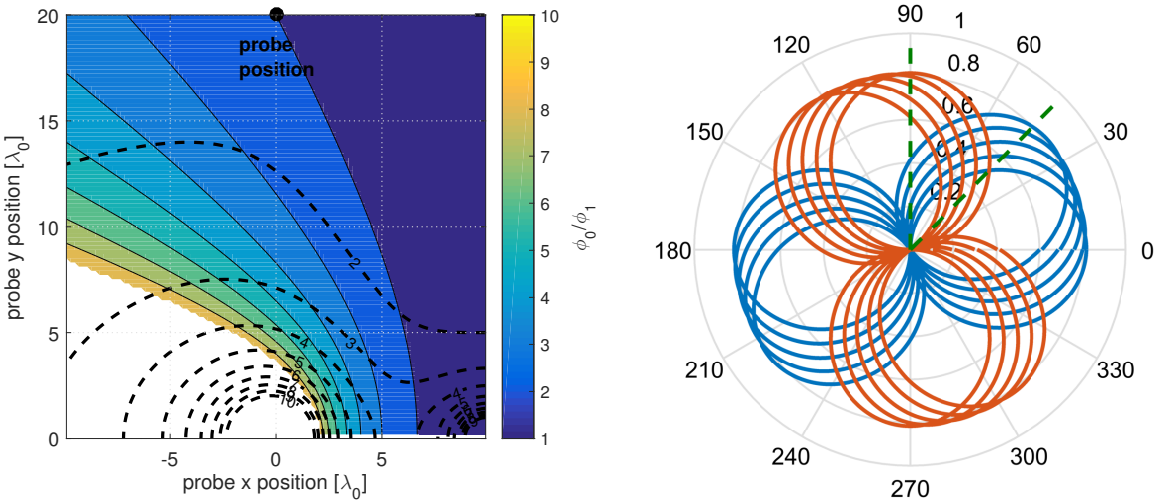

(a) (b)

Figure 4.20 Parameters of the algorithm for achieving maximum efficiency in terms of mechanical rotation: (a) probe position with respect the measurement angle ratio and the system conditioning (dashed) (b) AUT rotations to be performed given a sampling angle $\phi_s = 9°$.

The measured ARP samples corresponding to each orientation as well as the combination of all measured samples are shown in Fig.4.21. The initial AUT orientation was taken at $\phi_o = -90°$ with respect to the reference AUT orientation. Consequently, the LOS sample corresponding to the initial orientation exactly coincides with the null. However, one can see that it is calculated with satisfying precision (around −60dB). Samples corresponding to remaining orientations are calculated with excellent precision, yielding a good agreement between the overall set of data calculated using the proposed method and the reference ARP. This may be verified by examining Fig. 4.22 which plots both relative and absolute ARP errors as function of the AUT orientation. Error corresponding to the initial orientation was not included in the graph because it yields a large value given that the calculate LOS sample is compared to a null reference level. The relative error is generally below −32dB whereas the absolute error is below 0.25dB. This

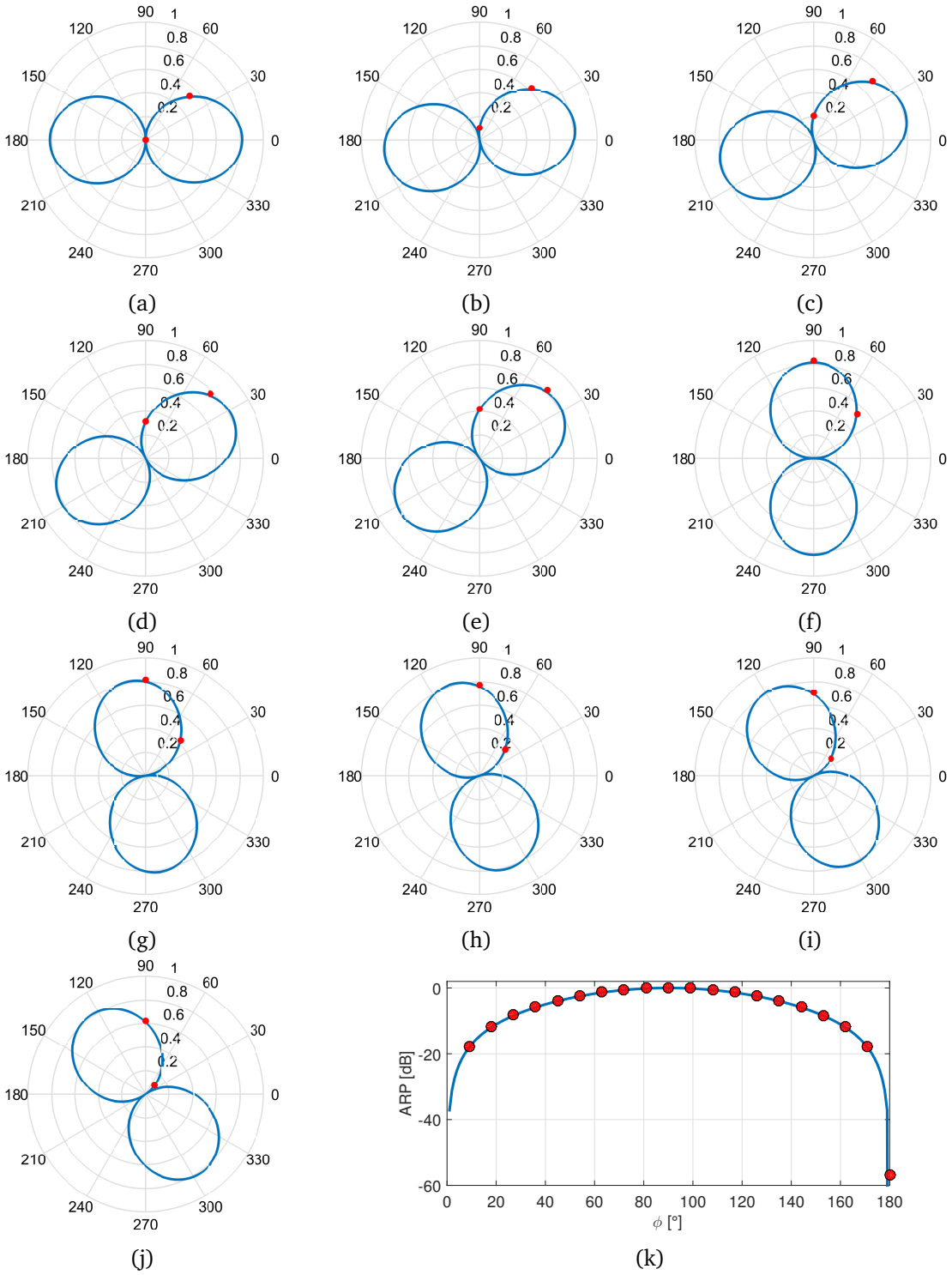

Figure 4.21 Rotation scenario with using a HWD in TE mode, plate at $x_p = 10\lambda_0$, UFBW= 4%; $\phi_s = 9°$, $m_s = 5$, $m_a = 2$ (results in [V]) (a) $\phi_o = -90°$ (b) $\phi_o = -81°$ (c) $\phi_o = -72°$ (d) $\phi_o = -63°$ (e) $\phi_o = -54°$ (f) $\phi_o = 0°$ (g) $\phi_o = 9°$ (h) $\phi_o = 18°$ (i) $\phi_o = 27°$ (j) $\phi_o = 36°$ (k) Orientations combined [dB].

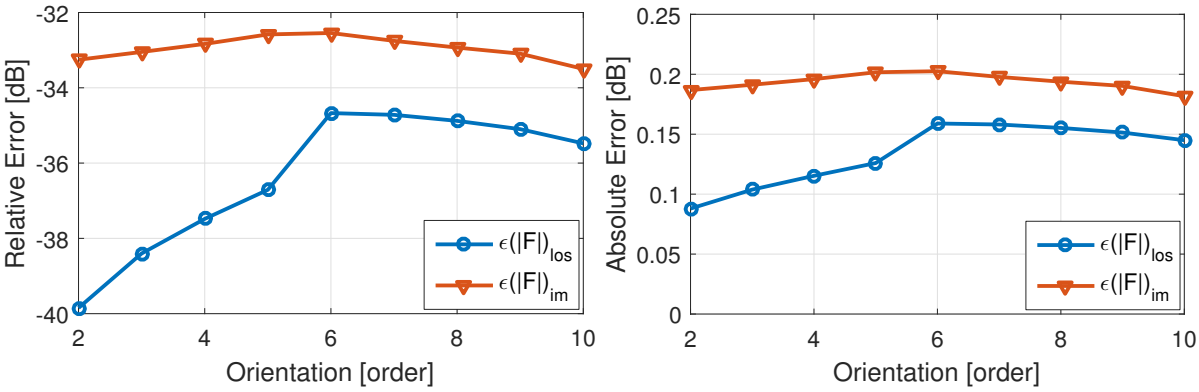

(a) (b)

Figure 4.22 ARP error as function of the AUT orientation of the rotation scenario. Error corresponding to the initial orientation omitted the calculated value is compared to a null reference value yielding a very large error: (a) Relative amplitude error (b) Absolute amplitude erro.r

highlights once again the usefulness of introducing frequency diversity to the TE model which improves both conditioning and ARP results.

In this scenario, 10 AUT orientations were required in order to measure 20 ARP samples uniformly distributed over the measurement range. This would take 20 AUT orientations in a classical measurement, showing the usefulness of the proposed method in reducing mechanical displacement and thus the measurement time. The simulated scenario with the relatively large sampling angle would correspond to validation processes performed to rapidly investigate the targeted radiation characteristics of designed antennas.

4.5 Finite Plate Scenarios

More realistic configurations involving plates of finite dimensions are simulated in order to have a closer insight into the impact of edge diffracted fields on ARP results. As mentioned earlier, several techniques to minimize the impact of diffracted fields exist in practice, most commonly the serrated edge reflectors which are widely used in CATRs and allow achieving precisions in the order of ±0.5dB over the quiet zone [79]. However, in order to stress on the manageability of the edge diffraction problem, a quite simpler technique is tested herein which is the curved edge reflector.

4.5.1 Impact of Edge and Corner Diffracted Fields

The basic test configuration is simulated using a finite rectangular plate truncated in the $y+$ direction at $h_{y+} = 10\lambda_0$, and in the $y-$ direction at $h_{y-} = -5\lambda_0$, and symmetrically at $h_{z\pm} = \pm 5\lambda_0$ along the z-axis, as shown in Fig. 4.23. This would correspond to physical

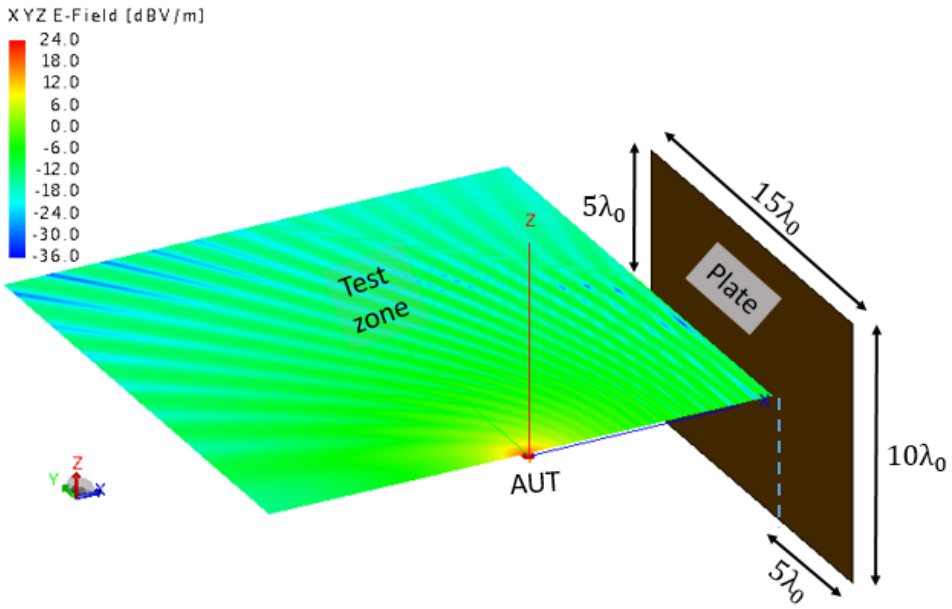

Figure 4.23 Realistic configuration containing a finite rectangular plate in order to assess the impact of edge diffracted fields.

dimensions of 4.5m×3m, which is quite large given the relatively low working frequency. The HWD is used in both transverse modes and the corresponding ARP error is plotted in Fig. 4.24. In agreement with the study conducted in Sec. 3.3.4, the figure shows considerably weak impact on LOS samples which generally maintain error levels below −40dB in zones of good conditioning, and in the lobe direction in the TE case. Nevertheless, numerical results partially disagree with the theoretical study near the reflection boundary where theoretical results, based on GTD, predicted an important impact even over LOS samples. This clearly follows from the limitation of the GTD in this region. On the other hand, the impact is very serious over image samples showing error levels below −20dB over the majority of the test zone. The impact is especially severe in the TE case as the plate is truncated exactly at the optimal position level eliminating as a result the upper half of the optimal conditioning region. These results highlight the vulnerability of image samples to edge diffracted fields, suggesting that rectangular plates with dimensions in the order of $10\lambda_0$-$20\lambda_0$ are too small to assume the validity of the image model. If the AUT-plate separation is reduced, then the optimal region with respect to edge diffraction is improved by connecting the LOS optimal region which, is near the AUT, with the image optimal region, which is near the plate. However, this has the inconvenience of augmenting the AUT diffraction level and eventually perturbing the AUT free-space radiation characteristics. A more effective approach would be modifying the plate edges such that diffracted waves are directed away from the test zone.

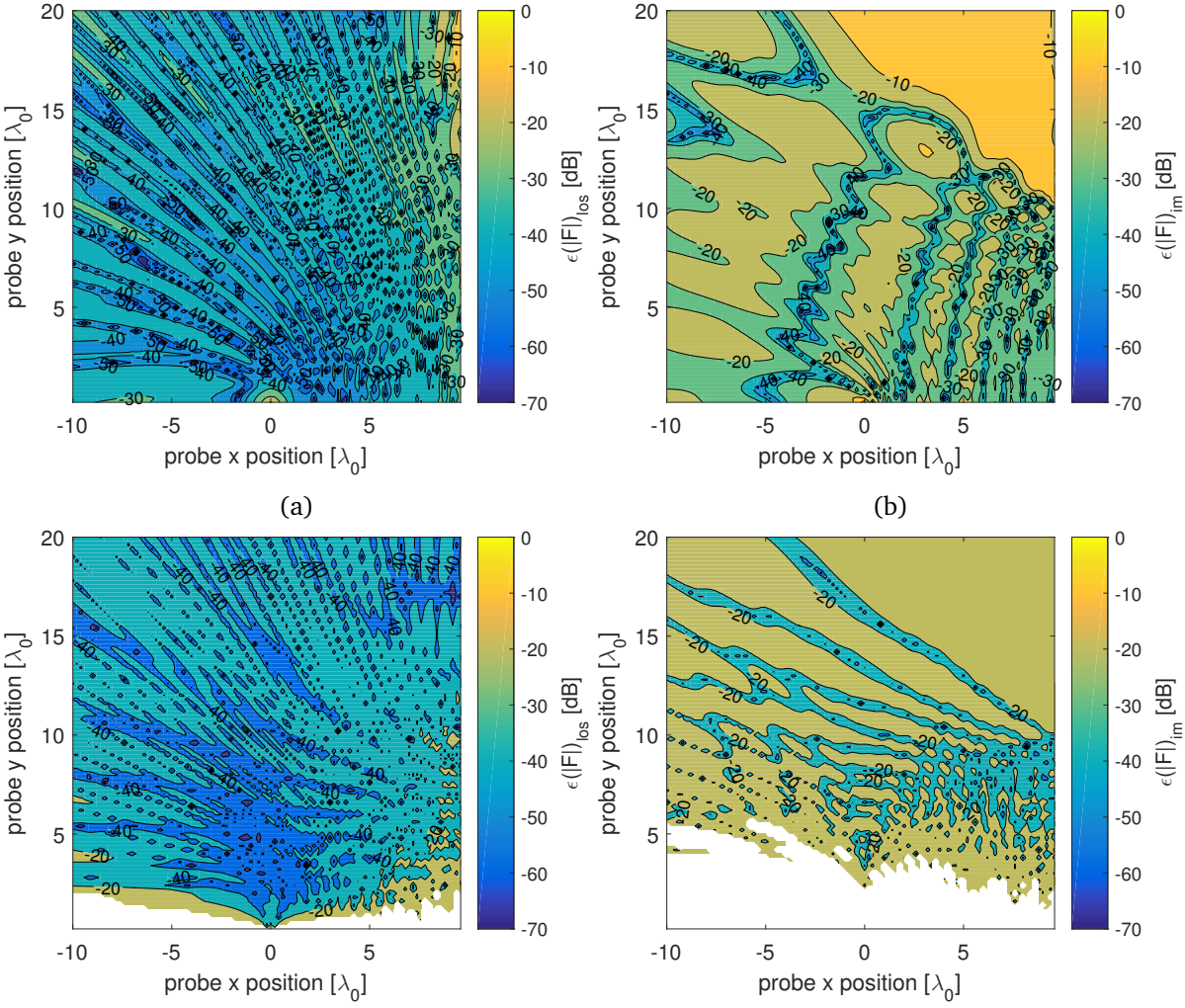

Figure 4.24 ARP error as function of the probe position and impact of edge and corner diffracted fields on ARP samples, the plate being truncated at $h_y = [-5\lambda_0, 10\lambda_0]$ and $h_z = \pm 5\lambda_0$, and positioned at $x_p = 10\lambda_0$. HWD. (a) TM LOS amplitude error, UFBW = 4% (b) TM image amplitude error UFBW = 4% (c) TE LOS amplitude error, basic model (d) TE image amplitude error, basic model.

4.5.2 Curved Edge Plate

One forward solution to reduce the edge diffraction problem is to minimize the edge discontinuity with respect to the illuminating wave by curving the edge. An example of a curved edge reflector designed starting from the rectangular plate used in the previous scenario is shown in Fig. 4.25. Each edge is extended curvedly up to $2\lambda_0$ in each direction such that waves hitting on edges are smoothly directed away from the test zone. Ideally, the curvature angle would be too small with the edge extension being as large as possible in order to effectively minimize the edge discontinuity.

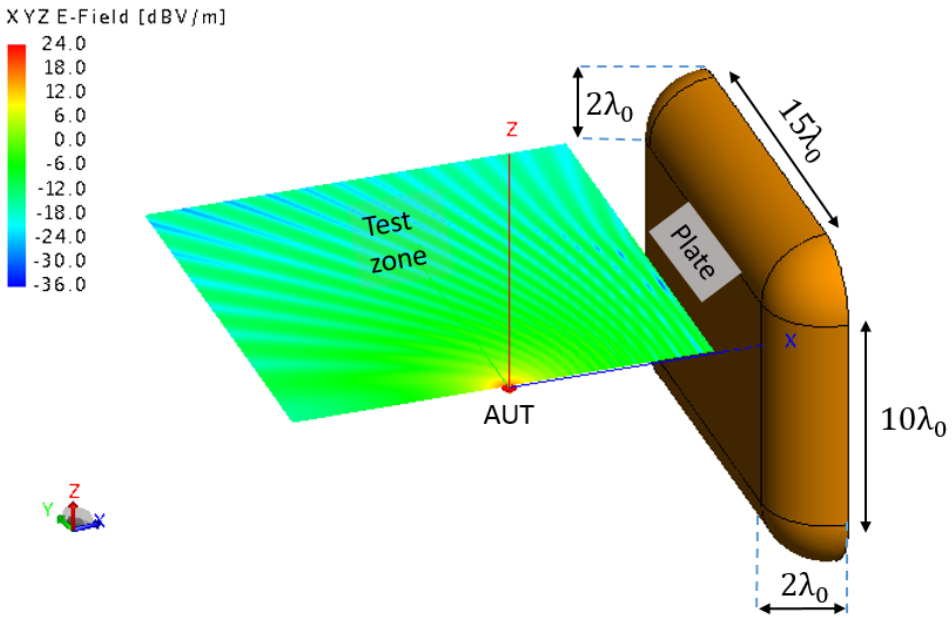

Figure 4.25 Curved edge reflector designed in order to reduce the edge diffraction problem.

ARP results corresponding to this configuration are depicted in Figs. 4.26a-4.26d. The image error is widely improved especially in the TM case where error over the majority of valid positions is below −40dB. Error is relatively reduced in the TE case as well, being below −30dB over the narrow optimal conditioning region pointed by the lobe. The TE results highlight the fact that valid positions in the basic model are very dependent on the plate dimensions. Accordingly, care must be given to the AUT-plate separation given the (y+)-edge position in order to ensure the existence of the optimal conditioned position and the well expansion of the optimal region around it. This implies that the (y+)-edge is at a larger vertical distance with respect to the AUT then the AUT-plate separation, i.e.,

$$h_{y+} > d. \tag{4.8}$$

This is verified by examining the results plotted in Figs. 4.26e-4.26f, which correspond to a curved edge plate whose flat section has a (y+) dimension equal to $h_{y+} = 15\lambda_0$. One may easily notice how the region of tolerated error is effectively enlarged in this case compared to the previous scenario. The performance of the curved edge reflector in the TE case may further be improved by introducing frequency diversity, which in addition to improving the ARP results, provides more freedom in terms of the optimal conditioning region with respect to the plate dimensions.

To conclude, we have shown that rectangular plates with dimensions in the order of $10\lambda_0$-$20\lambda_0$ introduce important diffracted fields that strongly perturb ARP image samples making their corresponding results too approximate. However, we have shown as well that the edge diffraction problem is totally manageable and may be minimized by several methods.

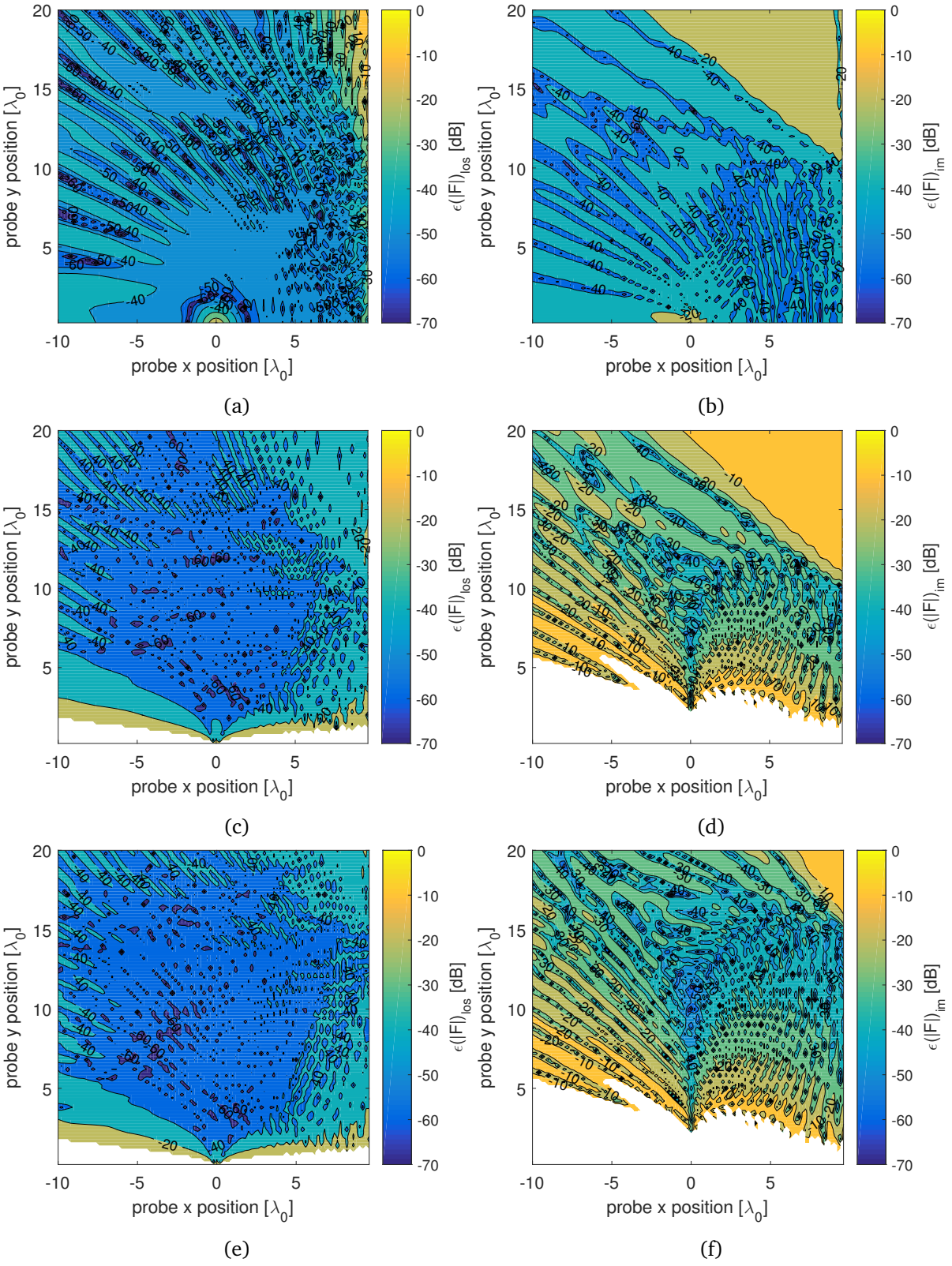

Figure 4.26 Example of the reduction of the edge diffraction problem using a curved edge reflector. The plate flat section having dimensions of $h_y = [-5\lambda_0, 10\lambda_0]$ and $h_z = \pm 5\lambda_0$. $x_p = 10\lambda_0$. HWD. (a) TM LOS amplitude error, UFBW = 4% (b) TM image amplitude error UFBW = 4% (c) TE LOS amplitude error, basic model (e) TE image amplitude error, basic model, $h_{y+} = 15\lambda_0$ (f) TE image amplitude error, basic model $h_{y+} = 15\lambda_0$.

Conclusion

In this chapter, the feasibility of the proposed concept of exploiting controlled echoes in ARP measurements was numerically validated using a comprehensive electromagnetic simulation software, FEKO. Different aspects related to the concept were also verified such as the importance of the developed conditioning models in ensuring the mathematical systems stability, as well as the various model systematic limitations which were proven to be manageable using typical measurement configurations. The usefulness of the concept in accelerating the measurement process was highlighted by applying a developed rotation algorithm that allowed to cut down the mechanical rotation effort to a half with respect to classical measurements. It is important to point out that the presented numerical results does not take into account the impact of practical systematic error sources which are inevitable in real-life measurements. The presented results are however useful in shedding light about measurement guidelines and the different precautions to be taken regarding the set-up dimensions, the working frequency bandwidth, the probe position, and the model approximations in order to count for the practical viability of the proposed concept.

Chapter 5

Extensions to the Basic Configuration: Preliminary Study

Contents

This chapter explores the possibility of extending the proposed concept to more complex configurations involving more than a single controlled reflection. The objective being to extend the spatial diversity in order to be able to measure several ARP samples at a time, which would -theoretically- further accelerate the measurement process. A preliminary study is conducted essentially to verify the theoretical viability of a couple of models developed based on the single-plate model.

5.1 Introduction

The first part of this work presented a study of the proposed measurement concept exploiting echoes based on the single-plate configuration which may be considered as the simplest configuration in terms of controlled echoes generation. The simplicity of the proposed set-up involving a single controlled echo conveniently justified a set of approximations that were applied in order to simplify the developed models, and which proved to hold under manageable conditions. This approach offered many advantages, mainly a solid analytical study in order to predict optimal probe positions that guarantee the stability of the mathematical systems, which is necessary for the validity of the output results. The study showed that such optimal probe positions are generated using typical measurement parameters. Moreover, the simplicity of the single-plate configuration allowed to highlight the usefulness of the concept in accelerating the measurement process. Rotation algorithms in order to achieve maximum efficiency in terms of mechanical displacement were developed and showed that mechanical displacement effort may be cut to a half of that of a classical measurement, which would theoretically result in cutting the measurement time to a half as well.

In this chapter, a preliminary study is conducted in order to verify the possibility of extending the concept to more complex configurations involving larger sets of controlled reflections. A brief discussion about possible methods of extending the basic single-plate configuration in order to generate multiple controlled reflections is first presented. After that, two configurations of different complexity levels are taken as examples, and are separately studied based on results carried over the single-plate configuration. The study conducted in the present chapter is essentially theoretical and focuses on the mathematical viability of each model, and on the eventual usefulness carried by configurations involving multiple reflections in further accelerating the measurement process.

5.2 Extending the Basic Configuration

Multiple controlled reflections may be generated by introducing a set of additional plates to the single-plate configuration. In this work, we will consider introducing one additional plate which would result in a two-plate configuration. Let us suppose that the new plate is also perpendicular to the working azimuthal plane such that all generated reflections would lie on the working plane. Keeping these considerations in mind, two main classes of configurations are considered: configurations of intersecting plates, which will be referred to as *dihedral* configurations, and configurations of non-intersecting plates.

Dihedral configurations are mainly characterized by the dihedral angle which is the intersection angle between the two plates seen by the AUT, say ϕ_{in}, which determines the number of reflected signals. The intersection angle must be in this case smaller than 180° to ensure the generation of multiple reflections. Image theory can be used in order to predict the number

of generated reflections provided that the intersection angle is equal to 180° divided by any positive integer [80],

$$\phi_{in} = \frac{180^\circ}{n}, \quad n \in \mathbb{N}^*. \tag{5.1}$$

In the limiting case, $n = 1$ ($\phi_{in} = 180^\circ$), the configuration is transformed back to the single-plate configuration. Hence, n should be greater than unity in order to ensure the generation of multiple reflections. If the intersection angle does not obey Eq. 5.1, other methods may be used to analyze the generated reflections such as interpolation in order to handle intermediate angles [81], or analysis involving cylindrical functions in order to handle arbitrary angles[82]. The number of generated images N_i corresponding to Eq. 5.1 is expressed as follows,

$$N_i = 2n - 1. \tag{5.2}$$

Examples of dihedral configurations are shown in Figs. 5.1a and 5.1b for $n = 2$ and $n = 3$ respectively. The first configuration corresponds to a right intersection angle $\phi_{in} = 90^\circ$, and results in the generation of three images, while in the second configuration $\phi_{in} = 60^\circ$ which generates five images. It should be made clear that, as for the single-plate configuration, dihedral configurations are widely used in practice, most commonly the Active (Kraus) Corner Reflector [83]. However, once again, interest in these applications is generally in altering the radiating source free-space characteristics in order to produce new characteristics such as larger gain and wider operating bandwidth, whereas in this work the aim is at retrieving the radiating source free-space characteristics and exploiting echoes in order to accelerate the process.

If the two plates do not intersect, such as in Fig. 5.1c, the configuration may generally be approximated as a dihedral configuration provided that the two plates are of sufficiently large dimensions. One particular configuration of non-intersecting plates is the parallel-plate configuration which allows the generation of an infinite set of controlled echoes. In this chapter, the right dihedral configuration ($\phi_{in} = 90^\circ$) and the parallel-plate configuration are studied in order to explore the possibility of extending the concept to configurations involving sets of multiple echoes of finite and infinite dimensions.

5.3 Dihedral Configuration

A closer insight into the right dihedral configuration is provided in Fig. 5.2. The AUT may a priori be placed anywhere between the two plates, which is unlike the active corner reflector, where the radiating source is generally placed near the corner symmetrically between the two plates. Assuming PEC conditions, positions of the three generated virtual sources are easily retrieved by using image theory. Taking the AUT position as the origin of the working azimuthal

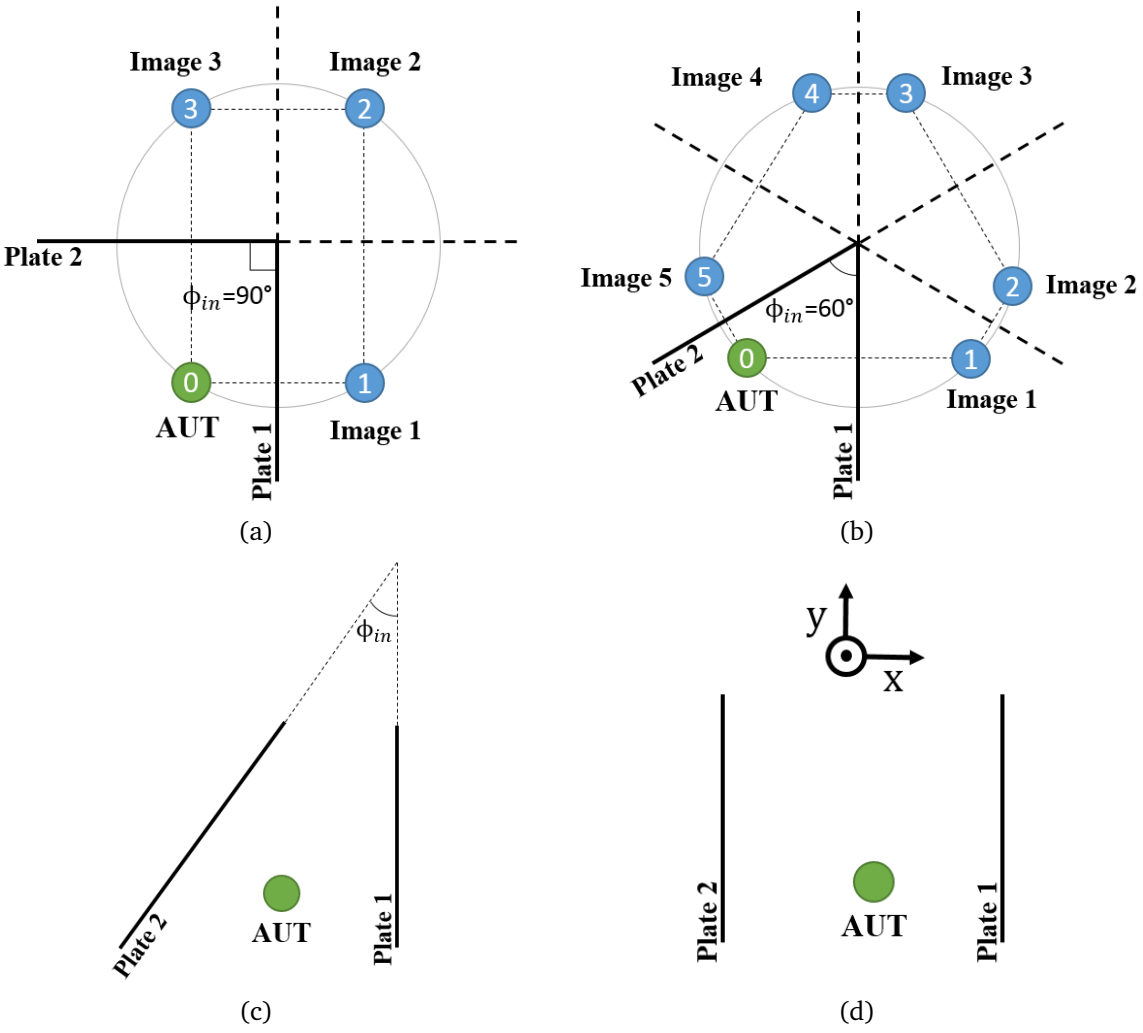

Figure 5.1 Extending the single-plate configuration in order to generate multiple controlled reflections (a) Dihedral configuration, $\phi_{in} = 90^\circ$ (b) Dihedral configuration, $\phi_{in} = 60^\circ$ (c) Non-intersecting plates configuration (d) Parallel-plate configuration.

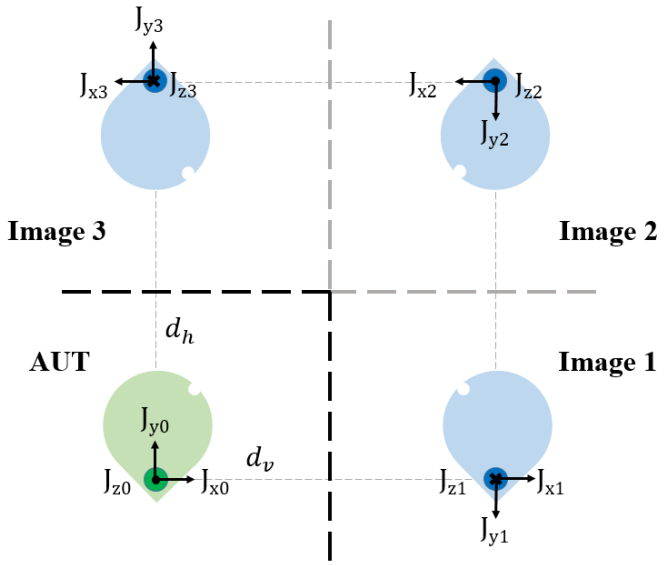

Figure 5.2 Graphical representation of the dihedral configuration with insight into excitation polarizations related to each image.

plane, and assuming the vertical and horizontal plates are positioned at distances d_v and d_h from the AUT, then the three images positions are expressed as follows,

$$\begin{aligned} \text{image 1}: &\quad (x_1, y_1) = (2d_v, 0), \\ \text{image 2}: &\quad (x_2, y_2) = (2d_v, 2d_h), \\ \text{image 3}: &\quad (x_3, y_3) = (0, 2d_h). \end{aligned}$$

It follows that the distance separating each source from the measurement point r_i and the corresponding measurement angles ϕ_i may be retrieved by applying a Cartesian-to-spherical coordinates transformation with care to the ARP orientation of each source as shown in Fig. 5.2.

5.3.1 Mathematical Model

As for the single-plate configuration, the model is simplified in order to assess the concept mathematical viability. Accordingly, the two plates are considered lossless and of infinite extent and the AUT dimensionless and frequency independent. Assuming far-field conditions, the $\mathbf{E} = \mathbf{GF}$ model is maintained, the difference being only in the system dimensions and the sources excitations polarizations. The number of unknowns in the right dihedral case being four, i.e., the ARP LOS plus the three images samples, this sets the dimension of the unknown ARP vector, which is the second dimension of the system matrix, and a lower bound of the first dimension of the system matrix which is the dimension of the measured field vector.

5.3.1.1 TM case

A minimum of four frequencies is necessary to balance the mathematical system. The corresponding $\mathbf{G}_{TM}$ matrix is then a 4×4 matrix formed by applying a Hadamard product between the free-space Green's matrix $\mathbf{G}_o$ and a polarization matrix $\mathbf{P}$,

$$\mathbf{G} = \mathbf{G}_o \circ \mathbf{P}, \tag{5.3}$$

The free-space Green's matrix $\mathbf{G}_o$ contains the free-space Green's function samples corresponding to each source at each frequency,

$$G_o(i,j) = \frac{1}{r_j} \mathrm{e}^{-\mathrm{j}\frac{2\pi}{c} f_i r_j}, \quad 0 \leq i,j \leq 3$$

The distribution model of frequency samples making the working frequency vector impacts the system conditioning as it defines the degree of orthogonality between each two rows of the system matrix. The model adopted in this work has frequency samples linearly distributed over the working bandwidth with the reference frequency being the smallest frequency,

$$\begin{gathered} \mathbf{f} = [f_0 \; f_1 \; f_2 \; f_3]', \\ \text{with} \quad \frac{f_{i+1} - f_i}{f_0} = \frac{\mathrm{UFBW}}{3}, \quad 0 \leq i \leq 2. \end{gathered} \tag{5.4}$$

As we are going to show later, the choice of the uniform distribution of frequency samples was motivated by its simplicity regarding the conditioning study, whereas the choice of setting the reference frequency as the smallest working frequency is, as for the single-plate case, motivated by the fact that the proposed concept is more adapted to high frequencies in terms of set-up requirements.

The polarization matrix $\mathbf{P}$ is formed by concatenating a row polarization vector $\mathbf{p}$ along the first dimension four times in order to effectively sum up the contributions of the four sources at each of the four frequencies. The polarization vector is easily retrieved from Fig. 5.2 by noticing that the first and last images correspond to a single reflection, making their corresponding J_z excitations out of phase by 180° with respect to the AUT excitation, while the second image corresponds to a double reflection making its J_z excitation in phase with the AUT excitation,

$$\mathbf{P} = \begin{bmatrix} -1 & 1 & -1 & 1 \\ -1 & 1 & -1 & 1 \\ -1 & 1 & -1 & 1 \\ -1 & 1 & -1 & 1 \end{bmatrix}.$$

The overall system is then expressed as follows,

$$\underbrace{\begin{bmatrix} E(f_0) \\ E(f_1) \\ E(f_2) \\ E(f_3) \end{bmatrix}}_{\mathbf{E}_p} = \underbrace{\begin{bmatrix} -\frac{1}{r_0}e^{-j\frac{2\pi}{c}f_0 r_0} & \frac{1}{r_1}e^{-j\frac{2\pi}{c}f_0 r_1} & -\frac{1}{r_2}e^{-j\frac{2\pi}{c}f_0 r_2} & \frac{1}{r_3}e^{-j\frac{2\pi}{c}f_0 r_3} \\ -\frac{1}{r_0}e^{-j\frac{2\pi}{c}f_1 r_0} & \frac{1}{r_1}e^{-j\frac{2\pi}{c}f_1 r_1} & -\frac{1}{r_2}e^{-j\frac{2\pi}{c}f_1 r_2} & \frac{1}{r_3}e^{-j\frac{2\pi}{c}f_1 r_3} \\ -\frac{1}{r_0}e^{-j\frac{2\pi}{c}f_2 r_0} & \frac{1}{r_1}e^{-j\frac{2\pi}{c}f_2 r_1} & -\frac{1}{r_2}e^{-j\frac{2\pi}{c}f_2 r_2} & \frac{1}{r_3}e^{-j\frac{2\pi}{c}f_2 r_3} \\ -\frac{1}{r_0}e^{-j\frac{2\pi}{c}f_3 r_0} & \frac{1}{r_1}e^{-j\frac{2\pi}{c}f_3 r_1} & -\frac{1}{r_2}e^{-j\frac{2\pi}{c}f_3 r_2} & \frac{1}{r_3}e^{-j\frac{2\pi}{c}f_3 r_3} \end{bmatrix}}_{\mathbf{G}_{TM}} \underbrace{\begin{bmatrix} F(\phi_0) \\ F(\phi_1) \\ F(\phi_2) \\ F(\phi_3) \end{bmatrix}}_{\mathbf{F}}. \tag{5.5}$$

5.3.1.2 TE case

The minimum number of required frequencies in order to balance the mathematical system in the TE case is half the number of unknowns, that is, two. This is due to the default overdetermination of the TE problem having two measurable field components for each ARP sample. The system matrix is formed by a similar Hadamard product to the TM case but with the introduction of the projection matrix **M**:

$$\mathbf{G}_{TE} = \mathbf{G}_o \circ \mathbf{M} \circ \mathbf{P} \tag{5.6}$$

The projection matrix of the basic TE model ($N_f = 2$) is expressed as follows,

$$\mathbf{M} = \begin{bmatrix} \mathbf{M}_x \\ --- \\ \mathbf{M}_y \end{bmatrix} = \left[\begin{array}{cccc} -\sin\phi_0 & -\sin\phi_1 & -\sin\phi_2 & -\sin\phi_3 \\ -\sin\phi_0 & -\sin\phi_1 & -\sin\phi_2 & -\sin\phi_3 \\ ----- & ----- & ----- & ----- \\ \cos\phi_0 & \cos\phi_1 & \cos\phi_2 & \cos\phi_3 \\ \cos\phi_0 & \cos\phi_1 & \cos\phi_2 & \cos\phi_3 \end{array}\right]$$

If more then two frequencies are used, then each section of the matrix is extended by introducing a similar row accounting for the new frequency. The polarization matrix of the basic model is easily retrieved from Fig. 5.2, and may be extended the same way when introducing new frequencies, i.e., by introducing similar rows in each section to account for the new frequencies,

$$\mathbf{P} = \begin{bmatrix} \mathbf{P}_x \\ --- \\ \mathbf{P}_y \end{bmatrix} = \left[\begin{array}{cccc} 1 & 1 & -1 & -1 \\ 1 & 1 & -1 & -1 \\ - & - & - & - \\ 1 & -1 & -1 & 1 \\ 1 & -1 & -1 & 1 \end{array}\right],$$

The overall system of equations is expressed as follows,

$$\underbrace{\begin{bmatrix} E_x(f_0) \\ E_x(f_1) \\ \vdots \\ E_x(f_{N_f-1}) \\ --- \\ E_y(f_0) \\ E_y(f_1) \\ \vdots \\ E_y(f_{N_f-1}) \end{bmatrix}}_{\mathbf{E}_p} = \underbrace{\begin{bmatrix} -\frac{e^{-j\frac{2\pi}{c}f_0 r_0}}{r_0}\sin\phi_0 & -\frac{e^{-j\frac{2\pi}{c}f_0 r_1}}{r_1}\sin\phi_1 & \frac{e^{-j\frac{2\pi}{c}f_0 r_2}}{r_2}\sin\phi_2 & \frac{e^{-j\frac{2\pi}{c}f_0 r_3}}{r_3}\sin\phi_3 \\ -\frac{e^{-j\frac{2\pi}{c}f_1 r_0}}{r_0}\sin\phi_0 & -\frac{e^{-j\frac{2\pi}{c}f_1 r_1}}{r_1}\sin\phi_1 & \frac{e^{-j\frac{2\pi}{c}f_1 r_2}}{r_2}\sin\phi_2 & \frac{e^{-j\frac{2\pi}{c}f_1 r_3}}{r_3}\sin\phi_3 \\ \vdots & \vdots & \vdots & \vdots \\ -\frac{e^{-j\frac{2\pi}{c}f_{N_f-1} r_0}}{r_0}\sin\phi_0 & -\frac{e^{-j\frac{2\pi}{c}f_{N_f-1} r_1}}{r_1}\sin\phi_1 & \frac{e^{-j\frac{2\pi}{c}f_{N_f-1} r_2}}{r_2}\sin\phi_2 & \frac{e^{-j\frac{2\pi}{c}f_{N_f-1} r_3}}{r_3}\sin\phi_3 \\ ----- & ----- & ----- & ----- \\ \frac{e^{-j\frac{2\pi}{c}f_0 r_0}}{r_0}\cos\phi_0 & -\frac{e^{-j\frac{2\pi}{c}f_0 r_1}}{r_1}\cos\phi_1 & -\frac{e^{-j\frac{2\pi}{c}f_0 r_2}}{r_2}\cos\phi_2 & \frac{e^{-j\frac{2\pi}{c}f_0 r_3}}{r_3}\cos\phi_3 \\ \frac{e^{-j\frac{2\pi}{c}f_1 r_0}}{r_0}\cos\phi_0 & -\frac{e^{-j\frac{2\pi}{c}f_1 r_1}}{r_1}\cos\phi_1 & -\frac{e^{-j\frac{2\pi}{c}f_1 r_2}}{r_2}\cos\phi_2 & \frac{e^{-j\frac{2\pi}{c}f_1 r_3}}{r_3}\cos\phi_3 \\ \vdots & \vdots & \vdots & \vdots \\ \frac{e^{-j\frac{2\pi}{c}f_{N_f-1} r_0}}{r_0}\cos\phi_0 & -\frac{e^{-j\frac{2\pi}{c}f_{N_f-1} r_1}}{r_1}\cos\phi_1 & -\frac{e^{-j\frac{2\pi}{c}f_{N_f-1} r_2}}{r_2}\cos\phi_2 & \frac{e^{-j\frac{2\pi}{c}f_{N_f-1} r_3}}{r_3}\cos\phi_3 \end{bmatrix}}_{\mathbf{G}_{TE}} \underbrace{\begin{bmatrix} F(\phi_0) \\ F(\phi_1) \\ F(\phi_2) \\ F(\phi_3) \end{bmatrix}}_{\mathbf{F}} \tag{5.7}$$

One may notice how the systems complexities in both transverse models naturally grows when the number of contributing images rises.

5.3.2 Conditioning Issues

Retrieving ARP samples corresponding to both the TM and TE cases consists in inverting the corresponding matrices equations (Eq. 5.5 and Eq. 5.7). This brings the discussion of conditioning which measures the concept mathematical viability. The objective being to know if it is possible to achieve well-conditioned systems using typical measurement parameters, and whether it is possible, as function of these parameters, to predict optimal positions in terms of conditioning. However, unlike the single-plate configuration, it seems very difficult to opt for an analytical approach in studying conditioning due to the complexity of the system matrices. The approach adopted herein to overcome this difficulty is mainly qualitative and is based on the study carried over the single-plate configuration.

The dihedral configuration may theoretically be decomposed into three single-plate configurations in order to handle the contribution of each image. The first and last images correspond to physical single-plate configurations as they are generated by the vertical and horizontal plates respectively. On the other hand, the second image, which corresponds to the double reflection by the two plates, may be modeled as being generated by a hypothetical diagonal plate perpendicularly bisecting the line segment between the AUT and the second image. Accordingly, results of the single-plate conditioning study may be projected over each image in order to understand the global conditioning behavior of the dihedral configuration.

5.3.2.1 TM Model

Conditioning in the basic single-plate TM model is governed by two parameters: the working UFBW which defines optimal hyperbolas, and the distances spread which defines conditioning circles. In the right dihedral case, the frequency vector is characterized by a set of three UFBWs. The first being the global working UFBW which is defined by the smallest and highest working frequencies, and which thus defines the degree of orthogonality between the first and last system matrix rows. The two remaining UFBWs are respectively one third and two thirds of the global UFBW defining the degree of orthogonality between the first and second, and first and third system matrix rows respectively. The choice of the uniform distribution of frequency samples is advantageous in simplifying the conditioning study in the sense that it is sufficient to study the degree of orthogonality between the first row and each of the remaining rows rather than assessing all possible two-row combinations. For example, the degree of orthogonality between the first and second rows is exactly the same as the degree of orthogonality between each two consecutive rows as they yield exactly the same projection factor given the same fractional bandwidth characterizing each two consecutive rows. This would not be the case if the four frequency samples were distributed otherwise. Recalling the properties of optimal hyperbolas discussed in Sec. 2.3.2.2, as function of the AUT-plate separation with respect to the working UFBW, there exists three possibilities for the existence of optimal hyperbolas: non existence, existence of the first-order hyperbola, and existence of higher order hyperbolas. Accordingly, three families of optimal hyperbolas are considered in the right dihedral case, each family corresponding to each UFBW, which in terms of the three plates positions determines the existing hyperbolas corresponding to each plate. By the same token, each distances spread defines three conditioning circles corresponding to the three plates. As discussed in Sec. 2.3.2.3, the conditioning circle corresponding to the hypothetical diagonal plate would by default have the larger diameter as the related AUT-plate separation is always larger compared to the remaining plates. Keeping these considerations in mind, regions of optimal conditioning are then regions where optimal hyperbolas from the three families and the three conditioning circles are most likely to intersect, modeling the fact that the system matrix rows form a closely orthogonal set.

In order to highlight these aspects, results of an example of a right dihedral configuration are shown in Figs. 5.3a-5.3d. The set-up in this example is symmetrical with $d_v = d_h = 10\lambda_0$, and the global UFBW is set equal to 6%. The test zone is enlarged with respect to the single-plate test zone having $40\lambda_0 \times 40\lambda_0$ dimensions bounded from the right and top by the plates. Figs. 5.3a-5.3c plots in order the projection factors between the first and each of the remaining rows with the corresponding optimal hyperbola families (dashed). Each hyperbola family is plotted using a different color (green, red, black in ascending UFBW order). An example of conditioning circles corresponding to $\rho = 0.6$, which was taken as the maximum tolerated value in the single-plate case, is plotted in all the figures (dotted). The covered test zone dimensions allow

to clearly visualize large sections of conditioning circles. In the first figure which corresponds to the narrower UFBW ($UFBW_1 = 2\%$), only the first-order optimal hyperbola corresponding to the hypothetical diagonal plate exists, pointing towards the down left corner where it intersects with optimal conditioning circles creating an optimal region. The projection factor takes high values around the AUT and near the dihedral corner (upper right corner). In the second figure, the $UFBW_2 = 4\%$ is wide enough in order to generate first-order optimal hyperbolas corresponding to the three plates, the one corresponding to the hypothetical plate being pushed near the corner where it creates a small optimal region. Optimal hyperbolas corresponding to the physical plates point towards the down left corner where they intersect with optimal conditioning circles creating once again an optimal zone in this region. The projection factor takes high values in this case near the two plates, in the immediate vicinity of the dihedral corner, and once again around the AUT. Finally, in the third figure the UFBW= 6% pushes first-order hyperbolas towards the corresponding plates and generates the second order hyperbola related to the hypothetical plate. Consequently, the optimal region near the upper right corner is rather enlarged with respect to the precedent figure, and diagonal positions pointing towards the down left corner become ill-conditioned. It is interesting to note that the second order hyperbola corresponding to the hypothetical plate at UFBW= 6%, coincides with the first-order hyperbola corresponding to the same plate at UFBW=2%. This is easily verified by referring to Eq. 2.27 that expresses the real semiaxis a_n which is the determinant factor of the hyperbola shape,

$$\text{at } \Delta f_{u1} = 2\% = \frac{\Delta f_u}{3} \longrightarrow a_0 = \frac{1}{4\Delta f_{u1}} = \frac{3}{4\Delta f_u},$$
$$\text{at } \Delta f_u = 6\% \longrightarrow a_1 = \frac{2+1}{4\Delta f_u} = \frac{3}{4\Delta f_u}.$$

The global conditioning is somewhat a superposition of the three projection factors maps. Optimal conditioned zones are areas where the three projection factors take optimal values. Whereas ill-conditioned zones are areas where at least one of the three projection factors take high values. This is to translate the fact that the system is well-conditioned only when the matrix rows are all -closely- orthogonal to each others. The same can be seen in Fig. 5.3d which plots the condition number pattern of the studied configuration. The condition number takes it lowest values (< 10) in two symmetrical regions near the diagonal in the bottom left corner where the three projection factors take their lowest vales. Otherwise, the condition number takes high values and dramatically grows around the AUT, near the plates and the dihedral corner, and along the diagonal. Positions around the AUT are by default ill-conditioned because of the large distances spread between the small LOS distance and the relatively larger images distances. Positions near the plates are also ill-conditioned as the matrix tends towards singularity having the LOS distance and the distance of the image generated from each plate being approximately equal, which creates a redundancy in the matrix columns. Positions near the corner create a

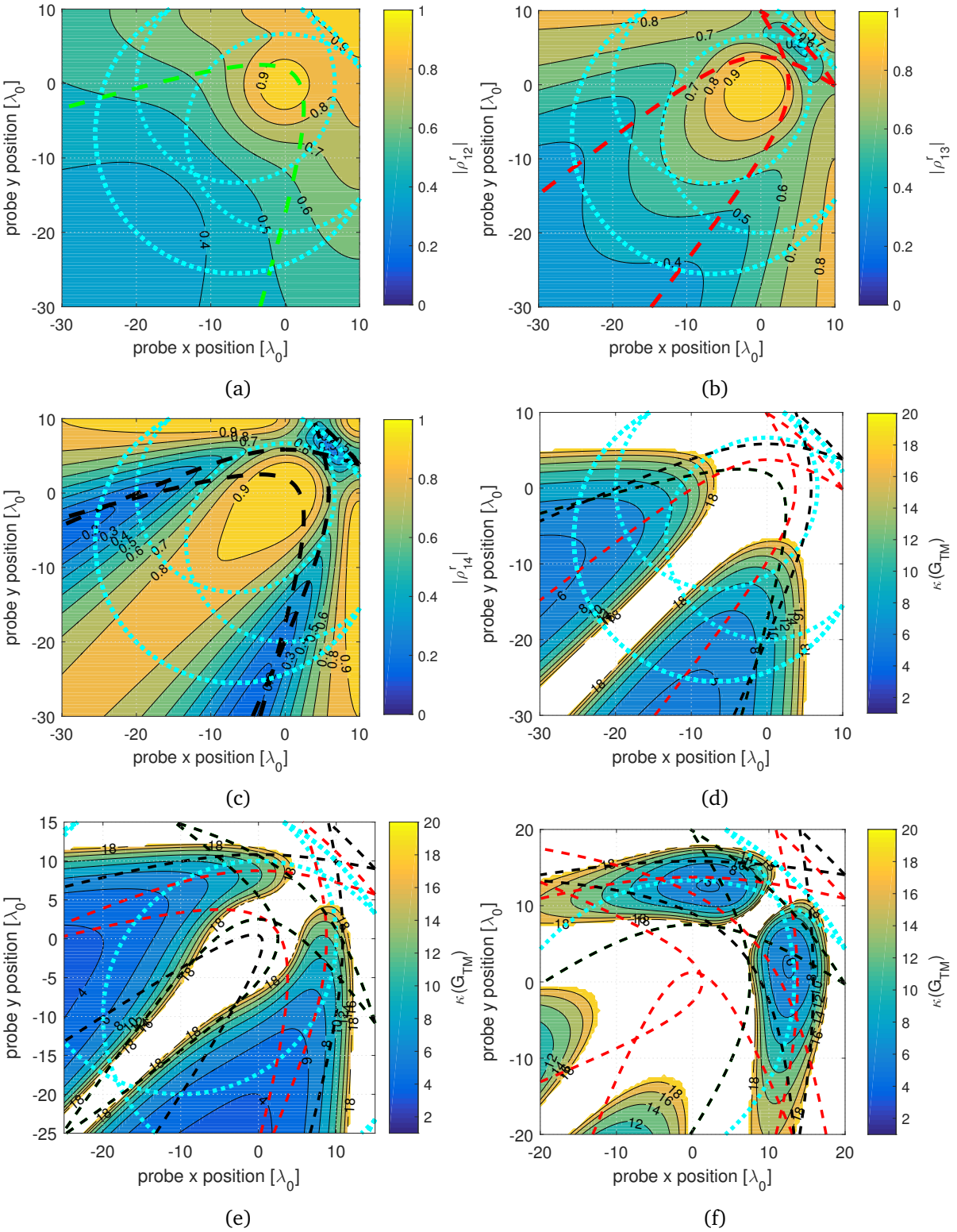

Figure 5.3 Conditioning patterns and impact of optimal hyperbolas (dashed) and conditioning circles (dotted) as function of the set-up dimensions. Dihedral configuration, TM case, $FBW = 6\%$, $N_f = 4$: (a) $\rho^r_{12}(\mathbf{G}_{TM})$, $d_v = d_h = 10\lambda_0$ (b) $\rho^r_{13}(\mathbf{G}_{TM})$, $d_v = d_h = 10\lambda_0$ (c) $\rho^r_{14}(\mathbf{G}_{TM})$, $d_v = d_h = 10\lambda_0$ (d) $\kappa(\mathbf{G}_{TM})$, $d_v = d_h = 10\lambda_0$ (e) $\kappa(\mathbf{G}_{TM})$, $d_v = d_h = 15\lambda_0$ (f) $\kappa(\mathbf{G}_{TM})$, $d_v = d_h = 20\lambda_0$.

redundancy between all the matrix columns with all sources being approximately equidistant from the probe. Finally, diagonal positions are ill-conditioned in this scenario because the system matrix is singular in this region due to the symmetry of the set-up making the first and last images equidistant from diagonal positions. If the set-up is not symmetrical, then positions equidistant from the first and last images are deviated from the diagonal.

One may notice that the global condition number in this scenario is relatively high even with the quite large test zone dimensions, attaining an optimal value $\kappa(\mathbf{G}_{TM})_{\text{opt}} \approx 5.2$. This may be explained by noticing that the system parameters make optimal hyperbolas corresponding to the three families less likely to fall in the same zone. In order to overcome this, one of three solutions may be applied. The first is by pushing the probe to further positions from the AUT in order to reduce the distances spread such that optimal hyperbolas intersect with conditioning circles corresponding to lower projection factors. This however may require large set-up dimensions in order to achieve suitable conditioning levels. Alternatively, the two remaining solutions consists in adapting the working UFBW to the AUT-plate separations in order to effectively distribute optimal hyperbolas over the test zone, either by augmenting the AUT-plate separations or by augmenting the working UFBW.

An example of the impact of augmenting the AUT-plate separations while keeping the same test zone dimensions, which may be performed by moving the AUT, is shown in Fig. 5.3e where $d_v = d_h = 15\lambda_0$. In this case the global condition number pattern is improved reducing the ill-conditioned area and improving the optimal conditioning level to around $\kappa(\mathbf{G}_{TM})_{\text{opt}} \approx 3.3$. This is mainly because the chosen AUT-plate separations allowed the generation of a higher number of optimal hyperbolas with first-order hyperbolas being pushed closer to the plates and second order hyperbolas being directed towards the diagonal improving as a result the global conditioning. However, augmenting the AUT-plate separations is not necessarily advantageous as it may, once becoming too large, introduce a large number of worst hyperbolas which would intersect with optimal hyperbolas corresponding to other families reducing as a result the optimal zones. The same can be seen in Fig. 5.3f where $d_v = d_h = 20\lambda_0$. One may notice that the majority of optimal hyperbolas are concentrated near the plates generating two symmetric narrow optimal regions, while the rest of the test zone is dominated by an ill-conditioned region due to the impact of wost hyperbolas. These set-up dimensions are adapted for a narrower global UFBW, typically 4%.

The same impacts may be achieved by rising the working UFBW, as shown in Fig 5.4. Figs 5.4a-5.4f shows results when adapting the working UFBW to the original configuration having $d_v = d_h = 10\lambda_0$, by applying a UFBW = 9%. Unlike the previous scenario, in this case the first hyperbolas family corresponding to $\text{UFBW}_1 = 3\%$ contains first-order hyperbolas related to the three plates. Moreover, the third hyperbolas family corresponding to the global UFBW contains second order hyperbolas related to the physical plates and even a third order hyperbola related to the hypothetical plate. The higher number of intersecting optimal hyperbolas improves the global conditioning shape and levels, pushing positions with relatively low conditioning levels

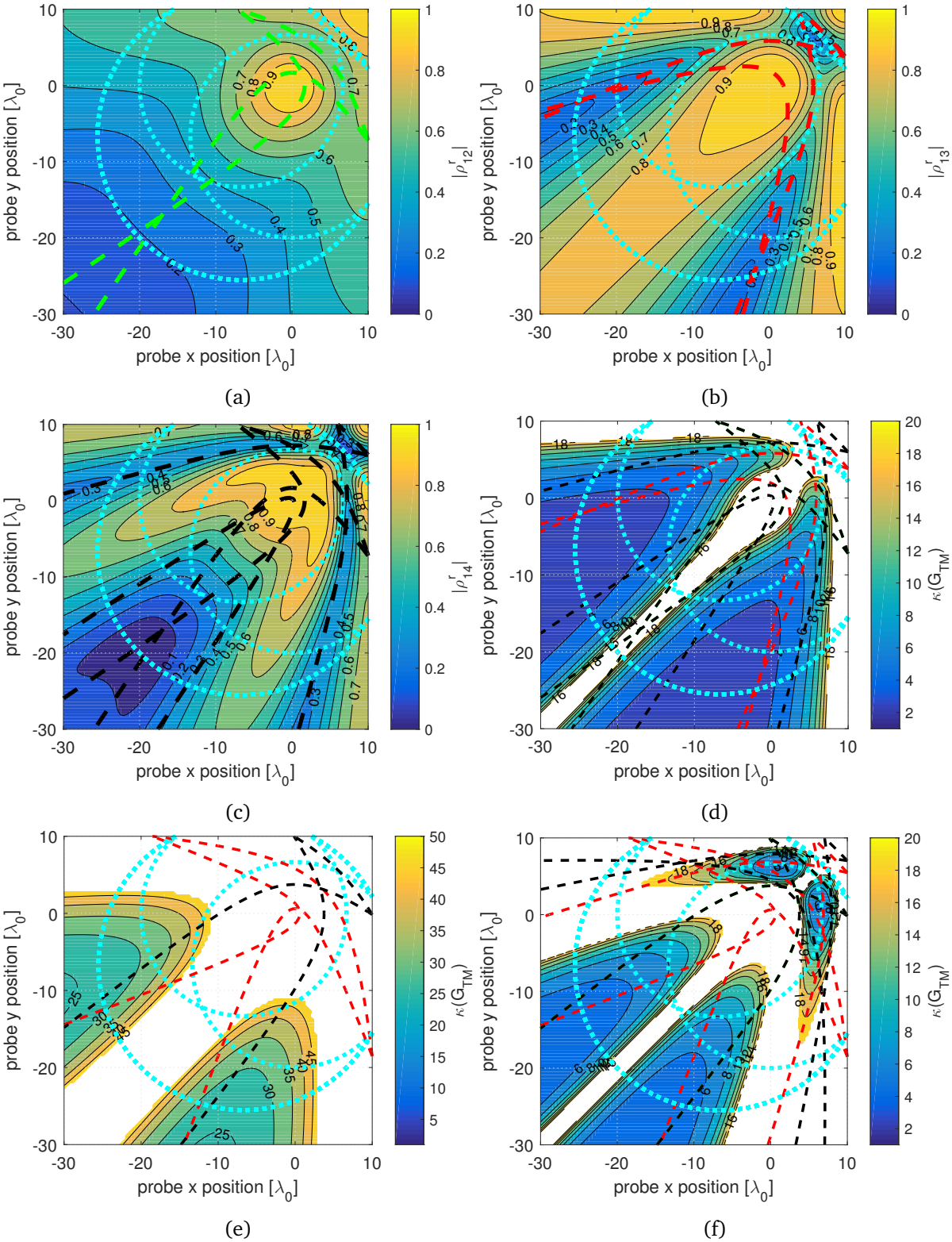

Figure 5.4 Conditioning patterns the impact of optimal hyperbolas (dashed) and conditioning circles (dotted) as function of the operating UFBW. Dihedral configuration, TM case, $d_v = d_h = 10\lambda_0$: (a) $\rho^r_{12}(\mathbf{G}_{TM})$, UFBW=9% (b) $\rho^r_{13}(\mathbf{G}_{TM})$, UFBW=9% (c) $\rho^r_{14}(\mathbf{G}_{TM})$, UFBW=9% (d) $\kappa(\mathbf{G}_{TM})$, UFBW=9% (e) $\kappa(\mathbf{G}_{TM})$, UFBW=4% (f) $\kappa(\mathbf{G}_{TM})$, UFBW=12%.

towards the plates and the corner, and improving the optimal level over the test zone to attain $\kappa(\mathbf{G}_{TM})_{\text{opt}} \approx 2.2$. If the UFBW is not adapted to the AUT-plate separations, whether being too narrow or too large, this would negatively impacts conditioning. For instance, Fig. 5.4d shows the condition number pattern when applying a global UFBW $= 4\%$. In this case the matrix is ill-conditioned almost all-over the test zone ($\kappa(\mathbf{G}_{TM}) \geq 25$). The same UFBW has worked well with the single-plate configuration using the same AUT-plate separation. It did not work in this case because the first hyperbolas family corresponding to UFBW/3 is actually an empty set with no AUT-plate separation respecting the criterion of generation of optimal hyperbolas. Consequently, the projection factor between the first and second rows is generally high allover the test zone, amplifying the global condition number as a result. On the other hand, rising the working UFBW has a similar effect as enlarging the AUT-plate separations may introduce worst hyperbolas which intersect optimal hyperbolas from other families. This is shown in Fig. 5.4e, where an UFBW$= 12\%$ is used. The impact of worst hyperbolas is clear as it reduces the size of optimal conditioning zones.

Globally, we may conclude that achieving well-conditioned systems in the TM case is possible provided that the UFBW is adapted to the set-up dimensions. Relatively larger operating UFBWs or set-up dimensions are required in order to achieve condition numbers of the same level as in the single-plate configuration. The required larger UFBWs are due to the higher number of used frequency samples (4) which need to be well spaced in order for the matrix rows to form a closely orthogonal set. If a narrow UFBW is implied, then the AUT-plate separations should be enlarged to guarantee the generation of optimal hyperbolas. The studied examples showed that using typical narrow UFBW ($< 6\%$), AUT-plate separations in the order of $10\lambda_0 - 20\lambda_0$ allowed to achieve condition number below 4 using a $40\lambda_0 \times 40\lambda_0$ test zone. Positions near the dihedral corner and in the immediate vicinity of the two plates are generally ill-conditioned and require very large UFBWs or AUT-plate separations in order to -partially- improve conditioning. If the set-up is symmetric, then diagonal positions are systematically ill-conditioned as the matrix is singular over these positions.

5.3.2.2 TE Model

Conditioning in the basic single plate TE model is governed by optimal circles over which the projection matrix $\mathbf{M}$ is unitary and whose conditioning is biased by conditioning circles defined by the distances spread. When introducing frequency diversity, optimal hyperbolas defined by the working UFBW also contribute to conditioning by enlarging the optimal zone. In the right dihedral case, an optimal circle is generated relative to each plate resulting in a total of three optimal circles. Moreover, frequency diversity which is necessary to balance the mathematical system introduces optimal hyperbolas relative to each plate. Perusing with the same reasoning as in the TM case, zones of optimal conditioning would be zones where the three optimal circles are most likely to intersect with the generated optimal hyperbolas and

conditioning circles corresponding to low projection factors. Recalling the conditioning pattern of the basic single-plate TE model, optimal zones are essentially in the vicinity of the plates where optimal circles intersect conditioning circles corresponding to lowest projection factors. Optimal hyperbolas may then be generated either to enlarge the optimal zone by using narrow UFBWs such that they are oriented far from the corresponding plates, or in order to optimize the conditioning level in the narrow region near the plate by using a high UFBW.

An example highlighting the discussed considerations is shown in Figs. 5.5a-5.5g for the same set-up used in the TM scenario ($d_v = d_h = 10\lambda_0$) with a UFBW=3%. Figs. 5.5a-5.5c plot respectively the projection factors between the first column and each of the remaining columns of the projection matrix highlighting the optimal circles corresponding to each plate. Correlation coefficients are calculated using the matrix columns rather than rows in order to eliminate the impact of the distances spread which is visualized using conditioning circles. The three optimal circles are located in the vicinity of the dihedral corner depending exclusively on distances separating each plate from the AUT. Figs. 5.5e-5.5f plot respectively the projection factors between the first column and each of the remaining columns of the free-space Green's function highlighting the generated first-order optimal hyperbolas corresponding to each plate. Except for the hypothetical plate which is relatively far from the AUT, the chosen UFBW directs the optimal hyperbolas far from the corresponding plates. The global condition number pattern is plotted in Fig. 5.5g showing, as expected, optimal regions near the plates with lowest values in regions where optimal hyperbolas intersects optimal circles. In this scenario the chosen parameters allowed achieving an optimal value $\kappa(\mathbf{G}_{TE})_{\text{opt}} \approx 5$. It is interesting to note that diagonal positions in the basic TE model are also ill-conditioned as is the case for the TM model. The matrix singularity in the TE case being less forward and may be spotted by noticing that the LOS and second image angles are either equal to $\frac{\pi}{4}$ or $\frac{3\pi}{4}$, hence,

$$\{\phi_0, \phi_2\} = \{\frac{\pi}{4}, \frac{3\pi}{4}\} \Rightarrow \begin{cases} \sin\phi_0 = \cos\phi_0 \\ \sin\phi_2 = \cos\phi_2 \end{cases}$$

On the other hand, the first and last images angles are complementary, it follows,

$$\phi_1 + \phi_3 = \frac{\pi}{2} \Rightarrow \begin{cases} \cos\phi_3 = \sin\phi_1 \\ \sin\phi_3 = \cos\phi_1 \end{cases}$$

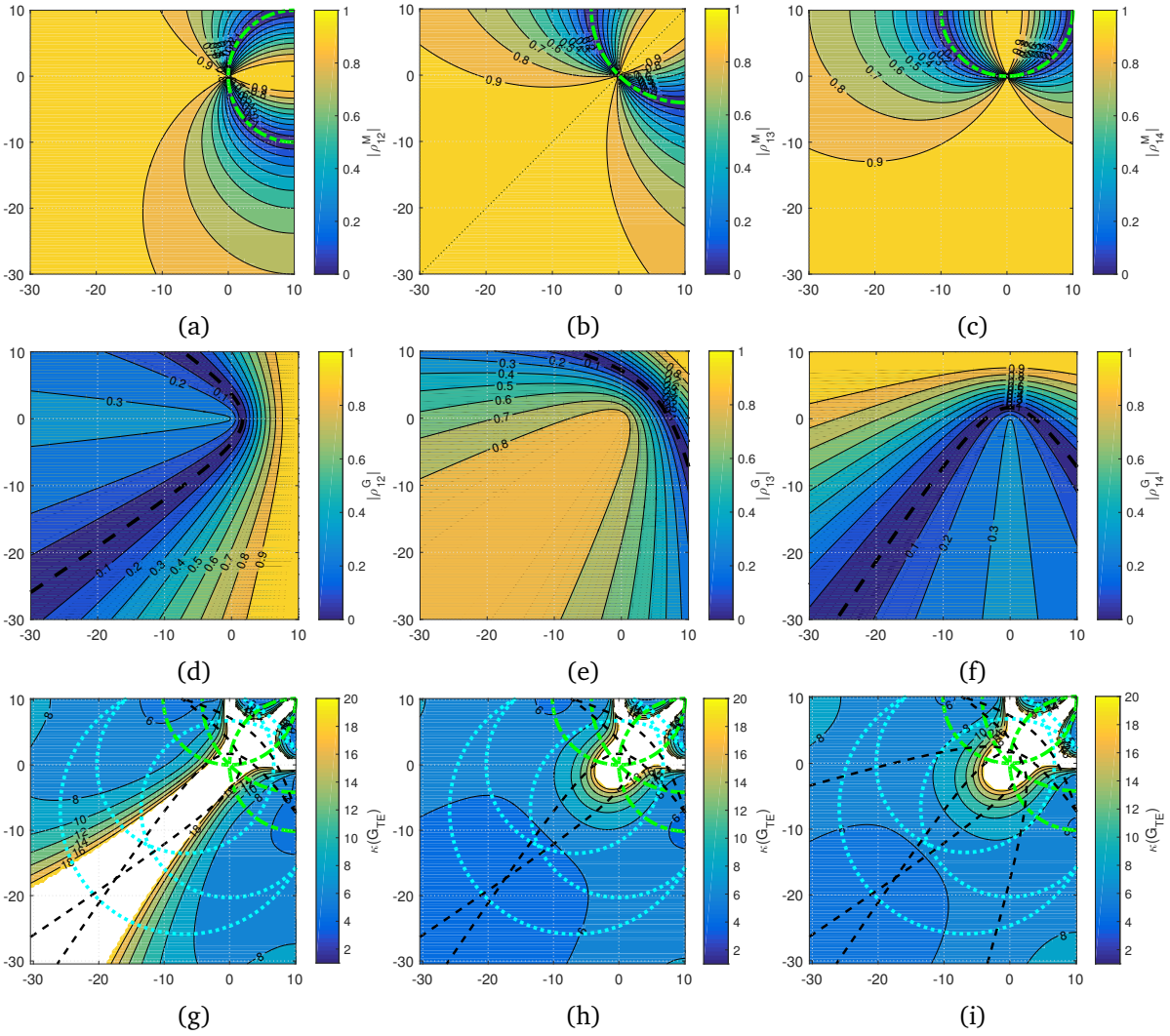

Figure 5.5 Conditioning patterns and impact of optimal hyperbolas (dashed), optimal circles (dot-dashed), and conditioning circles (dotted). dihedral configuration, TE case, $FBW = 3\%$, $d_v = d_h = 10\lambda_0$: (a) $\rho^c_{12}(\mathbf{M})$, $N_f = 2$ (b) $\rho^c_{13}(\mathbf{M})$, $N_f = 2$ (c) $\rho^c_{14}(\mathbf{M})$, $N_f = 2$ (d) $\rho^c_{12}(\mathbf{G})$, $N_f = 2$ (e) $\rho^c_{13}(\mathbf{G})$, $N_f = 2$ (f) $\rho^c_{14}(\mathbf{G})$, $N_f = 2$, (g) $\kappa(\mathbf{G}_M)$, $N_f = 2$ (h) $\kappa(\mathbf{G}_{TE})$, $N_f = 3$ (i) $\kappa(\mathbf{G}_{TE})$, $N_f = 4$.

Accordingly, the system matrix may be rewritten as follows,

$$\mathbf{G}_{TE}^{\text{diag}} = \begin{bmatrix} -\frac{e}{r_0}e^{-j\frac{2\pi}{c}f_0 r_0}\sin\phi_0 & \frac{e}{r_1}e^{-j\frac{2\pi}{c}f_0 r_1}\sin\phi_1 & -\frac{e}{r_2}e^{-j\frac{2\pi}{c}f_0 r_2}\sin\phi_2 & \frac{e}{r_1}e^{-j\frac{2\pi}{c}f_0 r_1}\cos\phi_1 \\ -\frac{e}{r_0}e^{-j\frac{2\pi}{c}f_1 r_0}\sin\phi_0 & \frac{e}{r_1}e^{-j\frac{2\pi}{c}f_1 r_1}\sin\phi_1 & -\frac{e}{r_2}e^{-j\frac{2\pi}{c}f_1 r_2}\sin\phi_2 & \frac{e}{r_1}e^{-j\frac{2\pi}{c}f_1 r_1}\cos\phi_1 \\ ----- & ----- & ----- & ----- \\ \frac{e}{r_0}e^{-j\frac{2\pi}{c}f_0 r_0}\sin\phi_0 & -\frac{e}{r_1}e^{-j\frac{2\pi}{c}f_0 r_1}\cos\phi_1 & \frac{e}{r_2}e^{-j\frac{2\pi}{c}f_0 r_2}\sin\phi_2 & -\frac{e}{r_1}e^{-j\frac{2\pi}{c}f_0 r_1}\sin\phi_1 \\ \frac{e}{r_0}e^{-j\frac{2\pi}{c}f_1 r_0}\sin\phi_0 & -\frac{e}{r_1}e^{-j\frac{2\pi}{c}f_1 r_1}\cos\phi_1 & \frac{e}{r_2}e^{-j\frac{2\pi}{c}f_1 r_2}\sin\phi_2 & -\frac{e}{r_1}e^{-j\frac{2\pi}{c}f_1 r_1}\sin\phi_1 \end{bmatrix}. \tag{5.8}$$

One may easily notice that the sum of the first and third rows is equal to the sum of the second and fourth rows, implying that one row may be expressed as a linear combination of the remaining rows. However, unlike the TM case, the singularity in the TE case is not systematic; it may be overcome by introducing new rows to the matrix by using more than two frequencies such that a linearly independent set of four rows is created. This is shown in Fig. 5.5h where three frequencies are used with the same global UFBW (3%). The figure shows that the singularity over diagonal positions between the AUT and the bottom left corner is clearly overcome attaining condition numbers in the order of 4.5 over certain positions. Rising the number of working frequencies further is not necessarily advantageous as it introduces narrower UFBWs between consecutive frequency samples that may yield no optimal hyperbolas and hence would not improve the global conditioning pattern. This is highlighted in Fig. 5.5i where four frequencies are used with the same UFBW, showing generally higher condition number levels with respect to the previous scenario. However, one may notice that in both scenarios diagonal positions near the dihedral corner are still ill-conditioned despite the non-singularity of the matrix. This is in fact due to the global UFBW applied in both scenarios (UFBW = 3%) which, as discussed earlier, generates optimal hyperbolas directed far from corresponding plates leaving the zone near the dihedral corner free from optimal hyperbolas. This may be overcome by applying a higher UFBW such that optimal hyperbolas are pushed towards the corresponding plates. An example is shown in Fig. 5.6 by applying two larger UFBWs (9% and 12%) and setting $N_f = 4$ such that the same TM-frequency parameters are used. The figure shows how rising the working UFBW improves conditioning near the dihedral corner, especially at 12%. However, an UFBW= 9% allowed to achieve a better global conditioning pattern due to the better distribution of optimal hyperbolas over the test zone given the set-up dimensions. In this scenario, optimal condition numbers as lows as $\kappa(\mathbf{G}_{TE})_{\text{opt}} \approx 2.2$ are achieved around the diagonal near the test zone bottom-left corner, which keep improving as the distance from the AUT rises, and which is the same optimal zone for the TM model.

We may conclude that achieving well-conditioned systems in the TE model is easier with respect to the TM model as it is less restricted by requirements in terms of set-up dimensions

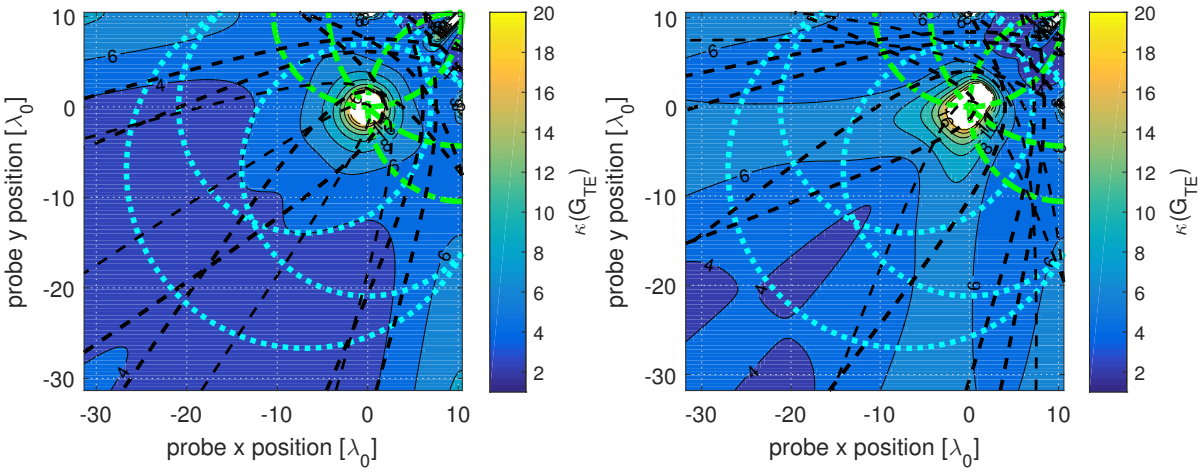

Figure 5.6 Adapting frequency parameters to the set-up dimensions. Dihedral configuration, TE case, $d_v = d_h = 10\lambda_0$, $N_f = 4$ (a) $\kappa(\mathbf{G}_{TE})$, UFBW= 9% (b) $\kappa(\mathbf{G}_{TE})$, UFBW= 12%.

and operating UFBWs. Conditioning in the basic TE model is somewhat the dual of the TM model as optimal regions are near the plates. However, diagonal positions in the basic TE model are also ill-conditioned if the set-up is symmetric. Using the same frequency parameters for both models allows achieving common optimal regions, along with improving the general TE conditioning pattern by eliminating the singularity over diagonal positions.

5.3.3 Angles Distribution and Mechanical Displacement Reduction

In what preceded it was shown that achieving well-conditioned systems is possible at specific positions depending on configuration parameters for each transverse model. At this level it is convenient to assess the usefulness of the proposed configuration in reducing the mechanical effort as function of valid positions. The objective being to know whether it is possible to develop rotation scenarios with maximum efficiency, i.e., allowing to theoretically cut the classical mechanical effort by four, or at least to be able to generally quantify the eventual mechanical effort reduction.

Evaluating the efficiency of the method requires a knowledge of the measured angles as function of the chosen probe position. Developing a position-angles mapping in the right dihedral case seems very difficult given the complexity of the configuration. Recall that the analytical formulation of the position-angles mapping in the single-plate configuration (Sec. 2.4.1) yielded a quartic equation for the simplest case. Hence developing a general algorithm in order to achieve maximum efficiency in the right dihedral case seems cumbersome. The complexity of the right dihedral configuration makes it convenient to assess the covered angles distribution as function of the probe position qualitatively, with the aim of developing rotation

scenarios specific to certain effective positions in terms of the covered angles, which may be retrieved numerically.

Globally, three configurations in terms of covered angles may be derived from the right dihedral configuration as function of the probe position in each of the four azimuthal quarter-planes. These configurations are depicted in Fig. 5.7, and may be summarized as follows,

- Configuration 1: The probe positioned in the quarter-plane containing the dihedral corner. In this case all covered angles lie in the same quarter-plane containing the dihedral corner, as shown in Fig. 5.7a.
- Configuration 2: The probe positioned in one of the quarter-planes adjacent to the quarter plane containing the dihedral corner. In this case covered angles are distributed over the half-plane formed by the two previous quarter-planes, as shown in Figs. 5.7b and 5.7c.
- Configuration 3: The probe positioned in the diagonal quarter-plane with respect to the quarter plane containing the dihedral corner. In this case covered angles are distributed allover the azimuthal plane with each angle being in a different quarter-plane as shown in Fig. 5.7d.

A rotation algorithm would generally be possible in one of three cases. The first when the four covered angles are linearly spaced such that the difference between each two consecutive angles $\Delta\phi$ is constant. Setting the sampling angle ϕ_s as an integer ratio of $\Delta\phi$,

$$m_b = \frac{\Delta\phi}{\phi_s}. \tag{5.9}$$

The AUT would be rotated $m_b - 1$ times before applying a jump of $(3m_b + 1)\phi_s$ in order to avoid interference between already covered angles and angles yet to be covered. Such an algorithm is most likely possible using configurations 1 and 3 where it seems theoretically possible to achieve uniform angles distribution. Using configuration 1, this algorithm would yield a maximum rotation efficiency if the covered range by the measurement angles is an integer ratio of 2π,

$$\phi_3 - \phi_1 = \frac{2\pi}{n}, \tag{5.10}$$

n being typically greater than 4 as all covered angles in this case lie in the first quadrant. This algorithm would perform well in this case for the TE model as it is possible to achieve well conditioned systems using positions in the first quadrant. Unfortunately, it would be hard to apply it in the TM model as positions in the first quadrant are generally ill-conditioned unless very large UFBWs or AUT-plates separations are introduced. This should not be the case when using configuration 3 as the probe is positioned in the third quadrant where optimal conditioned positions are easily achieved for both transverse models when using common frequency parameters. Achieving maximum efficiency in this case requires that the four measurement

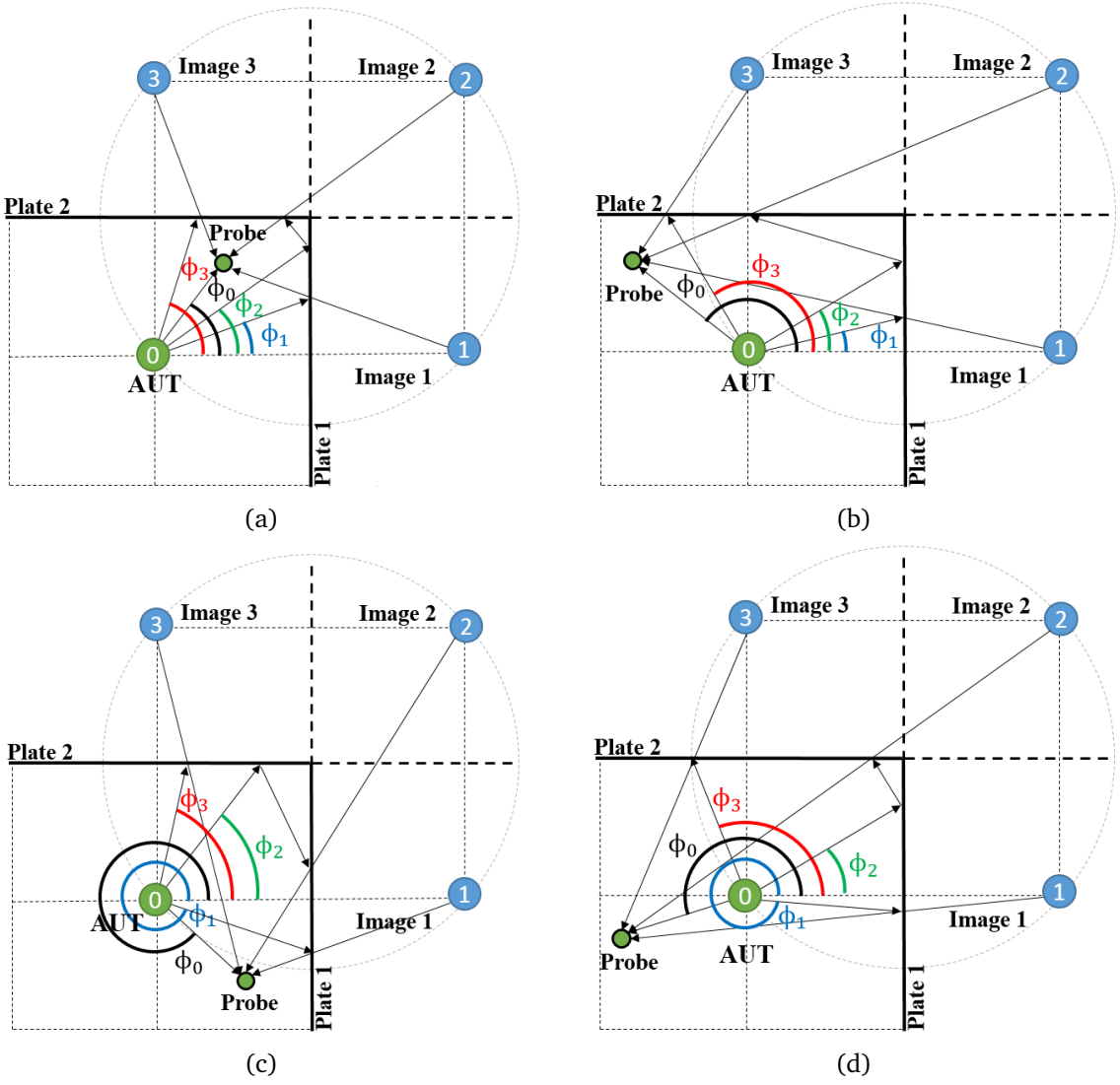

Figure 5.7 Angles distribution as function of the probe position: (a) All angles in the quarter-plane containing the dihedral corner (b) Angles distributed over a half-plane, first case (c) Angles distributed over a half-plane, second case (d) Angles distributed over all the azimuthal plane.

angles are uniformly distributed over the azimuthal plane, i.e., $\Delta\phi = \frac{\pi}{2}$ which seems hard to achieve. Alternatively, it is easily verified that a mechanical rotation reduction factor of 3 is achievable by neglecting the contribution of the first image and positioning the probe such that the remaining three measurement angles are uniformly distributed over an angular range $\Delta\phi_r$ which is equal to an integer ratio of the azimuthal range,

$$\Delta\phi_r = \phi_0 - \phi_2 = 2(\phi_3 - \phi_2) = \frac{2\pi}{n}. \tag{5.11}$$

In this case the AUT would be rotated $m_b - 1$ times before applying a jump of $(2m_b + 1)\phi_s$ in order to avoid interference between already covered angles and angles yet to be covered.

The second case where it is theoretically possible to develop an effective rotation algorithm is most related to configuration 2, where as shown by Figs. 5.7b and 5.7c, measurement angles are split into two groups each being in a different quarter-plane. Suppose that angles of the same group are characterized by a constant difference say $\Delta\phi_1$, which for instance would be expressed as follows using configuration 2 as depicted by Fig. 5.7b,

$$\phi_0 - \phi_3 = \phi_2 - \phi_1 = \Delta\phi_1. \tag{5.12}$$

A rotation algorithm of maximum efficiency would be possible if the difference between the two groups is an integer multiple of $\Delta\phi_1$,

$$\phi_3 - \phi_2 = \Delta\phi_2 = n\Delta\phi_1, \tag{5.13}$$

along with the global covered range by the measurement angles being an integer ratio of the azimuthal range,

$$\phi_0 - \phi_1 = \Delta\phi_r = \frac{2\pi}{m}. \tag{5.14}$$

In this case, a sampling angle equal to an integer ratio of $\Delta\phi_1$ should be applied,

$$\phi_s = \frac{\Delta\phi_1}{m_b}, \tag{5.15}$$

and hence a jump of $(m_b + 1)\phi_s$ is performed after each m_b rotations, and a jump of $\Delta\phi_2 + \phi_s$ is performed after each nm_b rotations. This algorithm has the advantage of being related to configuration 2 which requires placing the probe in either the second or the fourth quadrant which are characterized by the easiness of achieving well-conditioned positions. However, it has the inconvenience of the apparent difficulty of finding positions whose corresponding angles respect the set of listed criteria (Eqs. 5.12-5.15).

The last case where an effective rotation algorithm is conceivable, and where a theoretical mechanical rotation reduction factor of 3 is achievable consists in using diagonal positions, which is possible using either configuration 1 or 3. In this case, the contribution of the second

image is neglected; the remaining three angles being uniformly distributed over the covered angular range,

$$\Delta\phi = |\phi_3 - \phi_0| = |\phi_0 - \phi_1|, \tag{5.16}$$

the AUT would be rotated in the same fashion as in the first case algorithm that targeted a rotation effort reduction of 3. Unfortunately, this algorithm cannot be used in a TM model as diagonal positions are systematically ill-conditioned due to the system matrix singularity.

Globally, we may conclude that effective mechanical effort reduction is achievable in the right dihedral case using specific probe positions that yield uniform distributions of measurement angles. These positions and related angles may be retrieved numerically and may be tabulated for standard set-up dimensions.

5.3.4 Discussion about Practical Considerations

At this stage the mathematical viability of the simplified model of the right dihedral configuration and its theoretical usefulness in accelerating the measurement process being assessed, it is convenient to discuss the practical limitations of the proposed model. Generally, these are the same limitations discussed in the single-plate case and which may be amplified in the right dihedral case due to the configuration complexity. A brief discussion is presented here with focus on model related limitations.

The first limitation comes from the adopted far-field model, which is however independent from the configuration complexity level and is solely function of the tested antenna and the operating frequency. Hence, discussions held when dealing with the single-plate configuration also hold for the right dihedral configuration. The second limitation comes from the impact of the plates on the AUT free-space radiation resistance, and which was considered negligible in the single-plate configuration for useful AUT-plate separations. The presence of the second plate in the dihedral case amplifies the induced current by the normally reflected waves but the overall impact shall remain very weak for useful AUT-plate separations. The author of [81] noted that a separation between a HWD and the corner of a right dihedral reflector equal to $S = 0.35\lambda$ is sufficient to consider the dipole radiation resistance equal to its free-space radiation resistance. Next there are diffracted fields by the AUT aperture and the plates edges and corners which are naturally amplified due to the impact of the second plate. The study conducted in the single-plate case showed that positions near the plate are generally the best protected against the two types of diffractions. Keeping the same reasoning for the dihedral case, this would mean that positions near the corner in particular are very suitable in terms of diffracted fields, while positions diagonally away from the corner are very exposed to diffracted fields. As shown earlier, theses are -in general- respectively ill-conditioned and well-conditioned positions. Consequently, care must be given to these two error sources which were shown to be manageable with several solutions to reduce their respective impacts. Another error source

which is amplified in the right dihedral case is the infinitesimal losses introduced by the plates due to their finite conductivity, which would be amplified at the second image level. For instance, assuming that both plates have a common scalar reflection coefficient Γ modeling the amplitude attenuation of the reflected wave,

$$\Gamma = 1 - \delta, \tag{5.17}$$

where δ is the corresponding amplitude attenuation which is assumed very small. The second image would be characterized by the square of this reflection coefficient,

$$\Gamma^2 \approx 1 - 2\delta, \tag{5.18}$$

Consequently, infinitesimal losses introduced by the plates, are doubled at the second image level. The proposed models need to be updated by applying a Hadamard product between the simplified system matrices and a scalar reflection coefficients matrix modeling losses corresponding to each image. An error on estimating these losses would then be amplified at the ARP sample corresponding to the second image.

Finally, the developed models need also to be updated in order to take into account the frequency impact on the free-space ARP. Considering the general TM and TE models which involve the use of four frequency samples, the simplified system matrices may be updated by multiplying them with a diagonal matrix containing the three adapted α-terms,

$$\mathbf{G} = \boldsymbol{\alpha}\mathbf{G}_{\text{simplified}}, \tag{5.19}$$

$$\text{with } \boldsymbol{\alpha}_{TM} = \begin{bmatrix} 1 & 0 & 0 & 0 \\ 0 & \alpha_1 & 0 & 0 \\ 0 & 0 & \alpha_2 & 0 \\ 0 & 0 & 0 & \alpha_3 \end{bmatrix} \tag{5.20}$$

$$\text{and } \boldsymbol{\alpha}_{TE} = \begin{bmatrix} \boldsymbol{\alpha}_{TM} & | & 0 \\ --- & & --- \\ 0 & | & \boldsymbol{\alpha}_{TM} \end{bmatrix} \tag{5.21}$$

The approach adopted in order to estimate the frequency impact in the single-plate case, which involves a single α-term, and which consisted in spanning the space of solutions worked because the corresponding problem showed to be convex. The same approach may be applied in the basic right dihedral TE model which involves the use of two frequency samples, and thus a single α-term. In order to be able to solve for the three α-terms in the general right dihedral problem the corresponding error function should be assessed in order to verify if the problem is

convex. Global optimization methods may be used to solve this issue. This effort has not been performed in the present work and is left as a perspective.

5.3.5 Numerical Results

Numerical results to highlight the viability of the proposed method are presented for a right dihedral configuration using plates of infinite extent [1]. The α terms modeling the frequency impact on the free-space ARP are retrieved from Table 4.1 where they were calculated using the approach adopted in the single-plate model.

Results for the TM case are shown in Fig. 5.8 which compares the relative amplitude ARP error corresponding to the HWD and the bicone. In this scenario the configuration of Fig. 5.3e is used, which is characterized by equal AUT-plate separations $d_v = d_h = 15\lambda_0$ and an UFBW= 6%. The considered test zone is a $20\lambda_0 \times 10\lambda_0$ zone located below the diagonal at the positions shown in Fig. 5.8. The condition number pattern over the test zone is plotted in Fig. 5.8a showing relatively accepted values (< 5) over almost half the test zone and average values over the rest of the test zone < 12. Interestingly, error is generally lower in the bicone case than in in the dipole case. This is explained by the low level of the AUT-diffraction in the bicone case compared to the dipole case, as it was shown in Sec. 4.3.3; the impact of the AUT-diffraction in the present scenario being higher due to the contribution of the second plate. The LOS error in both cases is generally weak being below -40dB in the bicone case and below -35dB in the dipole case. Image error in the bicone case is more important at the second image level, oscillating between -32dB and values as low as -70dB in the well conditioned zone, and rises up to values in the order of -22dB in the ill-conditioned region at the right of the test zone. Otherwise error is higher over samples corresponding to the third image, where it is up-bounded by -24dB, then samples corresponding to the first images where it is up-bounded by -28dB. These results may be explained by extending the error spread rule retrieved for the single-plate model, and which stated that error spread is generally governed by the distances spread making image samples more vulnerable to error than LOS samples. In the dihedral case, the vulnerability of image samples to error is ordered by the distance separating each image from the probe. Accordingly, the second image samples are by default the most vulnerable to error due to the larger distance separating the second image from the test zone, while distances corresponding to the first and third images depend on the probe position with respect to the vertical and horizontal plates respectively. The test zone being closer to the first plate in the considered scenario, distances corresponding to the first image are consequently smaller than distances corresponding to the third image, making the related error lower. However, the error spread rule, which was developed based on a Gaussian model, should not be systematically generalized for the dihedral case independently of the considered

[1] Strictly speaking, the used plates are of finite dimensions as FEKO allows the generation of a single infinite PEC ground. The infinite plates are modeled by deactivating edge and corner diffracted rays, which is possible in FEKO using UTD plates, such that only direct and reflected rays are considered.

error source. This is highlighted by considering image errors corresponding to the dipole, where the third image error is generally higher than the second image error. The error pattern of the third image samples, being higher in the middle of the test zone where it rises to values above −30dB, and decays symmetrically as the probe is moved horizontally to the sides, suggests that the third image samples are impacted by the AUT position, which in this case is located between the test zone and the third image. Given the higher RCS of the dipole, the AUT is considered as an obstacle for vertically incidenting rays from the third image. This adds another criterion for choosing valid probe positions as each image has a related shadow region as function of its position with respect to the AUT and which depends on the AUT RCS.

Results for the TE case using the same configuration and frequency parameters are shown in Fig. 5.9 where both AUTs are oriented to the reference TE orientation (parallel to $\hat{x}$). Conditioning in this case is better than in the TM case which, as discussed earlier, follows from the system over-determination, being up-bounded by around 5.5. However, error is generally larger in the TE case than in the TM case; which is mainly due to the contribution of the field radial component. The LOS error is very low for both AUTs being below −40dB over the majority of the test zone. Error corresponding to the first and second images is considerably lower in the dipole case, whereas error corresponding to the third image is relatively lower in the bicone case. A general explanation of these observations is the low impact of the AUT diffraction over results corresponding to the dipole compared to the TM case, which is exclusively caused by the contribution of the horizontal plate; the ARP null being oriented towards the vertical plate. Hence, error is mainly due to the far-field model assumption, which holds better for the dipole due to its smaller dimensions. The first image error is particularly high in the bicone case, oscillating around −20dB over the majority of the test zone while error corresponding to samples of the remaining images for the same antenna is generally lower than −30dB. This may be explained by noticing that the first image samples correspond to angles closer to directions of weak power emission, which are characterized by a stronger impact of the field radial component, and a larger relative error as well; error being compared locally. On the other hand, error corresponding to the third image is larger in the dipole case, with values above −30dB over the majority of the test zone, most probably due to the impact of the AUT position given the error pattern which is similar to the TM error pattern corresponding to the same image. The dipole having larger RCS, it forms an obstacle to rays related to the third image with larger impact than in the bicone case. These results highlight the efficiency of the proposed method in retrieving ARP samples once optimal conditions are combines; that is when using optimal positions in terms of conditioning and applying the correct α terms, along with controlling the impact of the the various diffracted fields.

An additional advantage of the larger spatial diversity created by the dihedral configuration, other than further accelerating the measurement, is improving the performance of the regression. This is shown in Fig. 5.10 where a Gaussian RBF regression was applied to a set of eleven probes linearly spaced by $2\lambda_0$, corresponding to a horizontal cut at the top of the studied test

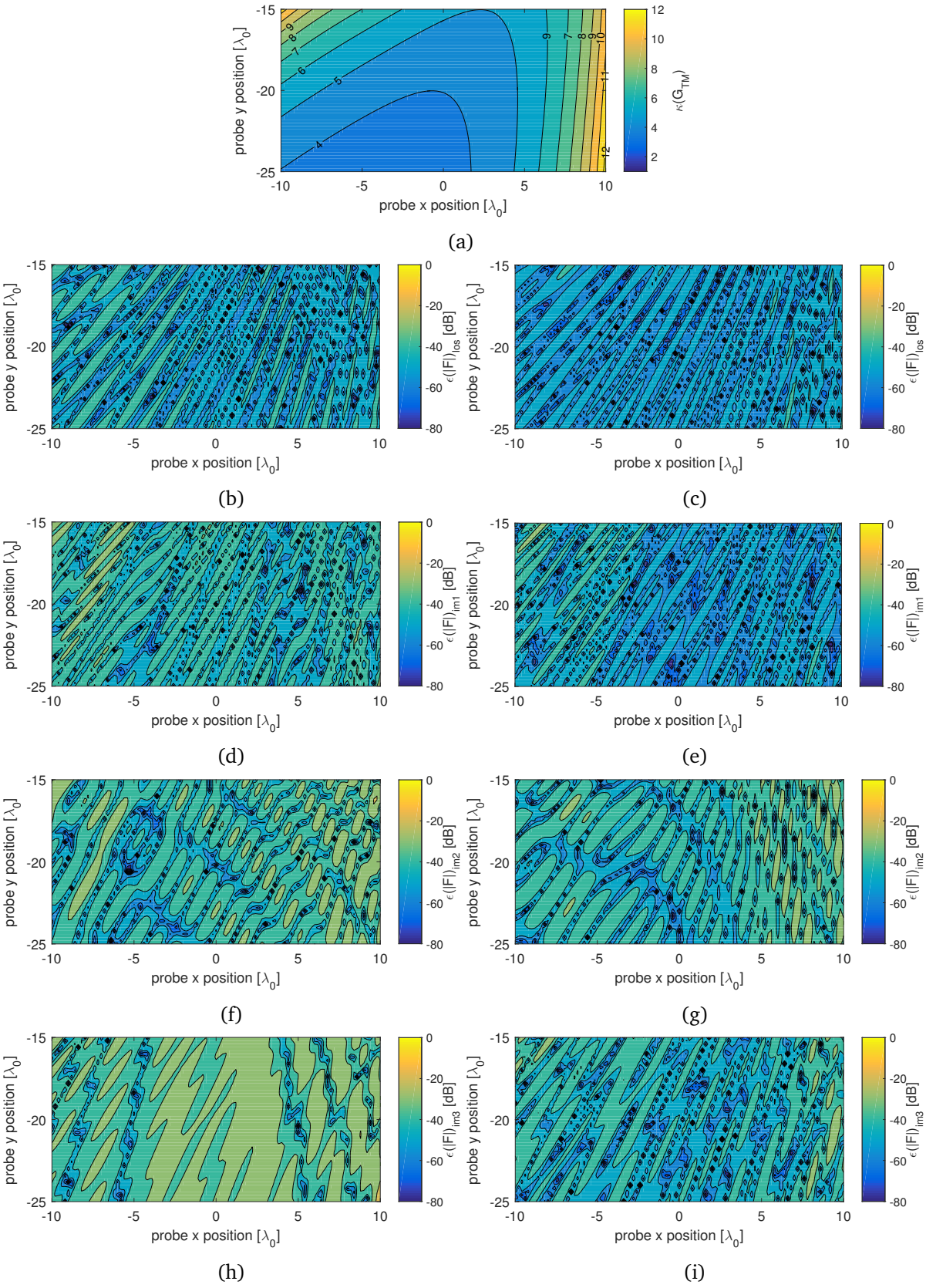

Figure 5.8 ARP error as function of the probe position in a hypothetical scenario (infinite PEC plates). Right dihedral configuration, TM case, $x_{pv} = x_{ph} = 15\lambda_0$, $FBW = 6\%$: (a) $\kappa(\mathbf{G}_{TM})$ (b) $\epsilon(\mathbf{F})_{los}$, HWD (c) $\epsilon(\mathbf{F})_{los}$, bicone (d) $\epsilon(\mathbf{F})_{im1}$, HWD (e) $\epsilon(\mathbf{F})_{im1}$, bicone (f) $\epsilon(\mathbf{F})_{im2}$, HWD (g) $\epsilon(\mathbf{F})_{im2}$, bicone (h) $\epsilon(\mathbf{F})_{im3}$, HWD (i) $\epsilon(\mathbf{F})_{im3}$, bicone.

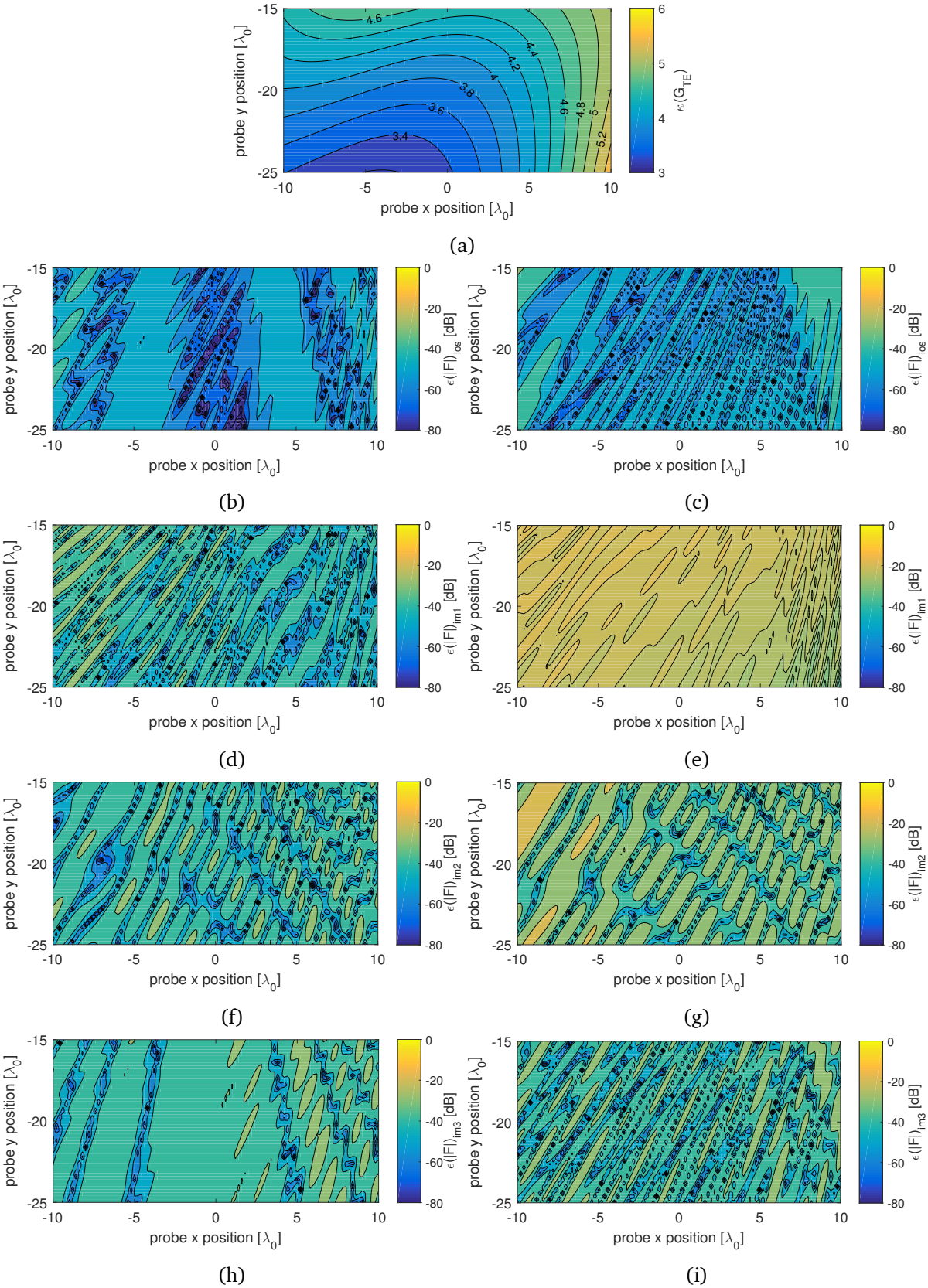

Figure 5.9 Performing the inversion with hypothetical infinite PEC plates, right dihedral configuration, TE case, $x_{pv} = x_{ph} = 15\lambda_0$, $FBW = 6\%$: (a) $\kappa(\mathbf{G}_{TM})$ (b) $\epsilon(\mathbf{F})_{los}$, HWD (c) $\epsilon(\mathbf{F})_{los}$, bicone (d) $\epsilon(\mathbf{F})_{im1}$, HWD (e) $\epsilon(\mathbf{F})_{im1}$, bicone (f) $\epsilon(\mathbf{F})_{im2}$, HWD (g) $\epsilon(\mathbf{F})_{im2}$, bicone (h) $\epsilon(\mathbf{F})_{im3}$, HWD (i) $\epsilon(\mathbf{F})_{im3}$, bicone.

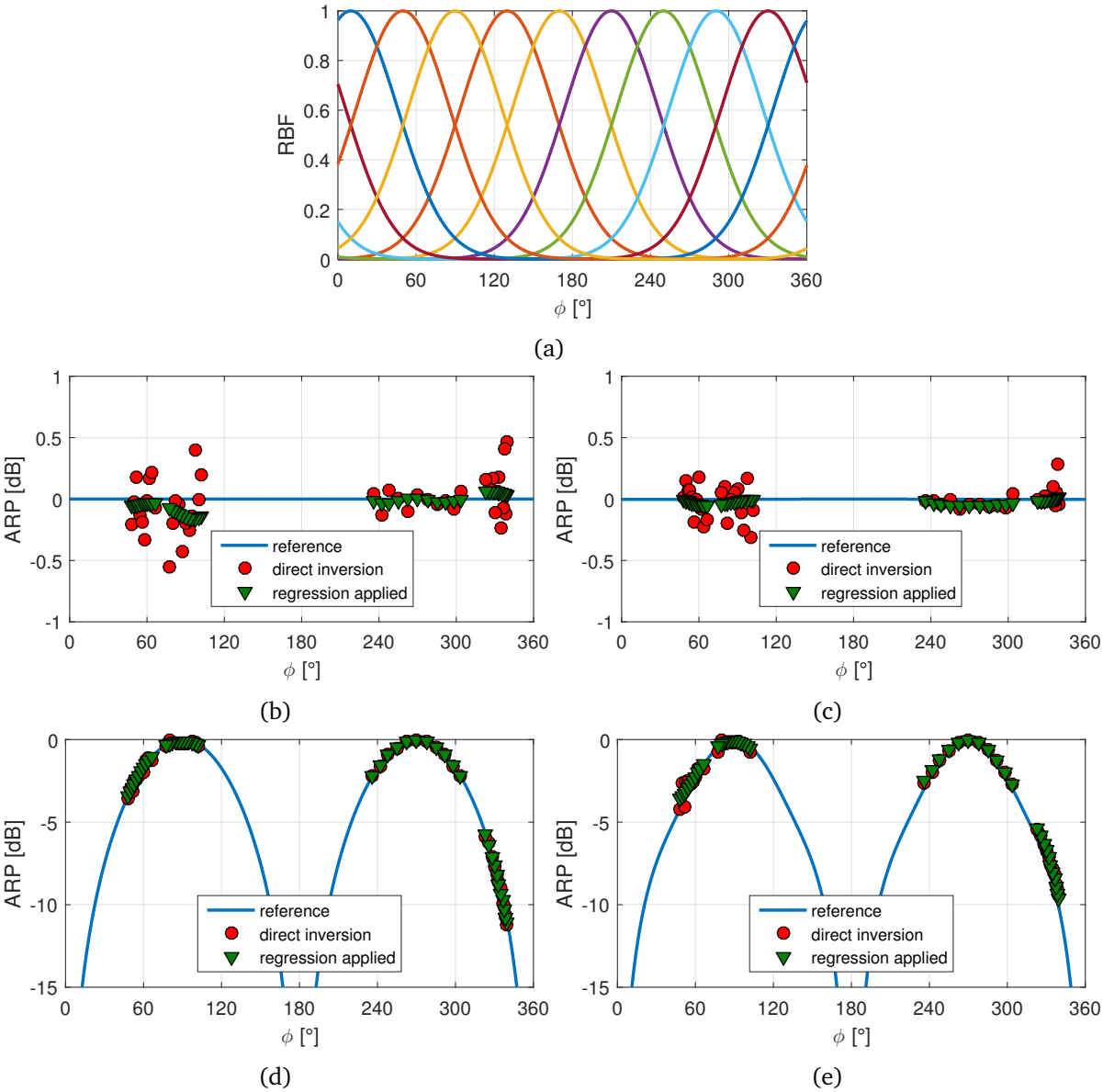

Figure 5.10 Applying linear regression to reduce the ARP error with 11 probe positions $(x_i, y_i) = (-10\lambda_0 : 2\lambda_0 : 10\lambda_0, -15\lambda_0)$: (a) Regression functions, Gaussian RBFs, $N_r = 10$, $s = 36°$ (b) Calculated ARP samples, TM mode, HWD (c) Calculated ARP samples, TM mode, bicone (d) Calculated ARP samples, TE mode, HWD (e) Calculated ARP samples, TE mode, bicone.

zone. As shown in the figure, the large number of measured samples improve the performance of the regression which reduces the maximum absolute error from ±0.6dB to ±0.2dB, and from ±0.4dB to ±0.1dB for the HWD and the bicone respectively in the TM mode. An equally adequate performance is observed is the TE mode, where regression reduced the maximum absolute error from ±0.5dB to ±0.2dB in the dipole case, and from ±1.5dB to ±0.5dB in the bicone case. Note that we are referring to the absolute error here rather than the relative error. One may notice the usefulness of extending the single-plate configuration in further accelerating the measurement. In this scenario, the measured samples are split into two groups, the LOS and the first image samples in one group (to the right in the figures), and the second and third image in the other group (to the left in the figures). Hence, samples of the first group correspond to a single-plate configuration, while samples of the second group represent the extension carried by the right dihedral configuration, which covers an angular range 250% larger than the range covered by samples of the first image. Although this scenario does not highlight the maximum efficiency that could be carried using an effective rotation scenario, it is however useful in highlighting the advantage of the right dihedral configuration with respect to the single-plate configuration.

5.4 Parallel-Plate Configuration

The parallel-plate configuration has the particularity of generating an infinite set of controlled echoes. A graphical representation of the set-up and the corresponding image theory model is shown in Fig. 5.11. The AUT is positioned between the two plates at distances d_1 and d_2 from the first and second plates respectively. If we refer to the source order by the number of reflections underwent by the corresponding echo, then as shown in Fig. 5.11, the image theory models this configuration by extending the original set-up horizontally in both directions with a mirror effect alternating the source orientation and position within the virtual set-up corresponding to each order [84]. Accordingly, horizontal positions of the virtual sources are retrieved by a simple algorithm that takes into account the mirror effect, the vertical positions being the same as the AUT vertical position. Images' positions may be expressed by the following equations,

$$\text{odd order images: } x^n = \begin{cases} (n+1)d_1 + (n-1)d_2 & \text{right images} \\ -\left[(n+1)d_2 + (n-1)d_1\right] & \text{left images} \end{cases}, \; n \in 2\mathbb{N}^* + 1 \tag{5.22}$$

$$\text{even order images: } x^n = \begin{cases} n(d_1+d_2) & \text{right images} \\ -n(d_1+d_2) & \text{left images} \end{cases}, \; n \in 2\mathbb{N}^* \tag{5.23}$$

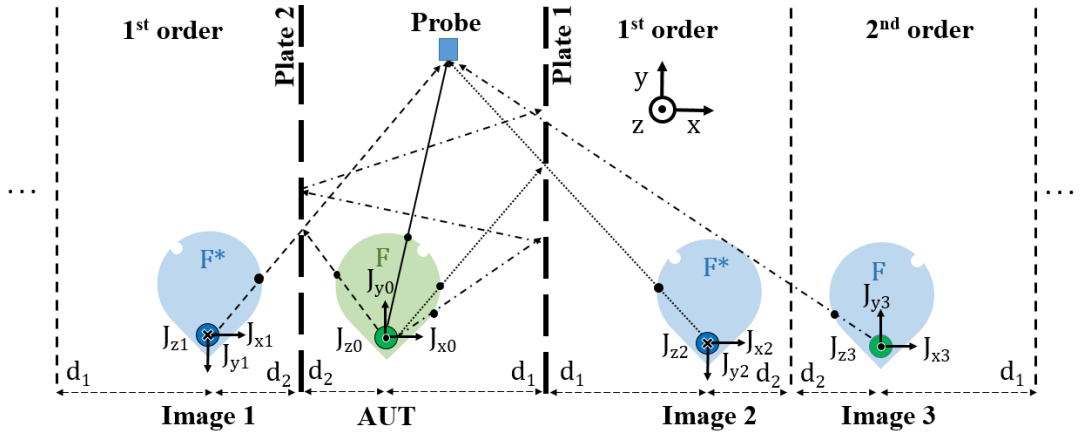

Figure 5.11 Graphical representation of the parallel-plate configuration with insight into the polarization of the closet three images into the AUT.

Measurement angles are then retrieved by applying a forward Cartesian-to-spherical coordinates transformation. Fig. 5.11 also provides an insight into the polarization of the excitation of each image, showing the normal component with respect to the plate (J_x) unchanged at the images level, whereas parallel components (J_y and J_z) alternating their directions at each image order.

The field intercepted by the probe is the superposition of the field generated by the AUT and fields generated by all the images. A mathematical model requires truncating the number of contributing images in order to allow a numerical implementation. It is then convenient to study the impact of truncating the infinite number of images on the proposed model.

5.4.1 Truncating the Number of Contributing Images

The aim of this study is the assessment of the level of field error resulting from truncating the number of contributing images, the actual number being infinite. Several factors suggest that the number of images may be truncated to relatively small numbers. The first being the fact that the image order and the corresponding distance separating it from the probe grow proportionally. Accordingly, higher order images are positioned far from the probe and hence they contribute less to the overall field. Moreover, by taking into account small losses introduced by the plate which attenuate the field amplitude after each reflection, then fields generated by higher order images, which correspond to higher numbers of reflections, are more attenuated with respect to fields corresponding to lower order images. Also, if the AUT is directive, then if it is oriented such that directions of weak power emission are directed towards the plate, the contribution of higher order images is cut down more rapidly. Truncating the number of contributing images is also motivated by the fact that higher order images correspond to measurement angles that tend rapidly towards the $[0°, 180°]$-range limits for useful set-up dimensions. This is highlighted in Fig. 5.12 which shows angles covered by two different set-ups respectively characterized by equal AUT-plate separations $d_1 = d_2 = 5\lambda_0$ and $d_1 = d_2 = 10\lambda_0$, the probe being positioned

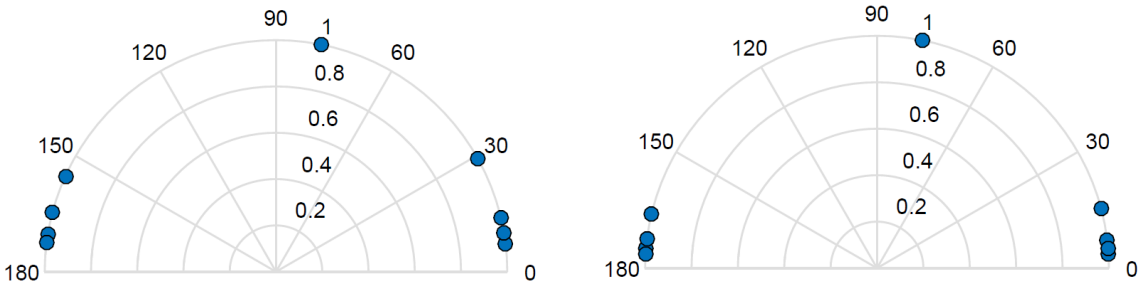

Figure 5.12 Angles covered by the parallel plates configuration as function of the AUT-plates separations. Probe positioned at $(x, y) = (1\lambda_0, 5\lambda_0)$, number of considered images $N_i = 6$ (a) $d_1 = d_2 = 5\lambda_0$ (b) $d_1 = d_2 = 10\lambda_0$.

at $(x, y) = (1\lambda_0, 5\lambda_0)$. Considering the contribution of a total number of eight images equally distributed over the right and left sides (up to fourth order images), the first set-up shows low angular contribution of the two highest order sets with respect to each others, having angles covered by both sets being very close. Rising the AUT-plate separations with respect to the AUT-probe separation further reduces the angular contribution of higher order images, as is the case for the second set-up where all sets other than first-order images cover close angles. Accordingly, higher order images contribute less to the measurement, which motivates truncating the number of contributing images. Finally, the number of images N_i determines the dimensions of the mathematical system, setting a lower limit to the number of required frequency samples in order to balance the system, which is equal to the number of images plus the AUT ($N_f = N_i + 1$) in the TM model, and half that number in the basic TE model. Consequently, rising the number of contributing images requires the ability of well predicting the associated frequency impact on the free-space ARP, which is naturally more complicated for higher numbers of frequency samples.

To verify the field error due to the truncation, a synthetic study based on the far-field model is conducted by comparing the field generated using a variant number of images to a reference field calculated by a sufficiently large number of images, N_{ref}, set to 300 here. Results generated using the two set-ups used in order to assess the angular contribution of higher order images (Fig. 5.12) are shown in Fig. 5.13 for a number of contributing images varying between 1 and 30. Figs. 5.13a and 5.13b show results for an AUT with a hypothetical isotropic ARP. Using the first set-up, error is very high over the E_y component being above -10dB for all considered number of images, whereas it is considerably lower over the E_x component being generally below -20dB down to less than -30dB for $N_i > 15$. On the other hand, error over the TM component E_z is considerably high for $N_i < 5$ (> -20dB) but is attenuated gradually to very low levels, oscillating between -20dB and -60dB. In order to explain these observations, note that TE fields are biased by the corresponding measurement angles in addition to the natural attenuation following the distance separating each source from the probe. Normalizing all

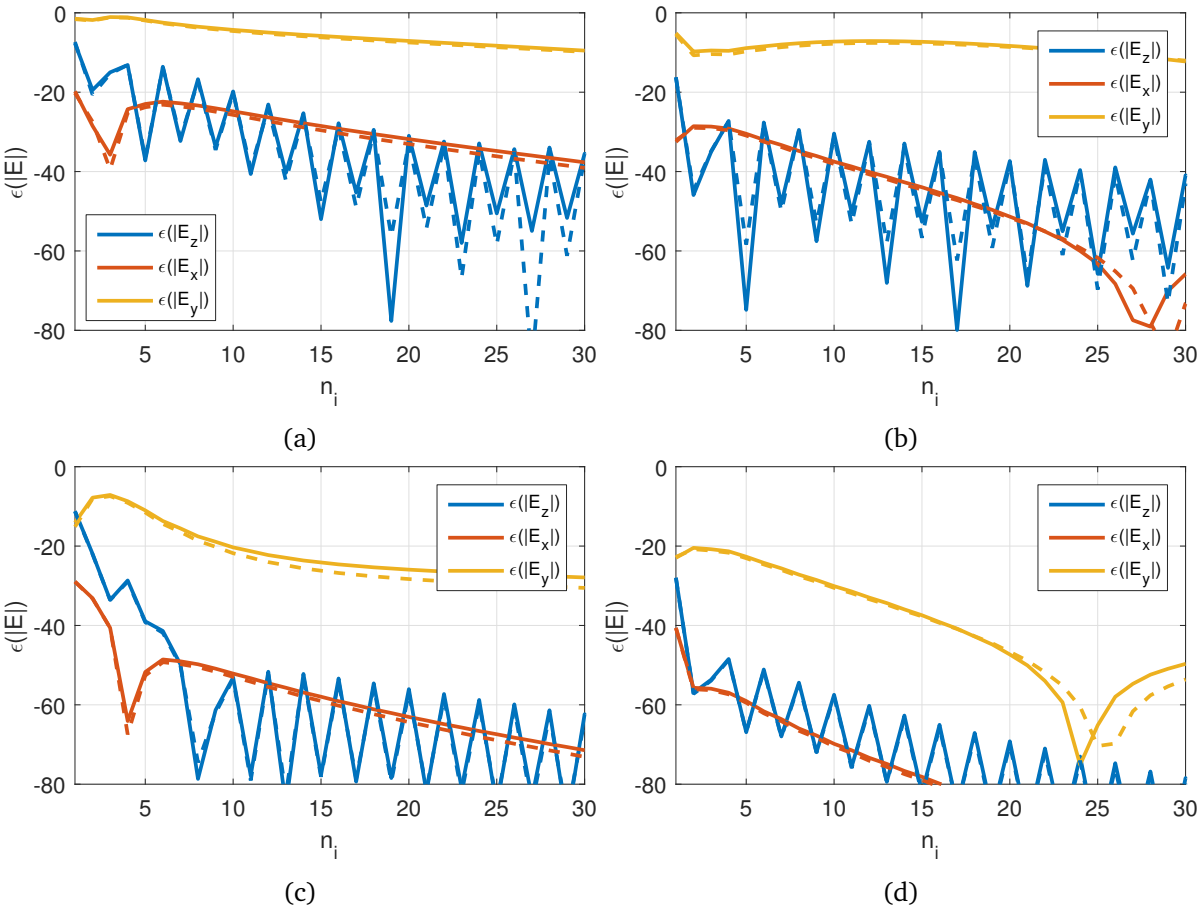

Figure 5.13 Field relative amplitude error as function of the number of contributing images, reference taken using 300 images, and impact of a scalar amplitude attenuation of 1% introduced by the plate (dashed): (a) $d_1 = d_2 = 5\lambda_0$, isotropic ARP (b) $d_1 = d_2 = 10\lambda_0$, isotropic ARP (c) $d_1 = d_2 = 5\lambda_0$, sinusoidal ARP (d) $d_1 = d_2 = 10\lambda_0$, sinusoidal ARP.

quantities with respect to the common ARP value (isotropic case), the relative field amplitude error for each component may be expressed by the following equations,

$$\epsilon\left[E_x(N_i)\right] = \frac{\left|\left\|\sum_{i=0}^{N_i} -G_{TE}^i \sin\phi_i\right\| - \left\|\sum_{i=0}^{N_{\text{ref}}} -G_{TE}^i \sin\phi_i\right\|\right|}{\left\|\sum_{i=0}^{N_{\text{ref}}} -G_{TE}^i \sin\phi_i\right\|} \tag{5.24}$$

$$\epsilon\left[E_y(N_i)\right] = \frac{\left|\left\|\sum_{i=0}^{N_i} p_i G_{TE}^i \cos\phi_i\right\| - \left\|\sum_{i=0}^{N_{\text{ref}}} p_i G_{TE}^i \cos\phi_i\right\|\right|}{\left\|\sum_{i=0}^{N_{\text{ref}}} p_i G_{TE}^i \cos\phi_i\right\|}, \tag{5.25}$$

where G^i is the free-space Green's function corresponding to the i$^{\text{th}}$ image, and p_i is the polarization term to take into account the alternating orientations of the J_y excitation corresponding to images of different orders,

$$p_i = \begin{cases} 1 & \text{even image order} \\ -1 & \text{odd image order} \end{cases} \tag{5.26}$$

Recalling that higher order images correspond to measurement angles in the vicinity of the $[0°, 180°]$-range limits, consequently their corresponding E_y fields are amplified with respect to lower order images by the projection operator $(\cos\phi_i)$, in contrast with E_x components where fields corresponding to higher order images are rapidly attenuated by the projection operator $(\sin\phi_i)$. The E_y components related to lower order images (and to the LOS) are particularly very attenuated given the chosen probe position, i.e.,

$$\phi_i \longrightarrow \frac{\pi}{2} \text{ when } i \longrightarrow 0,$$

making the contribution of higher order images as important as lower order images.

On the other hand, the TM component E_z is exclusively attenuated by the distance separating each source from the probe. The corresponding error may be expressed as follows,

$$\epsilon\left[E_z(N_i)\right] = \frac{\left|\left\|\sum_{i=0}^{N_i} p_i G^i_{TE}\right\| - \left\|\sum_{i=0}^{N_{\text{ref}}} p_i G^i_{TE}\right\|\right|}{\left\|\sum_{0=1}^{N_{\text{ref}}} p_i G^i_{TE}\right\|}, \tag{5.27}$$

which explains the gradual attenuation of the corresponding error. Enlarging the AUT-plates separations reduces the general error as images are pushed away from the the probe. As shown by Fig. 5.13b, which corresponds to the second set-up ($d_v = d_h = 10\lambda_0$), error over the E_x and E_z components is reduced to levels below -30dB for $N_i > 2$. However, error over the E_y component remains high, around -10dB, due to the important contribution of higher order images. The impact of small losses introduced by the plate in reducing the contribution of higher order images is assessed by introducing a scalar reflection coefficient equal to $\Gamma = 0.99$. Results are plotted in the same figures using dashed style. The impact is generally very weak and may be neglected for the considered image numbers.

Figs 5.13c and 5.13d show results for an AUT having a sinusoidal ARP, which would correspond to the azimuthal cut of the HWD ARP in TE mode when oriented in the reference orientation set in the previous chapters. In this case, the APR nulls being directed towards the two plates, 5 images are sufficient using the first set-up to reduce error over both E_x and E_z components below -40dB; error over the E_y component remaining generally high, exceeding

−30dB for all considered number of images. Using the second set-up, error may be neglected over the E_x and E_z components for useful numbers of images, with error over the E_y component considerably reduced to levels below −30dB for $N_i \geq 10$. From theses results we may conclude that useful AUT-plates separations, in the order of $10\lambda_0$, are sufficient to truncate the number of contributing images to less than 10 images, with error over the E_y component, and general error when directions of maximum power emission are directed towards the plates may be reduced by applying linear regression.

5.4.2 Mathematical Model

Mathematical models for the TM and TE modes may be developed following the same approach as for the single-plate and dihedral configurations, i.e., by introducing frequency diversity in order to balance the mathematical systems. The only difference with the parallel-plate configuration is the fact that the number of considered images N_i, which defines the system dimensions, is set manually rather than being naturally defined by the configuration. The choice of N_i should however approximate the number of contributing echoes in order to reduce the truncation error. The same set of simplifying approximations is maintained, i.e., the plates are considered PEC and of infinite extent, and the AUT dimensionless and frequency independent. These assumptions shall simplify the conditioning study.

5.4.2.1 TM Case

The number of frequencies required to balance the mathematical system in the TM model is at least equal to the number of considered sources, which is $N_i + 1$. A square system matrix is characterized by $N_f = N_i + 1$, and is formed by applying a Hadamard product similar to the one describing the dihedral TM model (Eq. 5.3) between the free-space Green's matrix and the polarization matrix. The frequency vector characterizing rows of the free-space Green's matrix is generated using the same model which is by having frequency samples being uniformly spaced over the working UFBW. Whereas the polarization matrix is generated based on Eq. 5.26 taking into account the alternating orientations of the TM excitation corresponding to images of different orders. Accordingly, the system is expressed as follows,

$$\begin{bmatrix} E(f_0) \\ E(f_1) \\ \vdots \\ E(f_{N_i}) \end{bmatrix}_{\mathbf{E}_p} = \begin{bmatrix} p_1 \frac{e^{-j\frac{2\pi}{c}f_0 r_1}}{r_0} & p_2 \frac{e^{-j\frac{2\pi}{c}f_0 r_2}}{r_1} & \cdots & \frac{e^{-j\frac{2\pi}{c}f_0 r_0}}{r_3} & \cdots & p_{N_i-1}\frac{e^{-j\frac{2\pi}{c}f_0 r_{N_i-1}}}{r_{N_i-1}} & p_{N_i}\frac{e^{-j\frac{2\pi}{c}f_0 r_{N_i}}}{r_{N_i}} \\ p_1 \frac{e^{-j\frac{2\pi}{c}f_1 r_1}}{r_0} & p_2 \frac{e^{-j\frac{2\pi}{c}f_1 r_2}}{r_1} & \cdots & \frac{e^{-j\frac{2\pi}{c}f_1 r_0}}{r_3} & \cdots & p_{N_i-1}\frac{e^{-j\frac{2\pi}{c}f_1 r_{N_i-1}}}{r_{N_i-1}} & p_{N_i}\frac{e^{-j\frac{2\pi}{c}f_1 r_{N_i}}}{r_{N_i}} \\ \vdots & \vdots & & \vdots & & \vdots & \vdots \\ p_1 \frac{e^{-j\frac{2\pi}{c}f_{N_i} r_1}}{r_0} & p_2 \frac{e^{-j\frac{2\pi}{c}f_{N_i} r_2}}{r_1} & \cdots & \frac{e^{-j\frac{2\pi}{c}f_{N_i} r_0}}{r_3} & \cdots & p_{N_i-1}\frac{e^{-j\frac{2\pi}{c}f_{N_i} r_{N_i-1}}}{r_{N_i-1}} & p_{N_i}\frac{e^{-j\frac{2\pi}{c}f_{N_i} r_{N_i}}}{r_{N_i}} \end{bmatrix}_{\mathbf{G}_{TM}} \begin{bmatrix} F(\phi_1) \\ F(\phi_2) \\ \vdots \\ F(\phi_0) \\ \vdots \\ F(\phi_{N_i}) \end{bmatrix}_{\mathbf{F}}. \tag{5.28}$$

Note that sources in the mathematical model are sorted by referring to the image model as depicted by Fig. 5.11 by setting the first source as the leftmost image and going rightward.

5.4.2.2 TE Case

The number of frequencies required in order to balance the mathematical system in the TE model is half the number of considered sources. However, recalling the studies carried over the single-plate and dihedral configurations, one would expect that using the same number of frequencies as in the TM model, which over-determines the system, is advantageous in terms of both conditioning and ARP results. The system matrix is formed by applying a Hadamard product similar to the one describing the dihedral TE model (Eq. 5.6) between the free-space Green's matrix, the projection matrix, and the polarization matrix. The polarization matrix keeps entries related to the E_x component unchanged, and alternates signs of entries related to the E_y component based on Eq. 5.26. Accordingly, the system matrix may be expressed as follows,

$$\begin{bmatrix} E_x(f_0) \\ E_x(f_1) \\ \vdots \\ E_x(f_{N_f-1}) \\ --- \\ E_y(f_0) \\ E_y(f_1) \\ \vdots \\ E_y(f_{N_f-1}) \end{bmatrix}_{\mathbf{E}_p} = \begin{bmatrix} -\frac{e^{-j\frac{2\pi}{c}f_0 r_1}}{r_1}\sin\phi_1 & -\frac{e^{-j\frac{2\pi}{c}f_0 r_2}}{r_2}\sin\phi_2 & \cdots & -\frac{e^{-j\frac{2\pi}{c}f_0 r_0}}{r_0}\sin\phi_0 & \cdots & -\frac{e^{-j\frac{2\pi}{c}f_0 r_{N_i}}}{r_{N_i}}\sin\phi_{N_i} \\ -\frac{e^{-j\frac{2\pi}{c}f_1 r_1}}{r_1}\sin\phi_1 & -\frac{e^{-j\frac{2\pi}{c}f_2 r_2}}{r_2}\sin\phi_2 & \cdots & -\frac{e^{-j\frac{2\pi}{c}f_3 r_0}}{r_0}\sin\phi_0 & \cdots & -\frac{e^{-j\frac{2\pi}{c}f_4 r_{N_i}}}{r_{N_i}}\sin\phi_{N_i} \\ \vdots & \vdots & \vdots & \vdots & & \\ -\frac{e^{-j\frac{2\pi}{c}f_{N_f-1} r_1}}{r_1}\sin\phi_1 & -\frac{e^{-j\frac{2\pi}{c}f_{N_f-1} r_0}}{r_2}\sin\phi_2 & \cdots & -\frac{e^{-j\frac{2\pi}{c}f_{N_f-1} r_0}}{r_0}\sin\phi_0 & \cdots & -\frac{e^{-j\frac{2\pi}{c}f_{N_f-1} r_{N_i}}}{r_{N_i}}\sin\phi_{N_i} \\ ------ & ------ & ------ & ------ & ------ & ------ \\ p_1\frac{e^{-j\frac{2\pi}{c}f_0 r_1}}{r_1}\cos\phi_1 & p_2\frac{e^{-j\frac{2\pi}{c}f_0 r_2}}{r_2}\cos\phi_2 & \cdots & \frac{e^{-j\frac{2\pi}{c}f_0 r_0}}{r_0}\cos\phi_0 & \cdots & p_{N_i}\frac{e^{-j\frac{2\pi}{c}f_0 r_{N_i}}}{r_{N_i}}\cos\phi_{N_i} \\ p_1\frac{e^{-j\frac{2\pi}{c}f_1 r_1}}{r_1}\cos\phi_1 & p_2\frac{e^{-j\frac{2\pi}{c}f_2 r_2}}{r_2}\cos\phi_2 & \cdots & \frac{e^{-j\frac{2\pi}{c}f_3 r_0}}{r_0}\cos\phi_0 & \cdots & p_{N_i}\frac{e^{-j\frac{2\pi}{c}f_4 r_{N_i}}}{r_{N_i}}\cos\phi_{N_i} \\ \vdots & \vdots & \vdots & \vdots & & \\ p_1\frac{e^{-j\frac{2\pi}{c}f_{N_f-1} r_1}}{r_1}\cos\phi_1 & p_2\frac{e^{-j\frac{2\pi}{c}f_{N_f-1} r_0}}{r_2}\cos\phi_2 & \cdots & \frac{e^{-j\frac{2\pi}{c}f_{N_f-1} r_0}}{r_0}\cos\phi_0 & \cdots & p_{N_i}\frac{e^{-j\frac{2\pi}{c}f_{N_f-1} r_{N_i}}}{r_{N_i}}\cos\phi_{N_i} \end{bmatrix}_{\mathbf{G}_{TE}} \begin{bmatrix} F(\phi_1) \\ F(\phi_2) \\ \vdots \\ F(\phi_0) \\ \vdots \\ F(\phi_{N_i}) \end{bmatrix}_{\mathbf{F}} \tag{5.29}$$

Ideally, $N_f = N_i + 1$ such that the same frequency parameters are used for both transverse models.

5.4.3 Conditioning Issues

As for the right dihedral case, the conditioning study for the parallel-plate configuration, which is further more complex, is also based on the single-plate model. The approach adopted herein is by reducing the parallel-plate configuration to a set of single-plate configurations, mainly two single-plate configurations as first-order images have generally the most important impact. Accordingly, the behavior of the condition number is studied with respect to optimal hyperbolas, optimal circles, and conditioning circles developed in the single-plate study.

5.4.3.1 TM Model

The TM model requires using a relatively large number of frequencies to balance the system given the relatively high number of considered images with respect to previously studied models. This implies dividing the global working UFBW to much narrower UFBWs, which as shown for the dihedral case, would require the smaller UFBW which models the projection between each two successive rows to be large enough in order to allow the generation of an optimal hyperbola. The subtility of the TM model follows from the fact that this would result in enlarging the global UFBW which yields the generation of higher order optimal hyperbolas but also worst hyperbolas which interfere with optimal hyperbolas from other families and reduces the optimal zone. As an illustration let us consider a number of examples of the behavior of the condition number as function of the operating UFBW as depicted in Fig. 5.14. The set-up used in these scenarios is characterized by equal AUT-plate separations $d_1 = d_2 = 12\lambda_0$, and a $40\lambda_0 \times 24\lambda_0$ test zone bounded by the two plates from the sides and by the AUT from the bottom. Conditioning circles corresponding to $\rho = 0.3$, and optimal hyperbolas corresponding to each scenario are superposed to each related conditioning pattern. Note that, for simplicity and in order to have more proper plots, only first-order hyperbolas are plotted. Fig. 5.14a shows the conditioning pattern when considering a number of images $N_i = 6$, with an UFBW=8% which is somewhat adapted to the configuration parameters. The symmetry of the set-up induces a symmetrical conditioning pattern with two identical optimal regions in each half of the test zone. Unlike the single-plate and dihedral configurations, conditioning in this case does not necessarily improve when the AUT-probe separation grows. Instead, the condition number takes its minimum value ($\kappa(\mathbf{G}_{TM})_{\text{opt}} \approx 4.7$) at a vertical AUT-probe separation around $20\lambda_0$, and raises gradually as the probe is moved in all directions. In view of this, positions near the AUT, near the plate, at the horizontal center of the test zone, and at large distances from the AUT ($40\lambda_0$) are all ill-conditioned. Optimal conditioned regions are characterized by the intersection of a large number of optimal hyperbolas with conditioning circles corresponding to low projection factors. The chosen UFBW along with the AUT-plate separations were such that optimal hyperbolas are very well distributed over the test zone such that their intersections with conditioning circles yielded large optimal regions. If the UFBW is reduced, or similarly if the AUT-plate separations are reduced, optimal hyperbolas are pushed away from the corresponding plates towards the x-axis, which pushes optimal regions towards the AUT near which optimal hyperbolas are most likely to intersect each others. The same can be seen in Fig. 5.14b where an UFBW=7% is applied generating optimal regions centered at a vertical AUT-probe separation around $12\lambda_0$. However, the optimal condition number value in this case has raised to $\kappa(\mathbf{G}_{TM})_{\text{opt}} \approx 6.7$ which may be explained by recalling that reducing the UFBW (or the AUT-plates separations) reduces the degree of orthogonality between the matrix successive rows which negatively impacts the global conditioning. If the UFBW is further reduced, this may lead to successive rows being approximately parallel which would dramatically degrade conditioning. The same can be seen

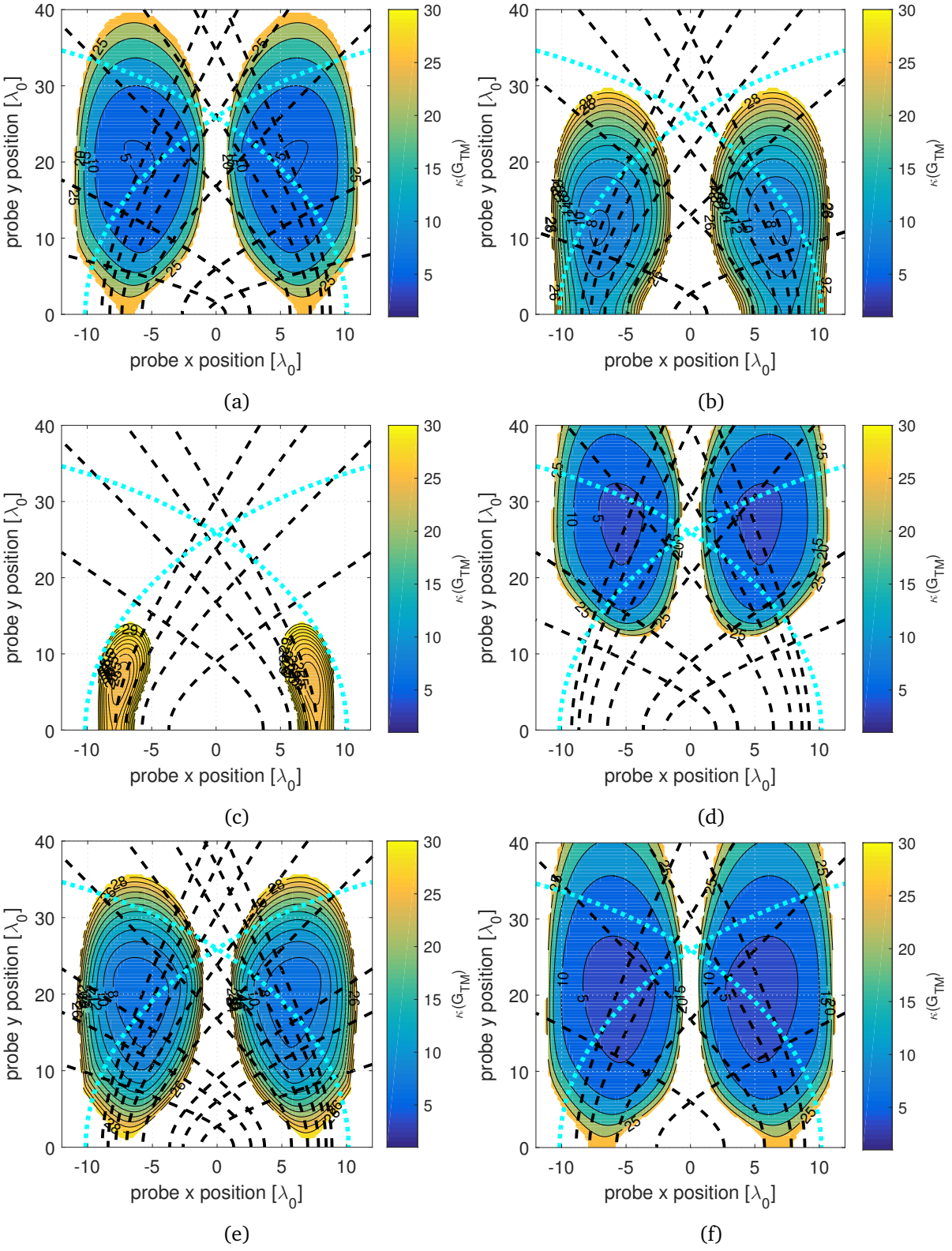

Figure 5.14 Evolution of the condition number versus the probe position as function of the operating UFBW and the number of considered images, and relationship with optimal hyperbolas (dashed) and conditioning circles (dotted). Parallel-plate configuration, $d_1 = d_2 = 12\lambda_0$ (a) UFBW= 8%, $N_i = 6$ (b) UFBW= 7%, $N_i = 6$ (c) UFBW= 6%, $N_i = 6$ (d) UFBW= 9%, $N_i = 6$ (e) UFBW= 8%, $N_i = 8$ (f) UFBW= 8%, $N_i = 4$.

in Fig. 5.14c where further reducing the UFBW to 6% amplified the condition number to levels above 25 all-over the test zone. If the UFBW is raised above the adapted value (or if the AUT-plates separations are enlarged), this would result in first-order hyperbolas being pushed towards corresponding plates pushing the intersection zone, which is the conditioning optimal zone further from the AUT. This is highlighted by Fig. 5.14d where an UFBW= 9% is applied, pushing optimal zones around vertical AUT-plates separations equal to $25\lambda_0$. In this case the optimal condition number value is not negatively affected; it may even be improved as shown by Fig. 5.14d ($\kappa(\mathbf{G}_{TM})_{\text{opt}} \approx 3.6$). However, the size of the corresponding optimal region is reduced due to the appearance of worst hyperbolas. In this scenario the size reduction of the optimal region was not very important because the UFBW was more or less still adapted to the set-up dimensions. This would not be the case if wider UFBWs or AUT-plates separations are introduced, which may reduce the size of optimal regions to very narrow levels.

The condition number is also function of the number of considered images which governs the number of frequency samples. As stated earlier, raising the number of images implies raising the number of frequency samples which divides the global UFBW into narrower UFBWs reducing the degree of orthogonality between the system matrix successive rows. The same can be seen in Fig. 5.14e, where the number of considered images is raised to $N_i = 8$ for a configuration characterized by an UFBW= 8%. The difference with respect to Fig. 5.14a ($N_i = 6$) is clear as conditioning is degraded in terms of both the optimal region size and the optimal condition number level which is raised to $\kappa(\mathbf{G}_{TM})_{\text{opt}} \approx 6.3$. On the contrary, reducing the number of considered images is advantageous in terms of conditioning as it provides a larger degree of freedom in setting the configuration parameters, namely the set-up dimensions and the UFBW in order to achieve well conditioned positions. This is highlighted in Fig. 5.14f, where reducing the number of considered images to $N_i = 4$ largely improved conditioning with respect to the previous scenario, enlarging optimal regions to almost takeover the test zone, and reducing the optimal condition number value down to $\kappa(\mathbf{G}_{TM})_{\text{opt}} \approx 3.2$.

It is convenient, and perhaps easier, to also assess regions of ill-conditioning pointed out earlier. Similarly to the single-plate and dihedral configurations, regions in the vicinity of the AUT and the plate are ill-conditioned because of the large distances spread for the former and due to the fact that the system matrix tends towards singularity in the latter. On the other hand, positions far from the AUT require large UFBWs in order to guarantee the intersection between the different optimal hyperbolas and conditioning circles corresponding to low projection factors. If this is not the case, then the low distances spread characterizing AUT-probe separations that are large compared to the AUT-plates separations becomes disadvantageous as it makes the system matrix tends towards singularity, having its columns defined by relatively similar distances. Finally, centered positions between the two plates are ill-conditioned in all the studied scenarios because the system matrix was singular over theses positions. This may be easily verified by noticing that the matrix over these positions is redundant having columns related to same order images being exactly the same; which follows from the fact that same order images are

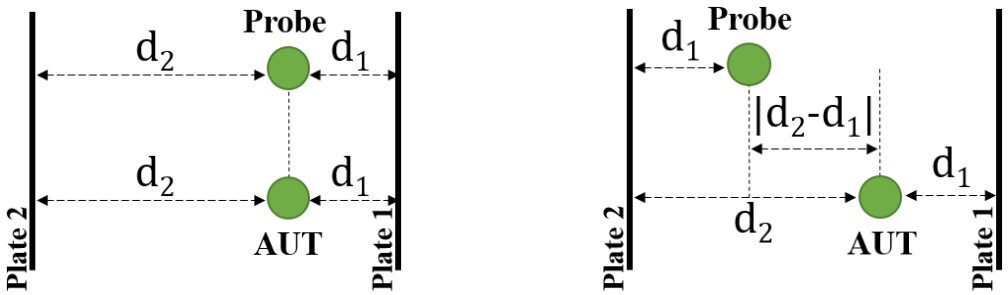

Figure 5.15 Parallel-plate configurations to avoid as they yield singular system matrices: (a) The AUT and the probe placed at a common horizontal position (b) The distance separating the AUT from one plate is equal to the distance separating the probe from the other plate.

equidistant from the test zone horizontal center due to the set-up symmetry. This is however a special case that may be generalized by noticing that whenever the probe faces the AUT, as depicted by Fig. 5.15a, the corresponding system matrix is singular. This follows from the fact that even-ordered images are by definition equidistant from the AUT, as stated by Eq. 5.23, and which is essentially a horizontal distance as all images are at the same vertical level as the AUT. It follows that if the probe is at the same horizontal level as the AUT, i.e., $x = x'$, then even ordered image are equidistant from the probe as well. This means that in this case the system matrix columns related to even ordered images are redundant, which yields a singular matrix. If the probe faces the AUT at the center of the test zone, as was the case in the studied scenarios, then all images of the same order are equidistant from the probe, yielding a system matrix of rank $\frac{N_i}{2}+1$ instead of the full rank N_i+1 necessary for the system matrix to be well conditioned. Another configuration that yields a singular matrix is when the distance separating the AUT from one plate is equal to the distance separating the probe from the other plate, as shown in Fig. 5.15b. In this case odd-ordered images are equidistant from the plate, which is easily verified by noticing that the horizontal distance separating the AUT and the probe is the difference between the distances separating the AUT from the two plates,

$$d^h_{\text{AUT-probe}} = \left|d_2 - d_1\right|. \tag{5.30}$$

Distances separating odd ordered images from the probe are then retrieved from Eqs. 5.22 and 5.30 yielding,

$$d^{2n+1}_{\text{right images-probe}} = d^{2n+1}_{\text{left images-probe}} = (2n+1)(d_1+d_2), \quad n \in \mathbb{N}^*, \tag{5.31}$$

generating as a results a singular matrix. Accordingly, both configurations depicted by Fig. 5.15 must be avoided in order to keep the possibility of achieving well-conditioned systems.

Globally, we may conclude that achieving well-conditioned systems using the parallel-plate TM model is possible using typical measurement parameters, although being more constrained with respect to previously studied configurations due to the higher complexity of the associated model. Achieving well-conditioned systems requires adapting the number of contributing images to the frequency parameters which in their turn should be adapted to the set-up dimensions. Reducing the number of images is advantageous in terms of conditioning.

5.4.3.2 TE Model

The TE model is characterized by the contribution of the projection matrix whose impact on conditioning in the single-plate configuration was modeled by the optimal circle over which the LOS and image fields are orthogonal. This reasoning was extended to the dihedral case with success because the corresponding model may be decomposed into three single-plate configurations with convenient simplifying approximations. This is however not the case with the parallel-plate model which is generally characterized by a larger number of contributing images which implies an approximation when reducing it to two single-plate configurations. This approximation was of relatively lower impact in the TM model due to the lower complexity of the system matrix with respect to the TE system matrix. Hence, the validity of the approach adopted to explain the behavior of the condition number up to this point mainly depends in this case on the dimensions of the system matrix which is defined by the adopted number of contributing images. To illustrate this, consider the examples shown in Figs. 5.16a-5.16d which shows the conditioning pattern for various considered numbers of images using a set-up characterized by equal AUT-plate separations $d_1 = d_2 = 12\lambda_0$, and applying an UFBW= 6%. The test zone is extended up to $60\lambda_0$ in the positive y direction in order to illustrate more clearly the behavior of the condition number. In these examples the basic TE model is used, i.e., by applying the minimum required number of frequency samples in order to balance the mathematical system. Conditioning circles corresponding to $\rho = 0.1$, and optimal hyperbolas corresponding to first-order images are superposed to the figures. Fig. 5.16a shows the conditioning pattern for the simplest case; when considering only the two first-order images ($N_i = 2$). By adding the AUT, in this case the total number of considered sources is three, which necessitates two frequencies in order to balance the system, generating as a result four equations which over-determines the system. The agreement with the single-plate model in this case is excellent, showing optimal positions exactly where the two optimal circles intersect the plates and where the two optimal hyperbolas intersect each others. Notice here that the figure axes are not plotted with the same scale, which explains the shape of the two optimal circles (dot-dashed). Fig. 5.16b shows the conditioning pattern when considering second order images ($N_i = 4$) and applying $N_f = 3$ frequency samples. Optimal circles corresponding to second order image are also plotted in the figure, showing the conditioning pattern barely described by the contribution of first-order images whose corresponding optimal hyperbolas intersect at the limit of the optimal zone. In

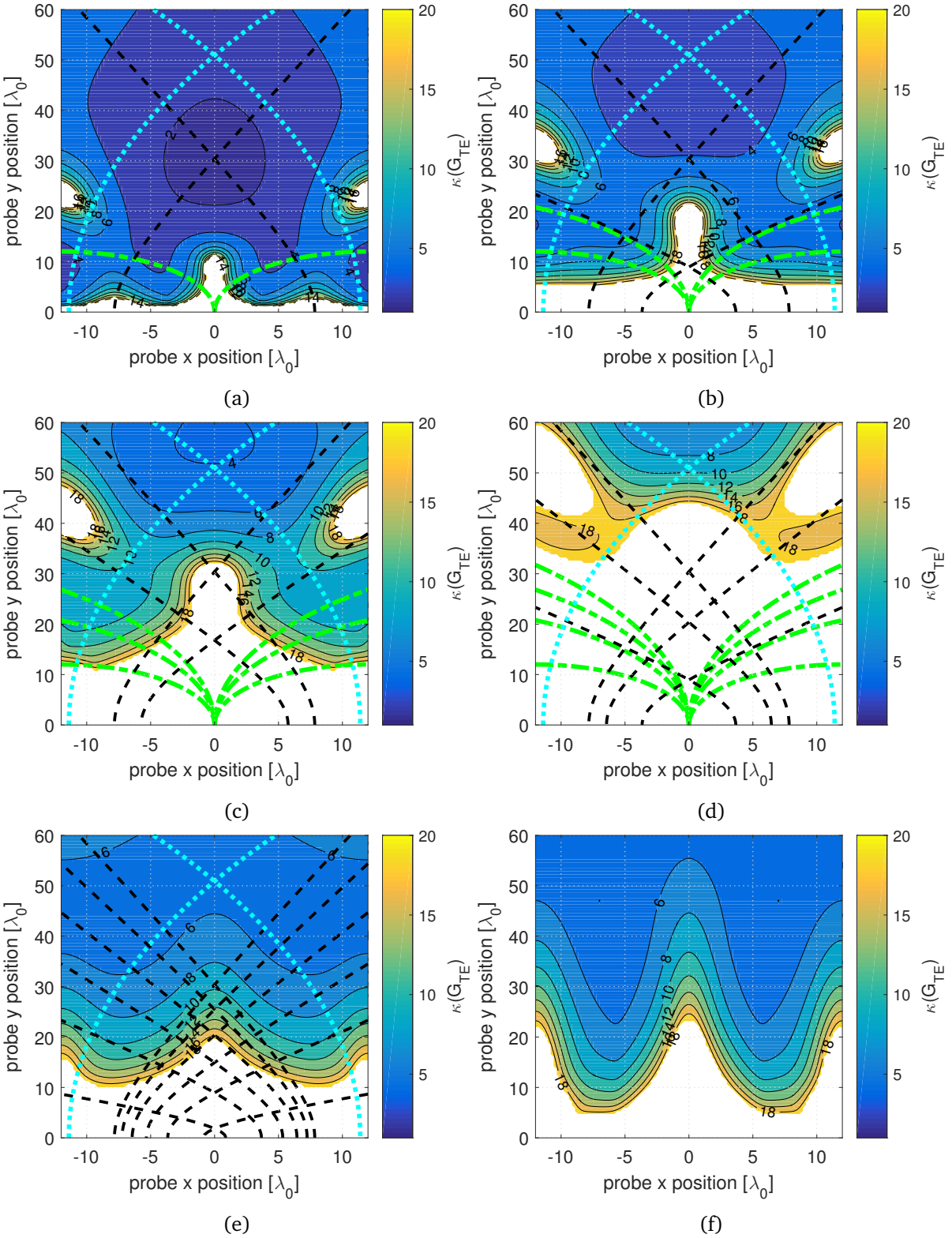

Figure 5.16 Evolution of the condition number versus the probe position as function of the number of considered images and the frequency parameters, and relationship with optimal hyperbolas (dashed), optimal circles (dot-dashed), and conditioning circles (dotted). Parallel plates configuration, $d_1 = d_2 = 12\lambda_0$ (a) UFBW= 6%, $N_i = 2$, $N_f = 2$ (b) UFBW= 6%, $N_i = 4$, $N_f = 3$ (c) UFBW= 6%, $N_i = 6$, $N_f = 4$ (d) UFBW= 6%, $N_i = 8$, $N_f = 5$ (e) UFBW= 6%, $N_i = 8$, $N_f = 9$ (f) UFBW= 8%, $N_i = 10$, $N_f = 11$.

this case the optimal zone is pushed further from the AUT. If the number of considered images is further raised, first-order images fail to describe the behavior of the condition number which is dominated by optimal hyperbolas corresponding to all images, as shown by Figs 5.16c-5.16d which correspond to $N_i = 6$ and $N_i = 8$ respectively. Notice that in Fig. 5.16d in particular, optimal circles corresponding to considered images do not generate any optimal regions near the plate. This is to translate the fact that fields corresponding to different images cannot be orthogonal to the AUT field at the same position; the only position where different optimal circles intersect each others being the AUT position itself.

The advantage of the TE model is the default over-determination with respect to the TM model and which may be verified by applying the same frequency parameters. Fig. 5.16e show the conditioning pattern corresponding to the last considered scenario ($N_i = 8$) tested with the number of frequencies necessary to balance the corresponding TM model, i.e., $N_f = 9$. This would generate eighteen equations for nine unknowns, which widely improves conditioning with respect to the basic model, generating positions with optimal conditioning levels around $\kappa(\mathbf{G}_{TM})_{\text{opt}} \approx 4.6$ at vertical distances lower than $40\lambda_0$. This advantage gives more freedom under the TE model in terms of measurement parameters with respect to conditioning. For instance, Fig. 5.16f plots the conditioning pattern when using $N_i = 10$ images with an UFBW=8%, showing positions with optimal values as lows as $\kappa(\mathbf{G}_{TM})_{\text{opt}} \approx 4.5$ at vertical AUT-plates separations lower than $40\lambda_0$.

Globally, we may conclude, as for previously studied configurations, that achieving positions with good conditioning levels using typical measurement parameters in the parallel-plate TE case is easier than in the corresponding TM case, which follows from the default over-determination of the TE model with respect to the TM model. Positions near the plates may be used in the TE case, but in the context of a complete measurement, common optimal positions which are described by optimal hyperbolas are the best option.

5.4.4 Discussion about the Method Efficiency in Reducing Mechanical Displacement

The theoretical advantage provided by the parallel-plate configuration in reducing the mechanical effort given the larger number of associated controlled echoes, is dramatically limited by the poor angular distribution of covered angles for most useful set-up dimensions. This was already highlighted in examples depicted by Fig. 5.12, showing that typically image sets with orders higher than 3 cover close angles, in a scenario where the probe was located near the center of a symmetrical set-up. It is easily verified that this observation may be generalized to set-ups of arbitrary dimensions provided that the AUT-plate separations are comparable to the vertical AUT-probe separation. The same can be seen in Figs. 5.17a and 5.17b which show constellations of covered angles using a symmetrical configuration with $d_1 = d_2 = 10\lambda_0$ and two probe positions $(x, y) = (5\lambda_0, 10\lambda_0)$ and $(x, y) = (9\lambda_0, 10\lambda_0)$ respectively. The number of considered images is

$N_i = 10$ which takes into account up to fifth-order images. In both situations angles covered by images of orders higher than three are close, if not redundant. Better angles distributions are achieved if the vertical AUT-probe separation is raised with respect to the AUT-plates separations. This is highlighted by Figs. 5.17c and 5.17d which show covered angles when reducing the AUT-plates separations to $d_1 = d_2 = 5\lambda_0$ and keeping the same vertical AUT-probe separation by placing the probe at $(x, y) = (1\lambda_0, 10\lambda_0)$ and $(x, y) = (4\lambda_0, 10\lambda_0)$ respectively. In the first case, fifth order images cover clearly distinct angles with respect to third order images, showing a better general angles distribution with respect to the first two scenarios. In the second case, the probe being closer to the right plate, the highlighted improved distribution is reduced, having several images of different order covering very close angles. It should be noted that although enlarging the vertical AUT-probe separation with respect to the AUT-plates separations improves the angles distribution, it requires larger UFBWs in order to ensure well-conditioning of the system. Hence, configurations that are advantageous in terms of angles distribution, are generally disadvantageous in terms of conditioning. The opposite case is also true, as optimal conditioning requires comparable AUT-probe and AUT-plate separations, which as shown here, is disadvantageous in terms of angular distribution.

Interesting constellations of covered angles may be achieved by using non-symmetrical configurations. This is shown in Figs. 5.17e and 5.17f where the left plate is very close to the AUT with respect to the right plate, with $d_1 = 9\lambda_0$ and $d_2 = 1\lambda_0$. The probe being placed midway between the two plates at $(x, y) = (4\lambda_0, 10\lambda_0)$ in the first case, showing a very good distribution of covered angles with almost all images contributing with distinct angles, and close to the right plate $(x, y) = (4\lambda_0, 10\lambda_0)$ in the second case, showing a rather limited distribution with respect to the first case. It is interesting to note that when the probe is placed near one of the plates (Figs. 5.17b, 5.17d and 5.17f), covered angles are separated into several groups of close angles, which suggests the conceivability of an effective rotation algorithm. Unfortunately, situations when either the AUT or the probe or both are near the plates (Figs. 5.17b, 5.17d, 5.17e and 5.17f) are generally ill-conditioned in the TM model as the system matrix tends towards singularity under these configurations.

The outlined observations concerning angular distributions in the parallel-plate model suggest that developing a rotation algorithm in order to achieve maximum efficiency in terms of mechanical effort reduction in the same fashion as for previously studied models is very difficult and probably of not practical interest as it would require further truncating the number of contributing images to very low levels in order to have more control over covered angles. This limitation may be overcome by exploiting the large spatial diversity provided by the parallel plates model by applying linear regression. The large number of measured samples which would be multiplied by the number of rotations or probe positions is expected to improve the performance of linear regression. Accordingly, the AUT may be rotated such that a minimum interference between already measured angles and angles yet to be measured occurs, given the

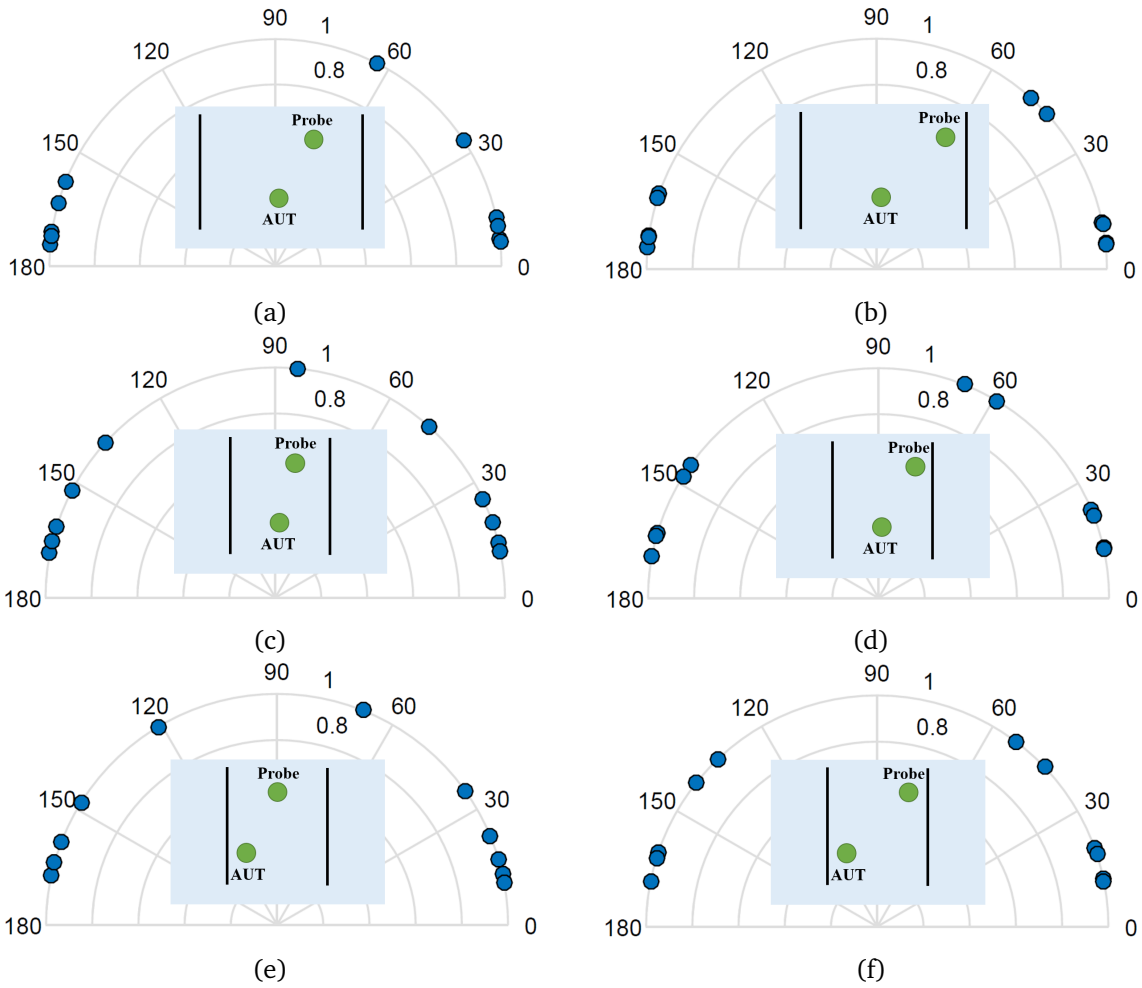

Figure 5.17 Angles covered py the parallel plates configuration as function of the AUT-plate separations and the probe position, number of considered images $N_i = 10$ (a) $d_1 = d_2 = 10\lambda_0$, probe at $(x, y) = (9\lambda_0, 10\lambda_0)$ (b) $d_1 = d_2 = 10\lambda_0$, probe at $(x, y) = (9\lambda_0, 10\lambda_0)$ (c) $d_1 = d_2 = 5\lambda_0$, probe at $(x, y) = (1\lambda_0, 10\lambda_0)$ (d) $d_1 = d_2 = 5\lambda_0$, probe at $(x, y) = (4\lambda_0, 5\lambda_0)$ (e) $d_1 = 1\lambda_0$, $d_2 = 9\lambda_0$, probe at $(x, y) = (4\lambda_0, 10\lambda_0)$ (f) $d_1 = 1\lambda_0$, $d_2 = 9\lambda_0$, probe at $(x, y) = (7.5\lambda_0, 5\lambda_0)$.

angular range covered by the chosen number of contributing images. Then, linear regression may be introduced in order to improve the final ARP results.

5.4.5 Discussion about the Model Practical Considerations

From a geometrical point of view, the parallel-plate configuration is a forward extension of the single-plate set-up and may be regarded as a double single-plate configuration. Consequently, all error sources related to the single-plate configuration are amplified in the parallel-plate case. The impact on the AUT free-space radiation characteristics and the AUT-diffracted field are amplified by the contribution of the second plate, which is also the case of edge and corner diffracted fields. Optimal positions with respect to edge diffracted fields associated to one plate are in the vicinity of the same plate, which is essentially a region exposed to diffracted fields from the second plate. However, as discussed in Chapter 3, these error sources are totally manageable and may be minimized by several techniques. An error in estimating losses introduced by the plate is expected to be amplified at higher-order images which correspond to echoes undergoing multiple reflections, which further motivates truncating the number of contributing images.

The parallel-plate model limitation is particularly caused by two factors. The first being the truncation of the infinite number of contributing images which implies that all reflections that are not taken into account in the mathematical model are considered as spurious reflections. Although the contribution of these reflections may be reduced as function of the set-up dimensions and the ARP orientation, as discussed in Sec. 5.4.1, generally a rather high number of images, typically $N_i > 10$, needs to be taken into account in order to minimize the field error into accepted levels. However, as was shown in Sec. 5.4.3, raising the number of contributing images is disadvantageous in terms of conditioning as it implies rising the number of frequency samples necessary to balance the mathematical models, which requires either large UFBWs or large set-up dimensions. In order to overcome this limitation, one possible approach would be by adapting the observation to the model, that is by truncating the number of contributing images to the measured field, either physically by using absorbing material or numerically by applying time gating [85]. The characteristics of echoes that are not taken into account in the mathematical model being totally predictable, the absorbing material should be adapted to the angular range covered by corresponding images, and the time window to the signals arrival times. The second limitation of the simplified model is related to the frequency impact on the free-space ARP. The model should be updated in a similar fashion as for the right dihedral case, which is by multiplying the system matrices by a matrix $\boldsymbol{\alpha}$ taking into account the amplitude and phase variations of the radiated field at each applied frequency with respect to the reference frequency. The larger number of considered images implies a larger number of unknown α-terms that have to be solved. This highlights the dilemma related to the choice of the number N_i of considered images, as rising it provides a larger number of covered angles and reduces the field error due to the truncation, but at the same time it negatively impacts conditioning and

complicates the task of solving for the ARP frequency dependence. As stated in Sec. 5.3.4, solving for the $\boldsymbol{\alpha}$ matrix involving more than one term is left as a perspective for future work.

5.4.6 Numerical Results

Numerical results to highlight the theoretical viability of the parallel-plate model and related aspects are presented in a scenario involving two infinite plates. The HWD is used as AUT and is positioned midway between the two plates with $d_1 = d_2 = 15\lambda_0$. Such relatively large AUT-plate separations are chosen in order to be able to generate convenient well-conditioned positions using an appropriate UFBW given the narrow-band character of the HWD. Accordingly, a global UFBW= 6% is applied and the number of contributing images is set to $N_i = 6$ (up to third order images), implying a number of frequency samples equal to $N_f = 7$, which is the required number to balance the TM model. The test zone is bounded from the sides by the two plates, from the bottom by the AUT position, and is extended up to vertical positions equal to $30\lambda_0$. FEKO allows to control the maximum number of generated reflections using UTD plates, which is set to 100 here. Hences, images up to 100^{th} order are considered in forming the reference field, which is equivalent to a total number of $N_{\text{ref}} = 200$ images. The six α-terms necessary to predict the frequency impact on the free-space ARP are retrieved from Table 4.1.

Results for the TM-isotropic case are shown in Fig. 5.18. Fig. 5.18a plots the corresponding condition number pattern showing two symmetrical optimal regions around the two optimal positions at $(x_{\text{opt}}, y_{\text{opt}}) = (\pm 8\lambda_0, 20\lambda_0)$ with condition number levels $\kappa(\mathbf{G}_{TM})_{\text{opt}} = 5.6$. Generally, ARP error levels are considerably high and are proportional to the corresponding source order. In other words, LOS samples show the lowest error levels, being generally between -40dB and -20dB almost allover the test zone. Then, error is amplified as function of the image order, oscillating between -35dB and -10dB in the optimal conditioned region over samples corresponding to first-order images, between -30dB and -5dB over samples corresponding to second order images, and between -25dB and 0dB over narrower regions over samples corresponding to third order images. This is in obvious agreement with the error spread rule retrieved for the single-plate case, which predicted forward proportionality between ARP error levels and distances separating corresponding sources from the probe. The generally high error levels highlight the impact of truncating the number of images when their contribution into the reference field is important. Minimizing the contribution of higher order images would then minimize the observed ARP error. The same can be seen in Fig. 5.19 which plots results for the TE-directive case with the AUT being oriented in the reference TE orientation (parallel to $\hat{x}$), such that ARP nulls are directed towards the two plates. Conditioning in this case is improved with respect to the TM case, having the optimal region extended up to certain positions near the plates and at the center of the test zone, with optimal values around $\kappa(\mathbf{G}_{TM})_{\text{opt}} = 3.7$ at $(\pm 8\lambda_0, 30\lambda_0)$. Keeping in mind the vulnerability of samples corresponding to directions of weak power emission to all sorts of error sources, error is generally tolerable in well-conditioned

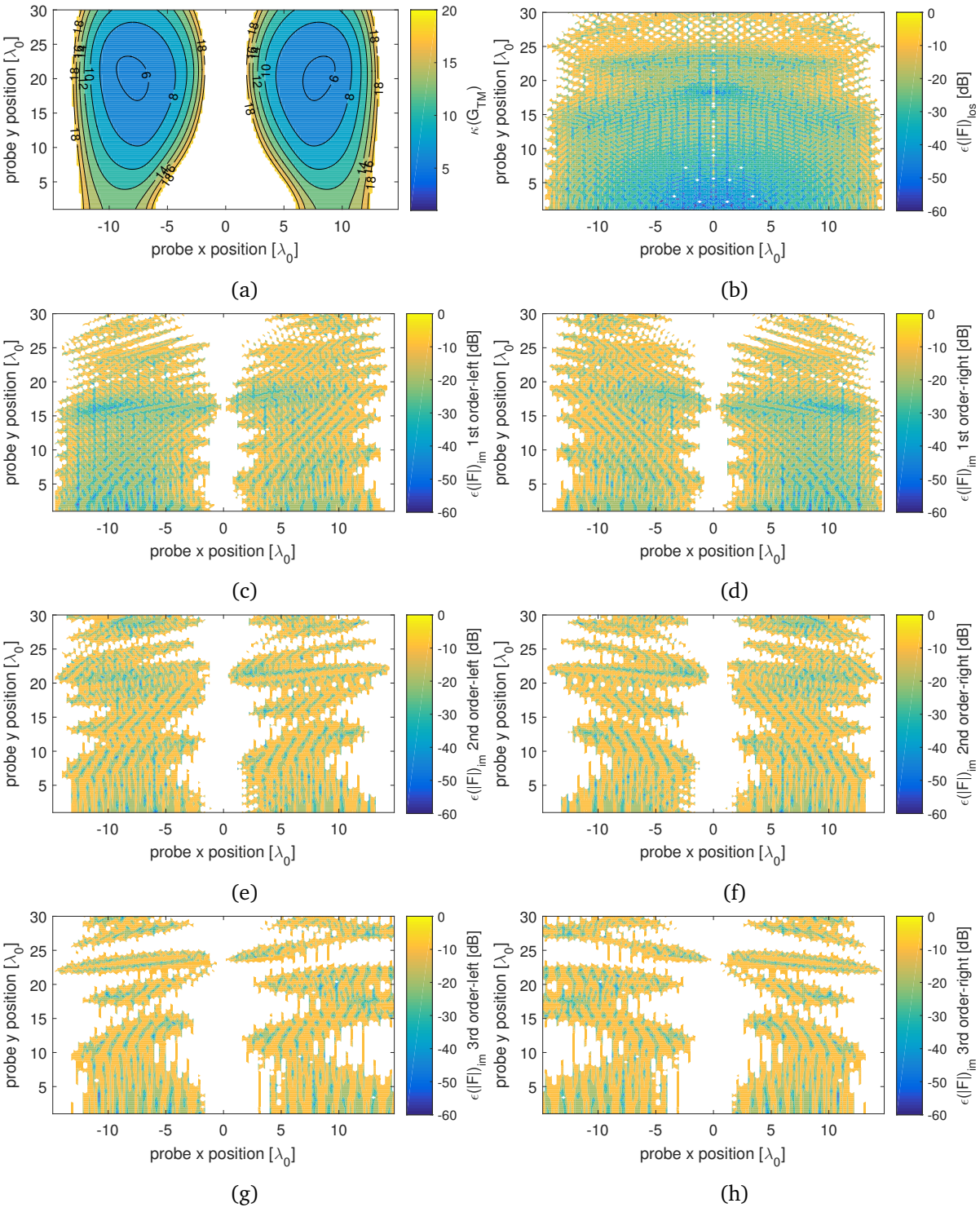

Figure 5.18 ARP error as function of the probe position in a hypothetical scenario (infinite PEC plates) using HWD as AUT. Parallel-plate configuration, TM case, $d_1 = d_2 = 15\lambda_0$, $FBW = 6\%$: (a) $\kappa(\mathbf{G}_{TM})$ (b) $\epsilon(\mathbf{F})_{\text{los}}$ (c) $\epsilon(\mathbf{F})_{\text{im}}$, left 1$^{\text{st}}$ order image (d) $\epsilon(\mathbf{F})_{\text{im}}$, right 1$^{\text{st}}$ order image (e) $\epsilon(\mathbf{F})_{\text{im}}$, left 2$^{\text{nd}}$ order image (f) $\epsilon(\mathbf{F})_{\text{im}}$, right 2$^{\text{nd}}$ order image (g) $\epsilon(\mathbf{F})_{\text{im}}$, left 3$^{\text{rd}}$ order image (h) $\epsilon(\mathbf{F})_{\text{im}}$, right 3$^{\text{rd}}$ order image.

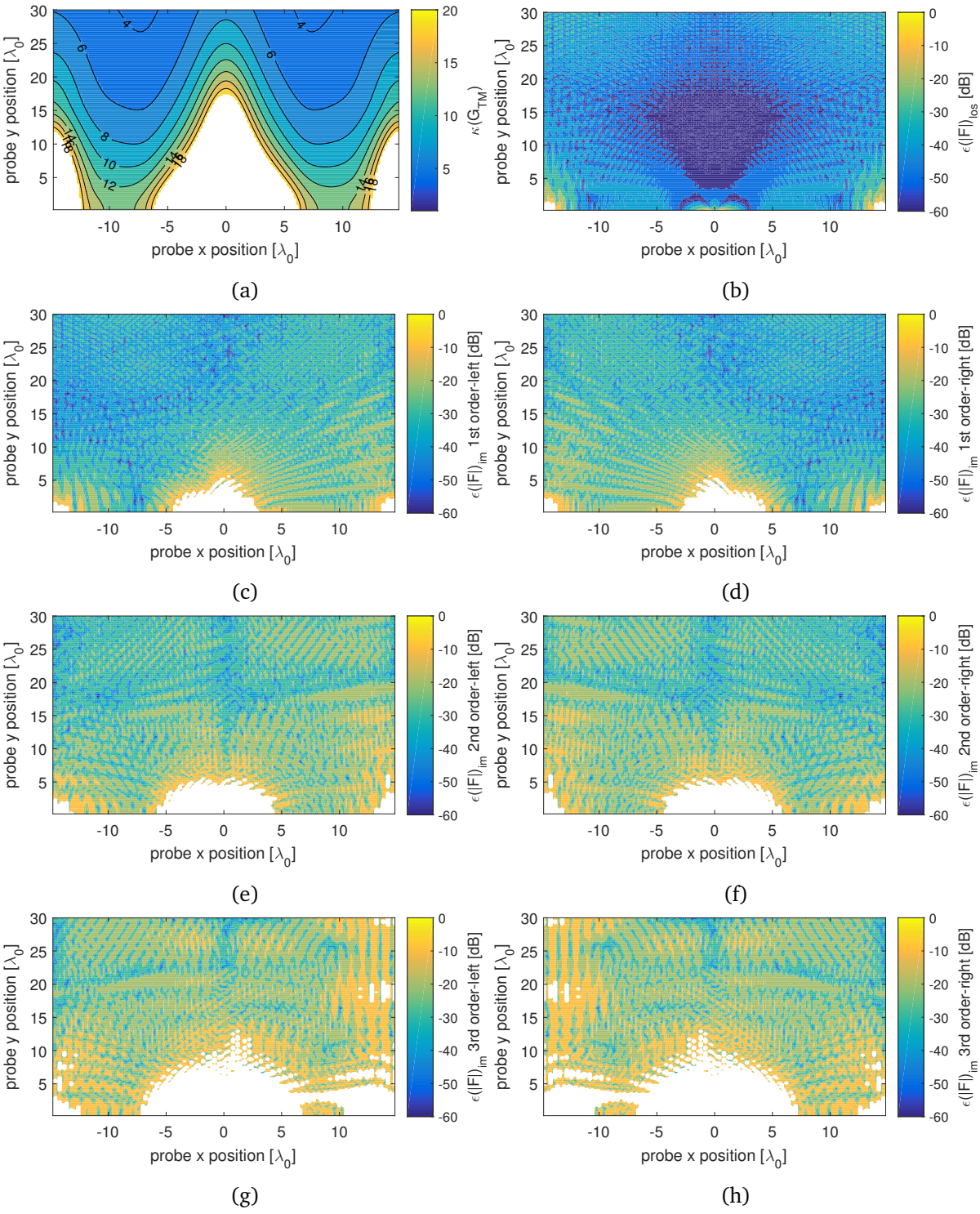

Figure 5.19 ARP error as function of the probe position in a hypothetical scenario (infinite PEC plates) using HWD as AUT. Parallel-plate configuration, TE case, $d_1 = d_2 = 15\lambda_0$, $FBW = 6\%$: (a) $\kappa(\mathbf{G}_{TE})$ (b) $\epsilon(\mathbf{F})_{\text{los}}$ (c) $\epsilon(\mathbf{F})_{\text{im}}$, left 1$^{\text{st}}$ order image (d) $\epsilon(\mathbf{F})_{\text{im}}$, right 1$^{\text{st}}$ order image (e) $\epsilon(\mathbf{F})_{\text{im}}$, left 2$^{\text{nd}}$ order image (f) $\epsilon(\mathbf{F})_{\text{im}}$, right 2$^{\text{nd}}$ order image (g) $\epsilon(\mathbf{F})_{\text{im}}$, left 3$^{\text{rd}}$ order image (h) $\epsilon(\mathbf{F})_{\text{im}}$, right 3$^{\text{rd}}$ order image.

zones especially for samples corresponding to lower order sources. The LOS error is very low almost all-over the test zone showing levels as low as −60dB in the lobe direction. Samples corresponding to first-order images also show considerably low error levels, being generally below −30dB in well conditioned positions pointed by the lobe. The error levels are relatively larger for samples corresponding to higher order sources, but remain quite tolerable over large sections of valid probe positions, generally oscillating between −35dB and −10dB in well-conditioned zones pointed by the lobe. These results highlight the feasibility of the proposed method in retrieving the ARP samples with satisfying precision provided that the contribution of higher order images to the reference field is minimized.

The usefulness of the parallel-plate configuration in accelerating the measurement process and its advantage in terms of linear regression are highlighted in Fig. 5.20 which shows ARP samples for horizontal cuts of eight probe positions linearly spaced between the two plates. The vertical distance separating the set of probe positions from the AUT is varied in order to highlight aspects related to angles distribution. An RBF regression with five base functions having a spread equal to 36° confined in half the azimuthal plane (Fig. 3.21c) is applied in order to minimize the ARP error resulting from the direct inversion. Figs. 5.20a and 5.20b show respectively the TM and TE results for a vertical separation $y = 10\lambda_0$. In this case the angular distribution of measured samples is quite poor having the eight LOS samples largely spaced over around 110°, and the 48 image samples covering a total of 50° with smaller spacing, varying from 5° near the region covered by LOS samples, and up to less than 0.5° near the half-plane limits. One may however notice the excellent performance of linear regression which reduces the absolute ARP error in the TM case from ±30dB over samples corresponding to ill-conditioned positions near the plates up to ±1.5dB, and from ±6dB in regions of weak power emission in the TE case up to ±1.3dB. Note that samples in the TM case are displayed with a maximum ±10dB error for a better visualization. As discussed in Sec. 5.4.4, raising the vertical AUT-probe separation with respect to the AUT-plate separations improves the angular distribution of measured samples. The same can be seen in Figs. 5.20c and 5.20d which show results for $y = 20\lambda_0$. In this case the range covered by LOS samples is reduced to around 70° and the range covered by images to is enlarged to around 90° with a better general distribution of covered angles. In this scenario the measurement is almost complete over half the plane with a sampling angle varying from less than 1° to a maximum of 10° in the range covered by LOS samples, and this by using only 8 probe positions. The linear regression is very effective, reducing the global measurement error to ±1dB. The angular distribution is further improved by further raising the vertical AUT-probe separation, as is the case for results shown in Figs. 5.20e and 5.20f which are generated using $y = 30\lambda_0$. In this case the LOS samples cover around 50° with a maximum sampling angle of 8°, whereas images cover around 100° with much smaller sampling angles that go below 0.5°.

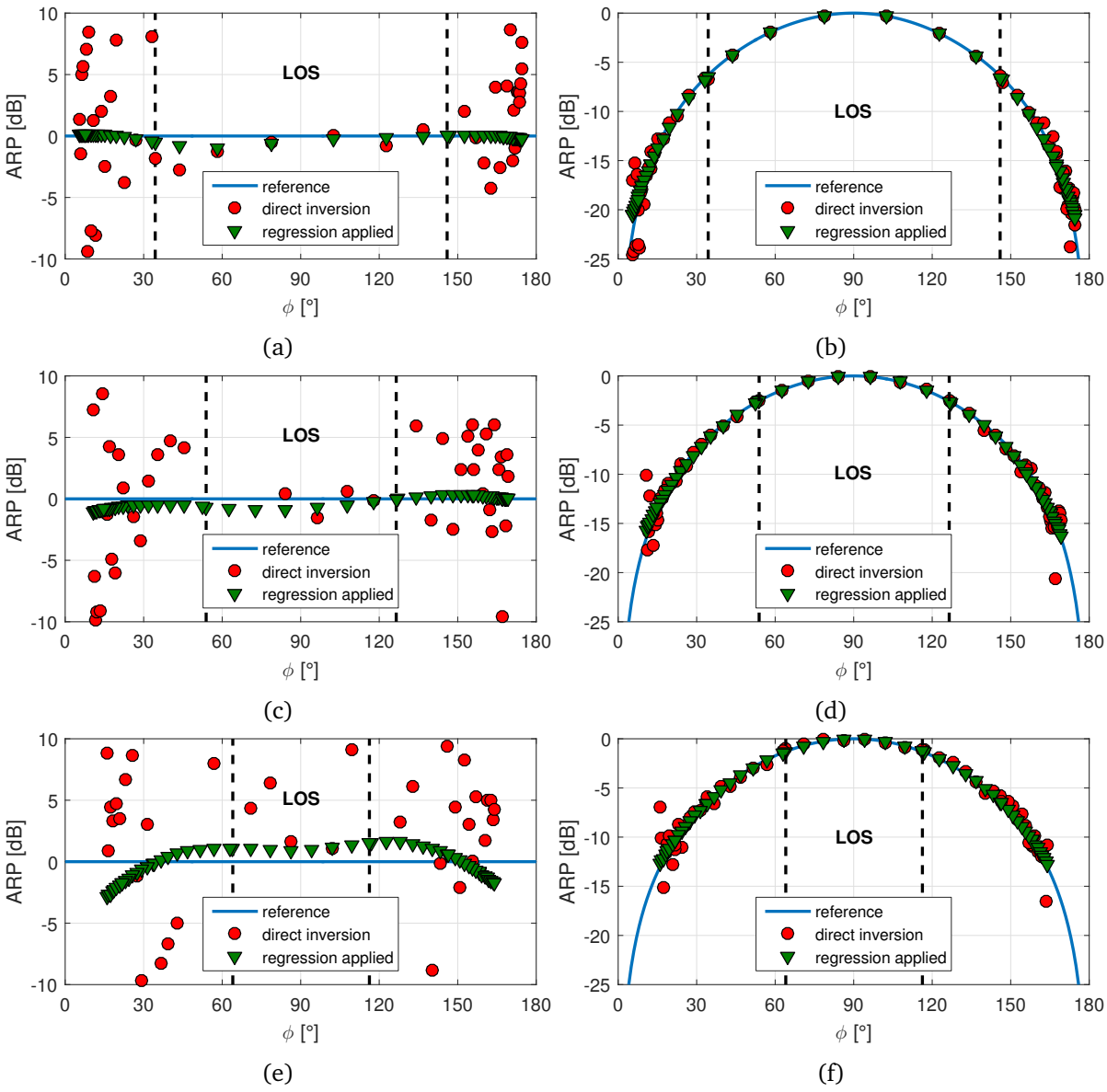

Figure 5.20 ARP samples calculated using 8 probe positions linearly spaced between the two plates for variant vertical separations, and application of RBF regression in order to reduce error, $N_r = 5$, $s = 36°$: (a) $y = 10\lambda_0$, TM (b) $y = 10\lambda_0$, TE (c) $y = 20\lambda_0$, TM (d) $y = 20\lambda_0$, TE (e) $y = 30\lambda_0$, TM (f) $y = 30\lambda_0$, TE

The regression is particularly less effective in the TM case with respect to previous scenarios, reducing the maximum error to around ±3dB, which is due to the poor distribution of error attaining considerably larger values below than above the reference ARP.

These results highlight advantages carried by the larger number of generated echoes introduced by the parallel-plate configuration in reducing both the required mechanical displacement and the measurement error.

Conclusion

This chapter explored the possibility of extending the proposed concept to configurations involving multiple echoes. Two configurations were studied: the right dihedral configuration which allows the generation of three controlled echoes, and thus provides ARP information related to four measurement angles, and the parallel-plate configuration which allows the generation of an infinite set of controlled echoes. The study focused on the metamathematical viability of the developed models to verify the possibility of generating well-conditioned systems using typical measurement parameters in terms of set-up dimensions and operating bandwidths. Due to the complexity of the systems, the study was mainly qualitative and was based on results carried over the single-plate configuration.

Results related to the right dihedral configuration showed the possibility of attaining well-conditioned systems using affordable set-up dimensions ($r < 40\lambda_0$) and relatively narrow UFBWs (6%). Achieving well conditioned systems in the TE model is easier and requires less set-up and frequency requirements because of the over-determination of the problem. A brief discussion concluded on the theoretical possibility of developing rotation algorithms of maximum efficiency allowing to cut down the measurement time by four with respect to classical measurements. The soundness of the model and its efficiency in reducing mechanical effort were highlighted via numerical simulations. The large number of acquired data samples, which is four times the number of measurements, made linear regression very efficient in reducing the ARP error to levels below ±1dB in hypothetical scenarios affected by error due to the far-field model assumption and the AUT-diffraction. The impacts of remaining error sources, which showed to be manageable, may as well be minimized by regression.

The parallel-plate model required a truncation study of the number of contributing images to be processed in the calculations given the infinite number of the "actual" contributing images. The various studies concluded on the viability of developed models provided that a compromise on the chosen number of contributing images is achieved as function of the measurement parameters and the tested ARP. Enlarging the number of contributing images rises the number of measured ARP samples in each measurement and reduces error due the truncation but degrades conditioning and implies larger set-up dimensions and frequency bandwidths in order to guarantee a minimum stability of the system, and vice versa. Although it is hard to analytically express the usefulness of the parallel-plate configuration in reducing the mechanical effort with respect to classical measurements, a measurement scenario showed that an almost complete half azimuthal scan with a sampling angle no larger than $8°$ was achieved using only 8 probe positions. The large number of measured ARP samples made linear regression very efficient in reducing the absolute ARP error from levels as large as ±30dB to levels as lows as ±1dB, highlighting the viability of the method.

One important aspect that was not covered in the present work, which is central to the feasibility of the concept, is the estimation of the ARP frequency dependence when involving

multiple unknowns modeling the impact of each frequency sample. A convexity study of the corresponding cost function is necessary to shed light about the possible solutions to such problems. Global optimization methods may be used in this context in order to solve for the multiple α-terms and the regression coefficients that best fit the model to a set of observed data samples.

General Conclusion

In this work, an ARP measurement concept aiming at speeding up the characterization process using cost efficient systems involving highly-reflective metallic plates was introduced. The proposed paradigm consists in generating a set of controlled echoes which directly contribute to the measurement in addition to the LOS signal and extracting the ARP information carried by all the generated signals concurrently. The proposed paradigm challenges the traditional measurement paradigm stating that useful information is exclusively carried by the generated test signal, usually the LOS signal, which implies excessive, time consuming mechanical effort in order to perform a complete measurement; a limitation that is usually overcome using complex multi-probe systems. The particularity of the proposed paradigm with respect to recently developed measurement techniques in reverberating environments, which generally share the traditional measurement paradigm, is that echoes are controlled, i.e., their characteristics are predicted in a deterministic fashion.

The concept was applied to a far-field model. A choice that was motivated by its simplicity with respect to near-field models. The mathematical model is described by a system of equations in which retrieving the unknown ARP vector consists in inverting a matrix problem. The first dimension of the model is represented by the set of measurement angles over which the ARP samples are calculated, whereas the second dimension is generated by introducing frequency diversity in order to have a number of equations at least equal to the number of unknowns. Consequently, an important part of this work was devoted to the study of the mathematical stability of the model in order to ensure the accuracy of the ARP results.

The largest part of this manuscript handled in detail the simplest configuration in terms of controlled echoes, the single-plate configuration which allows the generation of a single controlled echo. Chapter 2 presented the corresponding developed models which were simplified in order to assess the viability of the proposed concept from a pure a mathematical point of view. The general 3D problem was decomposed into TM and TE polarizations in order to simplify the conditioning study by reducing the dimensions of the system matrices. The conditioning study highlighted the possibility of achieving mathematically stable systems using typical measurement parameters. Analytical expressions were developed in order to predict optimal positions in terms of conditioning as function of the set-up dimensions and the operating frequency bandwidth. The theoretical efficiency of the proposed concept in accelerating the measurement process was highlighted and two algorithms for achieving maximum efficiency, i.e., to reduce the

measurement time by a factor of 2 with respect to classical measurements, were developed. The first algorithm is based on a uniform measurement sampling angle equal to the difference of the two measurement angles, and is more adapted to the TE model as small sampling angles require placing the probe in the vicinity of the plate, which is by default the TE optimal region in terms of conditioning. The second algorithm, which is more general, is based on an integer ratio of the two measurement angles, and consists in performing a set of rotations before introducing an adapted jump in order to avoid interference between already covered angles and angles to be covered.

After that, Chapter 3 handled the various practical limitations of the developed models in order to verify the physical viability of the proposed concept. Impacts of a set of approximations applied in order to simplify the mathematical formulations, and hence generating a set of model-related errors, were analyzed. These model systematic limitations may be summarized in error due to the far-field model assumption, impact of the plate on the AUT free-space radiation resistance, diffracted fields by the AUT aperture and the plate discontinuities, and the plate losses. Conducted studies showed, based on synthetic results, the manageability of the various model-related error sources with various practical solutions to minimize their impacts. The tolerance of the developed models to the inevitable practical systematic errors was assessed as well, highlighting the importance of conditioning models developed in Chapter 2. Linear regression was then introduced in order to enhance the robustness of the proposed method by reducing the ARP error associated to the direct inversion. Regression was used in order to optimize the model as well by estimating the ARP frequency dependence which was modeled by a complex term α taking into account the amplitude and phase variations underwent by the field at the second working frequency. A numerical approach which consisted in spanning the space of solutions showed the problem in α and the unknown ARP vector to be convex. By applying regression, the correct value of α was estimated without a priori information about the ARP.

The feasibility of the proposed concept was then numerically assessed in Chapter 4 using a comprehensive electromagnetic simulation software, FEKO. Different aspects related to the concept were also verified such as the importance of developed conditioning models in ensuring the mathematical systems stability, and the various model systematic limitations which were proven to be manageable using typical measurement parameters. The usefulness of the concept in accelerating the measurement process was highlighted by applying the general developed algorithm based on integer ratios of measurement angles, which allowed to effectively cut down the mechanical displacement effort to a half with respect to classical measurements.

Finally, Chapter 5 explored the possibility of extending the proposed concept to configurations involving multiple echoes. Two configurations were studied: the right dihedral configuration which allows the generation of three controlled echoes, and the two-parallel plates configuration which allows the generation of an infinite set of controlled echoes. The study was focused on the metamathematical viability of the developed models to verify the possibility of generating

well-conditioned systems using typical measurement parameters and showed the possibility of achieving such systems using affordable set-up dimensions and relatively narrow operating bandwidths. Due to the complexity of the systems, the study was mainly qualitative and was based on results carried over the single-plate configuration. Efficiencies of both configurations in reducing the mechanical effort with respect to classical measurements were highlighted via numerical simulations. One aspect that was not covered in this work, is solving for the multiple α-terms modeling the impact of the different frequency samples used to balance the mathematical model. Global optimization methods may be used for this purpose.

Perspectives

This work opened the door for exploiting echoes, generally regarded as spurious signals, in an antenna measurements context. The conducted work being essentially a theoretical feasibility study, one forward perspective that follows is the experimental validation of the proposed concept which was not performed in this work due to time constraints. Experimentation would take into account practical error sources whose synthetic and numerical modeling is always subject to limitations. Multiple perspectives may be outlined. An essential improvement of the proposed concept would be by conducting a comprehensive study on the associated measurement dynamic range. In this work, the various error sources were theoretically and numerically highlighted and their impacts were studied with the aim of proving the practical viability of the concept. A knowledge about the measurement dynamic range would be very useful in defining applications of the proposed concept.

Another major perspective would be extending the concept to near-field models. In this work, the concept was exclusively developed based on a far-field model, a choice that was motivated by the simplicity of far-field models with respect to near-field models. This choice, however, is limited by the far-field distance necessary to approximate far-field measurement conditions, and which may be very large for certain antenna types. The concept may as well be applied in order to retrieve near field amplitude and phase values corresponding to several angles of generation at each probe position in order to reduce the associated mechanical effort.

Finally, a rather optimistic perspective that follows from this work is assessing the usefulness of other quantities that are usually treated as noise in the context of ARP measurements. For instance, diffracted fields by the plate edges and corners are adequately modeled by several high-frequency techniques. These fields, containing useful information about the ARP values of the corresponding directions of generation, may offer the possibility of a fruitful contribution to the measurement if the associated modeling error is not too large.

Résumé (French)

Le travail de cette thèse porte sur le domaine des mesures d'antennes, plus précisément la mesure du diagramme de rayonnement. Un diagramme de rayonnement d'antenne décrit la distribution angulaire de l'énergie rayonnée par une antenne. Cette caractéristique clé est très pertinente pour toutes applications impliquant des antennes, et est utilisée afin de récupérer d'autres propriétés importantes telles que la directivité et le gain.

Le développement et la croissance rapides de l'industrie des télécommunications, en particulier au cours de la dernière décennie, et sa généralisation à la vie quotidienne ont étendu le rôle des antennes en dehors des applications classiques, telles que la radiodiffusion et la défense, à une plus grande échelle d'applications. Le développement et la commercialisation des systèmes intelligents modernes ainsi que les concepts de connectivité tels que l'internet des objets, ont permis aux antennes de conquérir les dispositifs et équipements électroniques modernes. Par exemple, les voitures modernes peuvent avoir jusqu'à 24 différentes antennes installées sur le véhicule. Un nombre qui devrait encore augmenter dans les années à venir. En conséquence, une connaissance fiable des caractéristiques de rayonnement des antennes déployées est cruciale pour le bon fonctionnement du système intégral. Ces caractéristiques qui incluent le diagramme de rayonnement, l'efficacité de rayonnement, la bande passante, etc., sont généralement récupérées et vérifiées via des mesures. Ceci explique la pertinence du domaine des mesures d'antennes autant sur le plan académique qu'industriel.

Plusieurs techniques et procédures de mesure du diagramme de rayonnement ont été développées et améliorées au cours du dernier siècle. Ils sont généralement classés en termes de conditions de mesure qui dépendent –en partie- de la distance à laquelle la mesure est effectuée en deux catégories : technique de champ-lointain (CL) et techniques de champ proche (CP). Bien que ces techniques soient exposées à des différents types de non-idéalités, elles partagent le même type d'environnement de mesure anéchoïque dans lequel seulement le signal de test généré est considéré, tandis que les réflexions spéculaires provenant du site de mesure et des équipements de test sont réduites au minimum au cours du processus de caractérisation. Cela

découle du modèle de mesure commun formant la base des mesures classiques, qui consiste à acquérir l'information portée par le signal de test généré en vue de récupérer les caractéristiques de rayonnement l'antenne sous test (AST) dans la direction associée. Par conséquence, toute sorte de réflexion provenant du site de mesure et des équipements de test est considérée comme perturbatrice car elle modifie la valeur 'correcte' du signal de test. Dans cette perspective, deux principales limites des techniques classiques de mesure d'antennes peuvent être décrites. La première limitation est liée à l'effort de déplacement mécanique nécessaire pour effectuer une mesure complète. Communément, soit l'AST est mis en rotation ou bien le système de sondes est déplacé afin d'acquérir des valeurs de diagramme de rayonnement correspondant à des directions différentes jusqu'à ce qu'une figure complète soit obtenue. Cela se traduirait par un temps de mesure excessive qui peut être trop coûteux d'un point de vue industriel. Plusieurs techniques ont été développées pour surmonter cette limitation, la plus commune étant les systèmes multisondes, qui en revanche sont caractérisés par une électronique et une implémentation logicielle sophistiquées et présentent un coût plus élevé par rapport aux systèmes traditionnels. La seconde limitation est liée à la suppression des échos et des réflexions spéculaires provenant du site de mesure. Généralement, les mesures de diagramme de rayonnement se déroulent à l'intérieur de chambres entièrement anéchoïques (CA) dont les murs, le sol et le plafond sont couverts par des absorbants micro-ondes qui, en plus de leur coût élevé, nécessite un entretien régulier.

Très récemment, des efforts ont été faits afin de caractériser les antennes dans des environnements diffusifs, à savoir, en chambres réverbérantes. Le principal avantage des chambres réverbérantes par rapport aux chambres anéchoïques est leur coût d'installation et d'entretien relativement faible. Cependant, aussi contre-intuitif que cela puisse paraître, les techniques mises au point sont effectuées dans des environnements diffusifs essentiellement pour émuler des conditions de mesure en espace libre ; car l'information ciblée est exclusivement portée par le signal direct entre la source et l'AST, et donc les contributions des différentes réflexions provenant du site de mesure sont mis au rebut. En conséquence, ces techniques présentent les mêmes limitations en termes de déplacement mécanique et de temps de mesure que les techniques classiques.

Le principal motif derrière cette thèse est la nécessité croissante d'accélérer les procédures de mesure d'antennes. Un nouveau concept de mesure rapide est développé, basé sur un principe de diversité spatiale qui permet l'acquisition simultanée de plusieurs valeurs de diagramme de rayonnement correspondant à différents angles de mesure dans chaque réalisation. Le concept

proposé fournit une nouvelle contribution importante dans le sens où la diversité spatiale mis en évidence permettant d'accélérer le processus de mesure est générée en exploitant les échos qui sont générés en utilisant des systèmes économiques impliquant des plaques réfléchissantes. Bien que les échos soient exploités dans d'autres domaines, tels que les télécommunications avec la notion de propagation par trajets multiples, à notre connaissance, le présent travail constitut la première contribution à exploiter les échos dans un contexte de mesures d'antenne afin d'accélérer le processus de caractérisation. La particularité du concept proposé par rapport aux techniques réalisées en chambres réverbérantes est que les échos sont produits de façon contrôlée. Par conséquent, une approche déterministe est utilisée afin de récupérer leurs caractéristiques plutôt que l'approche statistique appliquée en milieux réverbérants. Le concept proposé remet en cause le paradigme de mesure commun partagé par les techniques classiques qui bannit les échos en les éxploitant afin d'accélérer le processus de caractérisation. Une diversité fréquentielle est introduite afin de générer un système d'équations équilibré où le vecteur inconnu contenant les valeurs du diagramme de rayonnement est récupéré en inversant un problème matriciel. Par conséquent, une attention considérable est accordée au conditionnement du modèle mathématique afin d'assurer la stabilité et la robustesse du système. Le concept a été validé numériquement avec des résultats très prometteurs. Au moment de la rédaction de ce manuscrit, une manip de mesure à CentraleSuepelc est en cours de préparation afin de valider le concept expérimentalement. Malheureusement, en raison de contrainte de temps, les résultats expérimentaux ne seront pas inclus dans ce manuscrit. Le concept a été protégé par un brevet d'invention international publié par l'Institut National Français de la Propriété Industrielle sous le numéro WO2016055739A3.

Le manuscrit est organisé comme suit. Le premier chapitre présente des notions élémentaires de la théorie de mesure d'antennes et les outils nécessaires afin de développer le concept proposé. Ensuite, les techniques de mesure classiques ainsi que des concepts développés récemment sont brièvement présentés avec une discussion des limitations communes résultant principalement du paradigme de mesure qu'ils partagent. Une vision globale sur le concept proposé est ensuite fournie avec un aperçu des objectifs de la thèse.

Les autres chapitres peuvent être divisés en deux parties. Les Chapitres 2, 3 et 4 analysent en détail la forme la plus simple du concept proposé en termes d'échos contrôlés, la configuration simple-plaque. Dans ce cas, un seul écho contrôlé est généré et sa contribution à la mesure avec le signal direct est évaluée. Le Chapitre 2 présente une étude détaillée de la viabilité du modèle d'un point de vue purement mathématique. Tout d'abord le modèle mathématique

est développé sous l'hypothèse des conditions de mesures en champ lointain qui a l'avantage d'être simple à formuler par rapport aux modèles champ proche. Le problème étant sous forme matriciel, une étude de conditionnement du système est effectuée afin de vérifier la possibilité de générer des systèmes d'équations bien conditionnés en utilisant des paramètres de mesure abordables en termes de dimensions de site et de bande passante de fonctionnement. Pour faciliter cette étude, le problème générale 3D est décomposé en polarisations TM et TE. Ainsi, des modèles de conditionnement précis avec des formules analytiques qui prédisent les positions optimales en termes de conditionnement sont développées. Une étude de l'utilité de la technique proposée pour réduire l'effort de déplacement mécanique, et donc accélérer le processus de mesure est également présentée, avec des algorithmes de rotation de l'antenne sous test permettant d'atteindre une efficacité maximale par rapport à une mesure classique, en réduisant le temps de mesure par un facteur 2. Une fois la viabilité mathématique est évaluée, une étude des limitations pratiques du modèle proposé est effectuée au Chapitre 3 afin de vérifier sa viabilité d'un point de vue physique. La tolérance du modèle à des erreurs pratiques systématiques, et à l'impact des phénomènes physiques qui ne sont pas pris en compte dans la formulation mathématique simplifiée sont évalués. Ces derniers se résument au limitation de l'hypothèse champs lointain et l'expression mathématique du champs associé, à l'impact de la paroi métallique sur les caractéristiques de rayonnement espace-libre de l'antenne sous test, à la contribution des champs diffractés par l'antenne sous test et par les bords et les coins de la paroi métallique, et au pertes introduites par la paroi métallique sur le signal réfléchi dues à sa conductivité finie. La robustesse de la méthode proposée est améliorée en introduisant la régression afin de réduire l'errer sur les valeurs de diagramme de rayonnement calculés via l'inversion directe. La régression est aussi utilisée afin d'estimer la variation subie par le diagramme de rayonnement en changeant la fréquence de travail. Après cela, le Chapitre 4 présente des résultats numériques mettant en évidence la faisabilité du concept et de l'efficacité du modèle adopté.

La deuxième partie du manuscrit, Chapitre 5, explore la possibilité d'étendre le concept proposé à des configurations plus complexes impliquant plusieurs échos contrôlés. Après une brève discussion sur quelques méthodes permettant la génération de multiples échos contrôlés, deux configurations sont étudiées en se basant sur les résultats obtenus avec la configuration simple-plaque. La première configuration, la configuration dièdre, permet la génération de trois échos contrôlées, alors que la seconde, la configuration à plaques parallèles, permet la génération d'un nombre infini d'échos contrôlés. La solidité des modèles développés ainsi que leur efficacité théorique pour accélérer le processus de caractérisation sont mis en évidence par les résultats numériques.

Enfin, une conclusion générale regroupant les accomplissements de cette thèse est présentée, suivie par des perspectives pour des futurs travaux.

Bibliography

[1] N. Koch, *Antennas for Automobiles*. INTECH Open Access Publisher, 2012.

[2] G. E. Evans, *Antenna measurement techniques*, vol. 1. 1990.

[3] A. S. Committee *et al.*, "Ansi/ieee std 149-1979 ieee standard test procedures for antennas," 1979.

[4] A. Yaghjian, "An overview of near-field antenna measurements," *IEEE Transactions on Antennas and Propagation*, vol. 34, no. 1, pp. 30–45, 1986.

[5] S. Loredo, M. R. Pino, F. Las-Heras, and T. K. Sarkar, "Echo identification and cancellation techniques for antenna measurement in non-anechoic test sites," *IEEE Antennas and Propagation Magazine*, vol. 46, no. 1, pp. 100–107, 2004.

[6] L. Duchesne, P. Garreau, N. Robic, A. Gandois, P. O. Iversen, and G. Barone, "Compact multi-probe antenna test station for rapid testing of antennas and wireless terminals," in *Personal, Indoor and Mobile Radio Communications, 2004. PIMRC 2004. 15th IEEE International Symposium on*, vol. 1, pp. 632–636, IEEE, 2004.

[7] G. Ferrara, A. Gifuni, and A. Sorrentino, "Test on antennas in a reverberating chamber and comparison with anechoic chamber," in *2012 6th European Conference on Antennas and Propagation (EUCAP)*, pp. 2154–2157, IEEE, 2012.

[8] A. Sorrentino, G. Ferrara, A. Gifuni, and M. Migliaccio, "Antenna pattern in a multipath environment emulated in a reverberating chamber," in *Antennas and Propagation (EuCAP), 2013 7th European Conference on*, pp. 3561–3565, IEEE, 2013.

[9] M. A. Garcia-Fernandez, D. Carsenat, and C. Decroze, "Antenna radiation pattern measurements in reverberation chamber using plane wave decomposition," *IEEE transactions on antennas and propagation*, vol. 61, no. 10, pp. 5000–5007, 2013.

[10] M. A. Garcia-Fernandez, D. Carsenat, and C. Decroze, "Antenna gain and radiation pattern measurements in reverberation chamber using doppler effect," *IEEE Transactions on Antennas and Propagation*, vol. 62, no. 10, pp. 5389–5394, 2014.

[11] P. Meton, *Etude et développement d'un concept de caractérisation rapide d'antennes basé sur le principe du retournement temporel du champ électromagnétique en chambre réverbérante*. PhD thesis, Université Paris Sud-Paris XI, 2015.

[12] A. A. Saleh and R. Valenzuela, "A statistical model for indoor multipath propagation," *IEEE Journal on selected areas in communications*, vol. 5, no. 2, pp. 128–137, 1987.

[13] G. L. Turin, F. D. Clapp, T. L. Johnston, S. B. Fine, and D. Lavry, "A statistical model of urban multipath propagation," *IEEE Transactions on Vehicular Technology*, vol. 21, no. 1, pp. 1–9, 1972.

[14] A. S. Committee *et al.*, "Ieee std 145-2013 ieee standard for definitions of terms for antennas," 2013.

[15] S. Emami, C. Corral, and G. Rasor, "Peak-to-average power ratio (papr), fractional bandwidth and processing gain of uwb schemes," in *Spread Spectrum Techniques and Applications, 2004 IEEE Eighth International Symposium on*, pp. 929–933, IEEE, 2004.

[16] W. Kunysz, "Antenna phase center effects and measurements in gnss ranging applications," in *Antenna Technology and Applied Electromagnetics and the American Electromagnetics Conf.(ANTEM-AMEREM), 14th Int. Symp., Ottawa, Canada*, pp. 5–8, 2010.

[17] J. A. Fordham, "An introduction to antenna test ranges, measurements and instrumentation," *Microwave Instrumentation Technologies LLC, IEEE EMC Society Newsletter*, 1998.

[18] M. Farouq, *Transformation de front d'ondes par des méthodes matricielles*. PhD thesis, Université Paris Sud-Paris XI, 2015.

[19] J. F. Aubin, "A brief tutorial on antenna measurements," *Microwave Journal*, vol. 48, no. 8, pp. 92–101, 2005.

[20] L. Hemming and R. Heaton, "Antenna gain calibration on a ground reflection range," *IEEE Transactions on Antennas and Propagation*, vol. 21, no. 4, pp. 532–538, 1973.

[21] C. A. Balanis, *Antenna theory: analysis and design*. John Wiley & Sons, 2008.

[22] R. F. Harrington, *Time-harmonic electromagnetic fields*. McGraw-Hill, 1961.

[23] Z. Liu, M. Bai, S. Ji, X. Fang, and X. Ye, "Impact on the performance of compact antenna test range due to surface deviation of the reflector," in *PIERS Proceedings*, 2014.

[24] L. H. Hemming, *Electromagnetic anechoic chambers*. Wiley Interscience, 2002.

[25] T.-H. Lee and W. D. Burnside, "Performance trade-off between serrated edge and blended rolled edge compact range reflectors," *IEEE Transactions on Antennas and Propagation*, vol. 44, no. 1, pp. 87–96, 1996.

[26] O. M. Bucci, M. D. Migliore, G. Panariello, and D. Pinchera, "Plane-wave generators: Design guidelines, achievable performances and effective synthesis," *IEEE Transactions on Antennas and Propagation*, vol. 61, no. 4, pp. 2005–2018, 2013.

[27] A. Capozzoli and G. D'Elia, "On the plane wave synthesis in the near-field zone," in *Proc. of the Int. Conf. on Antenna Tech., Ahmedabad, India*, pp. 273–277, 2005.

[28] H. Wang, J. Miao, J. Jiang, and R. Wang, "Plane-wave synthesis for compact antenna test range by feed scanning," *Progress In Electromagnetics Research M*, vol. 22, pp. 245–258, 2012.

[29] B. B. Baker and E. T. Copson, *The mathematical theory of Huygens' principle*, vol. 329. American Mathematical Soc., 2003.

[30] A. Ittipiboon, R. Oostlander, Y. M. Antar, and M. Cuhaci, "A modal expansion method of analysis and measurement on aperture-coupled microstrip antenna," *IEEE transactions on antennas and propagation*, vol. 39, no. 11, pp. 1567–1574, 1991.

[31] J.-C. Bolomey and F. E. Gardiol, *Engineering applications of the modulated scatterer technique*. Artech House, 2001.

[32] J. Richmond, "A modulated scattering technique for measurement of field distributions," *IRE Transactions on Microwave Theory and Techniques*, vol. 3, no. 4, pp. 13–15, 1955.

[33] J. G. Kostas and B. Boverie, "Statistical model for a mode-stirred chamber," *IEEE Transactions on electromagnetic compatibility*, vol. 33, no. 4, pp. 366–370, 1991.

[34] A. C. Newell, "Error analysis techniques for planar near-field measurements," *IEEE Transactions on Antennas and Propagation*, vol. 36, no. 6, pp. 754–768, 1988.

[35] M. Sierra-Castañer, A. Muñoz-Acevedo, F. Cano-Fácila, and S. Burgos, "Overview of novel post-processing techniques to reduce uncertainty in antenna measurements," *ADVANCED TOPICS IN MEASUREMENTS*, p. 179, 2012.

[36] M. Born and E. Wolf, *Principles of optics: electromagnetic theory of propagation, interference and diffraction of light*. CUP Archive, 2000.

[37] R. D. Straw, *The ARRL antenna book: The Ultimate Reference for Amateur Radio Antennas*. Amer Radio Relay League, 1980.

[38] M. M. Weiner, *Monopole antennas*. CRC Press, 2003.

[39] K. Fujimoto, *Mobile antenna systems handbook*. Artech house, 2008.

[40] S. L. C, "Radio antenna," July 28 1953. US Patent 2,647,211.

[41] S. Gregson, A. Newell, and G. Hindman, "Reflection suppression in cylindrical near-field antenna measurement systems–cylindrical mars," in *AMTA 31st Annual Meeting & Symposium, Salt Lake City, UT*, 2009.

[42] ISO, "80000-2: 2009," *Quantities and units–Part 2: Mathematical signs and symbols to be used in the natural sciences and technology*, 2009.

[43] S. J. Orfanidis, *Electromagnetic waves and Antennas, 2008*. Rutgers University, 2010.

[44] V. H. Rumsey, *Frequency independent antennas*. Academic Press, 2014.

[45] V. Rumsey, "Frequency independent antennas," in *1958 IRE International Convention Record*, vol. 5, pp. 114–118, IEEE, 1966.

[46] H. G. Schantz, *The art and science of ultrawideband antennas*. Artech House, 2015.

[47] A. Goldsmith, *Wireless communications*. Cambridge university press, 2005.

[48] G. H. Golub and C. F. Van Loan, *Matrix computations*, vol. 3. JHU Press, 2012.

[49] J. G. Van Bladel, *Electromagnetic fields*, vol. 19. John Wiley & Sons, 2007.

[50] K. Kuttler, *Linear algebra: theory and applications*. The Saylor Foundation, 2012.

[51] G. Strang and W.-C. Press, *Introduction to linear algebra*, vol. 3. Wellesley-Cambridge Press Wellesley, MA, 1993.

[52] N. J. Higham, "How accurate is gaussian elimination?," tech. rep., Cornell University, 1989.

[53] A. D. Polyanin and A. V. Manzhirov, *Handbook of mathematics for engineers and scientists*. CRC Press, 2006.

[54] R. C. Archibald, "Historical note on centers of similitude of circles," *The American Mathematical Monthly*, vol. 23, no. 5, pp. 159–161, 1916.

[55] B. Kim, "The circle of apollonius," *Mathematics Education Program J. Wilson, EMAT*, vol. 6690, 2009.

[56] G. Strang and W.-C. Press, *Introduction to linear algebra*, vol. 3. Wellesley-Cambridge Press Wellesley, MA, 1993.

[57] A. D. Polyanin and A. V. Manzhirov, *Handbook of mathematics for engineers and scientists*. CRC Press, 2006.

[58] G. Bartels, *GPS-antenna phase center measurements performed in an anechoic chamber*. Delft University Press, 1997.

[59] J. R. Wait, *Electromagnetic wave theory*. Harper & Row, 1985.

[60] D. M. Pozar, *Microwave engineering*. John Wiley & Sons, 2009.

[61] J. C. Stover, *Optical scattering: measurement and analysis*, vol. 2. SPIE optical engineering press Bellingham, 1995.

[62] G. D. Durgin, *The practical behavior of various edge-diffraction formulas*, vol. 51. IEEE, 2009.

[63] J. B. Keller, "Geometrical theory of diffraction*," *JOSA*, vol. 52, no. 2, pp. 116–130, 1962.

[64] A. Schuster, *An Introduction to the Theory of Optics*. E. Arnold, 1904.

[65] P. H. Pathak, G. Carluccio, and M. Albani, "The uniform geometrical theory of diffraction and some of its applications," *Antennas and Propagation Magazine, IEEE*, vol. 55, no. 4, pp. 41–69, 2013.

[66] R. G. Kouyoumjian and P. H. Pathak, "A uniform geometrical theory of diffraction for an edge in a perfectly conducting surface," *Proceedings of the IEEE*, vol. 62, no. 11, pp. 1448–1461, 1974.

[67] P. Y. Ufimtsev, "Method of edge waves in the physical theory of diffraction," tech. rep., DTIC Document, 1971.

[68] R. F. Harrington, *Field computation by moment methods*. IEEE Press, 1996.

[69] I. J. Gupta and W. D. Burnside, "Compact range measurement systems for electrically small test zones," *IEEE Transactions on Antennas and Propagation* , vol. 39, no. 5, pp. 632–638, 1991.

[70] J. Neter, M. H. Kutner, C. J. Nachtsheim, and W. Wasserman, *Applied linear statistical models*, vol. 4. Irwin Chicago, 1996.

[71] C. L. Lawson and R. J. Hanson, *Solving least squares problems*, vol. 15. SIAM, 1995.

[72] W. M. Lai, D. H. Rubin, D. Rubin, and E. Krempl, *Introduction to continuum mechanics*. Butterworth-Heinemann, 2009.

[73] S. Aiguo and L. Jiren, "Evolving gaussian rbf network for nonlinear time series modelling and prediction," *Electronics Letters*, vol. 34, no. 12, pp. 1241–1243, 1998.

[74] A. Torn and A. Zilinskas, *Global optimization*. Springer-Verlag New York, Inc., 1989.

[75] M. Avriel, W. E. Diewert, S. Schaible, and I. Zang, *Generalized concavity*, vol. 63. Siam, 2010.

[76] F. U. Manual, "Suite 7.0," *EM Software & Systems-SA (Pty) Ltd*, 2014.

[77] J. Song, C.-C. Lu, and W. C. Chew, "Multilevel fast multipole algorithm for electromagnetic scattering by large complex objects," *IEEE Transactions on Antennas and Propagation*, vol. 45, no. 10, pp. 1488–1493, 1997.

[78] F. C. Commission *et al.*, "Fcc report and order for part 15 acceptance of ultra wideband (uwb) systems from 3.1–10.6 ghz," *FCC, Washington DC*, 2010.

[79] J. Hartmann and D. Fasold, "Advanced serration design for compact ranges with utd," in *Proc. Antenna Measurements Technique Association, Symp., AMTA, Philadelphia, USA*, 2000.

[80] J. H. Jeans, *The mathematical theory of electricity and magnetism*. Cambridge University Press, 1908.

[81] J. D. Kraus, *Antennas*. {McGraw-Hill Education}, 1988.

[82] R. W. Klopfenstein, "Corner reflector antennas with arbitrary dipole orientation and apex angle," *Antennas and Propagation, IRE Transactions on*, vol. 5, no. 3, pp. 297–305, 1957.

[83] J. D. Kraus, "The corner-reflector antenna," *Proceedings of the IRE*, vol. 28, no. 11, pp. 513–519, 1940.

[84] E. Amador, *Modeles de compréhension par la théorie des images des phénomenes transitoires et du régime permanent en chambre réverbérante électromagnétique*. Emmanuel Amador, 2011.

[85] G. Breed, "Fundamentals of pulsed and time-gated measurements,"*Measurements*, vol. 2, p. 3, 2010.

Titre : Développement d'un Concept de Caractérisation Rapide d'Antennes Exploitant les Echos

Mots-clés : Caractérisation d'antennes, milieux non-anéchoiques, problèmes inverses

Résumé : Les techniques de mesure de diagramme de rayonnement d'antenne actuelles partagent un paradigme commun qui stipule que l'information utile est exclusivement portée par le signal de test généré. Cela implique un effort mécanique fastidieux en faisant tourner l'antenne sous test ou en déplaçant le système de sondes afin de couvrir des angles de mesure différents jusqu'à ce qu'une caractérisation complète soit effectuée ; une limitation qui est généralement surmontée en utilisant des systèmes multisondes coûteux. En outre, toute réflexion provenant du site de mesure et des équipements de test est considérée comme parasite perturbant le signal de test et ainsi elle est minimisée. Dans cette thèse, un concept de mesure du diagramme de rayonnement d'antenne remettant en cause ce paradigme commun est présenté comme un moyen d'accélérer le processus de caractérisation en utilisant des systèmes économiques. Le paradigme proposé consiste en la génération d'un ensemble d'échos contrôlés, en utilisant des configurations impliquant des plaques réfléchissantes, qui contribueraient directement à la mesure en couvrant différents angles, et récupérer les informations portées par l'ensemble des signaux générés simultanément. Une diversité fréquentielle est introduite afin de générer un système d'équations équilibré où le vecteur inconnu contenant les valeurs du diagramme de rayonnement est récupéré en inversant un problème matriciel. Par conséquent, une attention considérable est accordée au conditionnement du modèle mathématique afin d'assurer la stabilité et la robustesse du système. Trois configurations de différents niveaux de complexité en termes d'échos contrôlés sont étudiées, en mettant l'accent sur la configuration la plus simple impliquant un seul écho contrôlé. Des modèles ont été mis au point, avec des contraintes de conception des configurations proposées en termes de dimensionnement et de bandes passante de fonctionnement, mettant en évidence la viabilité mathématique du concept. Les aspects pratiques ont également été évalués en étudiant la tolérance des modèles développés vis-à-vis des erreurs systématiques, ainsi qu'à l'impact de l'application d'un ensemble d'hypothèses simplificatrices. La faisabilité du concept ainsi que son utilité pour accélérer le processus de caractérisation par rapport aux techniques classiques ont été mises en évidence par des simulations numériques. Ce travail ouvre la porte à l'exploitation des échos, généralement considérés comme perturbateurs, dans un contexte de mesure d'antennes.

Titre : Design of a Fast Antenna Characterization Method Exploiting Echoes

Keywords : Antenna radiation pattern measurements, non-anechoic environments, inverse problems

Abstract : Current antenna radiation pattern measurement techniques share a common paradigm which states that useful information is exclusively carried by the generated test signal. This implies an excessive, time consuming, mechanical effort by rotating the antenna under test or displacing the probe system in order to cover different measurement angles until a complete scan is performed ; a limitation that is typically overcome using costly multi-probe systems. Moreover, any reflection from the measurement site and test equipment is considered spurious as it perturbs the test signal and thus is minimized. In this thesis, an antenna radiation pattern measurement concept challenging this common paradigm is introduced as a mean of accelerating the characterization process using cost-efficient systems. The proposed paradigm consists in the generation of a set of controlled echoes, using set-ups involving highly-reflective plates, which would directly contribute to the measurement alongside the line-of-sight signal by covering different measurement angles, and retrieving the ARP information carried by the set of all generated signals concurrently. Frequency diversity is used in order to generate a balanced system of equations where the unknown ARP vector is retrieved by inverting a matrix problem. Consequently, a considerable attention is paid into the conditioning of the mathematical model in order to ensure the system stability and accuracy. Three configurations of different complexity levels in terms of controlled echoes are studied, with focus on the simplest configuration involving a single controlled echo. Models have been developed with design guidelines for the proposed configurations in terms of set-up dimensions and operating frequency bandwidth highlighting the mathematical viability of the concept. Practical issues were also assessed by studying the tolerance of developed models to systematic practical errors, as well as to the impact of an applied set of simplifying assumptions. The feasibility of the concept as well as its usefulness in accelerating the measurement process with respect to classical techniques were highlighted via numerical simulations. This thesis opens the door for exploiting echoes, generally regarded as a nuisance, in an antenna measurements context.

Université Paris-Saclay
Espace Technologique / Immeuble Discovery
Route de l'Orme aux Merisiers RD 128 / 91190 Saint-Aubin, France